



Out-of-equilibrium self-assembly approaches for new soft materials

Wouter E. Hendriksen

Out-of-equilibrium self-assembly approaches for new soft materials

Uit-evenwicht zelfassemblage methoden
voor nieuwe zachte materialen

Proefschrift

ter verkrijging van de graad van doctor
aan de Technische Universiteit Delft,
op gezag van de Rector Magnificus Prof. Ir. K. C. A. M. Luyben,
voorzitter van het College voor Promoties
in het openbaar te verdedigen op

3 december 2015 om 15.00 uur

door
Wouter Egbert-Jan HENDRIKSEN

Master of Science in Chemical Engineering,
Technische Universiteit Delft
geboren te Beverwijk, Nederland

Dit proefschrift is goedgekeurd door de
promotor: Prof.dr. J. H. van Esch
copromotor: Dr. R. Eelkema

Samenstelling promotie commissie:

Rector Magnificus	voorzitter
Prof.dr. J. H. van Esch	Technische Universiteit Delft
Dr. R. Eelkema	Technische Universiteit Delft

Onafhankelijke leden:

Prof. W. T. S. Huck	Rijks Universiteit Nijmegen
Prof. dr. ir. M.T. Kreutzer	Technische Universiteit Delft
Prof. dr. E.J.R. Sudhölter	Technische Universiteit Delft
Dr. T.M. Hermans	Université de Strasbourg
Prof. dr. S. J. Picken	Technische Universiteit Delft

Andere leden:

Prof. dr. ir. L. Brunsveld	Technische Universiteit Eindhoven
----------------------------	-----------------------------------

The work described in this thesis was carried out in the Advanced Soft Matter (ASM) group at the Technische Universiteit Delft, Faculty of Applied Sciences, in the department of Chemical Engineering. This research has been funded by the Netherlands Organization of Scientific Research (NWO), as part of the Complexity program.

© 2015, Wouter E. Hendriksen




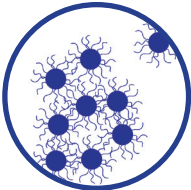
ISBN: 978-94-6186-559-5

Uitgeverij: TU Delft Library
Printed by: Gilderprint, Enschede



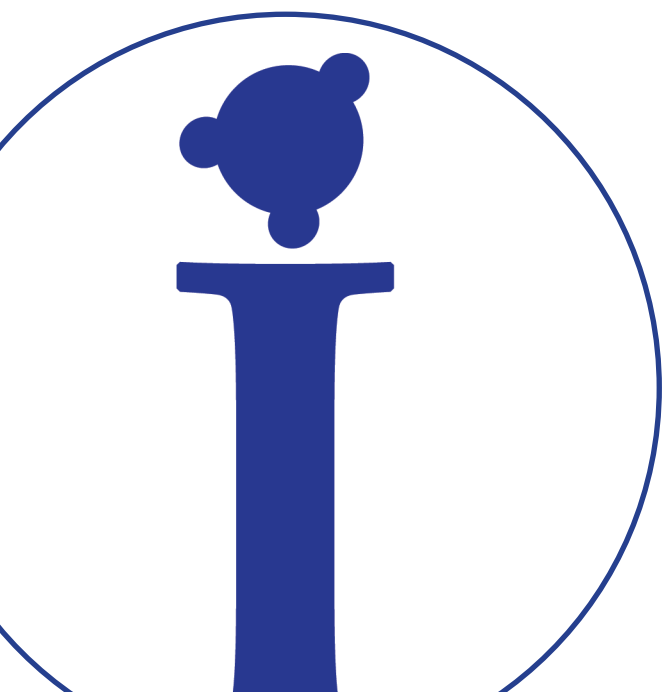
All rights reserved. The author encourages the communication of scientific contents and explicitly allows reproduction for scientific purpose, with proper citation of the source. Parts of this thesis have been published in scientific journals and copyright is subjected to different terms and conditions.

Table of contents

Chapter 1. Introduction	1	
1.1 Necessity of new material approaches		
1.2 Complexity in materials		
1.3 Challenges		
1.4 Outline of thesis		
1.5 References		
Chapter 2. Spatial and transient self-assembly for complexity in materials	7	
2.1 Introduction		
2.2 Soft matter, self-assembly and materials		
2.3 Reaction-diffusion, patterns and organization		
2.4 Out-of-equilibrium self-assembly		
2.5 Perspective on Nature inspired complex materials		
2.6 References		
Chapter 3. Transient assembly of active materials fueled by a chemical reaction	23	
3.1 Introduction		
3.2 Results and discussion		
3.3 Conclusions		
3.4 Experimental section		
3.4.1 Materials		
3.4.2 Methods		
3.4.3 Supporting experiments		
3.5 References		
Chapter 4. Out-of-equilibrium self-assembly of colloidal particles driven by a chemical fuel	59	
4.1 Introduction		
4.2 Results and discussion		
4.3 Conclusions		
4.4 Experimental section		
4.5 References		

Chapter 5. Non-equilibrium molecular self-assembly	73
5.1 Introduction	
5.2 General principles	
5.3 Fuelled self-assembly	
5.4 Bistability	
5.5 Autocatalysis	
5.6 Role of non-equilibrium thermodynamics for self-assembly	
5.7 Conclusion	
5.8 References	
Chapter 6. Spatial and chemical controlled self-assembled material by reaction-diffusion	93
6.1 Introduction	
6.2 Results and discussion	
6.3 Conclusions	
6.4 Experimental section	
6.5 References	
Chapter 7. Supramolecular binding of proteins to lipid bilayers	113
7.1 Introduction:	
7.2 Results and discussion	
7.3 Conclusions	
7.4 Experimental section	
7.5 References	
Summary	134
Samenvatting	136
Acknowledgements	138
About the author	143





Introduction

1.1 Necessity of new material approaches

Reasons to pursue scientific research are to explore new possibilities, to solve societal problems and to gain insights to how nature functions. Chemistry combines curiosity and utility to the service of mankind (1, 2). Functional materials are the chemical answer to solving societal problems and time is pressing to develop new solutions. The wide variety of current societal problems, such as the environmental impact of plastics, CO₂, energy storage, (chemical) pollution, and shortage of rare earth metals, ask for completely new solutions and innovative materials. An important challenge is the development of materials that can be recycled, or reused (2).

We curiously wonder how new solutions might be inspired by natural systems and how new insights can be applied. Zooming in on biological cells, one can observe many essential and fascinating processes occurring, such as cellular communication and transport, motility, and the dynamics of the cytoskeleton during multiplication (3). To organize and achieve functionality, these cellular systems use different approaches, such as reaction networks within multiple compartments, out-of-equilibrium self-assembly and reaction-diffusion processes (4-6). As such, cells achieve a complex microarchitecture of multiple compartments and structures, regulate dynamic patterns, show self-healing behavior and recycle building blocks. All these processes occur out-of-equilibrium under the consumption of energy and matter. Cells are a fascinating inspiration for new material approaches, but only if the principles can be translated to functional synthetic systems.

Nature is all about dynamics and biological materials are typically part of an energy or material loop in which they can be reused or recycled (3). This requires the input of energy in such a way that it is applied to the formation of materials. Nature applies the 'spontaneous' assembly of small molecules to build materials and structures, for example cell membranes and microtubules. In these materials, the self-assembly of small molecular building blocks is combined with activating reactions, that supply energy to the system and control dynamic structure formation. After activation of the building blocks the formed materials reside out-of-equilibrium. Over time, they will decay back to the original non-active building blocks and waste products, ready for a new cycle. In this fashion, micro- and macroscopic materials are formed out-of-equilibrium and can be controlled through chemical and/or physical parameters. Within the complexity of cells, these processes are an essential part of the spatial differentiation and transient self-organization. These out-of-equilibrium self-assembled materials offer an important scientific and technological opportunity (4).

1.2 Complexity in materials

An objective of this research is to combine insights of Complexity science with Material sciences. What is complexity in materials, can we synthesize a material with complex

properties? Complexity is the broadest research field to date, crossing bridges between chemistry, informatics, biology, physics, medical fields, ecology and many other fields (7). The uniqueness of this joint effort is that each subfield has a new viewpoint towards complexity and brings in new aspects, typical phenomena are for example networks, temporal oscillations and spatial patterns. However, across these fields one recognizes the synchronicity in these phenomena that seem to contain universal signatures.

A possible description of a complex system is the emergence of properties in a large group of interacting components, which are driven by local forces (8). These interactions can lead to different kind of patterns and shapes in materials that are expressed in both space and time. Examples of these patterns are zebra fish stripes (5), Ca^{2+} signaling waves between cells (9) and the dynamic nature of microtubules within cells (6). An interesting example of complexity in a large group of interacting components, is the behavior of a school of fish (4). The dynamics of the school can be described by a simple set of rules for the individual fish and through the interactions between the fish, results in the macroscopic behavior of the school of fish (10). These complex systems are typically non-linear in their dependence on the number of components and /or interactions, which makes them challenging to analyze. Complexity might be described as the not yet understanding of all these interactions and functions that lead to the complex organization of for example a cell or any living matter (11-16).

For complexity in chemistry, two research topics are typically considered important: reaction-diffusion (RD) systems and out-of-equilibrium self-assembly. The field of RD obtained its inspiration from the emergence of patterns in biological materials, such as the zebra fish skin patterns. The initial experimental developments in this field date back to the 1900s and more theoretical insights were obtained after the work of Turing in 1950s (16, 17). In RD systems two processes occur simultaneously, the diffusion of species and the reactions between these species, which can result in ordered patterns. The well-studied oscillating system of the Belousov-Zhabotinsky (BZ) reaction (18), has led to the development of a mature research field with theoretical understanding of non-linearity and pattern formation (19). So far, organic chemistry has not been extensively been applied in RD systems.

Out-of-equilibrium self-assembly is an important aspect in natural systems and scientific interests dates back to the initial works by Prigogine in the 1970s on dissipative self-sustained structures (20). In these systems, self-assembled states occur outside of equilibrium and require the continuous influx of energy to sustain stable states (21). These states therefor show a dependence on the energy flux through the system resulting in properties such as adaptability, self-healing and recyclability. As the natural patterns and dynamic cellular behavior are an important motivation for studying RD and out-of-equilibrium self-assembled systems, it is surprising that so far only limited research has been performed on molecular systems for these approaches. Such molecular systems will lead to the development of new types of materials, with the related potential applications.

Natural systems and materials also pose challenges for new developments. Questions that need to be addressed are; which component is the most important in a complex material and how do the multiple interactions work together for obtaining a working system? To partly solve these questions research is done by extracting or producing the natural components of complex systems and searching for the minimal components necessary to obtain a functional system. Partly this research is limited by the high costs, economic and time, involved for these natural systems. These costs pose a potential risk for future applications of the envisioned research.

1.3 Challenges

In the current thesis we address multiple challenges to develop new material approaches based on the combination of self-assembly, reaction-diffusion and out-of-equilibrium processes. Active out-of-equilibrium materials are a step towards programmable materials, where the properties are determined by chemical fuels, time and reaction conditions. Self-healing behavior and recyclability of the initial compounds offer an attractive method for more sustainable applications of materials. Although the inspiration comes from the microscopic level of cells, future applications are envisioned to be macroscopic materials. In the process towards the self-organization of materials in space and time, the combination of reaction-diffusion with organic self-assembly offers the possibility to manipulate material shapes and patterns. The capability to construct and organize materials across multiple length scales, from the diffusion gradients of pre-patterned components offers an attractive potential for materials sciences. To use the versatility of proteins and enzymes, methods need to be developed for binding of these proteins to self-assembled materials in a reversible fashion.

The developments as described in this thesis are aimed at achieving the fascinating properties and functionalities similar to those observed in natural systems, with control over transient material formation and interactions with biological systems. However, scientists should not (re)produce living systems, but be inspired by and apply the observed fascinating functionalities of biological systems to new materials.

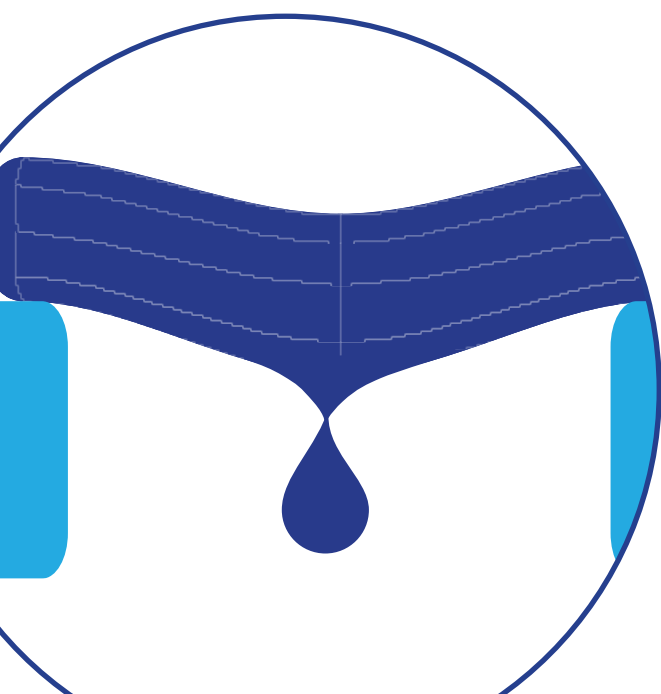
1.4 Outline of thesis

The aim of this work is to develop new approaches for soft materials, by self-assembly and out-of-equilibrium processes. Chapter 2 presents a literature overview of self-assembly, reaction-diffusion and out-of-equilibrium self-assembly. The chapter gives an insight to how biological systems combine these three aspects and what the current state-of-the-art is in science. Chapter 3 represents a general approach towards out-of-equilibrium formation of materials driven by a chemical reaction. Our design leads to control over material properties, such as stiffness and lifetimes, and strikingly shows a

microscopic dynamic behavior similar to that observed in microtubules, which formed the inspiration of the design. Chapter 4 represents an extension of the out-of-equilibrium self-assembly design towards the colloidal regime. In Chapter 5 a thermodynamic discussion is presented on out-of-equilibrium self-assembly. The introduction of reaction diffusion combined with organic self-assembly is discussed in Chapter 6. Here we show the formation of self-assembled structures of which shape and dimensions can be controlled. We further show the functionalization of the supramolecular structures with protein recognition sites. In the final Chapter 7, a supramolecular construct is presented for reversible binding of proteins to self-assembled bilayers.

1.5 References:

1. G. Whitesides, What Will Chemistry Do in the Next Twenty Years? *Angewandte Chemie International Edition in English* **29**, 1209-1218 (1990); DOI:10.1002/anie.199012091.
2. G. M. Whitesides, Reinventing Chemistry. *Angewandte Chemie International Edition* **54**, 3196-3209 (2015); DOI:10.1002/anie.201410884.
3. B. Alberts, A. Johnson, J. Lewis, M. Raff, K. Roberts, P. Walter, *Molecular Biology of the Cell*. (Garland Science, ed. 4th, 2002).
4. G. M. Whitesides, B. Grzybowski, Self-Assembly at All Scales. *Science* **295**, 2418-2421 (2002); DOI:10.1126/science.1070821.
5. S. Kondo, T. Miura, Reaction-Diffusion Model as a Framework for Understanding Biological Pattern Formation. *Science* **329**, 1616-1620 (2010); DOI:10.1126/science.1179047.
6. A. Desai, T. J. Mitchison, MICROTUBULE POLYMERIZATION DYNAMICS. *Annual Review of Cell and Developmental Biology* **13**, 83-117 (1997); DOI:10.1146/annurev.cellbio.13.1.83.
7. G. M. Whitesides, R. F. Ismagilov, Complexity in Chemistry. *Science* **284**, 89-92 (1999); DOI:10.1126/science.284.5411.89.
8. N. Boccarda, *Modeling Complex Systems*. Graduate Texts in Physics (Springer New York, New York, NY, 2010).
9. E. A. Newman, K. R. Zahs, Calcium Waves in Retinal Glial Cells. *Science* **275**, 844-847 (1997); DOI:10.1126/science.275.5301.844.
10. K. Tunström, Y. Katz, C. C. Ioannou, C. Huepe, M. J. Lutz, I. D. Couzin, Collective States, Multistability and Transitional Behavior in Schooling Fish. *PLoS Comput Biol* **9**, e1002915 (2013); DOI:10.1371/journal.pcbi.1002915.
11. B. A. Grzybowski, K. J. M. Bishop, C. J. Campbell, M. Fialkowski, S. K. Smoukov, Micro- and nanotechnology via reaction-diffusion. *Soft Matter* **1**, 114-128 (2005); DOI:10.1039/B501769F.
12. K. F. Mueller, Periodic Interfacial Precipitation in Polymer Films. *Science* **225**, 1021-1027 (1984); DOI:10.1126/science.225.4666.1021.
13. S. Kondo, R. Asai, A reaction-diffusion wave on the skin of the marine angelfish *Pomacanthus*. *Nature* **376**, 765-768 (1995); DOI:10.1038/376765a0.
14. M. M. Ayass, M. Al-Ghoul, I. Lagzi, Chemical Waves in Heterogeneous Media. *The Journal of Physical Chemistry A*, (2014); DOI:10.1021/jp509246s.
15. A. Nakamasu, H. Nakayama, N. Nakayama, N. J. Suematsu, S. Kimura, A Developmental Model for Branching Morphogenesis of Lake Cress Compound Leaf. *PLoS ONE* **9**, e111615 (2014); DOI:10.1371/journal.pone.0111615.
16. A. M. Turing, The Chemical Basis of Morphogenesis. *Philosophical Transactions of the Royal Society of London B: Biological Sciences* **237**, 37-72 (1952); DOI:10.1098/rstb.1952.0012.
17. R. E. Liesegang, Über einige eigenschaften von gallerten. 353-362 (1896).
18. A. N. Zaikin, A. M. Zhabotinsky, Concentration Wave Propagation in Two-dimensional Liquid-phase Self-oscillating System. *Nature* **225**, 535-537 (1970); DOI:10.1038/225535b0.
19. I. R. Epstein, K. Showalter, Nonlinear Chemical Dynamics: Oscillations, Patterns, and Chaos. *The Journal of Physical Chemistry* **100**, 13132-13147 (1996); DOI:10.1021/jp953547m.
20. G. Nicolis, I. Prigogine, *Self-Organization in Nonequilibrium Systems: From Dissipative Structures to Order Through Fluctuations*. (Wiley, New York, 1977).
21. M. Fialkowski, K. J. M. Bishop, R. Klajn, S. K. Smoukov, C. J. Campbell, B. A. Grzybowski, Principles and Implementations of Dissipative (Dynamic) Self-Assembly. *The Journal of Physical Chemistry B* **110**, 2482-2496 (2006); DOI:10.1021/jp054153q.



2

**Spatial and transient self-assembly for
complexity in materials**

2.1 Introduction

The functionality and complexity of Natural systems is a great inspiration for scientists and engineers, especially for the design and synthesis of new materials (1, 2). Self-healing, movement, growth, adaptability and pattern formation are examples of biological phenomena that acted as inspiration for new artificial designs. Biological systems achieve and maintain these intricate functions, tasks and structures by operating out-of-equilibrium through the consumption of energy and matter. Spatial differentiation of these transient supramolecular systems is achieved by the reaction and diffusion of molecular components (3, 4). The use of out-of-equilibrium self-assembly and reaction-diffusion will lead to the development of bio-inspired programmable materials by combining developments in the fields of chemistry, biology, physics and mathematical modeling (5, 6).

In Nature, multiple components self-assemble into functional structures, within cells for example double stranded DNA, folded proteins, and cellular membranes (7). The dynamics in cells are the archetypical example of the complexity within biological systems. These cellular dynamics are organized as reaction networks within multiple compartments with the aim to achieve a variety of functions, and through out-of-equilibrium self-assembly and reaction-diffusion processes these biological functions are achieved (8). Mitosis, the division of cells, is a remarkable example of how out-of-equilibrium self-assembled materials can perform intricate tasks, controlled in both spatial and temporal dimensions (9). During mitosis the parent DNA of the cell is replicated and split into two different sets of chromosomes, one for each corresponding nucleus (9-11). In the initial steps of this process, the replicated DNA ‘daughters’ are moved into opposite direction by self-assembled microtubule. The microtubules assemble out-of-equilibrium through the consumption of guanosine triphosphate (GTP) as a chemical fuel. Subsequently, motor proteins transport the DNA spindles over the microtubules (12). Reaction-diffusion processes of the molecular components contribute to the spatial organization, leading to the orientation in opposite directions (13, 14). Eventually the DNA ‘daughters’ are captured within a self-assembled membrane, forming the nucleus. This

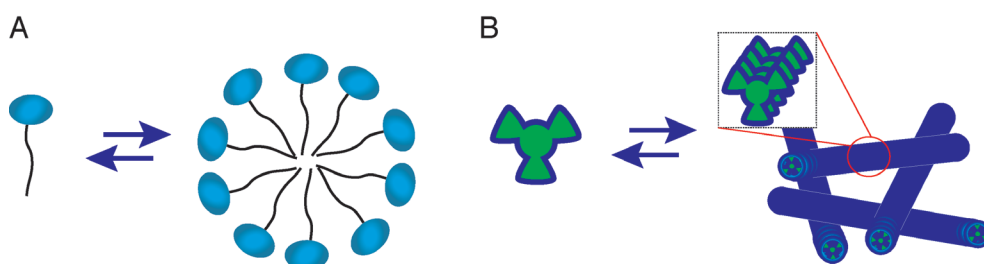


Figure 2.1 Self-assembly of monomers into ordered structures. Illustrations of surfactants that self-assemble into micelles (A) and small molecule gelators that self-assemble into a fibrous network (B).

simplistic description of a process that is essential to all living creatures, illustrates how the combination of self-assembly, out-of-equilibrium processes and reaction diffusion phenomena form a complex system that performs tasks in a spatial differentiated and transient manner.

In this chapter an overview is given of self-assembly, reaction-diffusion and out-of-equilibrium self-assembly. First, the basics of Self-Assembly (SA) are discussed for understanding how small molecules form well defined structures. To gain insights to how material shapes and patterns are formed in space, Reaction-Diffusion (RD) is introduced. Next, recent developments in out-of-equilibrium self-assembly are discussed for understanding the basics of time dependent properties. Finally, the main challenges for this thesis are placed in perspective.

2.2 Soft matter, self-assembly and materials

The spontaneous assembly of small molecules into well defined structures and materials, held only together by non-covalent interactions, offers great potential for both the development of materials and for understanding the fundamental processes of living systems (1, 8, 15). Some of the first discovered self-assembled structures, made from bile salts, puzzled researchers and they named these observed macromolecular structures 'complex' (16). In the last decades the field of small molecule SA has been expanding rapidly leading to new developments such as drug delivery systems (17), food products (18), cleanup of oil spills (19) and materials for cell growth (20).

SA of molecular monomers into ordered structures forms a simple approach to functional supramolecular materials (Fig. 2.1) (15, 21). At thermodynamic equilibrium conditions, these supramolecular materials assemble spontaneous and under changing conditions can be formed reversible. The flexibility in molecular design and self-organization into supramolecular structures makes SA materials attractive for applications (19). The incorporation of functional groups in small molecule SA offers the possibility to tune the functionality of supramolecular materials at the molecular level (21-23). When the SA molecules can be switched between aggregating and non-aggregation by a trigger, the materials become responsive and adaptive to external stimuli, for example as seen in gelation triggered by pH, temperature or light (21).

The self-assembly process of small molecules into larger aggregates can be described by using a simple model in which the monomers and aggregates are in equilibrium, also see Chapter 5 (15). The aggregates (A_n) consist of n monomers (M), with n being the aggregation number and monomers being for example surfactants or gelators (eq. 1). The formation of the aggregates then occurs above the critical aggregation concentration (CAC). At this concentration the chemical potentials of the monomers (μ_M) and aggregates (μ_N) are equal, and added monomers will form new aggregates to balance the potentials (eq. 2-3) (15).

$$nM \rightleftharpoons A_n \quad (1)$$

$$\mu_M^\theta + RT \ln x_M = \mu_n^\theta + \frac{RT}{n} \ln \frac{x_n}{n} \quad (2)$$

$$\frac{x_T}{x_{cac}} = \frac{x_M}{x_{cac}} + \frac{n(K * x_M)^n}{x_{cac}} \quad (3)$$

From this simple model an important insight is obtained, through the realization that in equilibrium there is a continuous exchange of monomers between the solution phase and the aggregated structures. These exchange dynamics are controlled by the rates of molecules binding and releasing and lifetimes range from very short for micelles to long for bilayers, from 15 μ s up to 100 hr. respectively (15). These dynamics are important to enable the aggregates to respond to changes in environmental conditions, self-healing behavior, and growth-shrinkage dynamics (7, 21).

Another important feature of self-assembly, is the assembly of molecular monomers, with sizes of angstroms (\AA), into structures with sizes ranging in the order of nanometer (nm) to micrometer (μ m) (15, 19). This formation of structures, aggregates or materials is interesting for applications, especially as this is typically in size ranges that are otherwise unpractical for top-down manufacturing strategies (24, 25).

Supramolecular self-assembly of small molecules produces ordered structures, which are functional and continuously exchange with the environment. Nature creatively uses self-assembly to make dynamic, and spatially distributed structures and materials, for functions such as communication, transport and movement.

2.3 Reaction-diffusion, patterns and organization

Reaction-diffusion offers an attractive strategy to control the spatial distribution of materials. In the Reaction-Diffusion (RD) model, reactants diffuse and react over time forming gradients of the product within the diffusion media. Additional interactions, such as autocatalysis or precipitation, lead to spatial and/or temporal structures that can be observed and applied (26-29). Two of the early pioneers of the RD phenomena were Liesegang with periodic precipitations in 1896 (32), and Luther with propagating waves in 1906 (33). Both realized that RD processes are important for the self-organization of molecules into patterns with length scales up to centimeters. It was the mathematician Turing who later proposed that the principles of RD could be responsible for morphogenesis in living systems (29). Today, the RD model is used to understand and study a wide variety of phenomena, such as rock (28, 34-36) and skin patterns (37, 38), bacterial colonization (39), Ca^{2+} propagating waves (40, 41) and morphogenesis (29) (Fig. 2.2). The periodic precipitations of Liesegang rings (42, 43) also have a remarkable resemblance to patterns as found in natural minerals with compositional zoning, such as Zebra rock (34) and iris agate (35) (Fig. 2.2 A,B). In recent years artificial periodic

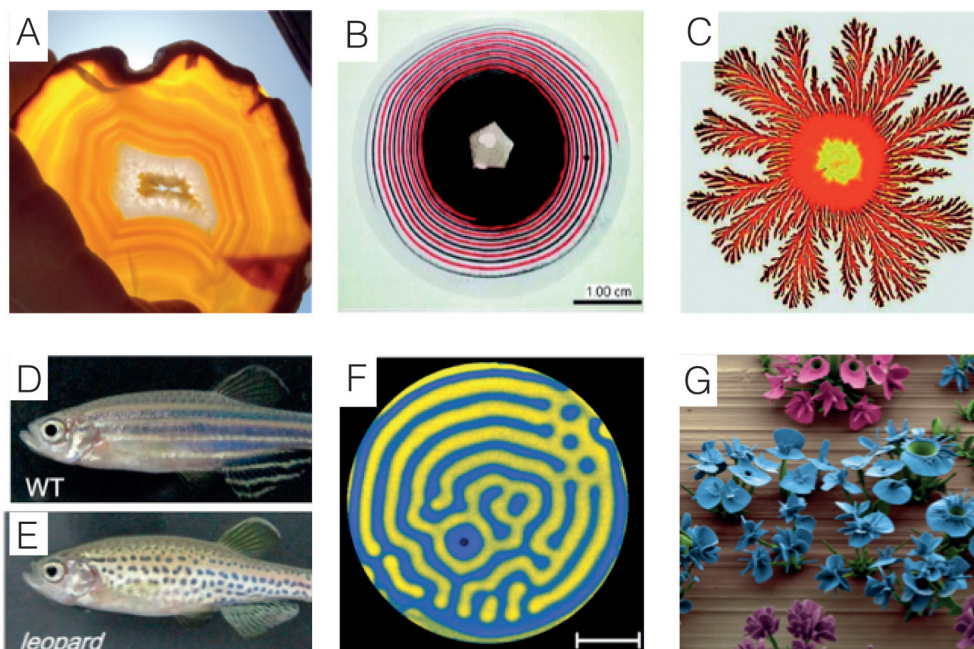


Figure 2.2 Pattern and structure formation in natural (A, C, D, E) and artificial systems (B, F, G). (A) Brazilian iris agate with rings as seen against the sun. (B) A two dimensional Liesegang pattern, in which a double spiral is observed (47). (C) Branching pattern of a *P. dendritiformis* bacteria (48). (D) Wild type (WT) zebra fish and a leopard zebra fish (E)(49), with skin patterns that have a resemblance to Turing patterns (F)(50). Hierarchical microarchitectures made of silicates in gradients of carbon dioxide (G)(44). (A) Image courtesy of Rock-your-world-gems.

precipitation systems have been used for constructing microarchitectures (44, 45) and in optical applications (28, 46).

The basic principles of RD systems can be illustrated by an example of an application in the medical field. In medical analysis, RD of antigens and antibodies is used to identify and quantify the antibodies by formation of precipitation lines (30, 31). This is performed in a simple RD setup, where a sample containing antigens is placed in the center of a diffusion matrix, with known antibodies placed around it at a fixed distance (Fig. 2.3). The components diffuse towards each other and react at the crossing of the gradients to form complexes (Fig. 2.3B). These complexes are observed as white precipitates in the diffusion matrix and can be used to identify the antigen-antibody complexes. This illustrates the basic principles of RD systems, where multiple components diffuse and upon crossing react, to form gradients and patterns of the reaction products.

Despite the resemblance between artificial and natural RD systems, a proper understanding of the biological oscillating RD mechanisms is still in the making. The theoretical work on RD systems by of Luther and Turing laid the basis for the developments in propagating RD waves of oscillating reactions (26). Within chemical

sciences, a seminal reaction used to investigate RD phenomena is the oscillating Belousov-Zhabotinsky reaction (51). A solid theoretical understanding of pattern formation in RD processes has been obtained from studies on this system, which have found in 2D and 3D to form spiral waves, chaotic patterns and Turing patterns (26, 52-54). Systematic analysis of these patterns formed by chemical oscillators has been achieved through the introduction of continuously fed unstirred reactors, where component diffuse in a thin inert gel layer visualizing spatial patterns (55-59).

Computational studies show the potential of RD mechanisms for the formation of patterns. For most of the inorganic artificial systems the reaction and diffusion parameters are however hard to adjust, which limits the possibilities. To overcome these challenges new approaches are being developed, for example on the basis of DNA systems (60, 61). By ‘programming’ new chemical reaction networks, with orthogonal control over the reaction and diffusion rates arbitrary patterns were achieved. For example, attaching an inactive drag block on the DNA sequence led to slower diffusion and ‘programmed’ differences in front propagating behavior(60).

The combination of self-assembly and RD allows for the construction and self-organization of matter across multiple length scales and is of increased interest for material science (62-65). The propagating diffusion fronts interplay with reaction and self-assembly processes, and the self-assembling molecules organize into long-range patterns upon crossing of the critical aggregation concentrations. For nano-sized particles and crystallites in viscous environments, studies have shown that the morphology and chemical activity influenced the front propagation and thus affected the location where the self-assembled structures are formed (66, 67). Remarkably, the use of organic chemistry and SA for RD systems remains largely unexplored and in Chapter 6 we show a new approach towards organic RD based materials, with control over dimension and chemical functionality.

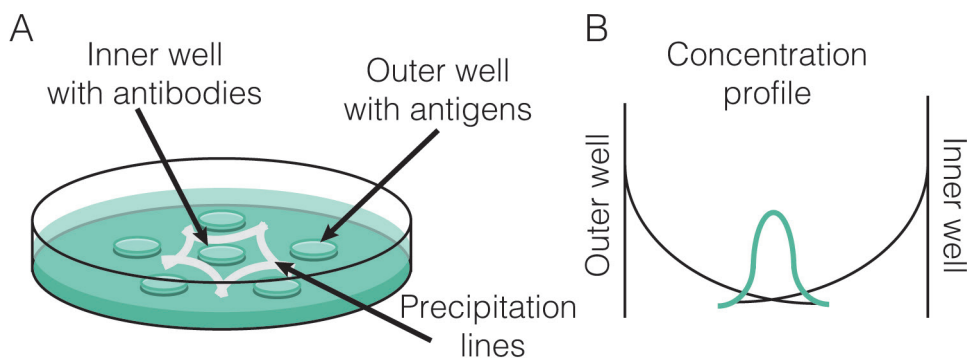


Figure 2.3 Reaction-diffusion in an Ouchterlony test. (A) Ouchterlony agar matrix, with cut out wells. Inner well contains antibodies, outer wells contain antigens. (B) Illustration of concentration profile between inner and outer well of antibodies and antigens, with in the middle the precipitate concentration.

In conclusion, the field of RD offers a toolbox and theoretical understanding for development of organized materials across multiple length scales. New types of materials are foreseen through the use of RD systems combined with organic SA, in which the RD parameters can be used for organizing material structures and shapes.

2.4 Out-of-equilibrium self-assembly

Self-assembly of structures under out-of-equilibrium conditions is an exciting scientific challenge and offers insights into the complexity of natural systems. In cells and tissue, self-assembly creates dynamic aggregates that are formed driven by energy conversion. This out-of-equilibrium self-assembly in cells creates adaptive, organized and self-replication behavior that depend on the energy delivered. Here we discuss the developments in recent years that come from four research fields: artificial cells, fuel driven nano-propulsion, out-of-equilibrium self-assembling systems and materials. First artificial cells are discussed to illustrate the potential of SA systems on their way towards equilibrium. Second, the use of chemical fuels is introduced by fuel driven motion of nanoparticles. Then the self-assembly in out-of-equilibrium systems is discussed to relate energy dissipation with self-assembly. Finally, the formation out-of-equilibrium materials are treated in which a fuel driven chemical reaction activates a molecular self-assembly process.

Artificial cells

A growing interest is seen in the development of artificial cells, which are inspired by the complexity of the natural machinery within cells (68, 69). Scientists are developing the most important aspects, such as the cellular compartments and the multiplication of these 'cells' (Fig. 2.4A)(70, 71), and information multiplication within the 'cells' (72). For example, biochemical reaction networks for the transcription and translation machinery were incorporated in liposomes. These systems were then used for the multiplication of DNA and synthesizing proteins from DNA templates, through the supply of molecular components (72-74). Fascinatingly, recently it has been shown that the interactions between self-replication of DNA and self-reproduction of cellular membranes seem to control each other (75). It was observed that the cellular mimics that did not show DNA replication also did not show membrane reproduction, indicating cross-functional effects that were not anticipated (Fig. 2.4B). These small steps towards the development of artificial cells are interesting for the aim of 'growing' materials (71, 76). As mimics, these systems typically are on their way towards equilibrium, whereas biological growing cells require the continuous input of energy and matter to synthesize the building blocks and assemble the constructs. This input of 'energy' for the growth and multiplication for artificial cells offers a future challenge towards biomimetic systems.

Fuel driven propulsion

Achieving autonomous movement through the consumption of a fuel, much like an ordinary car but then on the nano scale, is a highly interesting development in current sciences and relates to the consumption of energy for function (77). Researchers have developed propulsion systems for nano-sized particles that use chemical fuels for mechanical motion (78). The decomposition reaction of dissolved H_2O_2 to H_2O and gaseous O_2 is typically used and is localized by using a metal catalyst. By placing the platinum (Pt) catalysts within a stomatocyte, the decomposition reaction of the fuel H_2O_2 to O_2 took place in the inner part and the expulsion of the gaseous waste product led to motion in the opposite direction (Fig. 2.5A)(79). Such momentum induced propulsion approaches have been successfully applied in different systems to achieve translational and rotational movement, using for example catalytic metal particles or immobilized molecular catalysts for localization of the reaction (80-82).

The combination of self-assembly and localized catalysts offer another approach to achieve fuel driven motion (fig 2.5C)(83). In such a system, a quantum dot has an enzyme attached to its surface to localize the motion inducing reaction. The motion is induced by the activation of precursor, yielding a peptide based gelator, which is capable

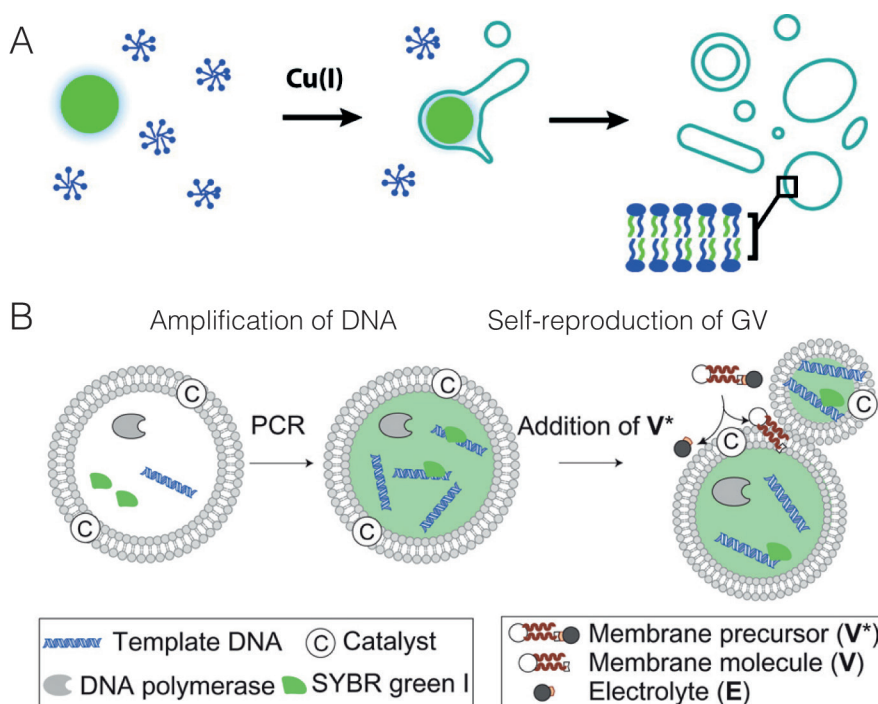


Figure 2.4 Artificial cell with multiplication. (A) Devaraj et al. showed a biomimetic model of membrane assembly, with a copper catalyzed click reaction forming a synthetic phospholipid (76). (B) Sugawara et al. found a chemical interaction between amplification of DNA (B-I, self-replication) and the self-reproduction of vesicles (B-II) (75).

of self-assembling. The biocatalytic activation of the precursor induced localized self-assembly forming fibrous structures on the surface of the quantum dot, which led to propulsion (84). This approach is similar to the biological propulsion of the bacteria *Listeria monocytogenes*, through the polymerization of actin (85). These examples show the relevance of motion in biological systems and the potential of coupling self-assembly with enzymatic reactions, for the propulsion of a nanoparticle carrier (86, 87).

Fuel driven movement is a first step towards out-of-equilibrium systems, which change in space and time and are inspired by biological examples. Autonomous movement can be induced by momentum or self-assembly processes, with catalysts localized to surfaces of the moving particles.

Out-of-equilibrium systems

In out-of-equilibrium systems, the self-assembly of the individual components occurs only during the dissipation of energy. The energy dissipation, i.e. consumption of fuel, activates the interactions for self-assembly and constructs self-assembled systems. The

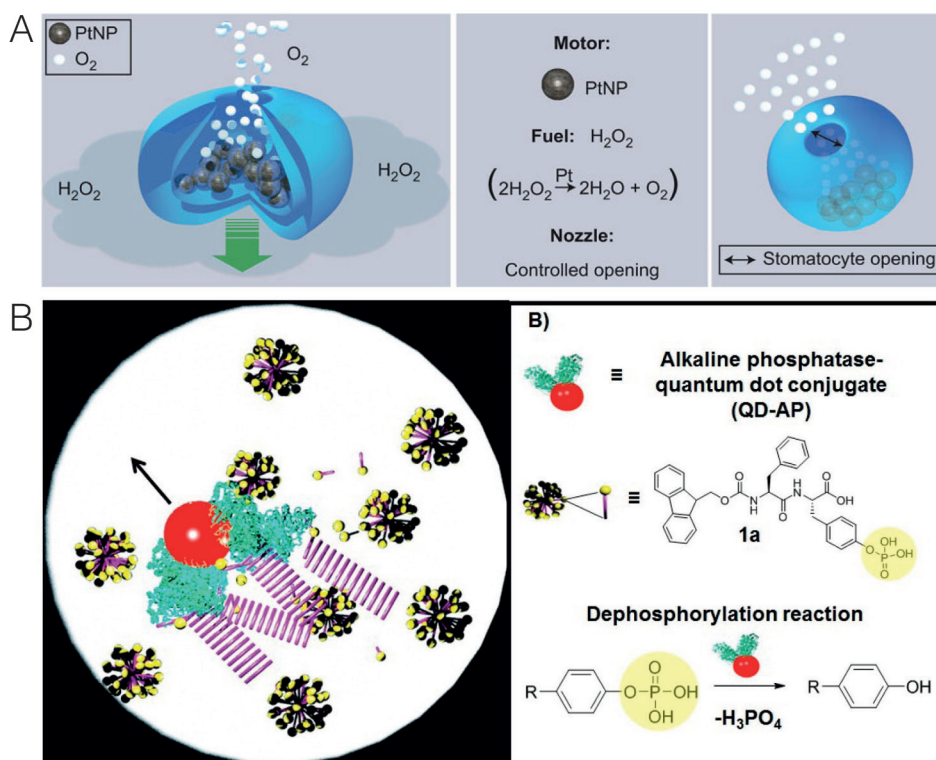


Figure 2.5 Fuel driven propulsion systems. (A). A stomatocyte filled with platinum catalyst was propelled by the expulsion of gaseous oxygen, leading to random motion of the stomatocytes as long as fuel (H_2O_2) was present, by van Hest et al. (79). Ulijn et al. showed the propulsion of a quantum dot with an enzyme attached to the surface, driven by the self-assembly of molecular fibers (83). These were formed locally by the dephosphorylation reaction of a non-active precursor.

use of physical energy sources, instead of chemical fuels, offers a wider range of driving forces with external control, such as light (88), dissolution processes (89, 90), electrical fields (91, 92), and magnetic fields (78).

Theoretical insights were achieved by observing systems of floating ferromagnetic spinners, which showed different forms of self-assembled patterns at different rotation speeds of the magnetic field (78, 93). The magnetic fields drive the spinners together, but the spinning of the disks generates vortices in the fluid that cause repulsion. This balance between the attractive and repulsive forces depended on the rotational forces, i.e. energy dissipation, and determined the patterns formed. The rate of energy dissipation in out-of-equilibrium self-assembling systems thus has a significant influence on the systems effective states (78, 93).

To achieve additional ‘functionalities’ in self-assembled systems under out-of-equilibrium conditions, several designs have been researched (77, 78, 80, 94, 95). For example, when polydimethoxysilane (PDMS) platelets have hydrophobic and hydrophilic sides, attractive capillary forces between platelets arise (78, 80). Catalytic consumption of H_2O_2 to gaseous O_2 was localized by a Pt platelet in the PDMS, and caused the propulsion of these platelets. During the movement, the platelets collided and self-assembled, upon which new functionalities were found such as the directed movement in a straight line. This ‘functionality’ of directionality only existed for as long as the system was out-of-equilibrium, i.e. moving.

In recent years impressive applications of out-of-equilibrium driven systems were achieved, as well as a better theoretical understanding of the thermodynamic forces. That the balance between attractive and repulsive forces controls the self-assembled states is an important insight, and it shows how the different states then depend on the flux of dissipated energy. In these self-assembled states, new functionalities arise that are only present as long as the system remains out of equilibrium.

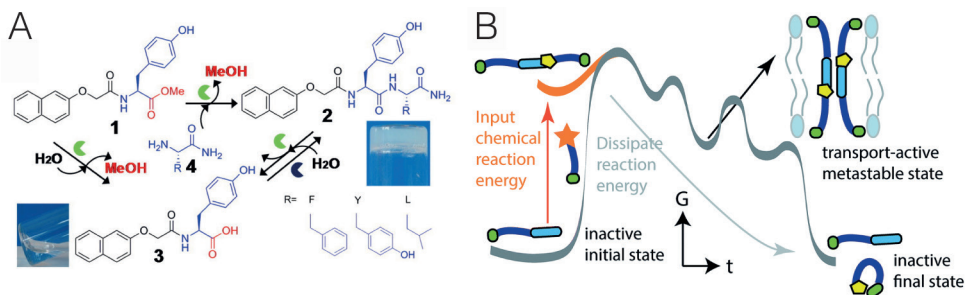


Figure 2.6 Out-of-equilibrium materials. (A) Ulijn *et al.* showed the formation of a gelatinous material that is formed through the enzymatic conversion of non-active precursor 1 to the active gelator 2 (96). (B) Fyles *et al.* prepared a dissipative membrane transport system, that was only able to incorporate into the membrane in an out-of-equilibrium situation. In this state, the system was able to transport ions across the membrane (100).

Out-of-equilibrium materials

Developing materials that exist under out-of-equilibrium conditions with properties that are controlled through consumption of chemical fuels, opens up new approaches for their design and application. New design strategies are being developed to achieve material formation under out-of-equilibrium conditions (94, 96-100). Typically in these strategies, a non-active precursor is activated by a reaction with the chemical fuel and thereafter the activated compound self-assembles. An important aspect of this process is the reversed reaction towards the initial starting compound, which should occur through a secondary mechanism creating waste, also see Chapter 3. A first example of this process was developed in our group and is extended in Chapters 3 and 4 (97). In short, the fuel driven alkylation of carboxylates activates a hydrogelator upon which self-assembly occurs. By aqueous hydrolysis, the formed products return to the non-active state, which can potentially be recycled by addition of new fuel.

Using bio-catalytic reactions, the out-of-equilibrium self-assembly of peptide nanofibers was achieved by Ulijn et al., creating gelatinous materials with time dependent material properties (Fig. 2.6). Overall this system dissipated energy to produce nanofibers from the individual components, but did not (yet) show multiple cycli of material formation (96). In a reversed design, the gelatinous material was the equilibrium condition and consumption of a fuel (ATP) led to the formation of a liquid. This approach was even tested within mice to show in-vivo hydrogel formation (98).

In natural systems, the out-of-equilibrium structures are a route towards specific functions. To develop a catalytic system that depends on aggregation, the redox controlled self-assembly of peptides, containing histidines as catalytic sites was researched. These systems were biocompatible and showed hydrogelation upon reduction of an incorporated selenium oxide functionality (94). Vitamin C was used to reduce the selenium oxide to selenide, invoking self-assembly of the peptides. Upon the addition of H_2O_2 , selenium was oxidized leading to disassembly of the peptides. Upon assembly, the catalytic activity of attached histidine units strongly decreased. As such, a biocompatible out-of-equilibrium material was achieved in which the catalytic activity can be turned on and off, depending on the aggregation state. Remarkably, in the work of Fyles et al., the out-of-equilibrium formation of a membrane-spanning pore was shown, enabling transport across membranes (100).

In conclusion, out-of-equilibrium materials are rapidly gaining interest, especially in the field of small molecule hydrogelators. Control over their material properties are shown via reactions with chemical fuels, leading to time and fuel dependent material properties. The programmable properties of out-of-equilibrium materials will lead to new possibilities and applications.

2.5 Perspective on Nature inspired complex materials

How do we achieve a level of complexity comparable to biological cells? These biological

systems have the characteristic that they combine self-assembly with a complex organization of interactions and energy dissipation to achieve a functional system. Science is not yet capable of producing such complicated systems, which require multiple out-of-equilibrium systems working through interacting mechanisms. To understand the basic phenomena, new designs are made which combine multiple aspects, such as energy dissipation, out-of-equilibrium self-assembly and reaction diffusion. By combining the out-of-equilibrium processes with reaction-diffusion approaches, new possibilities will be created to organize matter across multiple length scales. The formation of temporary and spatial patterns of self-assembled materials would contribute to bringing the research fields of RD and out-of-equilibrium self-assembly closer together. In this chapter, it is also observed that for new out-of-equilibrium materials a combination needs to be made between self-assembly and a chemical reaction. When these systems are coupled to out-of-equilibrium processes, this will lead to the development of programmable materials that are time and fuel dependent. Especially the combination of multiple systems that contain interactions with each other would be a challenging endeavor and inevitably lead towards complexity of materials. The knowledge of building such systems is worthwhile on its own, but the application of these materials will drive the future breakthroughs.

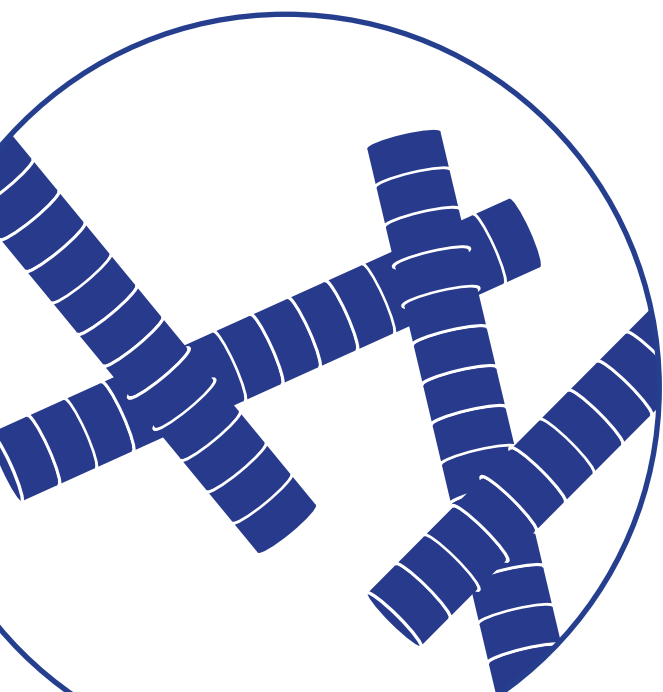
2.6 References:

1. G. Whitesides, What Will Chemistry Do in the Next Twenty Years? *Angewandte Chemie International Edition in English* **29**, 1209-1218 (1990); DOI:10.1002/anie.199012091.
2. G. M. Whitesides, R. F. Ismagilov, Complexity in Chemistry. *Science* **284**, 89-92 (1999); DOI:10.1126/science.284.5411.89.
3. S. Soh, M. Byrska, K. Kandere-Grzybowska, B. A. Grzybowski, Reaction-Diffusion Systems in Intracellular Molecular Transport and Control. *Angewandte Chemie International Edition* **49**, 4170-4198 (2010); DOI:10.1002/anie.200905513.
4. A. S. Mikhailov, B. Hess, Self-Organization in Living Cells: Networks of Protein Machines and Nonequilibrium Soft Matter. *Journal of Biological Physics* **28**, 655-672 (2002); DOI:10.1023/A:1021247024192.
5. D. E. Strier, S. Ponce Dawson, Turing Patterns Inside Cells. *PLoS ONE* **2**, e1053 (2007); DOI:10.1371/journal.pone.0001053.
6. N. Tompkins, N. Li, C. Girabawe, M. Heymann, G. B. Ermentrout, I. R. Epstein, S. Fraden, Testing Turing's theory of morphogenesis in chemical cells. *Proceedings of the National Academy of Sciences*, 201322005 (2014); DOI:10.1073/pnas.1322005111.
7. G. M. Whitesides, B. Grzybowski, Self-Assembly at All Scales. *Science* **295**, 2418-2421 (2002); DOI:10.1126/science.1070821.
8. B. Alberts, A. Johnson, J. Lewis, M. Raff, K. Roberts, P. Walter, *Molecular Biology of the Cell*. (Garland Science, ed. 4th, 2002).
9. K. Nasmyth, A meiotic mystery: How sister kinetochores avoid being pulled in opposite directions during the first division. *BioEssays* **37**, 657-665 (2015); DOI:10.1002/bies.201500006.
10. J. Liu, A. Desai, J. N. Onuchic, T. Hwa, An integrated mechanobiochemical feedback mechanism describes chromosome motility from prometaphase to anaphase in mitosis. *Proceedings of the National Academy of Sciences* **105**, 13752-13757 (2008); DOI:10.1073/pnas.0807007105.
11. K. H. Wrighton, Mitosis: Microtubule teamwork. *Nat Rev Mol Cell Biol* **11**, 231 (2010); DOI:10.1038/nrm2874.
12. P. Maddox, A. Straight, P. Coughlin, T. J. Mitchison, E. D. Salmon, Direct observation of microtubule dynamics at kinetochores in *Xenopus* extract spindles implications for spindle mechanics. *The Journal of Cell Biology* **162**, 377-382 (2003); DOI:10.1083/jcb.200301088.
13. B. G. Fuller, Self-organization of intracellular gradients during mitosis. *Cell Division* **5**, 5 (2010); DOI:10.1186/1747-1028-5-5.
14. P. Lenz, L. Søgaard-Andersen, Temporal and spatial oscillations in bacteria. *Nature Reviews Microbiology* **9**, 565-577 (2011); DOI:10.1038/nrmicro2612.
15. J. Israelachvili, *Intermolecular and surface forces*. (Academic Press, Burlington MA, ed. 3rd ed., 2011).
16. A. Rich, D. M. Blow, Formation of a helical steroid complex. *Nature* **182**, 423-426 (1958).
17. A. Friggeri, B. L. Feringa, J. Van Esch, Entrapment and release of quinoline derivatives using a

- hydrogel of a low molecular weight gelator. *Journal of Controlled Release* **97**, 241-248 (2004).
18. A. G. Marangoni, E. D. Co, Organogels: An Alternative Edible Oil-Structuring Method. *Journal of the American Oil Chemists' Society* **89**, 749-780 (2012); DOI:10.1007/s11746-012-2049-3.
 19. R. G. Weiss, P. Terech, *Molecular Gels*. R. G. Weiss, P. Terech, Eds., *Molecular Gels* (Springer Netherlands, 2006), pp. 1-13.
 20. M. P. Lutolf, J. A. Hubbell, Synthetic biomaterials as instructive extracellular microenvironments for morphogenesis in tissue engineering. *Nature Biotechnology* **23**, 47-55 (2005); DOI:10.1038/nbt1055.
 21. T. Aida, E. W. Meijer, S. I. Stupp, Functional Supramolecular Polymers. *Science* **335**, 813-817 (2012); DOI:10.1126/science.1205962.
 22. S. I. Stupp, Self-Assembly and Biomaterials. *Nano Letters* **10**, 4783-4786 (2010); DOI:10.1021/nl103567y.
 23. J. D. Hartgerink, E. Beniash, S. I. Stupp, Self-Assembly and Mineralization of Peptide-Amphiphile Nanofibers. *Science* **294**, 1684-1688 (2001); DOI:10.1126/science.1063187.
 24. G. M. Whitesides, J. P. Mathias, C. T. Seto, Molecular self-assembly and nanochemistry: a chemical strategy for the synthesis of nanostructures. *Science* **254**, 1312-1319 (1991); DOI:10.1126/science.1962191.
 25. G. M. Whitesides, J. K. Kriebel, B. T. Mayers, in *Nanoscale Assembly*, W. T. S. Huck, Ed. (Springer US, 2005), pp. 217-239.
 26. I. R. Epstein, K. Showalter, Nonlinear Chemical Dynamics: Oscillations, Patterns, and Chaos. *The Journal of Physical Chemistry* **100**, 13132-13147 (1996); DOI:10.1021/jp953547m.
 27. S. Kondo, T. Miura, Reaction-Diffusion Model as a Framework for Understanding Biological Pattern Formation. *Science* **329**, 1616-1620 (2010); DOI:10.1126/science.1179047.
 28. B. A. Grzybowski, *Chemistry in Motion*. (John Wiley & Sons, Ltd, 2009).
 29. A. M. Turing, The Chemical Basis of Morphogenesis. *Philosophical Transactions of the Royal Society of London B: Biological Sciences* **237**, 37-72 (1952); DOI:10.1098/rstb.1952.0012.
 30. O. Ouchterlony, Antigen — Antibody Reactions In Gels. *Acta Pathologica Microbiologica Scandinavica* **26**, 507-515 (1949); DOI:10.1111/j.1699-0463.1949.tb00751.x.
 31. G. Bailey, in *The Protein Protocols Handbook*, J. M. Walker, Ed. (Humana Press, 1996), pp. 749-752.
 32. R. E. Liesegang, Über einige eigenschaften von gallerten. 353-362 (1896).
 33. R. Luther, Räumliche Fortpflanzung chemischer Reaktionen. *Zeitschrift für Elektrochemie und angewandte physikalische Chemie* **12**, 596-600 (1906); DOI:10.1002/bbpc.19060123208.
 34. H.-J. Krug, H. Brandstädter, K. H. Jacob, Morphological instabilities in pattern formation by precipitation and crystallization processes. *Geologische Rundschau* **85**, 19-28 (1996); DOI:10.1007/BF00192056.
 35. P. J. Heaney, A. M. Davis, Observation and Origin of Self-Organized Textures in Agates. *Science* **269**, 1562-1565 (1995); DOI:10.1126/science.269.5230.1562.
 36. B. A. Grzybowski, K. J. M. Bishop, C. J. Campbell, M. Fialkowski, S. K. Smoukov, Micro- and nanotechnology via reaction-diffusion. *Soft Matter* **1**, 114-128 (2005); DOI:10.1039/B501769F.
 37. S. Kondo, R. Asai, A reaction-diffusion wave on the skin of the marine angelfish Pomacanthus. *Nature* **376**, 765-768 (1995); DOI:10.1038/376765a0.
 38. M. Yamaguchi, E. Yoshimoto, S. Kondo, Pattern regulation in the stripe of zebrafish suggests an underlying dynamic and autonomous mechanism. *Proceedings of the National Academy of Sciences* **104**, 4790-4793 (2007); DOI:10.1073/pnas.0607790104.
 39. E. O. Budrene, H. C. Berg, Complex patterns formed by motile cells of Escherichia coli. *Nature* **349**, 630-633 (1991); DOI:10.1038/349630a0.
 40. E. A. Newman, K. R. Zahs, Calcium Waves in Retinal Glial Cells. *Science* **275**, 844-847 (1997); DOI:10.1126/science.275.5301.844.
 41. K. G. Baimbridge, M. R. Celio, J. H. Rogers, Calcium-binding proteins in the nervous system. *Trends in Neurosciences* **15**, 303-308 (1992); DOI:10.1016/0166-2236(92)90081-1.
 42. K. F. Mueller, Periodic Interfacial Precipitation in Polymer Films. *Science* **225**, 1021-1027 (1984); DOI:10.1126/science.225.4666.1021.
 43. I. T. Benemann, M. Fialkowski, B. A. Grzybowski, Wet Stamping of Microscale Periodic Precipitation Patterns. *The Journal of Physical Chemistry B* **109**, 2774-2778 (2005); DOI:10.1021/jp047885b.
 44. W. L. Noorduin, A. Grinthal, L. Mahadevan, J. Aizenberg, Rationally Designed Complex, Hierarchical Microarchitectures. *Science* **340**, 832-837 (2013); DOI:10.1126/science.1234621.
 45. J. H. E. Cartwright, J. M. García-Ruiz, M. L. Novella, F. Otálora, Formation of Chemical Gardens. *Journal of Colloid and Interface Science* **256**, 351-359 (2002); DOI:10.1006/jcis.2002.8620.
 46. C. J. Campbell, R. Klajn, M. Fialkowski, B. A. Grzybowski, One-Step Multilevel Microfabrication by Reaction-Diffusion. *Langmuir* **21**, 418-423 (2005); DOI:10.1021/la0487747.
 47. C. Pan, Q. Gao, J. Xie, Y. Xia, I. R. Epstein, Precipitation patterns with polygonal boundaries between electrolytes. *Physical chemistry chemical physics: PCCP* **11**, 11033-11039 (2009); DOI:10.1039/b904445k.
 48. E. Ben-Jacob, H. Levine, Self-engineering capabilities of bacteria. *Journal of The Royal Society Interface* **3**, 197-214 (2006); DOI:10.1098/rsif.2005.0089.
 49. M. Watanabe, D. Watanabe, S. Kondo, Polyamine sensitivity of gap junctions is required for skin pattern formation in zebrafish. *Scientific Reports* **2**, (2012); DOI:10.1038/srep00473.
 50. J. Horváth, I. Szalai, P. D. Kepper, An Experimental Design Method Leading to Chemical Turing Patterns. *Science* **324**, 772-775 (2009); DOI:10.1126/science.1169973.
 51. A. N. Zaikin, A. M. Zhabotinsky, Concentration Wave Propagation in Two-dimensional Liquid-phase Self-oscillating System. *Nature* **225**, 535-537 (1970); DOI:10.1038/225535b0.
 52. T. Bánsági, V. K. Vanag, I. R. Epstein, Tomography of Reaction-Diffusion Microemulsions Reveals Three-Dimensional Turing Patterns. *Science* **331**, 1309-1312 (2011); DOI:10.1126/science.1200815.
 53. I. R. Epstein, V. K. Vanag, A. C. Balazs, O. Kuksenok, P. Dayal, A. Bhattacharya, Chemical Oscillators

- in Structured Media. *Accounts of Chemical Research* **45**, 2160-2168 (2012); DOI:10.1021/ar200251j.
54. T. Bánsági, O. Steinbock, Three-dimensional spiral waves in an excitable reaction system: Initiation and dynamics of scroll rings and scroll ring pairs. *Chaos: An Interdisciplinary Journal of Nonlinear Science* **18**, 026102 (2008); DOI:10.1063/1.2896100.
 55. P. De Kepper, I. R. Epstein, K. Kustin, M. Orban, Systematic design of chemical oscillators. Part 8. Batch oscillations and spatial wave patterns in chlorite oscillating systems. *The Journal of Physical Chemistry* **86**, 170-171 (1982); DOI:10.1021/j100391a007.
 56. P. De Kepper, I. R. Epstein, K. Kustin, A systematically designed homogeneous oscillating reaction: the arsenite-iodate-chlorite system. *Journal of the American Chemical Society* **103**, 2133-2134 (1981); DOI:10.1021/ja00398a061.
 57. G. Hu, J. A. Pojman, S. K. Scott, M. M. Wrobel, A. F. Taylor, Base-Catalyzed Feedback in the Urea-Urease Reaction. *J. Phys. Chem. B* **114**, 14059-14063 (2010); DOI:10.1021/jp106532d.
 58. K. Kovacs, R. E. McIlwaine, S. K. Scott, A. F. Taylor, An Organic-Based pH Oscillator. *J. Phys. Chem. A* **111**, 549-551 (2007); DOI:10.1021/jp068534v.
 59. V. K. Vanag, I. R. Epstein, Localized patterns in reaction-diffusion systems. *Chaos (Woodbury, N.Y.)* **17**, 037110 (2007); DOI:10.1063/1.2752494.
 60. A. S. Zadorin, Y. Rondelez, J.-C. Galas, A. Estevez-Torres, Synthesis of Programmable Reaction-Diffusion Fronts Using DNA Catalysts. *Physical Review Letters* **114**, 068301 (2015); DOI:10.1103/PhysRevLett.114.068301.
 61. S. M. Chirieleison, P. B. Allen, Z. B. Simpson, A. D. Ellington, X. Chen, Pattern transformation with DNA circuits. *Nature Chemistry* **5**, 1000-1005 (2013); DOI:10.1038/nchem.1764.
 62. R. Schulman, D. Doty, Designing ordered nucleic acid self-assembly processes. *Current Opinion in Structural Biology* **31**, 57-63 (2015); DOI:10.1016/j.sbi.2015.03.003.
 63. S. Mann, Self-assembly and transformation of hybrid nano-objects and nanostructures under equilibrium and non-equilibrium conditions. *Nature Materials* **8**, 781-792 (2009); DOI:10.1038/nmat2496.
 64. J. F. Douglas, K. Efimenko, D. A. Fischer, F. R. Phelan, J. Genzer, Propagating waves of self-assembly in organosilane monolayers. *Proceedings of the National Academy of Sciences* **104**, 10324-10329 (2007); DOI:10.1073/pnas.0703620104.
 65. C. Meier, Y. Wu, G. Pramanik, T. Weil, Self-Assembly of High Molecular Weight Polypeptide Copolymers Studied via Diffusion Limited Aggregation. *Biomacromolecules* **15**, 219-227 (2014); DOI:10.1021/bm401506a.
 66. H. Nabika, M. Sato, K. Unoura, Liesegang Patterns Engineered by a Chemical Reaction Assisted by Complex Formation. *Langmuir*, (2014); DOI:10.1021/la5003786.
 67. A. Sugawara, T. Ishii, T. Kato, Self-Organized Calcium Carbonate with Regular Surface-Relief Structures. *Angewandte Chemie International Edition* **42**, 5299-5303 (2003); DOI:10.1002/anie.200351541.
 68. J. W. Szostak, D. P. Bartel, P. L. Luisi, Synthesizing life. *Nature* **409**, 387-390 (2001); DOI:10.1038/35053176.
 69. P. L. Luisi, Autopoiesis: a review and a reappraisal. *Naturwissenschaften* **90**, 49-59 (2003); DOI:10.1007/s00114-002-0389-9.
 70. P. Walde, A. Goto, P.-A. Monnard, M. Wessicken, P. L. Luisi, Oparin's Reactions Revisited: Enzymic Synthesis of Poly(adenylic acid) in Micelles and Self-Reproducing Vesicles. *Journal of the American Chemical Society* **116**, 7541-7547 (1994); DOI:10.1021/ja00096a010.
 71. K. Kurihara, K. Takakura, K. Suzuki, T. Toyota, T. Sugawara, Cell-sorting of robust self-reproducing giant vesicles tolerant to a highly ionic medium. *Soft Matter* **6**, 1888 (2010); DOI:10.1039/c000857e.
 72. T. Oberholzer, R. Wick, P. L. Luisi, C. K. Biebricher, Enzymatic RNA Replication in Self-Reproducing Vesicles: An Approach to a Minimal Cell. *Biochemical and Biophysical Research Communications* **207**, 250-257 (1995); DOI:10.1006/bbrc.1995.1180.
 73. Z. Nourian, W. Roelofsen, C. Danelon, Triggered Gene Expression in Fed-Vesicle Microreactors with a Multifunctional Membrane. *Angewandte Chemie* **124**, 3168-3172 (2012); DOI:10.1002/ange.201107123.
 74. P. van Nies, Z. Nourian, M. Kok, R. van Wijk, J. Moeskops, I. Westerlaken, J. M. Poolman, R. Eelkema, J. H. van Esch, Y. Kuruma, T. Ueda, C. Danelon, Unbiased Tracking of the Progression of mRNA and Protein Synthesis in Bulk and in Liposome-Confined Reactions. *ChemBioChem* **14**, 1963-1966 (2013); DOI:10.1002/cbic.201300449.
 75. K. Kurihara, M. Tamura, K.-i. Shohda, T. Toyota, K. Suzuki, T. Sugawara, Self-reproduction of supramolecular giant vesicles combined with the amplification of encapsulated DNA. *Nature Chemistry* **3**, 775-781 (2011); DOI:10.1038/nchem.1127.
 76. I. Budin, N. K. Devaraj, Membrane Assembly Driven by a Biomimetic Coupling Reaction. *J. Am. Chem. Soc.*, (2011); DOI:10.1021/ja2076873.
 77. W. F. Paxton, S. Sundararajan, T. E. Mallouk, A. Sen, Chemical Locomotion. *Angewandte Chemie International Edition* **45**, 5420-5429 (2006); DOI:10.1002/anie.200600060.
 78. M. Fialkowski, K. J. M. Bishop, R. Klajn, S. K. Smoukov, C. J. Campbell, B. A. Grzybowski, Principles and Implementations of Dissipative (Dynamic) Self-Assembly. *The Journal of Physical Chemistry B* **110**, 2482-2496 (2006); DOI:10.1021/jp054153q.
 79. D. A. Wilson, R. J. M. Nolte, J. C. M. van Hest, Autonomous movement of platinum-loaded stomatocytes. *Nature Chemistry* **4**, 268-274 (2012); DOI:10.1038/nchem.1281.
 80. R. F. Ismagilov, A. Schwartz, N. Bowden, G. M. Whitesides, Autonomous Movement and Self-Assembly. *Angewandte Chemie International Edition* **41**, 652-654 (2002); DOI:10.1002/1521-3773(20020215)41:4<652::AID-ANIE652>3.0.CO;2-U.
 81. W. F. Paxton, K. C. Kistler, C. C. Olmeda, A. Sen, S. K. St. Angelo, Y. Cao, T. E. Mallouk, P. E. Lammert, V. H. Crespi, Catalytic Nanomotors: Autonomous Movement of Striped Nanorods. *Journal of the American Chemical Society* **126**, 13424-13431 (2004); DOI:10.1021/ja047697z.

82. J. Vicario, R. Eelkema, W. R. Browne, A. Meetsma, R. M. La Crois, B. L. Feringa, Catalytic molecular motors: fuelling autonomous movement by a surface bound synthetic manganese catalase. *Chemical Communications*, 3936-3938 (2005); DOI:10.1039/B505092H.
83. J. Leckie, A. Hope, M. Hughes, S. Debnath, S. Fleming, A. W. Wark, R. V. Ulijn, M. D. Haw, Nanopropulsion by Biocatalytic Self-Assembly. *ACS Nano* **8**, 9580-9589 (2014); DOI:10.1021/nn503875y.
84. J. Leckie, A. Hope, M. Hughes, S. Debnath, S. Fleming, A. W. Wark, R. V. Ulijn, M. D. Haw, Nanopropulsion by Biocatalytic Self-Assembly. *ACS Nano* **8**, 9580-9589 (2014); DOI:10.1021/nn503875y.
85. L. A. Cameron, M. J. Footer, A. v. Oudenaarden, J. A. Theriot, Motility of ActA protein-coated microspheres driven by actin polymerization. *Proceedings of the National Academy of Sciences* **96**, 4908-4913 (1999); DOI:10.1073/pnas.96.9.4908.
86. H. Hess, J. Clemmens, C. Brunner, R. Doot, S. Luna, K.-H. Ernst, V. Vogel, Molecular Self-Assembly of "Nanowires" and "Nanospools" Using Active Transport. *Nano Letters* **5**, 629-633 (2005); DOI:10.1021/nl0478427.
87. Y. Sumino, K. H. Nagai, Y. Shitaka, D. Tanaka, K. Yoshikawa, H. Chaté, K. Oiwa, Large-scale vortex lattice emerging from collectively moving microtubules. *Nature* **483**, 448-452 (2012); DOI:10.1038/nature10874.
88. R. Eelkema, M. M. Pollard, J. Vicario, N. Katsonis, B. S. Ramon, C. W. M. Bastiaansen, D. J. Broer, B. L. Feringa, Molecular machines: Nanomotor rotates microscale objects. *Nature* **440**, 163-163 (2006); DOI:10.1038/440163a.
89. S. Nakata, Y. Doi, H. Kitahata, Synchronized motion of a mobile boundary driven by a camphor fragment. *Journal of Colloid and Interface Science* **279**, 503-508 (2004); DOI:10.1016/j.jcis.2004.06.097.
90. S. Soh, K. J. M. Bishop, B. A. Grzybowski, Dynamic Self-Assembly in Ensembles of Camphor Boats. *The Journal of Physical Chemistry B* **112**, 10848-10853 (2008); DOI:10.1021/jp7111457.
91. H. Nakanishi, D. A. Walker, K. J. M. Bishop, P. J. Wesson, Y. Yan, S. Soh, S. Swaminathan, B. A. Grzybowski, Dynamic internal gradients control and direct electric currents within nanostructured materials. *Nature Nanotechnology* **6**, 740-746 (2011); DOI:10.1038/nnano.2011.165.
92. S. O. Krabbenborg, J. Veerbeek, J. Huskens, Spatially Controlled Out-of-Equilibrium Host-Guest System under Electrochemical Control. *Chemistry – A European Journal*, n/a-n/a (2015); DOI:10.1002/chem.201501544.
93. K. V. Tretyakov, K. J. M. Bishop, B. A. Grzybowski, The dependence between forces and dissipation rates mediating dynamic self-assembly. *Soft Matter* **5**, 1279 (2009); DOI:10.1039/b811254a.
94. X. Miao, W. Cao, W. Zheng, J. Wang, X. Zhang, J. Gao, C. Yang, D. Kong, H. Xu, L. Wang, Z. Yang, Switchable Catalytic Activity: Selenium-Containing Peptides with Redox-Controllable Self-Assembly Properties. *Angewandte Chemie International Edition* **52**, 7781-7785 (2013); DOI:10.1002/anie.201303199.
95. J. Palacci, S. Sacanna, A. P. Steinberg, D. J. Pine, P. M. Chaikin, Living Crystals of Light-Activated Colloidal Surfers. *Science* **339**, 936-940 (2013); DOI:10.1126/science.1230020.
96. S. Debnath, S. Roy, R. V. Ulijn, Peptide Nanofibers with Dynamic Instability through Nonequilibrium Biocatalytic Assembly. *Journal of the American Chemical Society* **135**, 16789-16792 (2013); DOI:10.1021/ja4086353.
97. J. Boekhoven, A. M. Brizard, K. N. K. Kowlgi, G. J. M. Koper, R. Eelkema, J. H. van Esch, Dissipative Self-Assembly of a Molecular Gelator by Using a Chemical Fuel. *Angewandte Chemie International Edition* **49**, 4825-4828 (2010); DOI:10.1002/anie.201001511.
98. Z. Yang, G. Liang, L. Wang, B. Xu, Using a Kinase/Phosphatase Switch to Regulate a Supramolecular Hydrogel and Forming the Supramolecular Hydrogel in Vivo. *Journal of the American Chemical Society* **128**, 3038-3043 (2006); DOI:10.1021/ja057412y.
99. A. K. Das, I. Maity, H. S. Parmar, T. O. McDonald, M. Konda, Lipase-Catalyzed Dissipative Self-Assembly of a Thixotropic Peptide Bolaamphiphile Hydrogel for Human Umbilical Cord Stem-Cell Proliferation. *Biomacromolecules* **16**, 1157-1168 (2015); DOI:10.1021/bm501835v.
100. A. K. Dambeniaks, P. H. Q. Vu, T. M. Fyles, Dissipative assembly of a membrane transport system. *Chemical Science* **5**, 3396-3403 (2014).



Transient assembly of active materials fueled by a chemical reaction

3

Fuel driven self-assembly of actin filaments and microtubules is a key component of cellular organization. Continuous energy supply maintains these transient biomolecular assemblies far from thermodynamic equilibrium, which fundamentally differs from current synthetic self-assembled systems at thermodynamic equilibrium. This work describes the transient self-assembly of synthetic molecules into active materials driven by the consumption of a chemical fuel, and in which properties and behavior such as lifetime, stiffness and self-regeneration capability are determined by reaction rates and fuel levels, instead of equilibrium composition. Analysis of fiber dynamics shows strongly non-linear behavior including stochastic fiber collapse and simultaneous growth and shrinkage, reminiscent of microtubule dynamics. These active materials are a key step towards synthetic self-organizing out-of-equilibrium systems.

This chapter is published: Boekhoven J., Hendriksen Wouter.E.*, Koper G.J.M., Eelkema R, van Esch J.H., Transient assembly of active materials fueled by a chemical reaction, Science, **349**, 1075 (2015). *Shared first authors.*

3.1 Introduction

Active self-assembly driven by chemical fuels is at the basis of many essential processes in living organisms, including cellular transport, cell motility, proliferation, and morphogenesis (1). Active self-assembled structures such as actin networks and microtubules (2) distinguish themselves from equilibrium self-assembled systems and materials (3) by their ability to utilize the free energy provided by the conversion of the fuel to achieve transient structure formation and to carry out work (4, 5); in addition, their behavior is controlled by the kinetics of fuel consumption instead of thermodynamic stability. The realization of artificial active materials created through a fuel-driven self-assembly process would further the understanding of kinetically controlled dynamic behavior and associated spatiotemporal organization. It would also open new opportunities for further developments in active separation and drug delivery, self-healing and adaptive materials, and autonomous chemical processes (6). The few artificial chemically fueled active self-assembling systems that have been reported typically use biological components such as DNA (7), enzymes (8) or protein building blocks (2, 9, 10), or they exploit an oscillating reaction to periodically shift the equilibrium of self-assembling (nano)particles (11). The use of complex biological components and oscillating reactions makes these systems expensive, complicated to use, and applicable to a limited range of working conditions. The only molecular fuel-driven self-assembly process has recently been developed in our lab (12), showing the formation of dispersed fibrous structures with very slow dynamics, inhibiting the formation of true artificial active materials. As of yet, it remains a challenge to achieve the formation of active materials where temporal material properties are controlled by fuel conversion kinetics.

3.2 Results and discussion

Here we report a general approach towards synthetic transient self-assembling molecular materials driven by the consumption of chemical energy, and in which lifetime, stiffness and regenerative behavior are controlled and can be tuned by the kinetics of fuel conversion. The system consists of simple chemicals that are commercially or synthetically available on multi-gram scale, and it can operate in water at room temperature, on timescales of hours to days. To our surprise, these new active materials display non-linear fiber dynamics, reminiscent of the dynamic instability observed in microtubules.

To arrive at a chemical fuel-driven active material, we coupled a switchable self-assembling system to a chemical reaction cycle, using the following design principles: (i) a molecule that can be switched between a non-associating state and an associating state by the removal and re-installment of a repulsive ionic charge; (ii) a chemical 'activation' reaction between the self-assembling molecule and a sacrificial reactant, i.e., the fuel, that removes the repulsive ionic charge of the self-assembling molecule, thereby activating

the self-assembling building block; (iii) a chemical “de-activation” reaction that restores the charge and returns the original charged self-assembling molecule; and (iv) different pathways for the activating and de-activating chemical reactions to form a reaction cycle driven by the consumption of the fuel. It should be noted that if the activating and deactivating reactions would proceed along the same path, adding a reactant would merely shift the chemical equilibrium, as is typically observed in triggered self-assembly processes (13, 14).

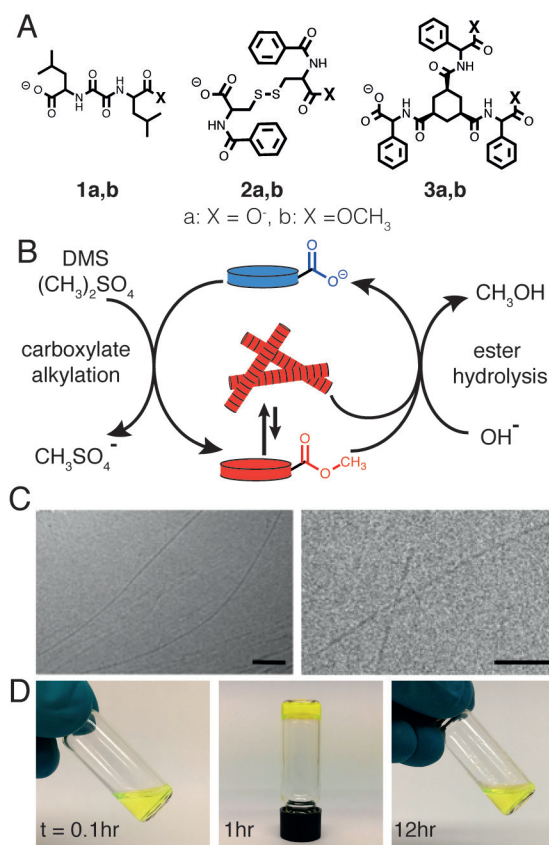


Figure 3.1. Chemically fueled transient self-assembly. (A) Chemical structures of tested molecular gelators 1, 2 and 3. (B) In a typical reaction cycle, carboxylate groups on the inactive self-assembling building blocks (1a, 2a, and 3a) react with methylating agent DMS ($(CH_3)_2SO_4$, the fuel) to give methyl esters 1b, 2b, and 3b (table S3.1, fig. S3.7)(19). These activated building blocks self-assemble into fibrous structures. Methyl esters can hydrolyze both in the assembled and free state to revert to the original inactive building block. One full cycle produces CH_3OH (methanol) and $CH_3SO_4^-$ (monomethylsulfate, MMS) as waste products. (C) Cryo-TEM micrographs of a gel of 2 at $t=120$ min ($pH\ 9$, $[2] = 50$ mM, $[DMS] = 100$ mM, scale bar = 100 nm). (D) A typical sample in a reaction cycle ($pH\ 11$, $[2] = 50$ mM, $[DMS] = 200$ mM) at $t=0.1$, 1, 12 h, with $1\ \mu M$ fluorescein added for coloring.

Self-assembling molecules containing anionic carboxylate groups in combination with an ester-forming carboxylate alkylation reaction as the activating reaction and an ester hydrolysis reaction as deactivating reaction can fulfill the abovementioned requirements. Here, the carboxylate carries a negative charge that can be removed by reaction with an alkylating electrophile fuel to form a neutral ester function. Esters can undergo spontaneous hydrolysis in aqueous environments, leading to the formation of a charged carboxylate and an alcohol waste product. As such, a carboxylate function can be used to control the molecular assembly process, by changing the net charge on the molecule through kinetically controlled alkylation and hydrolysis (Fig. 3.1).

Kinetic analysis of the alkylation of carboxylates to drive supramolecular assembly revealed that a substantial acceleration of the reaction kinetics as compared to our previous study is key to the formation of an active gel state (12). To reach this goal, we selected a more reactive alkylating agent and adjusted pH levels by means of a buffer to enable the formation and decay of supramolecular structures on timescales of hours instead of the previously reported 5 to 15 days (12). Increasing buffer concentrations resulted in a system capable of autonomously forming soft molecular materials without continuous pH adjustment, and a switch to monocarboxylates as the active gelators.

Using this system, we tested several molecular gelators containing two or three carboxylate moieties for the formation of active materials (**1-3**, Fig. 3.1). These bis- and tris-carboxylate gelators form isotropic aqueous solutions above the pK_a of their carboxylates ($pK_a \sim 4.5$). Active hydrogel materials were obtained during a reaction cycle of gelator **2** or **3** with the commercially available strong methylating agent dimethylsulfate (DMS, $(CH_3)_2SO_4$, Fig. 3.1) under hydrolytic (basic) conditions. In a typical reaction cycle, the batch-wise addition of DMS to buffered solutions of **1-3** results in its transient methylation, yielding methyl esters **1b**, **2b**, and **3b** (Fig. 3.1A,B, figs. S3.1 and S3.2)(19). Under these conditions gelator **1** forms a gelatinous precipitate but fails to form a hydrogel. We find that hydrogels of **2** and **3** consist of bundles of fibers of over a micrometer in length at high buffer concentrations, with individual fiber diameters of 8 and 10 nm, respectively (Fig. 3.1C, 3.4B, fig. S3.2)(19).

Focusing on **2**, more detailed kinetic investigations show that typically 20 min after addition of fuel the concentration of **2b** reaches a critical gelation concentration (CGC), where the formation of fibers leads to macroscopic, semitransparent gel materials (Fig. 3.1D). The CGC of **2b** was estimated from inverted tube tests and rheology experiments to be between 0.1 mM and 2.8 mM, but it could not be determined accurately because of the dynamic nature of the material (vide infra, table S3.4, fig. S3.5)(19). Over time, **2b** hydrolyzes back to **2a**, leading to the breakdown of fibers and the dissolution of these gels. In a reaction cycle at the relatively low pH value of 9, the hydrolysis reaction took place at a slow rate, producing gels that persist for weeks. Running a reaction cycle at higher pH values increased the rate of hydrolysis; as a result, the concentration of **2b** reached a maximum value after which it decreased to zero on the timescale of hours.

For instance, a gel formed at pH 11 had a lifetime of around 10 hours (15). Likewise, reducing the amount of fuel added at pH 11 resulted in a change in gel lifetime from 10 (initial fuel concentration $[\text{DMS}]_0=200 \text{ mM}$) to less than 4 hours ($[\text{DMS}]_0=175 \text{ mM}$). The timescales of gel formation and dissolution thus depend strongly on the reaction conditions employed. Moreover, the material properties and their time dependence change with changing reaction conditions. Hence, the reaction cycle, started by **2a** and DMS, constitutes a fuel-driven self-assembling system that can operate autonomously, at reaction cycle timescales of 4 to 10 hours, and that provides access to the active gel state.

The rheology of **2**- and **3**-based active materials showed the formation of gels and a rapid increase in gel stiffness after the addition of fuel (Fig. 3.2A, figs. S3.3 to S3.5)(19). At pH 9, the near absence of a deactivating hydrolysis reaction resulted in stiff gels with persistent storage moduli (G') in the 10 kPa range and a loss factor ($\tan \delta$) of ~ 0.03 for **2**; for **3** it resulted in a G' of 0.4 kPa with a $\tan \delta$ of ~ 0.5 . The storage and loss moduli are constant over a wide frequency range, which is typical behavior for soft fibrillar gels formed from supramolecular gelators (16). Higher pH values resulted in less stiff gels, and over time a declining storage modulus was observed, with a decay rate that increased with pH. Changing the initial concentration of fuel changed both the lifetime and the

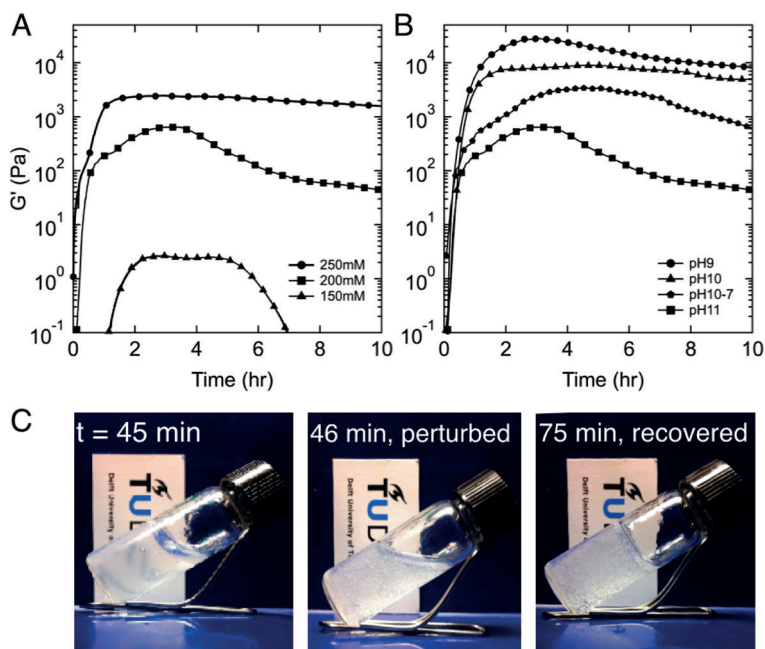


Figure 3.2. Macroscopic mechanical behavior of the active material. (A) Rheology time sweeps of solutions of **2** during a reaction cycle at varying DMS concentrations ($[\text{DMS}]_0=150$ to 250 mM , pH 11) and (B) at varying pH ($[\text{DMS}]_0=200 \text{ mM}$, pH 9 to 11). (C) Fuel-driven gel regeneration, photographs of an active gel of **2** before, directly after and 30 minutes after mechanical perturbation of the gel. All experiments: $[\text{2}]_0=50 \text{ mM}$.

maximum stiffness of the gels, with results ranging, for instance, from short-lived, very weak gels at $[\text{DMS}]_0 = 150 \text{ mM}$ to much stronger gels with lifetimes of multiple days at $[\text{DMS}]_0 = 250 \text{ mM}$ (Fig. 3.2B). The observed strong dependence on fuel concentrations and pH was confirmed by a kinetic reaction model for **2**. These materials also showed fuel-driven self-regenerating behavior after destructive mechanical perturbation. When destroyed during the first hours after the addition of fuel, gels of **2** quickly regain and surpassed the stiffness obtained before destruction (Fig. 3.2C, 3.3D-E, figs. S3.12 to S3.15) (19). This behavior is generally not observed in conventional low molecular weight gels near thermodynamic equilibrium. If perturbed late in the reaction cycle, when the fuel was depleted, the regeneration capability dropped below 1 and eventually was lost completely. Thus, the mechanical and regenerative behavior of these active materials is strongly dependent on the progression of the reaction cycle. Alternatively, we also showed that the system can operate under continuous flow conditions with a continuous supply of fuel, prolonging the lifetime of the material (Fig. S3.22)(19).

To link the observed macroscopic behavior to the molecular scale reactions, we performed a kinetic analysis of the active materials from gelator **2**. Starting from the pronounced dependence of gel life times on fuel concentration and pH, we developed a simple kinetic model based on two competing chemical reactions: the forward alkylation of **2a** to **2b** by DMS and the reverse hydrolysis of **2b** to **2a** (Fig. 3.1B). The direct hydrolysis of DMS to monomethyl sulfate (MMS) was also taken into account as a separate background reaction. Using kinetic data from HPLC and ^1H -NMR spectroscopy measurements, we determined the rate constants of all relevant reactions, allowing the construction of a kinetic model for the formation of **2b** (Fig. 3.3, Figs. S3.6 to S3.11)(19). We found that the rate of alkylation $k_1[\mathbf{2a}][\text{DMS}]$, with $k_1=2.5 \text{ M}^{-1}\text{h}^{-1}$ at pH 10, followed a linear decay until all DMS had been depleted and showed a marginal variation with the pH. The hydrolysis rate $k_2[\mathbf{2b}][\text{OH}^-]$, with $k_2=5.6 \cdot 10^4 \text{ M}^{-1}\text{h}^{-1}$ at pH 10 (table S3.3)(19), on the other hand is exponentially dependent on pH. Subtracting the hydrolysis rate from the alkylation rate gives the net rate of formation of **2b** (Fig. 3.3C).

Using these rates, we define two regimes through which the active gels progress: at first the system is in a growth regime where the alkylation of **2a** is the dominant reaction. Subsequently, the system moves to the decay regime in which hydrolysis is the dominant reaction. We applied this model to analyze the relationship between the behavior of the system and the governing chemical reactions over time. The model showed that, unlike systems assembling near thermodynamic equilibrium, the behavior of these fueled systems evolves over time and is strongly dependent on the various reaction parameters, especially fuel levels and pH. The lifetimes of these active gels are globally connected to the period where **[2b]** is high, which is controlled by the initial reaction parameters (pH, $[\mathbf{2a}]_0$, $[\text{DMS}]_0$), and can be predicted with the kinetic model (Fig. 3.3A,B). However, we observed a delay between **2b** over time $[\mathbf{2b}]_t$ (Fig. 3.3A) and the rheological behavior (Fig.

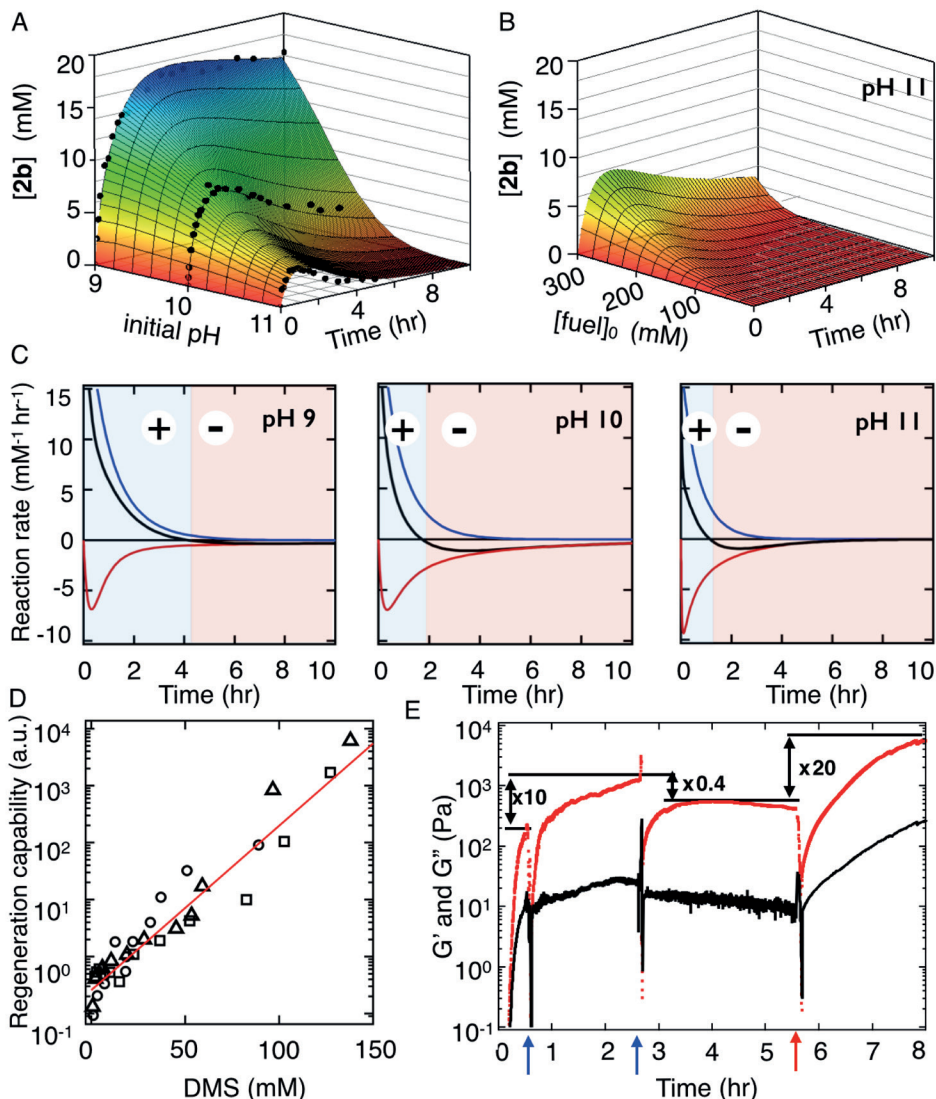


Figure 3.3. Kinetics of transient gelator formation. (A and B) The influence of reaction conditions on the concentration of **2b** over time. The black markers depict data points obtained from HPLC. The surface plots depict the kinetic model obtained (A) at different pH and (B) at different DMS concentrations with initial pH 11. (C) Rates of alkylation of **2a** (blue lines), hydrolysis of **2b** (red lines) and net formation of **2b** (black lines) against time at pH 9, 10 and 11 ($[\text{2a}] = 50$ mM, $[\text{DMS}] = 200$ mM), blue areas indicate net alkylation (+), red areas net hydrolysis (-). (D) The relative regeneration of the gels as determined by rheology versus the concentration of remaining fuel at the moment of perturbation (square, pH 9, triangle, pH 10, circle, pH 11, $[\text{2}]_0 = 50$ mM, $[\text{DMS}]_0 = 200$ mM, Fig. S12-15)(19). (E) Mechanical response of a gel after perturbation and addition of new fuel (G' (red), G'' (black)). Blue arrows at 0.5 and 2.7 hr. indicate perturbation by applying strain, the red arrow at 5.5 hr. indicates a perturbation and addition of 200 mM DMS. Values between horizontal black lines indicate relative regeneration ratios.

3.2A). This effect may indicate a nucleated growth mechanism of gel fiber formation, and was not accounted for in the kinetic model.

Most remarkable, however, is the observation that the gel state persists for periods extending far beyond the time when reasonable concentrations of **2b** were present. For instance, the pH 11 system contained a gel with $G' > 50$ Pa after 10 hours of reaction, even though **[2b]** has dropped below 0.6 mM after 5 hours. The dependence on reaction parameters and transient character of the system indicates kinetically controlled states that do not reside at thermodynamic minimum.

Using the model, we estimated the fuel concentration at any given time in the regeneration experiments. The regeneration capability (17) of these materials has an exponential dependence on the fuel concentration at the moment of perturbation (Fig. 3.3D), but appears independent of the pH, clearly showing that this behavior is fuel driven and is not significantly influenced by the hydrolysis rate (Fig. S3.12-3.15)(19). When $[DMS]_t < 20$ mM the gels are no longer able to fully regenerate, indicating that the rate of formation of **2b**, needed for network repair, becomes too small. The notion that the regeneration is fuel driven implies that it can be restored at any time by the addition of new fuel. Indeed, the addition of fuel to a gel that was unable to regenerate, restored its regeneration capability (Fig. 3.3E).

To gain more insight into the divergence between the timescales of the macroscopic behavior and the underlying chemical reaction network, we investigated the fiber dynamics of active gels from **2** with low and high hydrolysis rates (pH 9-11) using confocal microscopy (Fig. 3.4, movies S1-4, Fig. S3.16 to S3.21)(19). In all cases, after the addition of fuel, fiber growth is observed after a short lag period, coinciding with a rapid increase in gel stiffness (Fig. 3.4A, 3.2A). At pH 9, a rapid increase in the total fiber length was initially observed until the growth leveled off, and only very few shrinking fibers were observed (Fig. 3.4A). The active gels with higher hydrolysis rates (pH 10.7 to 11) also showed this rapid increase, but they reached a clear maximum after which the fibers entered a shrinking regime and the total fiber length decreased. The transition between these two regimes coincided with the moment when the gels reached their maximum storage modulus. Both the moment of transition between regimes and the rate of decrease in the total fiber length depended on the pH and matched with the evolution of the storage moduli of the gels (Fig. 3.4A, 3.2A). A significant total fiber length persists late in the reaction cycle, despite a negligible concentration of **2b**. All gels showed their highest level of structure (total fiber length, gel stiffness) midway in the reaction cycle.

At the microscopic level, several other unexpected observations are made (Fig. 3.4B). Instead of gradual and simultaneous shrinking of all fibers, the assemblies tend to collapse stochastically with rates up to $15 \mu\text{m}/\text{min}$ (Fig. 3.4A). The fibers shrunk only at their tips and do not fracture or dissolve along the fiber. Also, for a certain period both growing and shrinking fibers were observed in each other's proximity, randomly

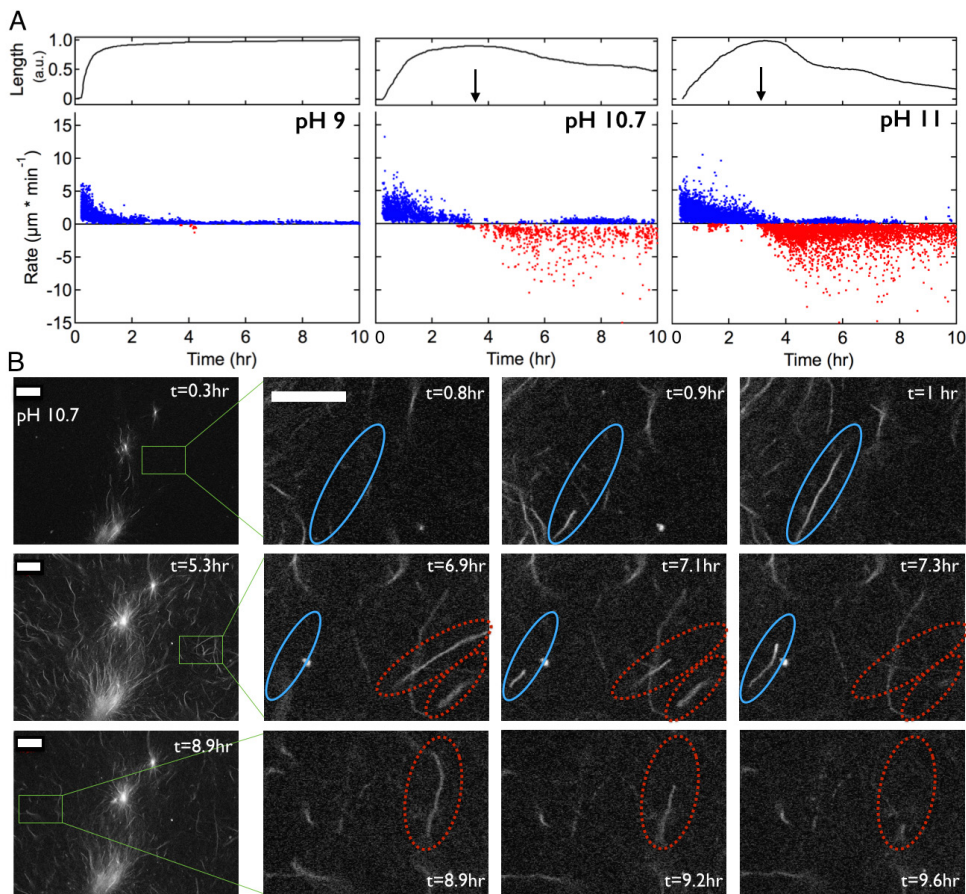


Figure 3.4. Microscopic analysis of the active material. (A) Upper panel: normalized total fiber length against time in the reaction cycle. Arrows indicate the reaction cycle time where G' reaches its maximum value (see Fig. 2A). Lower panel: rates of fiber growth (blue) and fiber shrinkage (red), at various pH. (B) Confocal micrographs over time, showing distinct fiber growth, shrinkage, and overlapping periods during a reaction cycle. Growing fibers are indicated in blue circles and shrinking fibers are indicated in red circles. All samples prepared with $[2] = 50$ mM, $[DMS] = 200$ mM, at pH 10.7. Scale bar = 10 μm.

distributed throughout the microscope focal plane (Fig. 3.4B, Figs. S3.18 to S3.21)(19). These observations are inconsistent with fiber dissolution driven by a decrease of the solution concentration of **2b**. Instead, these findings point to hydrolysis of **2b** taking place both in solution and within the fibers. The hydrolysis rate depends on the total concentration of **2b**, irrespective of the fraction bound in fibers (18). The observed fast, stochastic collapse of fibers suggests that they become unstable above a certain critical hydrolysis level of **2b**, at which moment they rapidly dissolve, which may account for the discrepancies between molecular reaction rates, and the macroscopic and microscopic behavior. These observations show surprising similarities to the behavior of microtubule (de)polymerization such as non-linear fiber dynamics and dynamic instability, which are

key ingredients in achieving out-of-equilibrium self-organization.

3.3 Conclusions

This work demonstrates the far-from-equilibrium self-assembly of molecular building blocks driven by a chemical fuel, leading to the transient formation of an active material. In these far-from-equilibrium materials, properties and behavior such as life time, stiffness and self-regeneration capability are determined by reaction kinetics and fuel levels rather than by equilibrium composition. These materials show non-linear fiber dynamics reminiscent of microtubule behavior, and they constitute a key step in the development of synthetic self-organizing out-of-equilibrium systems.

Chapter 3 Supporting Information

Transient Assembly of Active Materials Fueled by a Chemical Reaction

3.4 Experimental section

3.4.1 Materials

All materials (N,N'-Dibenzoyl-L-cystine (DBC, **2**), dimethyl sulfate (DMS), sodium tetraborate decahydrate, Nile red, D₂O) were purchased from Sigma-Aldrich and used as received. Compounds **1** and **3** were successfully synthesized according to literature procedures (20,21). Water was purified using a Millipore AFS 3 system (MQ water). All active gels were prepared in 500 mM borate buffered MQ water at pH 9, 10, 10.7 or 11. The pH of the borate solution was adjusted with concentrated aqueous solutions of NaOH or HCl. If precipitation of salts occurred during the preparation process, then the buffer solutions were shortly heated to achieve a clear solution.

Warning: dimethyl sulfate is highly toxic and should be handled in a fume hood using appropriate protective gear.

3.4.2. Methods

Nuclear Magnetic Resonance Spectroscopy (NMR)

¹H-NMR spectra were recorded using a Bruker Avance-300 spectrometer, operating at 300 MHz or a Agilent 400, operating at 400MHz. Spectra were recorded at 25 ± 0.2°C in H₂O with 10% D₂O, or DMSO-d₆ using solvent suppression to suppress the H₂O peak.

Active materials preparation

Active material samples were prepared adding the required amount of DMS (liq., neat) through a pipet to 0.5 mL solution of 50 mM **2**, 25mM of **1** or **3** in 500 mM borate buffer at the desired pH (pH 9, 10, 10.7, or 11) in a 2.5 mL vial. The vial was vortexed to induce dissolution of the DMS and the samples were used directly. Initial fuel-driven gelation experiments using phosphate buffers showed very similar behavior to borate buffer, indicating that the observed effects are not specific to the buffer employed.

Gelation tests by the inverted tube method

Time dependent gelation

Active material samples for time dependent gelation tests were prepared as described above (pH 11, 0.5 mL of 50 mM **2**), after which 9.5 μL (12.6 mg, 200 mM) DMS was added. The vial was vortexed to induce dissolution of the DMS and the samples were allowed to stand at 25 ± 1°C for a predetermined time (t = 15 min, 30 min, 45 min, etc.) using an individual sample for each time point. After the predetermined time, a vial was inverted (the "inverted tube test")(16). If the gel could support its own weight for more than 30 seconds, it was defined as a gel.

Fuel dependent gelation

Samples for fuel dependent gelation tests were prepared as described above (pH 11, 0.5 mL of 50 mM **2**), and appropriate amounts of DMS were added to obtain concentrations of 100, 150, 175, 200, 225, 250, 300 mM DMS. The vial was vortexed to induce dissolution of DMS and the samples were allowed to stand at 25 ± 1°C for 45 minutes. After this time, the sample was subjected to an inverted tube test.

Gel regeneration in vial

Samples gel regeneration in vial tests were prepared as described above (pH 11, 0.5 mL of 50 mM **2**), after which 9.5 μL (12.6 mg, 200 mM) DMS was added. The vial was vortexed to induce dissolution of the DMS and the samples were allowed to stand at 25 ± 1°C for a predetermined time (t = 15 min, 30 min, 45 min, etc.). After this time, a sample was subjected to an inverted tube test. If a gel was formed, it was physically perturbed by vortexing the gel 20 seconds at 2500 rpm, upon which, in all cases, a fluid was formed. After perturbation the gel was placed back at 25 ± 1°C and allowed to regenerate for a period of 30 minutes. After these 30 minutes another inverted tube test was performed to see if the gel had regenerated.

Active material spin-down

Active material was prepared as described above for pH 9, 200mM DMS, 1mL. After two hours of reaction the active materials were physically transferred to a centrifuge tube, containing a cutoff filter of 3000MW (Merck Milipore, Amicon® Ultra-4). A buffer was placed on top (1mL, 500mM Borate pH 9.2) followed by a 5 min., 7500rpm centrifuge spin cycle. This was repeated with another 1mL of buffer, now with 10 minutes of spinning and finally again a 10 minutes spin cycle with 1 mL of MQ water. The samples were

transferred to a round bottom flask, and freeze-dried for 12 hours.

High-Performance Liquid Chromatography Mass Spectrometry (HPLC-MS)

HPLC-MS was performed on a Shimadzu Liquid Chromatograph Mass Spectrometer, LCMS-2010, with a XBridge Shield RP, 18.5 μ m, 4.6x150mm column and a SPD-M20 diode array detector. Samples were prepared by diluting aliquots of the active gel 100 times with cold MQ-water. This diluted sample was directly injected into the HPLC. All samples were run on gradient of 50/50 to 80/20, MeOH/H₂O + 1% Et₃N. Negative and positive mode ESI were used for the assignment of the peaks and the concentrations of **2a** and **2b** were determined by integration of absorbance at 238 nm (Table S1). The extinction coefficients for **2a** and **2b** were assumed to be equal. The double methylated product (bis methyl ester of **2**) was not observed under any of the used conditions.

Table S1. Retention times and mass spectrometry data of **2a and **2b**.**

Compound	Retention time (min.)	m/z (measured)	m/z (calculated)
2a	1.4	447.1 (M - H ⁺)	447.07 (M - H ⁺)
2b	2.1	461.1 (M - H ⁺)	461.08 (M - H ⁺)

Cryogenic-Transmission Electron Microscopy (cryo-TEM)

A few microliters of active gel was deposited on a Quantifoil 3.5/1 holey carbon coated grid. A FEI Vitrobot was used to blot away the excess liquid and to plunge the grid into liquid ethane. Frozen-hydrated specimens were mounted in a cryo-holder (Gatan, model 626) and observed in a Philips CM 120 electron microscope, operating at 120 kV. Micrographs were recorded under low-dose conditions on a slow-scan CCD camera (Gatan, model 794).

Atomic force microscopy (AFM)

A NTMDT Ntegra AFM was operated in tapping mode at room temperature (25 °C). Samples were spin-coated on a Si wafer chip and used without further adjustments.

Rheology

Oscillatory experiments were performed using a rheometer (AR G2, TA instruments) in a strain-controlled mode, equipped with a steel plate-and-plate geometry of 40 mm in diameter and equipped with water trap. The temperature of the plates was controlled at 25 \pm 0.2°C.

Active material samples for rheology experiments were prepared as described above, at the desired pH (pH 9, 10, 10.7, or 11; 50 mM **2**, or 25mM **3**) and the appropriate amounts for different desired DMS concentrations. Directly after dissolving the DMS, 0.5 mL of the sample was positioned on the rheometer plate and the upper plate was brought down to its measuring position. Time sweeps were measured under 0.5% strain with a frequency of 1 Hz (6.28 rad/s). All measurements were performed in the linear viscoelastic region.

Samples for regeneration tests were prepared as described above (pH 9, 10, 10.7, or 11, 50 mM **2a** 200 mM DMS). After a predetermined time (t = 15 min, 30 min, 45 min, etc.), the sample was subjected to a strain sweep, from 0.01 to 300%, after which G' was lower than G'' (forming a fluid), ensuring complete destruction of the gel. After the strain sweep, the samples were analyzed for self-regeneration using a time sweep. The regenerative behavior was assessed at various times and each data point (t = 15 min, 30 min, 45 min, etc.) was obtained with a new sample.

Fuel dependent regeneration tests were performed with samples prepared as described above (50 mM **2a**, pH 11, 200 mM DMS). The sample was subjected to strain sweeps at 0.5 hours and 2.8 hours of the time sweep, to determine the relative regeneration. After the 2nd strain sweep, the G' was left to regenerate until after approximately 5.5 hours a plateau was observed. At this time the measurement was stopped,

the top-plate lifted and 9.5 μ L of DMS was added to the mixture. After repositioning the top-plate a strain sweep was performed to induce mixing of the added DMS and the regeneration of the G' was measured over time (Fig. 3.3).

Confocal Laser Scanning Microscopy (CLSM)

CLSM micrographs were obtained using a Zeiss LSM 710 confocal laser scanning microscope, with an excitation beam of 488 nm and 510-570 emission filter. Fluorescence was collected by means of a Zeiss 40x, 1.3 oil immersion objective and the sensitivity of detectors and filters were adjusted in order to obtain maximum signal to noise ratio. Images were recorded at least 15 μ m above the glass surface. Areas of 2048 by 2048 pixels were recorded corresponding to 210 μ m by 210 μ m. During the time series, a frame was recorded every minute.

Samples were prepared by mixing 5 mL of 2.5 mM Nile red in ethanol with 500 mL of 50 mM **2a** in 500 mM borate buffer at the appropriate pH. As a result the final concentration of Nile red was 25 μ M. The reaction cycle was started by addition of 9.5 μ L (12.6 mg, 200 mM) DMS. After addition of DMS the vial was vortexed for 1 minute to induce dissolution of the DMS after which a drop of the mixture was placed in a chamber made of a glass microscope slide and an inert rubber gasket, and then sealed with a second glass slide.

Fiber tracking

The fiber growth and shrinkage behavior was tracked using the MtrackJ (version 1.5.0, <http://www.imagescience.org/meijering/software/mtrackj/>) plugin for ImageJ (NIH, 1.6, <http://imagej.nih.gov/ij/>). Using MtrackJ, the endpoints of growing or shrinking fibers were determined between each frame. The software uses this dataset to calculate the growth or shrinkage rate between frames. Only fibers were selected which remained in focus during growing or shrinking. Only fibers that changed in length for longer than two frames and of which the remaining fiber stayed in focus were counted as valid data points. To ensure statistical reliability, at least 300 growing fibers per experiment were counted and as many as possible shrinking fibers were counted, reaching up to 300 fibers for pH 11. The datasets were analyzed using a code written in Matlab R2011b for visual representation and organization of the recorded data. The code is available on request.

3.4.3. Supporting Experiments

Active material precursors

Several carboxylic acid surfactants and hydrogelators are selected and investigated for the active material formation and properties. We selected several bis- and tris-acid hydrogelators; oxalylbisleucine (**1**), N,N'-dibenzoyl-L-cystine (**2**) and cis-,cis-cyclohexane-1,3,5-tricarbonyl-trisphenylglycine (**3**, Fig.3.1). These molecules were selected based on their carboxylic acid group and gelating capabilities, and were commercially available or successfully synthesized (20, 21). Initially, we also tested commercially available mono acid surfactants and hydrogelators, such as fatty acids and protected amino acids for active material formation. These were found to be not sufficiently soluble under the high buffer concentrations, as required for our experimental approach and were not further investigated, see table S2.

Table S2 Solubility of acid hydrogelators in Borate buffer and material formation upon reaction with DMS.

Compound	Oleic acid	Palmitic acid	Fmoc-Phe	Fmoc-PhePhe	Z-PhePhe	Ox(leu) ₂ , 1	DBC, 2	HPG, 3
Solubility in borate buffer	None	None	None	None	None	Well	Well	Well
Reaction DMS, 1hr	-	-	-	-	-	Precipitate	Gel	Gel
Reaction DMS, 24hr						Precipitate	Soft gel	Partly liquid

Active materials initial tests

Initial experiments are performed on the oxalyl bis-leucine (**1**), dibenzoyl cysteine (**2**), and cis-,cis-cyclohexane-1,3,5-tricarbonyl-trisphenylglycine (**3**), to determine their active material properties and working range.

Oxalyl bisleucine, **1**

To test **1** for the formation of active material upon addition of the DMS, initial tests were performed (Fig. S3.1). During these initial experiments it was observed that **1** formed precipitates, at three hours after the addition of DMS at DMS concentrations of 75mM up to 250mM (Fig S3.1B, C). Furthermore, for [DMS]₀ = 75 to 100mM the amount of precipitate visually decreased over the time of 30 days. This time and fuel dependent behavior of **1** was measured by turbidity measurements, monitoring at a wavelength of 640nm (Fig. S3.1 C). Samples were prepared as follows: solutions of 25mM **1a** in borate buffer (500mM, 3mL), with the pH adjusted to pH 9. At the start of the measurements, DMS was added at concentrations of 75 to 100mM, under continuous stirring at 25°C. For the turbidity measurements, a sample of 500 μL was taken from the bulk solution for analysis and returned afterwards. The container was properly sealed to prevent evaporation. It is observed that the turbidity increases after addition of the DMS, and the relative increase depends on the amount of fuel added. The time of full turbidity decrease is 10 days for the 75mM sample whereas the 100mM fuel remained turbid for 30 days. To analyze the content of the

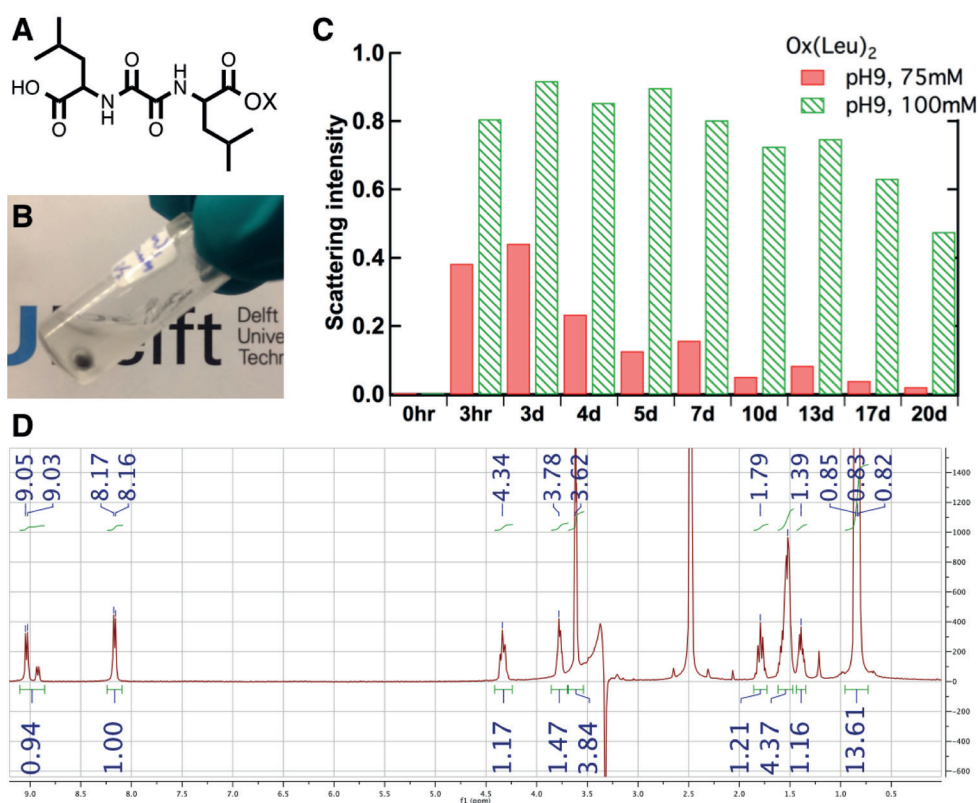


Figure S3.1: Active material of **1**

(A) The structure of oxalyl bisleucine **1**. Compound **1** forms a clear solution in borate buffer. (B) After addition of DMS (100mM), over time a precipitate is formed (25mM, pH9). (C) Light scattering at 640nm reveals that the intensity of the scattering depends on the concentration of DMS used and changes in time. (D) ¹H-nmr analysis of the filtrated, and dried, precipitate shows the formation of a methyl-ester (OCH₃, 3.62ppm, DMSO-d₆).

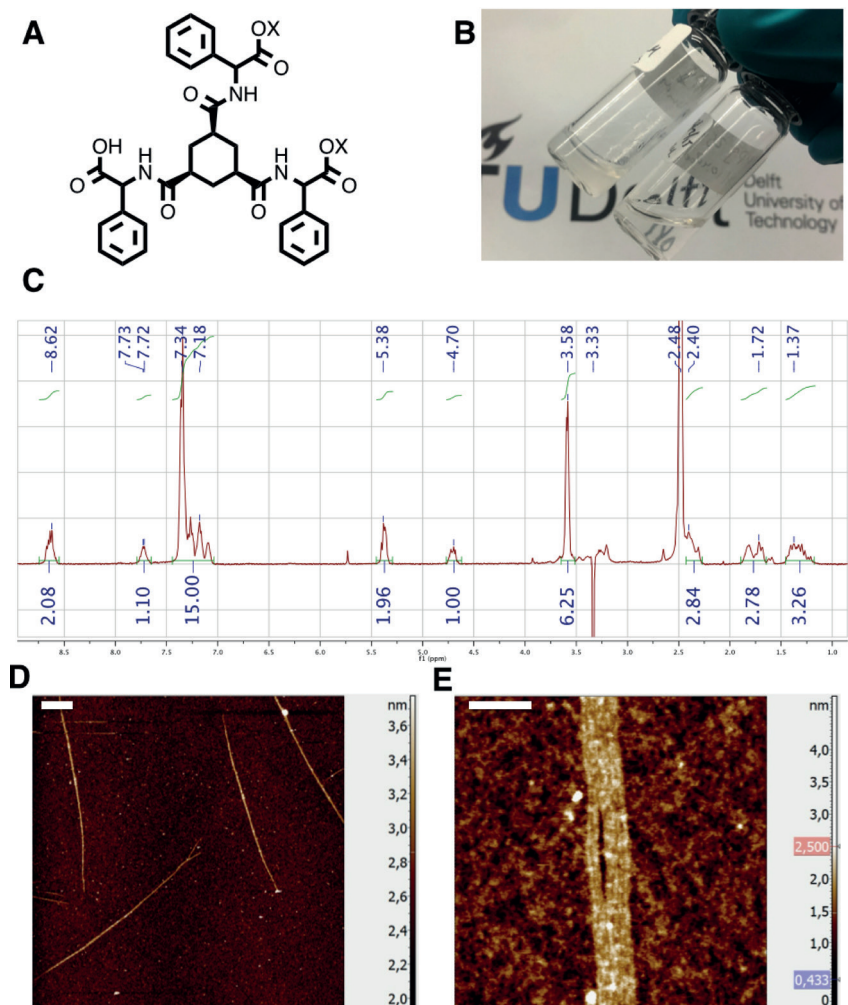


Figure S2: Active material of 3

(A) The behavior of *Cis-,cis-cyclohexane-1,3,5-tricarbonyl-trisphenylglycine 3* as an active material, which forms a clear solution in borate buffer. (B) After addition of DMS (100mM), over time a hydrogel is formed (25mM, pH9). (C) $^1\text{H-NMR}$ analysis of the spun-down, and dried, gel shows the formation of a methyl-ester (3.58ppm, DMSO- d_6 , H $_2$ O-suppressed). (D, E) AFM images show that **3** forms bundles of fibers with individual fiber diameter of 10nm and bundles of 70nm. Scalebars = $1\mu\text{m}$ (D), $0.1\mu\text{m}$ (E).

precipitate, fresh samples were prepared, spun-down and analyzed by $^1\text{H-nmr}$ (DMSO- d_6) (Fig. S3.1 D). The precipitate was found to contain the mono methyl ester **1b**, as indicated by the peak at 3.62ppm and relative integral values. Overall, **1** is observed to form an active material, as a precipitate of the methyl ester, with both time and fuel dependent properties.

Dibenzoylcysteine, 2

In the initial tests, it is observed that compound **2** forms an opaque hydrogel upon addition of DMS (Fig. 3.1, 3.2). Samples were prepared according to the active material protocol, described above. At minimum concentrations of $\sim 150\text{mM}$ of DMS gelation of the solution is achieved, whereas at lower concentrations a clear solution remains. Furthermore it is observed that the hydrogels formed at pH 9 are stiffer compared to a high pH, such as 11. The minimum amount of DMS necessary to obtain gelation is observed to be in

the order of 150mM, as determined by vial inversion after 1 hour. As **2** showed promising initial results, and it is commercially available, it was selected for further research on the active material properties, as described in this work.

Cis-,cis-cyclohexane-1,3,5-tricarbonyl-trisphenylglycine, 3

3 is also tested as an active material, in a similar fashion to the other precursors (Fig. S3.2). During initial gelation tests with the **3**, upon addition of DMS an opaque gel was formed over time (Fig. S3.2 B). Samples were prepared according to the active material protocol, at a concentration of 25mM **3**, due to low solubility of the precursor. As determined by the vial inversion test after three hours, it is observed that a minimum amount of 200mM DMS, at pH 10, is necessary to form a gel. At pH 11, no gel was formed during these experiments. AFM images show that **3** forms bundles of fibers with individual fiber diameter of 10nm (Fig S3.2 D, E). To determine the content of the hydrogel fibers, a fresh sample was prepared at pH 9, 200mM DMS. After gelation, the gel was spun-down, freeze-dried and analyzed by ¹H-NMR (DMSO-d₆, H₂O-suppressed). The fibers were found to contain the bismethyl ester of **3**, based on the relative integrals of the phenyl rings (7.34ppm) and methyl ester (3.58ppm) (Fig. S3.2 C). Results from both COSY, DOSY and HSQCAD nmr studies (data not shown) supported this finding but could not exclude other possibilities. As **3** is found to form an active material, in a gelatinous state, it is further analyzed by rheology simultaneous with **2** for comparison.

Rheology traces

Time trace rheology of 2

By means of oscillatory rheology the material properties of active gels were determined with 50 mM **2**, at different pH (9–11) values and DMS concentrations (150–250 mM) (Fig. S3.3). The gels formed with low hydrolysis rates (pH 9 and 10, [DMS] = 200 mM) typically showed a rapid increase in storage moduli. Within 0.1 hour after addition of DMS the materials obtained storage moduli in the range of 10 kPa and a tan δ of 0.03 (Fig. S3.3A, B). The G' and G'' were constant over a wide frequency range, as shown for pH 9 at 5 hours reaction time (Fig. S3.4). After 2-3 hours the storage moduli of these gels (pH 9, 10) decreased less than 0.5 orders of magnitude. The active gels with high hydrolysis rates (pH 10.7 and 11, [DMS] = 200 mM) also showed a rapid increase in storage moduli, although the gelation time is delayed (Table S4, Fig. S3.3 C, E). These gels reached a lower maximum storage modulus of 4 kPa for gels at pH 10.7 and only 800 Pa for gels at pH 11. Moreover, in time these gels showed a decrease in storage and loss moduli of 1 and 1.5 orders of magnitude with respect to the maximum obtained modulus for pH 10.7 and pH 11, respectively.

The gels formed at different DMS concentrations (pH 11) also show a dependence of their properties on the reaction conditions (Fig. S3.3D-F). The gelation time, i.e., the moment where the storage modulus exceeds the loss modulus ($G'/G'' > 1$), occurs 1 hour after addition for 150 mM DMS but almost directly after the addition of 250 mM DMS. Furthermore, the maximum storage modulus increases with the amount of DMS added to the reaction. After reaching the maximum moduli, the storage and loss moduli slowly decrease for high initial DMS concentrations, and rapidly decrease for lower initial concentrations of DMS, giving a liquid sample for 150 mM DMS after 7.5 hours (Fig. S3.3D). At this time, the storage and loss moduli have decreased 2 orders of magnitude to 10⁻² Pa for 150 mM DMS, and the gel is completely dissolved ($G'/G'' < 1$). All gels formed at higher DMS concentrations show slower decrease in the storage and loss moduli, and remain a gel on the timescale of the experiments.

Time trace rheology of 3

The time and pH dependence of the gels of **3** were analyzed by oscillatory rheology, at conditions of 25mM **3**, 500mM borate buffer, 200mM DMS and different initial pH (Fig. S3.5). For pH 9, the G' crosses the G'' after 30 minutes of the start of the reaction, which indicates the formation of a gel material. The storage modulus increases rapidly to reach a G' of 100 Pa after 2 hours, with a tan δ of ~0.5. A slight increase of the storage modulus is seen over time for the pH 9 sample, reaching final values of 400 Pa. For higher pH levels (pH 10, 10.5), slightly weaker gels are formed reaching maximum G' of 70 Pa and 25 Pa, respectively. At these higher hydrolysis rates, over time these gels showed a decrease in storage and loss moduli of 0.5 and 1 order of magnitude with respect to the maximum obtained modulus for pH 10 and 10.5, respectively. The weakness of these gels also caused significant noise in the measurement, which was observed repeatedly and randomly. At pH 11, however no gel formation is observed, indicating that the critical gel concentration is not reached under these conditions.

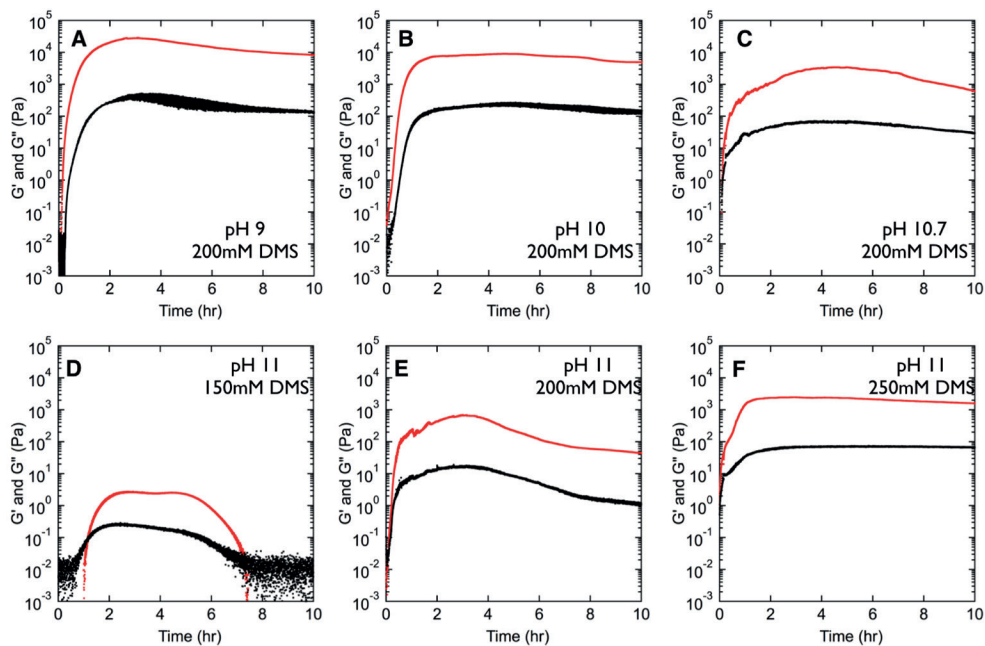


Fig. S3.3: Rheology over time

Rheology traces at different initial pH values (A, B, C, E) and different initial DMS concentrations (D, E, F) (50 mM of **2a** in borate buffer). The active gels were prepared by the general method. The red lines denote the storage moduli (G') and black lines the associated loss moduli (G'').

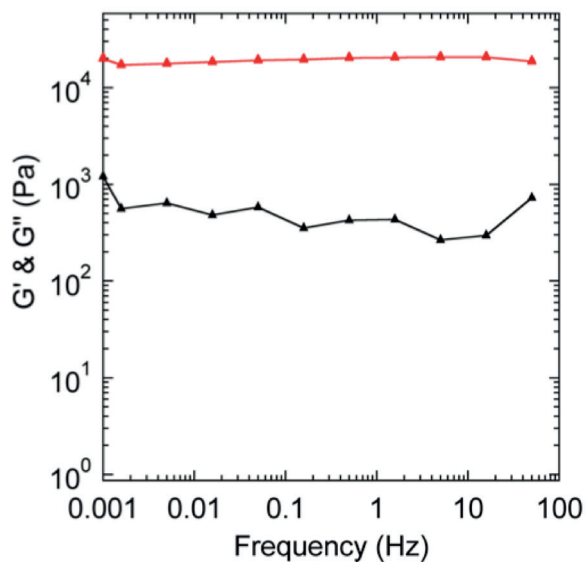


Fig. S3.4: Rheology

Frequency sweep at 5 hours in a reaction cycle (pH 9, [DMS] = 200 mM). The red line denotes the storage modulus (G'), the black line the associated loss modulus (G'').

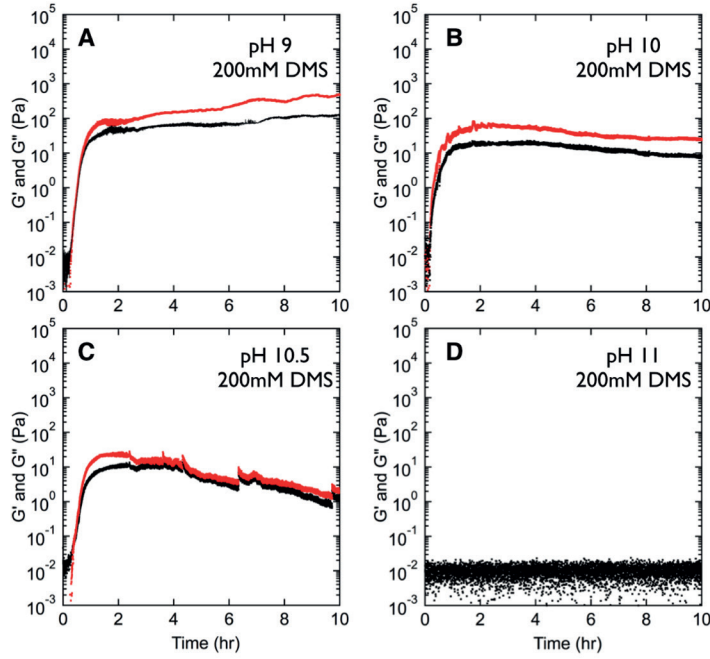
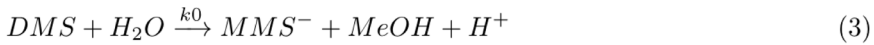


Fig. S3.5: Rheology over time of 3

Rheology traces at different initial pH values (9-11, A, B, C, E) at 200mM DMS, 25 mM of **3** in borate buffer. The active gels were prepared by the general method. The red lines denote the storage moduli (G') and black lines the associated loss moduli (G'').

Studies to determine rate constants

The following reaction scheme is used in the modeling of the time-dependent concentrations:



$$\frac{d[2a]}{dt} = -k_1[DMS][2a] + k_2[2b][OH^-] \quad (4)$$

$$\frac{d[2b]}{dt} = +k_1[DMS][2a] - k_2[2b][OH^-] \quad (5)$$

$$\frac{d[DMS]}{dt} = -k_0[DMS] - k_1[DMS][2a] \quad (6)$$

We applied the following procedure to determine the three reaction constants, k_0 , k_1 , k_2 in this kinetic model. First, initial values for k_0 , k_1 , k_2 were obtained from kinetic data for the concentrations of DMS and **2b**. Then the drift of the pH during a reaction cycle was determined and incorporated into the model, as described below. In the last step, the values of k_1 and k_2 were refined by a global optimization using the kinetic model with the concentration profiles of **2b** during a reaction cycle, at three different initial

pH values and taking the pH drift (see below) into account. The complete procedure with experimental determined data and obtained rate constants k_0 , k_1 , k_2 is as follows:

NMR experiment to determine k_0

Solvent suppressed ^1H -NMR was used to determine the hydrolysis rate constant of DMS in borate buffer. To a 2.5 mL aqueous solution of 500 mM borate (pH 9, 10 and 11) was added 23.8 mL DMS (31.6 mg, 100 mM) after which spectra were taken every 5 minutes giving 3 peaks: DMS 3.92 ppm (s), MMS 3.63 ppm (s), MeOH 3.29 ppm (s). Concentrations of DMS were calculated by the ratio of [DMS] to [MMS] taking into account that $[\text{DMS}] + [\text{MMS}] = 100 \text{ mM}$. The hydrolysis of DMS produces H^+ resulting in a drift of the pH. The pH drift during the reaction (see Figure S3.10) was not corrected but did not appear to have a significant influence on the rate constant since a linear correlation was obtained for $\ln[\text{DMS}]$ against time. The different values for k_0 at various pH values are contributed to the difference in ionic strength for the different initial pH. The experiments were performed in duplicate (Fig. S3.6).

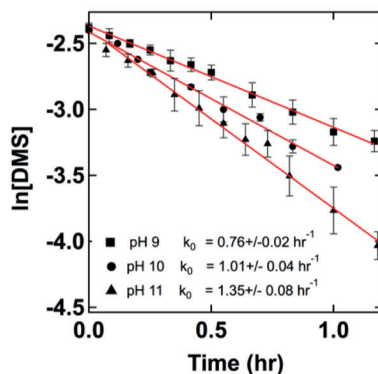


Fig. S3.6. Hydrolysis of DMS.

Natural logarithm of the concentration of DMS against time in the hydrolysis of DMS, as determined by ^1H -NMR. Linear fits give the first order rate constants (pH 9: $k_0 = 0.76 \text{ hr}^{-1}$, pH 10: $k_0 = 1.01 \text{ hr}^{-1}$, pH 11: $k_0 = 1.35 \text{ hr}^{-1}$), (squares pH 9, circles at pH 10, triangles at pH 11, red lines are linear fits).

HPLC-study to determine k_1 and k_2 .

To determine k_1 and k_2 the concentrations of **2a** and **2b** during a reaction cycle were followed by means of HPLC-MS. The concentrations were measured during a reaction cycle, by taking a 2.5 mL solution of 50 mM **2a** in 500 mM borate buffer at pH 9, 10, 11 in a 4 mL vial and adding 47.6 μL DMS (63.1 mg, 200 mM). The vial was vortexed to induce dissolution of DMS and stirred at $25 \pm 1^\circ\text{C}$. All cycles were performed in duplicate (Fig. S3.7). From these reaction cycles, k_1 and k_2 are determined by calculating the appropriate slopes (Fig. S3.7, Fig. S3.8), as described below.

To determine second order rate constant k_1 from the HPLC data in Fig. S3.7, the slope of the natural logarithm of **2a** against time is determined directly after the addition of DMS (Fig. S3.8). Based on k_0 and the maximum obtained concentrations of **2b**, it is estimated that 90% of the DMS during the reaction cycle is consumed by the hydrolysis reaction of DMS. Therefore it is assumed that in the first 0.5 hour of the reaction cycle, the DMS concentration can be calculated from the hydrolysis of DMS (eq. 3). Then plotting the natural logarithm of **2a** over $[\text{DMS}]_t$ versus time, according to equation 7, gives linear fits for all three conditions (Fig. S3.8). The linear fits validate the assumption that the DMS concentration can be estimated from the hydrolysis of DMS during the first 0.5 hours. The values of k_1 are obtained from the slopes of the fits, giving k_1 values of 3.0, 2.2, and $1.1 \text{ M}^{-1}\text{hr}^{-1}$ for pH 9, 10, 11, respectively.

$$\frac{\ln[2a]_t - \ln[2a]_0}{[DMS]_t} = -k_1 * t \quad (7)$$

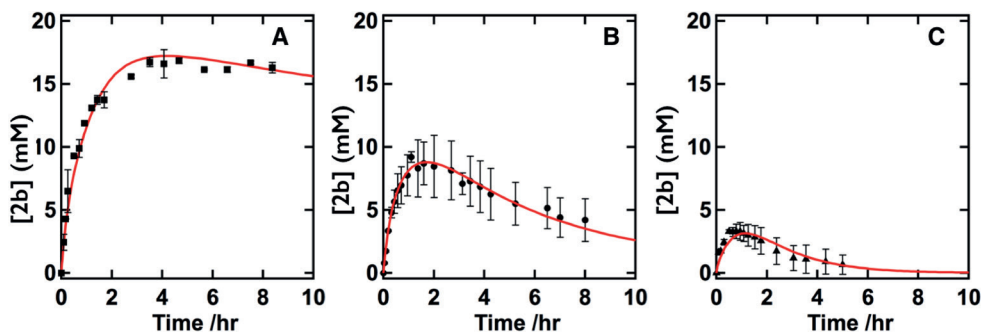


Fig. S3.7. Concentration profiles of 2b during reaction cycles.

Conditions: 50 mM **1**, 200 mM DMS, initial pH 9 (A) pH 10 (B) and pH 11 (C). The symbols mark the HPLC data plotted with standard error. The red line is the concentration profile of **2b** as calculated from the kinetic model using the optimized values for the rate constants k_0 , k_1 , k_2 correcting for the pH drift during a reaction cycle (vide infra, table S3, fig. S6).

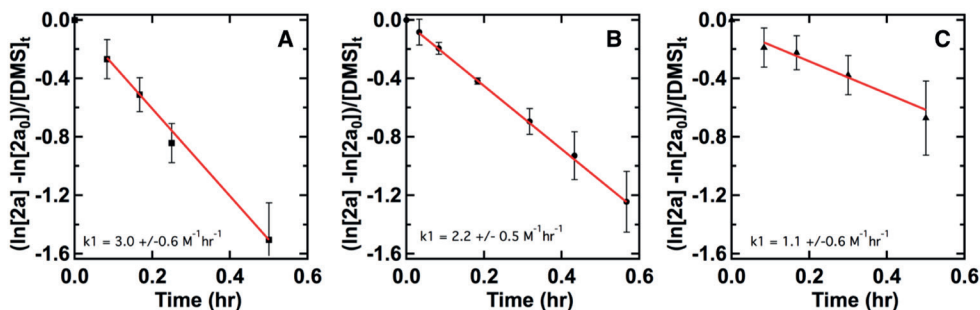


Fig. S3.8. Determination of k_1

k_1 was determined from a linear fit of $\ln[1]/[DMS]_t$ against time. Conditions: 50 mM **2a**, 200 mM DMS, initial pH 9 (A), pH 10 (B) and pH 11 (C). The red lines show the linear fits.

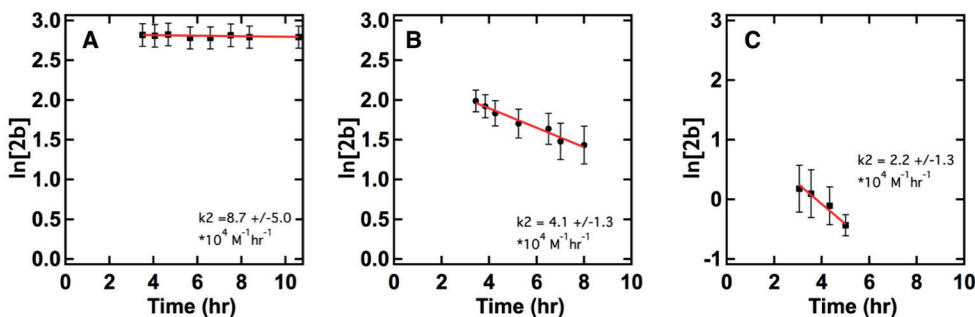


Fig. S3.9. Determination of k_2 by plotting $\ln [2b]$ versus time.

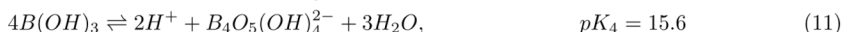
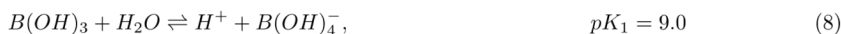
Conditions: 50 mM **2a**, 200 mM DMS, initial pH 9 (A) pH 10 (B) and pH 11 (C). k_2 was determined from the linear fit (red) of the natural logarithm of **2b** against time.

From the HPLC data in Fig. S3.7, the second order rate constant k_2 is estimated by plotting the slope of the natural logarithm of $[2b]$ against time (Fig. S3.9). To do so, only the data beyond $t = 3.5$ hours was used to assure that the hydrolysis of **2b** was the only reaction taking place (i.e., all DMS had been consumed). Furthermore, the pH was determined to remain nearly constant after 3.5 hours (Fig. S3.10). At each pH, linear fits of $\ln[2b]$ versus time were obtained, indicating that the hydrolysis of **2b** was the only reaction taking place under stable pH conditions (Fig. S3.9). The values of k_2 are obtained by correcting for the pH (*vide infra*), giving k_2 values of 8.7, 4.1, and 2.2 ($\times 10^4 \text{ M}^{-1}\text{hr}^{-1}$) for pH 9, 10, 11, respectively. The errors in k_2 are relatively large due to the low concentrations of OH⁻ combined with the measurement errors (table S3).

Drift in pH

The solution pH of any sample was found to decrease during each reaction cycle, despite buffering the solution. This pH drift will depend on the initial reaction conditions. To monitor this drift, the pH was measured during a reaction cycle, by taking a 2.5 mL solution of 50 mM **2a** and adding 47.6 μL DMS (63.3 mg, 200 mM) in 500 mM borate buffer at pH 9, 10, 11 in a 4 mL vial. The vial was vortexed to induce dissolution of DMS and stirred at $25 \pm 1^\circ\text{C}$. Measured pH is converted to $[\text{OH}^-]$, according to $[\text{OH}^-] = 10^{(14.2+\text{pH})}$. The pH drifted to lower values as a result of the reactions 2 and 3 (Fig. S3.10).

To estimate the pH drift during a reaction cycle, a balance equation for the borate buffer is made and added to the reaction kinetics model. The equilibrium distribution of the different borate species, is calculated based on the multiple reactions for the borate buffer (eq. 8-11) ($22(pK_{1-3})$, $23(pK_4)$). For pK_{a_y} , the reported value was found to give best results. To calculate the pH drift it is assumed that the pH is in equilibrium on the timescale of the experiments. The activity coefficients at different ionic strength are estimated based on the Davies equation, eq. 12 (24). The equations 8-12 are combined with the charge neutrality in solution and mass conservation during the reaction. The resulting set of equations is then numerically solved, using the least-squares routine LSQNONLIN in Matlab. The pH is numerically calculated, as part of the kinetic model described below. The model gave a close fit (dashed lines in Fig. S3.10A-C) for all pH values. The small deviations between the numerically calculated and measured pH are attributed to the complex nature of the borate buffer.



$$-\log(\gamma) = 0.5115z^2 \left(\frac{\sqrt{I}}{1 + \sqrt{I}} - 0.3I \right) \quad (12)$$

γ = average activity coefficient, pK = pK of borate species, z = charge, I = ionic strength

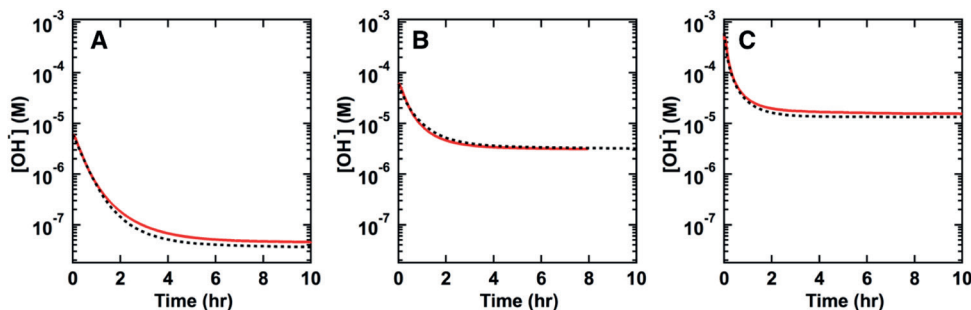


Fig. S3.10. The $[\text{OH}^-]$ drift over time.

The pH was measured over time, for reaction cycles starting with 50 mM **2a**, 200 mM DMS at initial pH 9 (A), pH 10 (B) and pH 11 (C). The measured pH is converted to $[\text{OH}^-]$ (red lines), according to $[\text{OH}^-] = 10^{(14.2+\text{pH})}$. The black dots are simulated pH values for the same conditions (50 mM **2a** and 200 mM DMS) as calculated by the kinetic model and taking the pH drift into account using the pH model described below.

Reaction kinetics model

The reaction kinetics model describes the time dependent concentration of **2a**, **2b**, DMS, MMS and OH⁻ using the differential equations 4-6 and the model. The equations 4-6 describe the time dependent methylation and hydrolysis rates of components **2a**, **2b** and the DMS concentrations. The background hydrolysis of DMS is first order in the DMS concentration and shows no dependence on the drift of pH, as shown by NMR experiments (Fig. S3.6). The resulting set of differential equations is numerically solved using the ode45 routine in Matlab, with the addition of the in-equilibrium calculated pH (eq. 8-11). The experimentally determined rate constants are used as initial values. As the uncertainties in k_1 and k_2 are large, these constants were allowed to be varied by the model during a fitting procedure, where the model is compared to the measured HPLC data (Fig. S3.7). Table S3.3 shows the found reaction constants and the errors in the parameters for the global fits at the different reaction conditions.

The fitted rate constants were used for obtaining the modeled data. The obtained results are plotted in Fig. S3.2 (red line), showing a good fit of the kinetics model and the measured concentrations. This model is then used to obtain the concentration profiles of **2b** at different initial pH and DMS concentrations (Fig. S3.11).

Table S3.3: Reaction constants as determined from data and model fits.

	pH 9	pH 10	pH 11
k_0 (hr⁻¹)	0.76 +/- 0.02	1.01 +/- 0.04	1.35 +/- 0.08
Fitted k_1 (M⁻¹hr⁻¹)	3.1 +/- 0.3	2.5 +/- 0.2	1.6 +/- 0.4
Fitted k_2 (10⁴M⁻¹hr⁻¹)	28 +/- 20	5.6 +/- 1.2	3.8 +/- 1.9

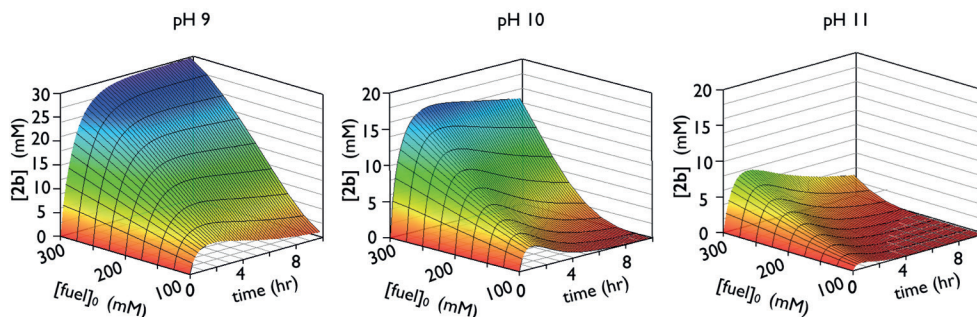


Fig. S3.11: Concentration profiles of reaction cycles depending on DMS concentrations.

Concentration of **2b** over time calculated by the kinetic model for different pH values and initial DMS concentrations.

Experiments to determine the Critical Gelation Concentration (CGC)

Using the inverted tube test, the macroscopic CGC was determined. As the behavior of the system changes over time during a reaction cycle, the time at which a gel is formed was determined. The concentration of **2b** at the gelation time was estimated by HPLC and the kinetic model described above (Fig. S3.11, table S3.4). It was observed that, at pH 11, gels were formed between 0.25 hours and 0.5 hours, which corresponds to a concentration between 2.1 and 3.1 mM, respectively ($CGC = 2.6 \pm 0.5$ mM), based on the HPLC and the kinetic model. To confirm this concentration, a second experiment was performed in which the $[DMS]_0$ was varied and the gel formation was determined with the inverted test tube. In this experiment, gels were only formed if 175 mM DMS or more was added. Next, the kinetic model is used to estimate the maximum concentration of **2b** for the different concentrations of DMS (Table S4, right side). From these maximum concentrations the corresponding CGC is determined to be between 2.4 and 3.1 mM ($CGC = 2.8$ mM \pm 0.3 mM). At DMS concentrations of higher than 350 mM phase separation occurs due to incomplete dissolution of DMS. Nevertheless these mixtures do form opaque gels. The average of the CGCs determined by both methods was used as an upper limit for the CGC (2.7 mM).

Table S3.4: Macroscopic morphology against time or $[DMS]_0$ during a reaction cycle at pH 11.

time (hr)	[2b] / mM	gel	regenerating		$[DMS]_0$	[2b] _{max} / mM	gel
0.0	0.0	no	-		0	0	no
0.25	2.1	no	-		100	1.3	no
0.5	3.1	yes	yes	← critical gelation concentration	150	2.4	no
0.75	3.6	yes	yes		200	3.9	yes
1	3.9	yes	yes		250	5.5	yes
1.5	3.7	yes	no				
2	3.2	yes	no				

Table S3.5: Rheological estimation of CGC. The concentration of 2b is estimated at the moment that G' crosses G'' , based on HPLC data and the kinetic model.

pH	Gelation $G'/G'' > 1$		Gel dissolution $G'/G'' < 1$	
	Time (hr)	Concentration of 2b (mM)	Time (hr)	Concentration of 2b (mM)
9	0.1 (+/-0.05)	2.5 (+/-1.4)	-	-
10	0.1 (+/-0.05)	2.0 +/-0.8)	-	-
10.7	0.2 (+/-0.075)	2.9 (+/-0.8)*	25 (+/- 2)	0.05 (+/-0.02)*
11	0.3 (+/-0.1)	2.45 (+/-0.7)	15 (+/- 2)	0.01 (+/-0.005)*

* Data estimated using kinetic model at relevant conditions.

To compare the above results and to gain insights into the gel dissolution, the gel point is also determined by rheology. Here, we use the point where the ratio G'/G'' becomes greater than one, and the gel dissolution point where the ratio G'/G'' becomes smaller than one (table S5). The associated concentrations of **2b** at these points are estimated based on the measured HPLC data (if available) and the kinetic model. Based on the measured data it was estimated that at the gel point $G'/G'' > 1$ (during formation), the concentration of **2b** is around 2.5 mM, which is in agreement with the observed macroscopic CGC (vide supra). The moment of gel dissolution ($G'/G'' < 1$) occurs after around 15 hours (pH 11), which is beyond the last experimentally measured concentration of **2b** (0.6 mM after 5 hours at pH 11). With the kinetic model the concentration of **2b** is estimated to be below 0.1 mM after 15 hours, at the moment of dissolution. This low value strongly deviates from the value observed during formation, indicating that the processes of gel formation and dissolution are not equivalent. It suggests that, during the later stages of a reaction cycle, the fibers also contain significant amounts of **2a** (Fig. S3.16, table S3.5).

Regeneration capability

The regeneration capability (RC) of the active gels (50 mM **2a**, 200 mM DMS with pH values of 9, 10 or 11) was determined by oscillatory rheology (Fig. S3.12, S3.13, S3.14, S3.15). After an initial time sweep of a set length, the samples were subjected to a strain sweep (max. strain 300%). For all samples it was observed that at the end of the strain sweep the G' was lower than the G'' , indicating that the samples have become fluid. After this strain sweep, regeneration of the gel rheology was measured with a time sweep. The regeneration capability was determined by dividing the G' just before the strain sweep and the maximum obtained G' after the strain sweep (Fig. S3.13, S3.14, S3.15). The concentration of DMS at the moment of each strain sweep was inferred from the kinetic model. Fig. S3.12 shows the regeneration capability in relation to the DMS concentrations for different initial pH values, in which each data point represents an individual experiment. At high DMS concentrations, all gels showed high RCs, reaching up to 6000 for pH 9, and the RCs show exponential dependence on the DMS concentration, independent of pH (Fig. 3.2, Fig. S3.12). Below the point where $RC=1$ no complete self-regenerating behavior is observed. For all pH values, $RC=1$ occurs at $[DMS]_t \sim 20$ mM, indicating that a minimum concentration of DMS is necessary for the regeneration of the gel network after mechanical perturbation.

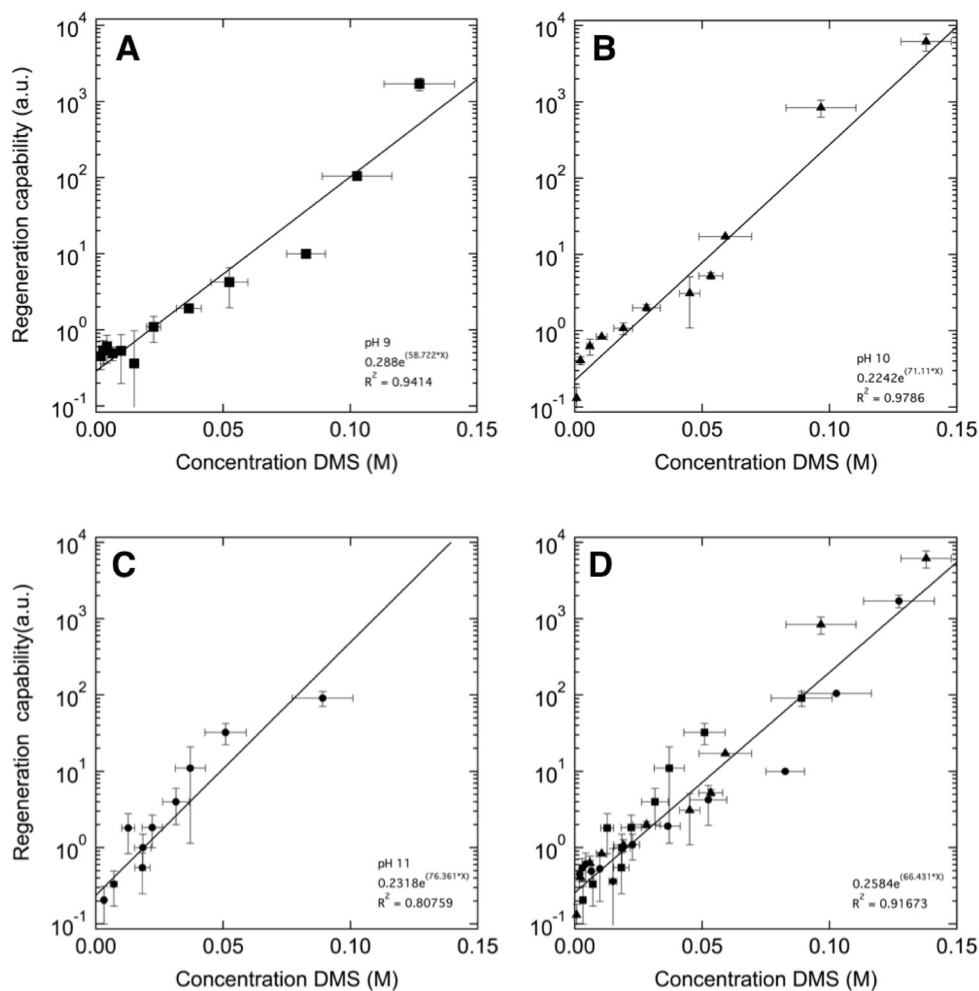


Fig. S3.12: Regeneration

DMS-dependent regeneration capability for pH 9, pH 10, pH 11. Regeneration capabilities as determined by rheology for initial pH of 9 (A, squares), 10 (B, triangles), 11 (C, circles) with estimated errors. In D all data plotted together as shown in the main article (Fig. 3), including errors. Lines are exponential fits to the data (insets show fit parameters and coefficient of determination) and each data point represents an individual experiment.

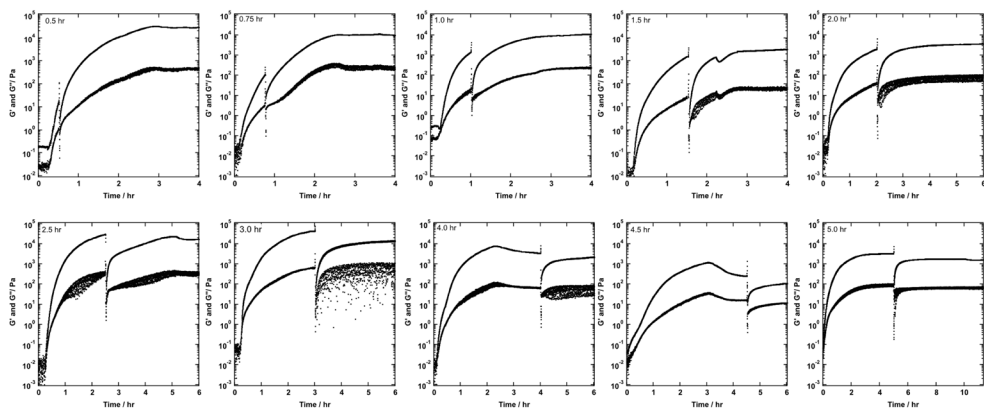


Fig. S3.13: Regeneration traces (rheology) at pH 9.

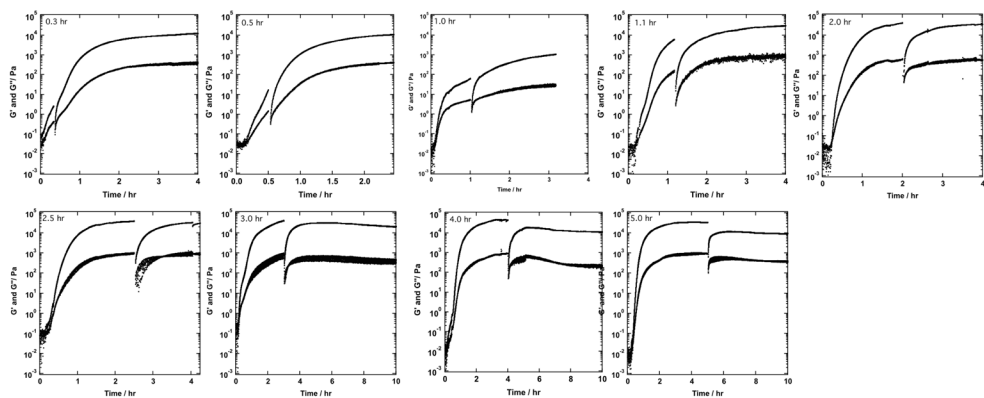


Fig. S3.14: Regeneration traces (rheology) at pH 10.

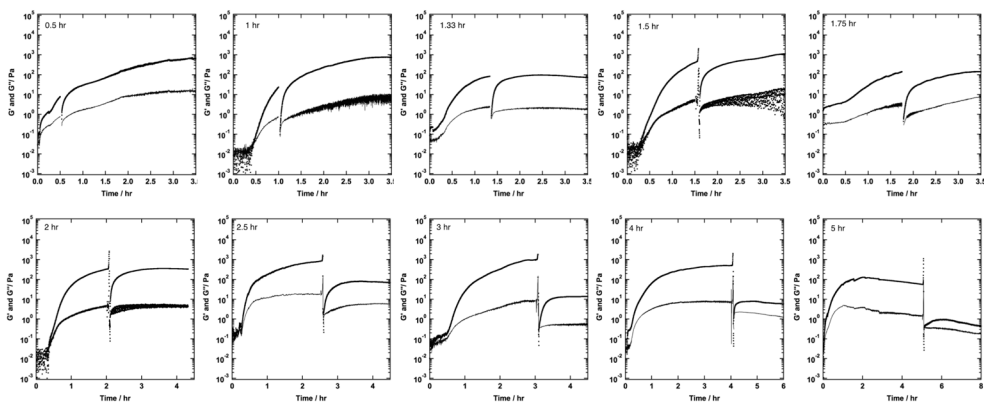


Fig. S3.15: Regeneration traces (rheology) at pH 11.

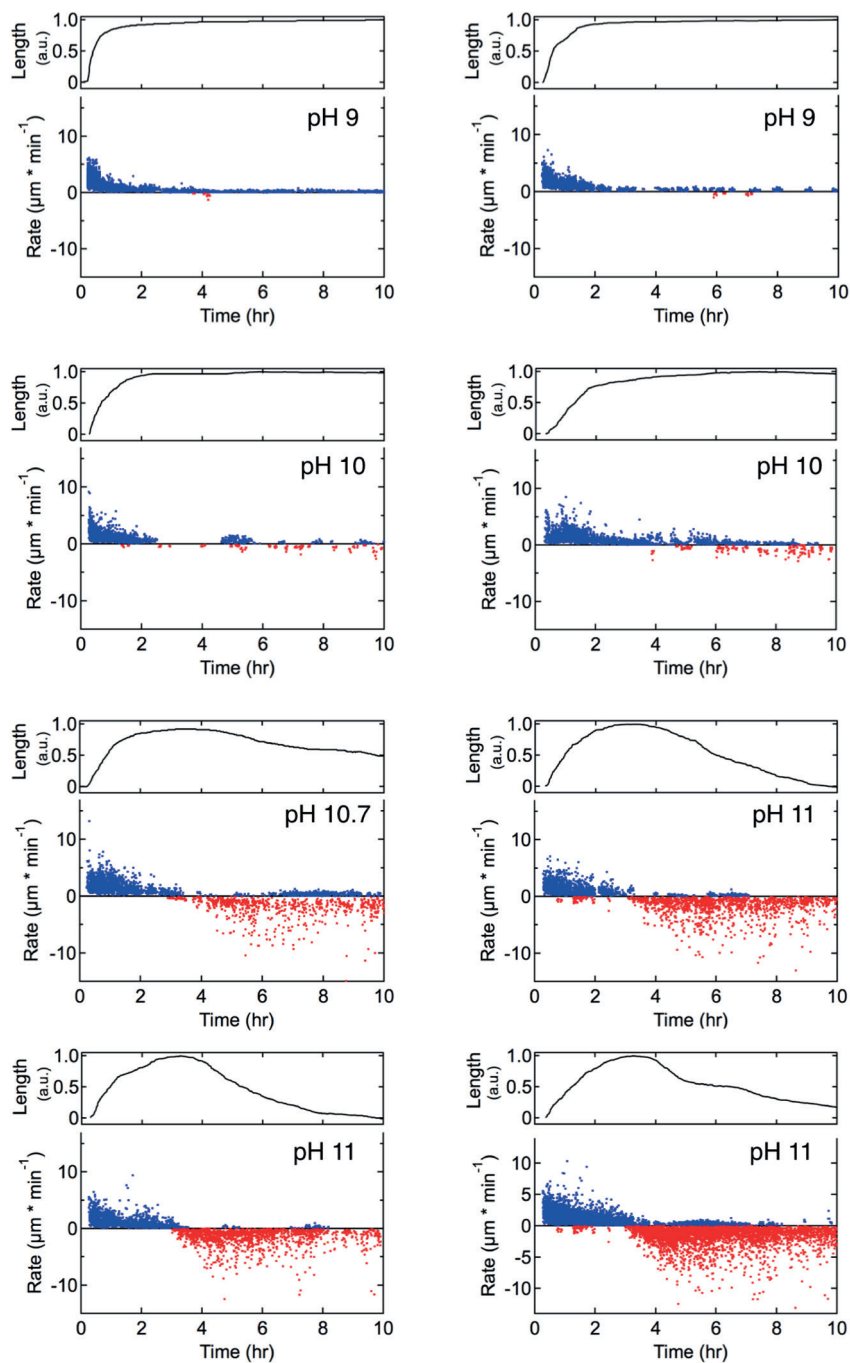


Fig. S3.16: Fiber growth rates.

Each data point is the rate of growth (blue) or shrinkage (red) of an individual fiber between two frames, as measured by confocal microscopy and analyzed using ImageJ. The total fiber length (top) is determined from the sum of the individual fibers and normalized to the maximum fiber length. Each panel represents an individual experiment, at the indicated pH.

Fiber Tracking

The growing and shrinking of gel fibers is tracked in-situ using confocal microscopy, to investigate the time dependent behavior of fiber dynamics. The growth and shrinking of fibers are represented as positive and negative growth rates, respectively. The rates at each time step for each measured fiber are visualized in a scatter plot of all the measured fibers during the experiments (Fig. S3.16). The lengths of the fibers at each time step are extracted and summed over time, of which the normalized records are plotted above the scatter plots.

All active gels showed a rapid increase in total fiber growth, after an initial delay of ~ 0.2 hours (Fig. S3.16). This growth typically leveled off after 4 hours, but a number of growing fibers are observed beyond this point. In all conditions the highest growth rates (15 $\mu\text{m}/\text{min}$) are observed directly at the beginning of the growth period, after which the growth rates decay over time. From the kinetic model it is observed that directly after the DMS addition the rate of alkylation is maximal, its rate of subsequent decrease depends on the pH (Fig. 3.3). Furthermore the increase in total fiber length occurs fastest in the gels with low hydrolysis rates, i.e. pH 9 and pH 10, for which 90% of the total fiber length growth occurs in the first 2 hours of the experiment. After this point the rate of growth decreases and the total fiber length levels off, showing slight decrease for pH 10 at the end of the experiment. These gels showed only few shrinking fibers, although pH 10 already contained a substantially larger amount of shrinking fibers compared to gels prepared at pH 9.

For gels with higher hydrolysis rates (pH 10.7 and pH 11), the growth of the total fiber length takes place at a lower rate, reaching maxima at 4.2 hours for pH 10.7 and at 3.2 hours for pH 11 (Fig. S3.16). The amount of shrinking fibers and the rate of shrinking of these fibers is observed to increase with pH, with rates as fast as $-10 \mu\text{m}/\text{min}$ (Fig. S3.16). In sharp contrast to the gels at pH 9 and 10, after 10 hours, the total fiber length has decreased to $\sim 50\%$ and $\sim 10\%$ for gels at pH 10.7 and pH 11, respectively, at which time the measurement was stopped.

From the kinetic model it is observed that the hydrolysis rate of **2b** increases with pH (Fig. 3.3, Fig. S3.7). There is a difference in time between the moments where the maximum concentration of **2b** is reached and of maximum fiber length. The moment of maximum fiber length occurs later in time compared to the maximum concentration of **2b**. Also the decrease of the total fiber length occurs slower compared to the hydrolysis of **2b**. For example, for pH 11 at 5 hours the measured concentration of **2b** equals 30% of the maximum concentration but still 70% of the total fiber amount is observed at this moment in time.

The normalized total fluorescence intensities of the measured frames during a time trace are plotted for different initial pH (Fig. S3.17). The total fluorescence equals the sum of all the imaged fibers during an experiment. These normalized fluorescence intensities show strong increases in the first 3 hours of each experiment after which they reach a maximum around 3.5 hours. The decrease in fluorescence

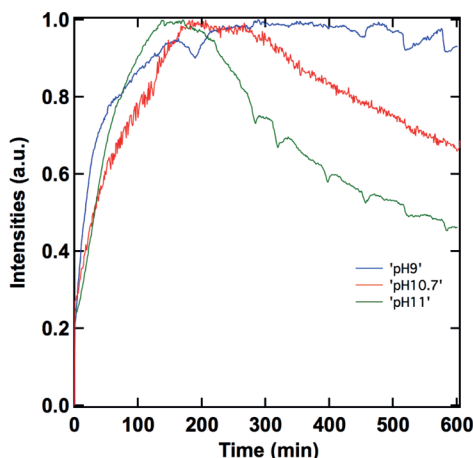


Fig. S3.17: Normalized fluorescence intensities for time series at different initial pH.

The measurements for samples of a) pH 9 (red line), b) pH 10.7 (black line), c) pH 11 (green line), all samples made with 50 mM **1**, 500 mM buffer and 200 mM DMS.

intensities shows a dependence on pH, decreasing to ~65% and ~40% for pH 10.7 and 11, respectively. These observations are in good agreement with the observations for the tracked fibers and indicate that the fiber tracking process covers a representative part of the sample.

Surface plots

To rule out the existence of large-scale gradients over the whole sample area during measurement, the individual fiber dynamics are plotted on a XY surface (Fig. S3.18-21). Using a code written in Matlab, the measured data is plotted in on a graph with the X,Y axes in μm and the color bars indicate the moments in time of fiber growth and shrinkage. It is observed that the growth of the fibers occurs randomly distributed over the surface. The number of growing fibers are evenly distributed in the X and Y direction, indicating that no large-scale gradient of the samples exist. The formed fibers are partly distributed in spheres around center points. For the shrinking fibers, the number and location of shrinking fibers are evenly distributed in the X and Y direction, again indicating that no large-scale gradient over the samples exist. It is observed that the occurrence of a shrinking fiber at a specific location does not directly lead to occurrence of more shrinking fibers in the close vicinity.

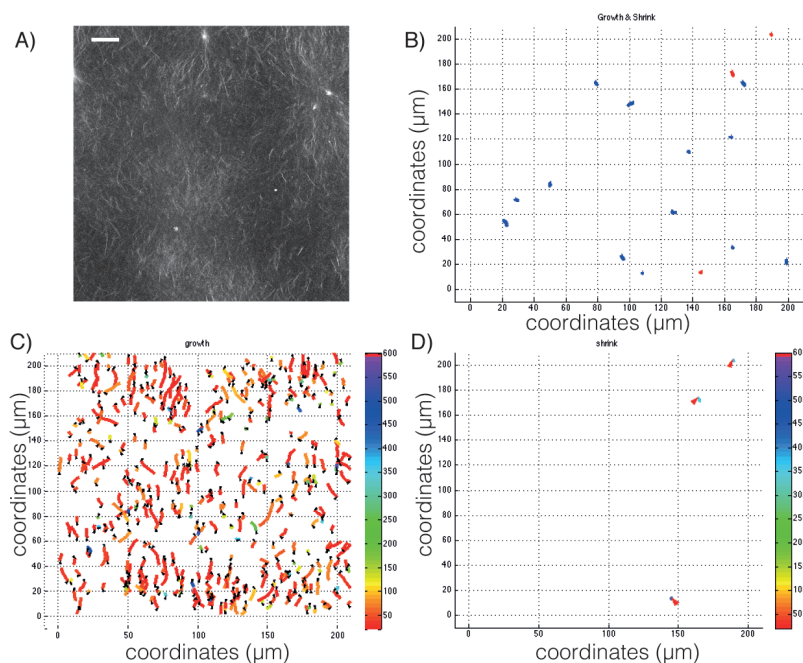


Fig. S3.18: Surface plots of fiber growth behavior at pH 9.

a) a representative confocal microscopy image (220x220 μm) during the measurement, b) is a surface plot of the period where both growing (blue) and shrinking fibers (red) are observed (6h-8h); c) and d) show all growing (c) and shrinking (d) fibers during the entire measurement, with the color bar indicating the moment of a fiber event in minutes.

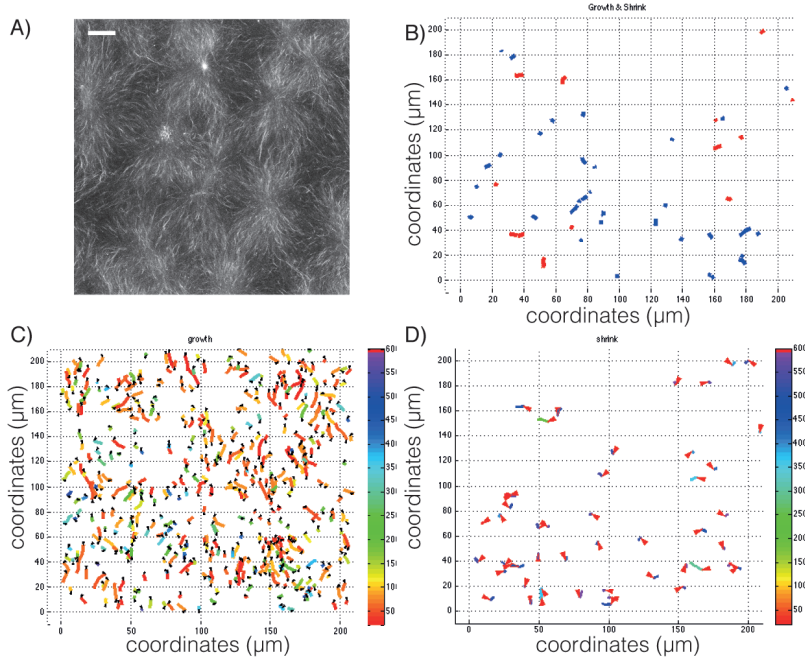


Fig. S3.19: Surface plots of fiber growth behavior at pH 10.

a) a representative confocal microscopy image (220x220 μm) during the measurement, b) is a surface plot of the period where both growing (blue) and shrinking fibers (red) are observed (6h-8h); c) and d) show all growing (c) and shrinking (d) fibers during the entire measurement, with the color bar indicating the moment of a fiber event in minutes.

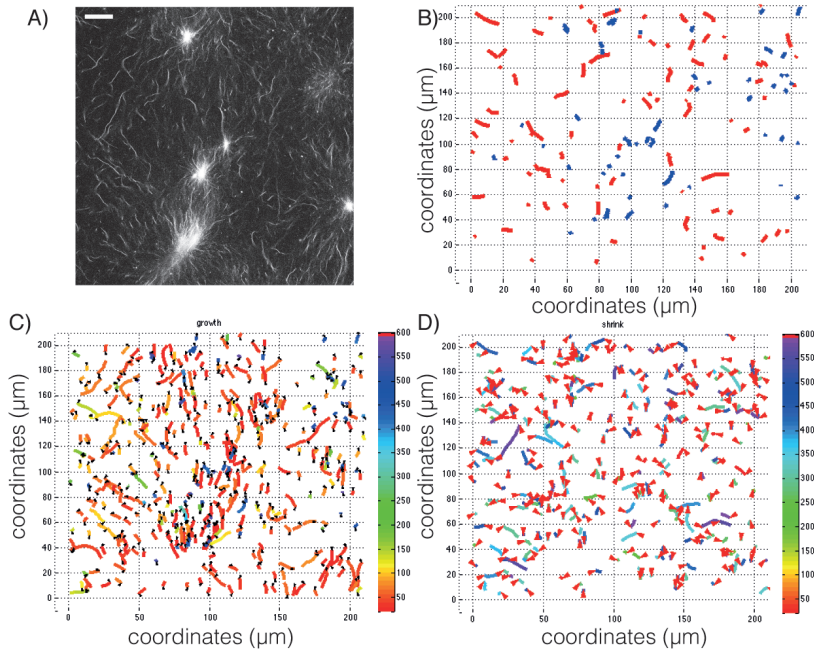


Fig. S3.20: Surface plots of fiber growth behavior at pH 10.7.

a) a representative confocal microscopy image (220x220 μm) during the measurement, b) is a surface plot of the period where both growing (blue) and shrinking fibers (red) are observed (6h-8h); c) and d) show all growing (c) and shrinking (d) fibers during the measurement, with the color bar indicating the moment of a fiber event in minutes.

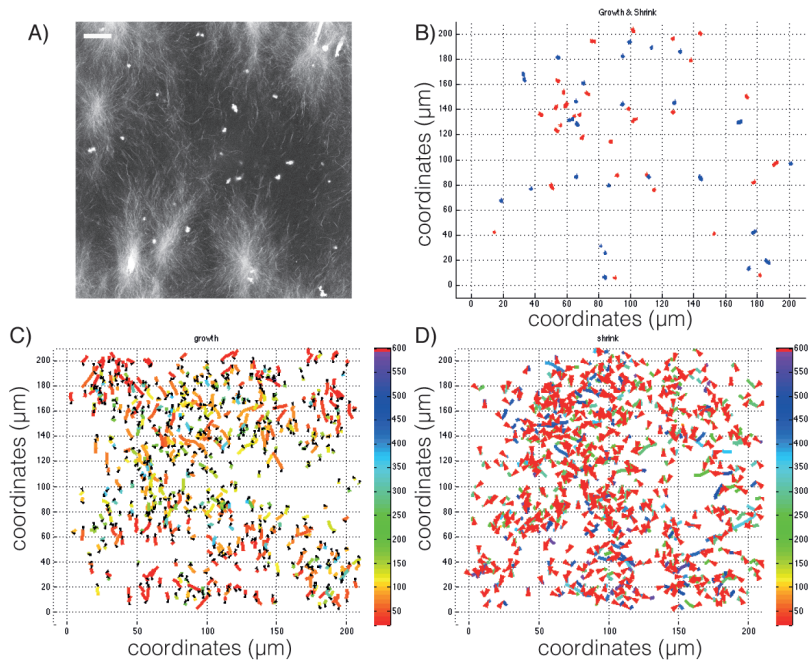


Fig. S3.21: Surface plots of fiber growth behavior at pH 11.

a) a representative confocal microscopy image (220x220 μm) during the measurement, b) is a surface plot of the period where both growing (blue) and shrinking fibers (red) are observed (4h-6h); c) and d) show all growing (c) and shrinking (d) fibers during the entire measurement, with the color bar indicating the moment of a fiber event in minutes.

Active material formation under continuous fuel addition

To keep a formed active material in an out-of-equilibrium situation, a setup for continuous addition of fuel was designed. An active material sample was prepared, by mixing a 1 ml solution of 50 mM 2a, in 500mM borate buffer at pH 10.7 with 18.8 μ l of DMS (200mM). After vigorous stirring, this solution is placed in a cuvette (2.5 ml) and sealed airtight with a cap. This cap was fitted with two tubes, an inlet and outlet of which the inlet was placed just above the active material level and the outlet at the top of the cuvette (Fig. S3.22A). The active material formation was allowed to form over an hour after which the flow for a continuous situation was started. The flow sequence consisted of the following steps:

Step	Time	Flow rate	Total Volume	Contains	Purpose
0	0	Injection	1 ml	50 mM 2a /500mM borate, 200mM DMS	Active material forming
1	1hr 20min	1ml/min	1 ml	50 mM 2a /500mM borate, pH 10	Filling of top/ ensure proper closure
2	1hr 21min	0.2ml/min	35 ml	50 mM 2a /500mM borate, pH 10	Supply of active material
		1 μ l/min	~160 μ l	DMS, pure	
3	4hr 20min	0.1ml/min	50 ml	50 mM 2a /500mM borate, pH 10	Slow down supply of active material
		0.2 μ l/min	~100 μ l	DMS, pure	
4	19hr 5min	0.1ml/min	50 ml	50 mM 2a /500mM borate, pH 10	Stop supply of DMS, decay of active material
5	27h 10m	0.02ml/ min	50 ml	50 mM 2a /500mM borate, pH 10	Decay of active material

The samples are analyzed by measuring their turbidity using UV-vis transmission at a wavelength of 640nm. Two samples were measured in each experiment, one batch sample and one continuous flow sample. The data was then normalized to the maximum of the batch sample.

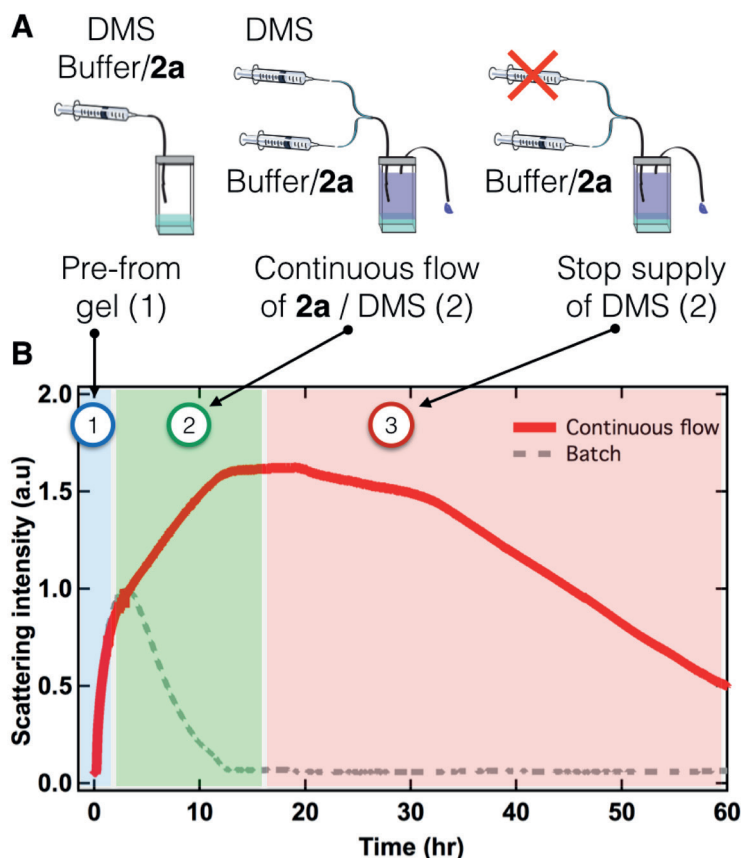


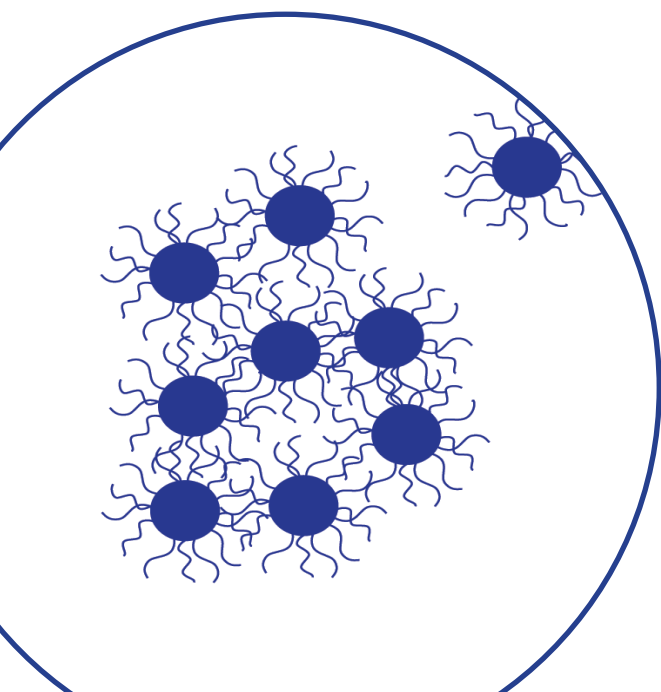
Fig. S3.22: Active material formation and decay during continuous flow experiment, followed by turbidity at 640nm.

Initially a gel is premade by injection of 50mM 2a, 200mM DMS in borate buffer, and left to stand for 1hr20min (A, 1). Then the continuous flow is started containing both DMS and 2 in borate buffer, to supply the gel with new fuel and to replace building blocks (A, 2). Eventually the flow of DMS is stopped, to let the active material decay (3). The scattering intensity is followed during this process of the sample with continuous flow (B, red line) and a batch process (B, grey line) without the flow procedure. Data are normalized to maximum of the (batch) control sample.

Three regimes are distinguished in the above plot: the initial growth of the active material, from 0 to 1h20, supply of the active material, from 1h20 to +/-16hr, and the decay of active material from about 20hr (Fig. S3.22). In grey a batch sample is visible, measured under identical conditions, but without the continuous flow. This batch sample has only added 1ml of pH10 buffer at the same moment that the flow starts for the continuous sample. The strong decay after 3 hours of the control sample is thus fully contributed to the hydrolysis reaction. In the initial phase of the continuous experiment (Step 1), 1mL of buffer containing 200mM fuel and 50mM gelator 2a are placed in the cuvette. From this point on a gel is formed, as indicated by an increase in scattering intensity. After 1hr20min, Step 2, the flow is started supplying the precursor 2a and the fuel to the system. In this regime (2) a further increase of scattering is observed, indicating that the supply of components causes an increase in the fiber concentration. Between 12 and 19 hours, a stabilization of the scattering occurs, after slowing down the supply of the fuel by decreasing the flow rate. This occurs with a lag time due to the mixing and diffusion processes taking place. After Step 4 at which the supply of the fuel is completely stopped, decay of the gel is observed. These observations indicate that the formation and decay of the active material can be controlled in a continuous experiment, by supplying both fuel and non-activated building block 2a.

3.5 References and Notes:

1. E. Karsenti, Self-organization in cell biology: a brief history, *Nat. Rev. Mol. Cell Biol.* **9**, 255-262 (2008).
2. F.J. Ndlec, T. Surrey, A.C. Maggs, S. Leibler, Self-organization of microtubules and motors, *Nature* **389**, 305-308 (1997).
3. T. Aida, E.W. Meijer, S.I. Stupp, Functional Supramolecular Polymers, *Science* **335**, 813-817 (2012).
4. A. Desai, T.J. Mitchison, Microtubule polymerization dynamics, *Annu. Rev. Cell Devel. Biol.* **13**, 83-117 (1997).
5. G.M. Whitesides, B.A. Grzybowski, Self-Assembly at All Scales, *Science* **295**, 2418-2421 (2002).
6. M. Fialkowski *et al.*, Principles and Implementations of Dissipative (Dynamic) Self-Assembly, *J. Phys. Chem. B* **110**, 2482-2496 (2006).
7. D.Y. Zhang, R.F. Hariadi, H.M.T. Choi, E. Winfree, Integrating DNA strand-displacement circuitry with DNA tile self-assembly, *Nat. Commun.* **4**, 1965 (2013).
8. S. Debnath, S. Roy, R.V. Ulijn, Peptide Nanofibers with Dynamic Instability through Nonequilibrium Biocatalytic Assembly, *J. Am. Chem. Soc.* **135**, 16789-16792 (2013).
9. F. C. Keber, E. Loiseau, T. Sanchez, S. J. DeCamp, *et al.*, Topology and dynamics of active nematic vesicles, *Science* **345**, 1135-9 (2014).
10. G. von Maltzahn, *et al.*, Nanoparticle Self-Assembly Directed by Antagonistic Kinase and Phosphatase Activities, *Adv. Mater.* **19**, 3579-3583 (2007).
11. I. Lagzi, B. Kowalczyk, D. Wang, B.A. Grzybowski, Nanoparticle Oscillations and Fronts, *Angew. Chem. Int. Ed.* **49**, 8616-8619 (2010).
12. J. Boekhoven *et al.*, Dissipative Self-Assembly of a Molecular Gelator by Using a Chemical Fuel, *Angew. Chem. Int. Ed.* **49**, 4825-4828 (2010).
13. R. Hirst *et al.*, Biocatalytic induction of supramolecular order, *Nature Chem.* **2**, 1089-1094 (2010).
14. Y. Gao, J. Shi, D. Yuan, B. Xu, Imaging enzyme-triggered self-assembly of small molecules inside live cells, *Nat. Commun.* **3**, 1033 (2012).
15. All pH values denote initial pH values. The pH decreases as the cycle proceeds as a result of the release of protons. The drift in pH is taken into account in the kinetic model.
16. R.G. Weiss, P. Terech, Ed. *Molecular Gels: Materials with Self-Assembled Fibrillar Networks*, (Springer, Dordrecht, 2006).
17. The regeneration capability is defined as the ratio between the gel strength (G') just before a strain sweep and the recovered maximum gel strength (G'), as determined by rheology, see SI.
18. K.J.C. van Bommel, M.C.A. Stuart, B.L. Feringa, J. van Esch, Two-stage enzyme mediated drug release from LMWG hydrogels, *Org. Biomol. Chem.* **3**, 2917-2920 (2005).
19. J. Makarević, *et al.* *Chem. Eur. J.* **7**, 3328-3341 (2001)
20. K.J.C Van Bommel *et al.*, *Angew. Chem. Int. Ed.* **43**, 1663-1667 (2004)
21. N. Ingri, *Acta. Chem. Scand.*, **17**, 3, 581-589 (1963)
22. L. Maya, *Inorg. Chem.*, **15**, 9, 2179-2183 (1976)
23. C.W. Davies, *J. Chem. Soc.*, 2093-2098 (1938)



Out-of-equilibrium self-assembly of colloidal particles driven by a chemical fuel

4

Colloidal particles with carboxylic acid carrying polymer hairs were prepared and found to show out-of-equilibrium self-assembly, fuelled by an alkylation reaction. The aggregates show transient self-assembly and can be recycled by multiple fuel additions. This work presents an extension of a general approach towards out-of-equilibrium self-assembly, driven by chemical fuels.

This chapter is based on collaborative work and will partly be published in the Ph.D. thesis of Bas van Ravensteijn (Utrecht Universiteit). A joined publication is in preparation.

4.1 Introduction

Out-of-equilibrium self-assembling materials that show transient properties upon energy dissipation are an exciting new challenge for science. This challenge is inspired by the complex dynamic behavior of biological systems (1), for example, spatiotemporal self-assembly, adaptability, self-healing and recyclability, as is observed in microtubule and cells (1, 2). Colloidal self-assembling systems offer a powerful strategy towards bottom-up design of mesoscopic structures, as determined by the surface chemistries, particle interactions and shape (3-5). For colloidal systems, a variety of energy driven strategies have been developed to achieve out-of-equilibrium self-assembly, with energy sources such as light, magnetic forces, and electric fields (6-12). For example, the light driven reversible self-assembly of gold particles has been applied to form a 'self-erasing inks' (13). The artificial colloidal systems for out-of-equilibrium self-assembly offer new insights, but remain relatively 'simple' compared to biological systems. These biological systems typically rely on the consumption of chemical fuels, such as the energy rich adenosine triphosphate (ATP). For example, when ATP reacts with actin ATP-actin is formed which has a stronger binding constant for the actin filaments. The altering of the chemical interactions between actins by reaction with ATP thus leads to self-assembly into filaments (14-16). Chemical fuel propelled motion of colloids upon decomposition of hydrogen peroxide has been achieved, leading to autonomous movement (8, 10, 17). Some of these chemical fuel propelled systems do show self-assembly, but only due to the collective motion of the particles (11). The use of chemical fuels to form self-assembled materials by adapting the chemical interactions between the building blocks is an open challenge for out-of-equilibrium colloidal systems.

Chemical fuel driven assemblies that are transient in time, form a new approach to out-of-equilibrium particle self-assembly. In small molecule self-assembly, several strategies are developed for fuel driven self-assembly, creating systems that form molecular gels, membranes, and membrane transport systems (18-20). Recently, a new approach to a chemical fuel driven out-of-equilibrium self-assembly for small molecules is developed by us as discussed in Chapter 3, (21). In this approach, the chemical fuel driven conversion of a carboxylate to an ester, removes an ionic charge and induces a self-assembly process. Under the hydrolytic conditions used, a second reaction hydrolyses the formed esters back to the acids, leading to disassembly. The whole reaction cycle produces out-of-equilibrium materials with controllable transient properties. Although the design principles were made for molecular systems, they are not limited to small molecules and can also be applied in other fields, and here we extend them to colloidal self-assembly.

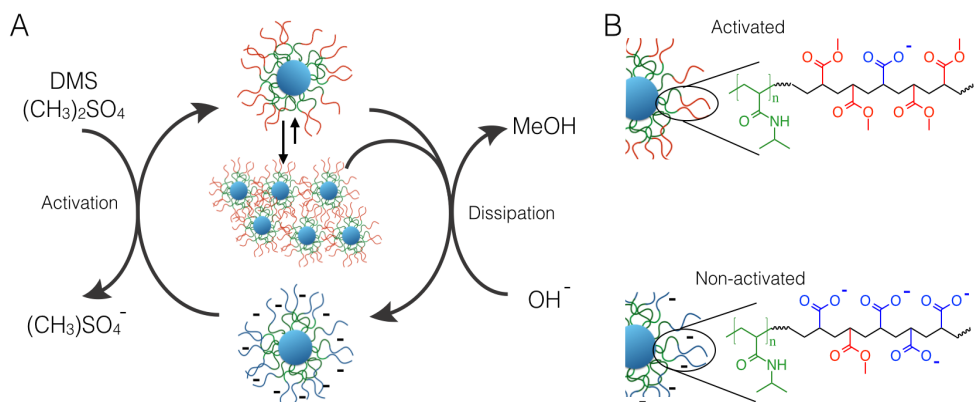


Figure 4.1. Out-of-equilibrium self-assembly of particles with polymer hairs, containing carboxylic acids. (A) In the reaction cycle, the dispersed colloids react with the chemical fuel, dimethylsulfate (DMS) to be activated and then self-assemble into aggregates. Over time the energy is dissipated, through the hydrolysis reaction and the particles disassembly. (B) In the non-active state the hairs contain more carboxylic acid groups, whereas in the activated state mainly the methyl esters are present.

4.2 Results & Discussion

Herein we present an out-of-equilibrium colloidal self-assembling system, driven by a chemical fuel with transient assemblies and recyclability of the building blocks (Fig. 4.1A). In previous work the activating reaction occurred through the methylation of a carboxylic acid by a sacrificial alkylating fuel, such as methyl iodide or dimethyl sulphate (DMS) (Chapter 3 (21)). To this end, we developed a colloidal particle with polymeric hairs (22) that contain carboxylic acids, which form stable colloidal dispersion under basic pH conditions due to steric stabilization and electrostatic repulsion (Fig. 4.1B). When reacting with the fuel, alkylation of the acids forms methyl esters and removes the electrostatic repulsion. The hydrophobic attraction between the methyl esters in the poly methyl methacrylate (PMMA) hairs then induces the aggregation of the particles. Under aqueous basic conditions, the formed esters are not stable and hydrolyze over time, reinstating the ionic charge. The addition of the chemical fuel pushes the balance between alkylation and hydrolysis towards alkylation and induces aggregation, but as the fuel is consumed the balance is reversed eventually leading to disassembly caused by the reinstated ionic charges.

The colloidal design contained two different aspects; Firstly, the presence of carboxylic groups for the fuel driven esterification which induces the aggregation. Secondly, the colloids should be stable at high ionic strengths due to the necessity of a buffer for keeping the pH at basic levels upon fuel addition. A neutral hydrophilic spacer between the colloid surface and the carboxylate terminal block provides steric stabilization for the colloidal stability (Fig. 4.1B). To this end we prepared particles

containing a polystyrene core, with hairs of poly(N-isopropylacrylamide) as hydrophilic spacer and polymeric methyl methacrylate mixed with methacrylic acids (pMMA/MA) as terminal block.

The particles were synthesized starting by a seeded emulsion polymerization to form polystyrene particles functionalized with atomic transfer radical polymerization surface initiators (SI-ATRP, Fig. 4.2A step I). Onto these particles hairs of hydrophilic poly(N-isopropylacrylamide) (pNIPAM) were grafted, that were then extended with poly methyl methacrylate (pMMA), through continued ATRP. As carboxylic acids are not compatible with ATRP, pMMA was selected and upon hydrolysis partly forms methacrylic acid (23, 24). Infrared (IR) spectroscopy confirmed that the synthesis of the described particles was successful, showing both the pNIPAM related signals at 3300 cm^{-1} , 1640 cm^{-1} , 1536 cm^{-1} and the pMMA signals at 1732 cm^{-1} . Also the hydrodynamic diameter of the particles increases from 350 nm for the polystyrene particles with ATRP surface initiator, to 670 nm for the polymer hair grafted particles. The polydispersity index (PDI) remains low after the complete grafting procedure, indicating that we obtained a stable dispersion of hairy colloids. Between particles with only pNIPAM hairs or pNIPAM-pMMA hairs no large difference is observed in the hydrodynamic diameter or in the PDI. This is in agreement with the low concentration of MMA used during synthesis and a high surface area, leading to smaller increase of size. To ensure that the acids groups are formed we analyze the zeta-potential of the particles and observe that at basic pH 11, a negative zeta potential of -15 mV is obtained. (Fig. 4.2C) At pH 3, a neutral zeta potential is observed, indicating that the methacrylic acid groups are protonated. DLS measurements also show that the hydrodynamic diameter increases from 680 nm at pH 11 to 980 nm at pH 3, which is in agreement with the optical micrographs (Fig. 4.2C, D). These results show that we have prepared colloids with carboxylic acid containing polymer brushes, and that protonation of the acid groups leads to aggregation.

DMS hydrolyses to form methyl sulphuric acid in aqueous solutions lowering the pH significantly (Fig. 4.1, also see Chapter 3). To keep the pH more stable borate buffered solutions are used. Upon dispersing the particles in the borate buffer, we find that the colloids form stable dispersions for multiple days at maximum concentrations of 75 mM borate buffer (based on boron). An injection of DMS in the buffer concentration with an initial pH 9, equaling 20 mM DMS in solution, leads to a final pH of 7 for a buffer concentration of 75 mM. Therefore, we use 10 mM DMS as a maximum fuel concentration, to minimize the pH drop and keep the pH above 7, preventing pH induced aggregation (Fig. 4.2C).

With this in hand we set out to explore the out-of-equilibrium self-assembly of our colloidal system, through the reaction with the chemical fuel dimethyl sulphate (DMS). The aggregation behavior is studied by addition of DMS, at concentrations between 0 and 10 mM, to buffer solutions of the carboxylic acid carrying particles. Based on reaction kinetic modeling in Chapter 3, we expect that most of the fuel has

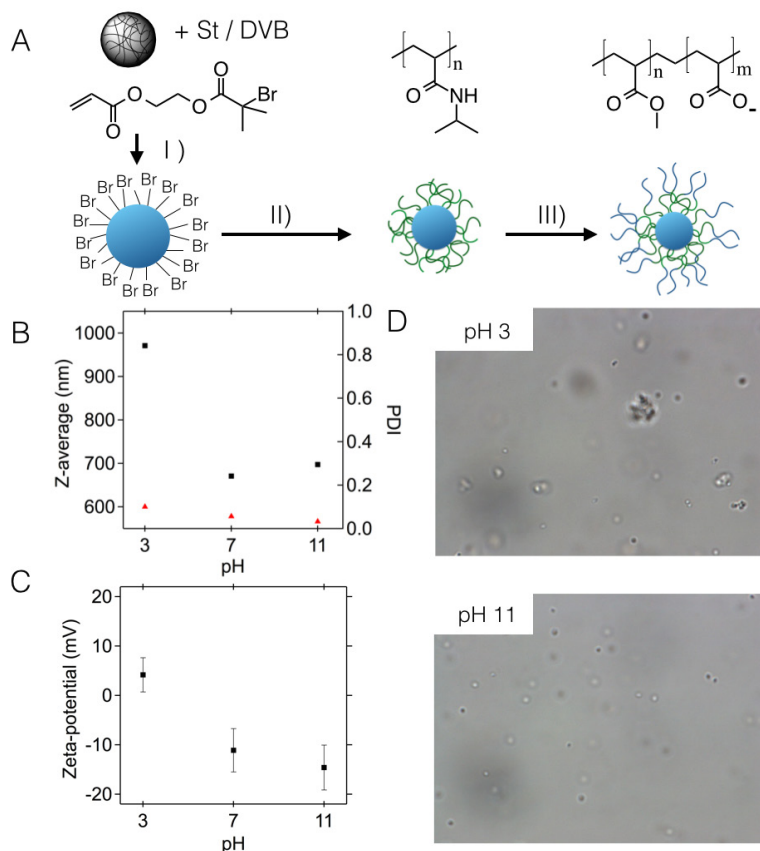


Figure 4.2. Synthesis of particles with polymer hairs and characterization.

(A) Particles synthesis, (I) colloidal ATRP initiators are formed by seeded emulsion polymerization with cross-linked polystyrene particles, styrene (ST), divinylbenzene (DVB), and 2-(2-bromoisobutyryloxy) ethyl acrylate (BIEA). On these ATRP initiators, (II) hydrophilic poly(*N*-isopropylacrylamide) (pNIPAM) brushes (green) are grafted followed by (III) a chain extensions reaction with methyl methacrylate (blue). (B) Hydrodynamic diameter (red square) and polydispersity indices (PDI, black squares) as determined by DLS of these particles in 75mM borate buffer, pH 3, 7, 11. (C) Zeta potential at pH 3, 7, 11 (D) Particles (pH 11) and aggregates (pH 3) as observed with optical microscope with a magnification of 60x.

reacted after 2 hrs, from which point on the hydrolysis is the main reaction occurring. Therefore, the samples are analyzed at 2 hrs and 24 hrs after the fuel addition by DLS and optical microscopy. We observe a significant increase in the hydrodynamic diameter and polydispersity index (PDI) after 2 hrs, indicating that aggregates are formed (Fig. 4.3A). These observations are consistent with microscopy images, in which we mainly observed aggregates (Fig. 4.3B). No fuel dependent trend is observed in the size of the formed aggregates, at two hours after fuel addition. These samples are stirred for an additional 24 hrs to let the hydrolysis and disassembly take place. After this period, the dispersions

are re-analyzed by both DLS and microscopy. In all cases the colloidal stability of the dispersion was regained. DLS showed that for both the hydrodynamic diameter and PDI similar values as before fuel addition are obtained. Also, in the micrographs only well dispersed colloidal particles are observed (Fig. 4.3B). These results show that a fuel induced aggregation occurs, and confirm that the aggregation process is reversed over time, in total forming an out-of-equilibrium self-assembly process.

As the colloidal aggregation process is based on random collisions, the low particle concentration limits the final aggregate size. To this end we measured the time dependent aggregation behavior at two different particle concentrations during the first 6 hrs and after 24 hrs by DLS. Upon addition of 10 mM DMS to dispersions of particles in buffer, we observe that over time aggregation occurs reaching a maximum at 2.5 hrs (Fig. 4.3C), at dilutions of 50 or 100 times (see experimental section) and under stirring conditions. At 50 times dilution a clear maximum of 950 nm is reached, after which it slowly decreases. At the lower particle density of 100 times dilution, we do observe a less pronounced increase in aggregate size, reaching a maximum of 850 nm. For both concentrations the dis-assembly process occurs over a period longer than 3 hours, eventually reaching stable dispersions after 24 hrs. This is consistent with the fast kinetics of alkylation and slower hydrolysis reaction as reported in Chapter 3. These results indicate that the aggregation process is dependent on the particle concentrations, and that the time scales are related to the alkylation and hydrolysis reaction.

We further observe that the maxima of obtained aggregate sizes are relatively lower compared to the previous obtained data (Fig. 4.3A, 4.3C). The difference between the experiments is the age of the particles in the two used stock solutions, as determined from the moment of synthesis. In the fuel dependent measurements, particle stock solutions were used within a week after synthesis, whereas for the concentration dependent measurements, we used stock solutions that were 3 months old. To check the reproducibility of fresh samples, we prepared new particles and measured the aggregate size upon addition of fuel and obtained sizes of ~1000nm for 100 times diluted samples. These results were similar to before, confirming that the age of the particles influences the fuel driven aggregation behavior. A possible explanation for this observation is the following; after synthesis, the polymer hairs partly consist of ester groups that further hydrolyze over time. In comparison to fresh particles, older particles will contain more acid groups, and thus upon addition of the same amount of fuel, not all acid groups will be converted to esters. This leads to a residual repulsion between particles, lowering the obtained aggregate sizes. This indicates that the maximum aggregate sizes are dependent on the amount of acid groups in the polymer hairs and residual charge after reaction with the alkylating fuel.

We investigated if the disassembly behavior was actually induced by the hydrolysis of the carboxylates on the polymer hairs, and not the cleavage of the polymer hairs. The *p*NIPAM polymer hairs are attached by an ester to the polystyrene core and could

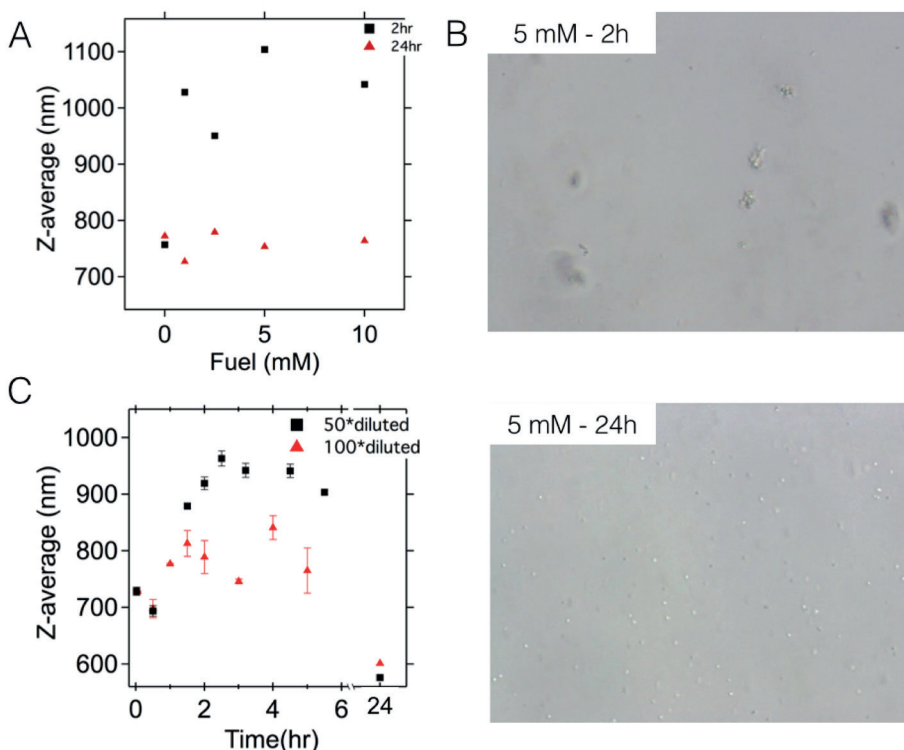


Figure 4.3. Transient self-assembly of particles

(A) Hydrodynamic diameters as measured 2 hrs and 24 hrs after addition of DMS, concentrations of 0-10 mM in 75 mM borate buffer, by Dynamic Light Scattering (DLS). Samples show aggregation at 2hrs and return to stable colloidal dispersions after 24hrs. (B) Optical microscopy images at 2 hrs and 24 hrs after fuel addition, 5mM DMS (optical microscope with a magnification of 60 x). (C) Hydrodynamic diameters as determined by DLS over time. Particles are diluted 50 and 100 times, see SI. DMS, 10mM, is added at $t = 0$, in 75mM borate buffer.

potentially hydrolyze under basic conditions. Therefore, we investigated the stability of the surface grafted polymer hairs by IR spectroscopy. We identified the normalized peak ratio between the amide stretch of the *p*NIPAM hairs, at 1644 cm^{-1} and polystyrene signal at 698 cm^{-1} of freshly prepared particles and after 14 days of stirring in borate buffer (75 mM, pH 9, Fig. 4.4B). This ratio was found to be almost identical showing that the polymer particle hairs are not cleaved from the surface over time. These observations show that the polymer hairs are stable under the used hydrolytic conditions during the experiments.

We do observe that there is difference in initial hydrodynamic size between freshly prepared particles and older batches. We also find that the older batches require higher concentrations of fuel to show aggregation, indicating that a larger number of carboxylic acid groups are present on the particles. These observations are in agreement with the

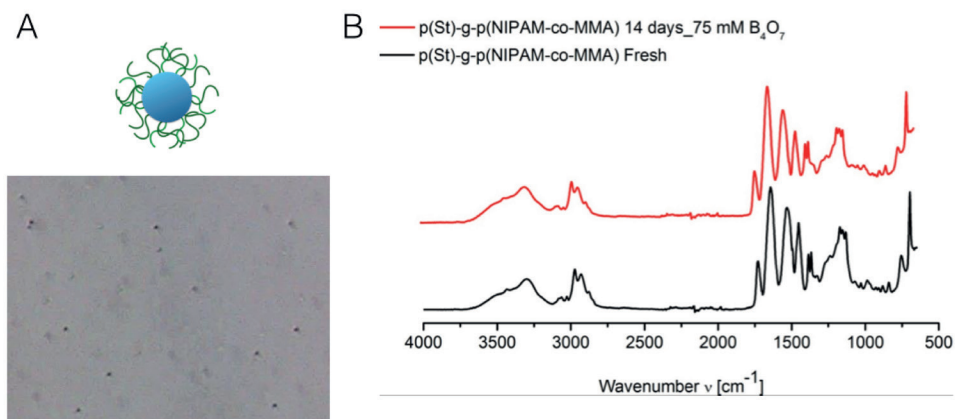


Figure 4.4. Necessity of acid groups and particle stability in borate buffer

(A) Optical microscopy image of pNIPAM grafted polystyrene particles in borate buffer pH 9, 75mM at 2 hrs after addition of 10mM DMS. No aggregates are observed (B) Infrared (IR) spectra of particles functionalized with pNIPAM and pMMA, fresh after synthesis (black) and after 14 days in borate buffer, 75mM, pH 9 (red).

concentration dependent aggregation behavior, as described above.

Another control was the use of samples with only pNIPAM brushes upon fuel addition, thus without the pMMA/MA terminal part. In these samples no significant increase of the hydrodynamic diameter was observed, 2 hrs after fuel addition (Fig. 4.4A). These observation underline that the out-of-equilibrium self-assembly of the polymer hair grafted particles, occurs through the alkylation and hydrolysis of the carboxylate moieties present on the hairs.

As an extension of the out-of-equilibrium self-assembly we attempted to recycle the used particles, by the injection of new fuel. We observed the transient aggregation upon addition of the first fuel by optical microscopy (Fig. 4.5). After 24 hrs the colloids are fully dispersed again. Upon addition of a second fuel shot, we again observe the aggregation followed by the disassembly after 24 hrs Adding a third fuel shot did lead to renewed aggregation but due to pH levels below 7, the pH driven aggregation could not be excluded (Fig. 4.2C). To overcome the problem of the strong pH change, which limits multiple reaction cycles, we recycled the particles by separation. In a new experiment we first perform a full reaction cycle of 24 hrs after which the particles are separated by centrifugation and re-dispersed in a fresh buffer solution. The re-dispersed colloids in fresh buffer have a size of 611 nm, similar to observed sizes before separation (Fig. 4.3C). Upon addition of 10 mM of DMS, after 2 hrs a size of 810 nm is measured. After 24 hrs the colloidal stability of the dispersion was regained and DLS showed similar hydrodynamic diameter values as before fuel, upon which a new (re)cycle could be started. As such, we are able to separate the 'waste', and recycle the colloids for a new fuelled induced aggregation cycle.

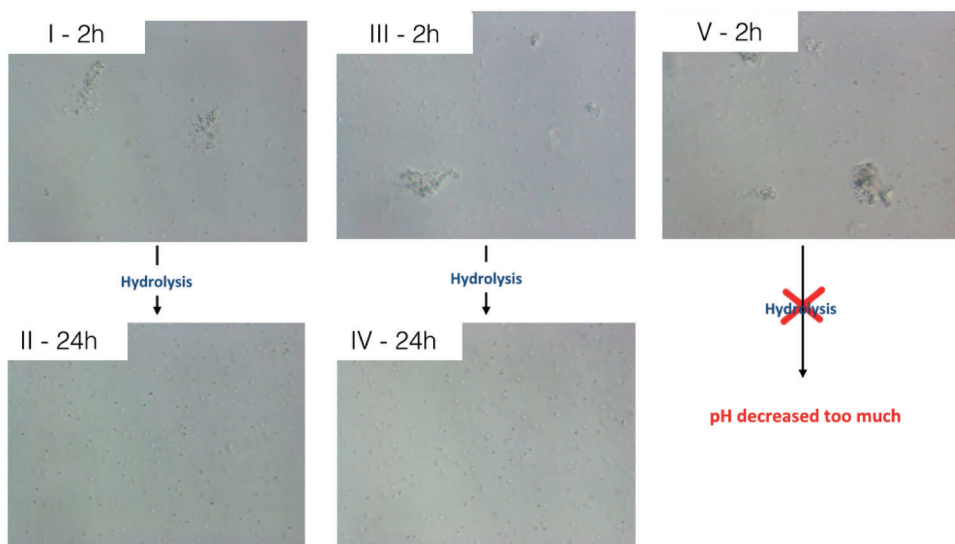


Figure 4.5. Repeated out-of-equilibrium particle aggregation, by multiple fuel addition. Optical microscopy images showing the particle aggregates at, (I) 2hrs(II) 24hrs after 1st fuel addition, (III) 2hrs and (IV) 24hrs after 2nd fuel addition and (V), 2hrs after 3rd fuel addition. Initial conditions: borate buffer 75 mM, pH 9, fuel addition equals 10mM DMS. After the 3rd step, the pH dropped below 7 at which the pH driven aggregation cannot be excluded.

4.3 Conclusions

We showed a colloidal system with out-of-equilibrium self-assembly fuelled by a chemical reaction. To this aim, we prepared polystyrene particles grafted with polymer brushes, consisting of the block-copolymer of *p*NIPAM and *p*MMA with partly containing carboxylic acids. Upon reaction with a chemical alkylating fuel, the carboxylates are methylated leading to aggregation of the particles. Over time the formed esters hydrolyze under the used hydrolytic conditions, restoring the negative charge on the outer parts of the polymer brushes, which induces dis-assembly of the aggregates. This process is transient in time, reaching a maximum aggregate size after 2.5 hrs and returning to stable solutions in 24 hrs. The particles can be reused, by direct addition of a new fuel injection or recycled by separation and re-dispersion in fresh buffer, to start a new fuel driven aggregation cycle. These results show that our previous proposed design rules can be extended from small molecule self-assembly towards other fields, such as colloidal self-assembly (Chapter 3). The development of the fuel driven colloidal self-assembly is an important step towards engineering out-of-equilibrium colloidal structures.

4.4 Experimental section

Acknowledgements

In this joined research project with dr. Bas van Ravensteijn en prof. dr. Willem Kegel, each made a significant contribution. I want to thank Bas for the synthesis of the polymer hair grafted particles, and a large part of the measurements. I also want to thank prof. Willem Kegel for help in setting up the research and checking the manuscript.

Materials.

Styrene (St, 99%), divinylbenzene (DVB, 55% mixture of isomers, tech. grade), methyl methacrylate (MMA, 99%), N-isopropylacrylamide (NIPAM, 97%), 2-bromoisobutryl bromide (BiBb, 98%), 2-hydroxyethyl acrylate (HEA, 96%, contains 200-650 ppm monomethyl ether hydroquinone as inhibitor), sodium sulfate (Na₂SO₄, ACS reagent, ≥ 99%, anhydrous), copper bromide (Cu(I)Br, 98%), N,N,N',N',N''-pentamethyldiethylenetriamine (PMDTA, 99%) and dimethyl sulfate (DMS, ≥ 99.8%) were obtained from Sigma Aldrich. Potassium persulfate (KPS, >99% for analysis), sodium bisulfite (NaHSO₃, ACS reagent) and pyridine (> 99%) were purchased from Acros Organics. Disodium tetraborate decahydrate (Na₂B₄O₇·10 H₂O, for analysis), sodium hydroxide (NaOH, ≥ 99%) and hydrochloric acid (HCl, 37% fuming, for analysis) were obtained from Merck. Methanol (MeOH, Exceeds ACS specifications) was obtained from J.T. Baker and dichloromethane (DCM, Peptide synthesis) from Biosolve. 2-(2-bromoisobutyryloxy) ethyl acrylate (BIEA) was prepared as described previously (22). The water used throughout all syntheses was purified using a Milli-Q water purification system.

Synthesis of 2-(2-bromoisobutyryloxy) ethyl acrylate (BIEA).

The synthesis of BIEA was adapted from reference 25 (25). A solution of 2-hydroxyethyl acrylate (40 mL, 348 mmol) and pyridine (31 mL, 383 mmol) in DCM (250 mL) was stirred and cooled in an ice bath. Under nitrogen atmosphere, a solution of 2-bromoisobutryl bromide (BiBb, 36.45 mL, 348 mmol) in DCM (50 mL) was added drop wise over the course of 1 h. During the addition a white precipitate was formed (HBr-pyridine). After complete addition of the BiBb solution, the reaction mixture was stirred an additional 3 h at room temperature.

The precipitate was filtered off and DCM was evaporated under reduced pressure. A yellow oil and additional precipitate was formed. The additional precipitate was filtered off and washed with DCM. The DCM from washing and the yellow oil were combined and washed with water (3 times, 50 mL per washing step). The oil phase was dried over Na₂SO₄ and finally, the DCM was evaporated under reduced pressure. The resulting yellow oil was distilled to complete the purification procedure yielding a colorless oil. ¹H-NMR: 400 MHz (CDCl₃) δ: 6.43 (d, 1H); 6.14 (dd, 1H); 5.85 (d, 1H); 4.4 (s, 4H); 1.9 (s, 6H).

Synthesis of brominated colloidal initiators (CPs-Br).

To prepare the brominated initiator colloids, a core-shell approach was chosen in which the cross-linked polystyrene colloids (CPs) particles served as seed particles for brominated core-shell particles. The two-step procedure can be summarized in the following way. In the first step, CPs were prepared using conventional emulsion polymerization. These particles were used in a seeded emulsion polymerization in which a shell of styrene, DVB and BIEA was grown around the core particles. The crude seed dispersion (25 mL) was introduced in a 100 mL round bottom flask, together with water (25 mL). The dispersion was heated to 70 °C and purged with nitrogen for 30 min. After degassing, a mixture of styrene (1 mL) and DVB (20 μL) was added. The mixture was stirred for 10 min after which BIEA (0.75 g) was injected. After 5 min of stirring, the polymerization was started by the addition of a degassed, aqueous KPS solution (32 mg in 5 mL water). The polymerization was allowed to run for 6 h after which the reaction was stopped by removing the flask from the oil bath. The particles were washed with water and ethanol three times. FT-IR (ATR) spectroscopy was used to confirm successful surface modification. Dynamic Light Scattering (DLS) showed a Z-average radius of 184 nm and a polydispersity index (PDI) of 0.028.

Atomic transfer radical polymerization (ATRP) on CPs-Br

NIPAM (0.88 mmol, 0.1 g) and Cu(I)Br (0.09 mmol, 13 mg) were weighed and transferred directly into an oven-dried Schlenk flask. A MeOH/H₂O mixture (7:3, v/v) (0.5 mL) was added and the solution was stirred for 5 minutes to let the NIPAM and the Cu(I)Br dissolve. A light green solution was obtained. After

complete dissolution, PMDETA (0.3 mmol, 63 μL) was added resulting in a blue / green mixture. The monomer / catalyst mixture was degassed by evacuation and refilling with nitrogen (3 cycles). In a separate Schlenk flask, the CPs-Br dispersed in a 7:3 (v/v) MeOH/ H_2O mixture (0.5 mL, 2 wt%) were degassed by evacuation and refilling with nitrogen (3 cycles). After degassing, the mixture was injected into the monomer / catalyst mixture under inert atmosphere. The resulting reaction mixture was white/green. After 2 hours, 0.1 mL of a degassed solution of MMA (0.1 mL) dissolved in the MeOH/ H_2O mixture (7:3, v/v) (1 mL) was injected under inert atmosphere. The ATRP reaction was allowed to run for 12 more hours at room temperature. After this period, the reaction was terminated by exposure of the mixture to air yielding an intense blue color. Particles were washed several times with MeOH, 50 mM aqueous NaHSO_3 solution and MilliQ water. The NaHSO_3 solution was used to facilitate the removal of the copper catalyst. Successful grafting was confirmed using IR spectroscopy and dynamic light scattering (DLS) measurements.

Dissipative aggregation of p(St)-g-p(NIPAM-co-MMA) colloids.

A dispersion containing p(St)-g-p(NIPAM-co-MMA) colloids (10 μL , solid content based on polystyrene core particles = 1 wt%) was diluted in disodium tetraborate decahydrate buffer (1.5 mL, 75–250 mM based on boron). The resulting dispersion was slightly sonicated. Finally, DMS was added. The concentration of fuel in the sample was varied between 0 and 10 mM. The samples were stirred for 2 h, after which the dispersion was probed for aggregation using optical microscopy and DLS. These analyses were repeated after 24 h to investigate the reversibility of the aggregation. The pH was monitored during the process to ensure a basic reaction environment. If colloidal stability was regained, a second dissipative cycle could be carried out by addition of fresh DMS. This process was repeated until the pH of the mixture dropped below 7.

Characterization.

Infrared (IR) spectra were obtained using a PerkinElmer FT-IR / FIR Frontier Spectrometer in attenuated total reflectance (ATR) mode. Measurements were carried out on powders obtained by drying the particle dispersion.

Dynamic light scattering (DLS) and zeta potential (ZP) measurements were performed using a Malvern Zetasizer Nano using highly diluted aqueous dispersions. Solutions are made in 50 times dilution, 40 μL of a 1 wt% dispersion in 2 mL water and 100 times dilution, 20 μL of a 1 wt% dispersion in 2 mL water. We estimated that these samples contained ~20 to ~10 nM of MMA for the 50 and 100 times diluted samples, respectively. DLS measurements were conducted using glass sample cells. The measurements consisted of 7 runs of 15 individual measurements in backscatter mode (173°) and were run at 20°C . An equilibration time of 5 minutes was applied to ensure that the dispersion was at the set temperature. The sizes of the colloids or aggregates are reported as a Z-average diameter and the corresponding polydispersity index (PDI). These values are obtained by using the cumulant method as described in reference (26). For the time series, the DLS measurements consisted of 2 runs of 15 individual measurements, to ensure short measurement time. The absolute values obtained for the Z-average diameter and the PDI for the aggregated dispersions are less reliable. Nevertheless, these values can still be used to verify if a colloidal dispersion is randomly aggregating, which results in higher Z-average diameters and PDI values.

For the ZP measurements, 7 runs of at least 50 individual measurements were used to obtain a statistically reliable potential. The electrophoretic mobilities and DLS measurements were carried out in aqueous solutions of pH 3, 7 and 11. Alternations of the pH were achieved by the addition of HCl or NaOH.

Optical microscopy images of the particles throughout this study were obtained using a Nikon Eclipse Ti-U inverted microscope equipped with an InfinityX scout camera. A $60\times$ magnification objective was used.

4.5 References

1. G. M. Whitesides, B. Grzybowski, Self-Assembly at All Scales. *Science* **295**, 2418-2421 (2002); DOI:10.1126/science.1070821.
2. B. Hess, A. Mikhailov, Self-organization in living cells. *Science* **264**, 223-224 (1994); DOI:10.1126/science.8146651.
3. S. Sacanna, M. Korpics, K. Rodriguez, L. Colón-Meléndez, S.-H. Kim, D. J. Pine, G.-R. Yi, Shaping colloids for self-assembly. *Nature Communications* **4**, 1688 (2013); DOI:10.1038/ncomms2694.
4. S. C. Glotzer, M. J. Solomon, Anisotropy of building blocks and their assembly into complex structures. *Nature Materials* **6**, 557-562 (2007); DOI:10.1038/nmat1949.
5. B. G. P. van Ravensteijn, W. K. Kegel, Colloids with Continuously Tunable Surface Charge. *Langmuir* **30**, 10590-10599 (2014); DOI:10.1021/la501993c.
6. R. Klajn, K. J. M. Bishop, B. A. Grzybowski, Light-controlled self-assembly of reversible and irreversible nanoparticle suprastructures. *Proceedings of the National Academy of Sciences* **104**, 10305-10309 (2007); DOI:10.1073/pnas.0611371104.
7. A. Snezhko, Non-equilibrium magnetic colloidal dispersions at liquid-air interfaces: dynamic patterns, magnetic order and self-assembled swimmers. *Journal of Physics: Condensed Matter* **23**, 153101 (2011); DOI:10.1088/0953-8984/23/15/153101.
8. D. A. Wilson, R. J. M. Nolte, J. C. M. van Hest, Autonomous movement of platinum-loaded stomatocytes. *Nature Chemistry* **4**, 268-274 (2012); DOI:10.1038/nchem.1281.
9. V. Sans, S. Glatzel, F. J. Douglas, D. A. Maclaren, A. Lapkin, L. Cronin, Non-equilibrium dynamic control of gold nanoparticle and hyper-branched nanogold assemblies. *Chemical Science* **5**, 1153-1157 (2014); DOI:10.1039/C3SC53223B.
10. W. F. Paxton, S. Sundararajan, T. E. Mallouk, A. Sen, Chemical Locomotion. *Angewandte Chemie International Edition* **45**, 5420-5429 (2006); DOI:10.1002/anie.200600060.
11. J. Palacci, S. Sacanna, A. P. Steinberg, D. J. Pine, P. M. Chaikin, Living Crystals of Light-Activated Colloidal Surfers. *Science* **339**, 936-940 (2013); DOI:10.1126/science.1230020.
12. H. Nakanishi, D. A. Walker, K. J. M. Bishop, P. J. Wesson, Y. Yan, S. Soh, S. Swaminathan, B. A. Grzybowski, Dynamic internal gradients control and direct electric currents within nanostructured materials. *Nature Nanotechnology* **6**, 740-746 (2011); DOI:10.1038/nnano.2011.165.
13. R. Klajn, P. J. Wesson, K. J. M. Bishop, B. A. Grzybowski, Writing Self-Erasing Images using Metastable Nanoparticle "Inks". *Angewandte Chemie International Edition* **48**, 7035-7039 (2009); DOI:10.1002/anie.200901119.
14. H. Hess, J. Clemmens, C. Brunner, R. Doot, S. Luna, K.-H. Ernst, V. Vogel, Molecular Self-Assembly of "Nanowires" and "Nanospools" Using Active Transport. *Nano Letters* **5**, 629-633 (2005); DOI:10.1021/nl0478427.
15. Y. Sumino, K. H. Nagai, Y. Shitaka, D. Tanaka, K. Yoshikawa, H. Chaté, K. Oiwa, Large-scale vortex lattice emerging from collectively moving microtubules. *Nature* **483**, 448-452 (2012); DOI:10.1038/nature10874.
16. D. Vavylonis, Q. Yang, B. O'Shaughnessy, Actin polymerization kinetics, cap structure, and fluctuations. *Proceedings of the National Academy of Sciences of the United States of America* **102**, 8543-8548 (2005); DOI:10.1073/pnas.0501435102.
17. J. Vicario, R. Eelkema, W. R. Browne, A. Meetsma, R. M. La Crois, B. L. Feringa, Catalytic molecular motors: fuelling autonomous movement by a surface bound synthetic manganese catalase. *Chemical Communications*, 3936-3938 (2005); DOI:10.1039/B505092H.
18. A. K. Dambeniek, P. H. Q. Vu, T. M. Fyles, Dissipative assembly of a membrane transport system. *Chemical Science* **5**, 3396-3403 (2014).
19. S. Debnath, S. Roy, R. V. Ulijn, Peptide Nanofibers with Dynamic Instability through Nonequilibrium Biocatalytic Assembly. *Journal of the American Chemical Society* **135**, 16789-16792 (2013); DOI:10.1021/ja4086353.
20. X. Miao, W. Cao, W. Zheng, J. Wang, X. Zhang, J. Gao, C. Yang, D. Kong, H. Xu, L. Wang, Z. Yang, Switchable Catalytic Activity: Selenium-Containing Peptides with Redox-Controllable Self-Assembly Properties. *Angewandte Chemie International Edition* **52**, 7781-7785 (2013); DOI:10.1002/anie.201303199.
21. J. Boekhoven, A. M. Brizard, K. N. K. Kowligi, G. J. M. Koper, R. Eelkema, J. H. van Esch, Dissipative Self-Assembly of a Molecular Gelator by Using a Chemical Fuel. *Angewandte Chemie International Edition* **49**, 4825-4828 (2010); DOI:10.1002/anie.201001511.
22. B. G. P. van Ravensteijn, Utrecht University, (2015).
23. L. S. Connell, J. R. Jones, J. V. M. Weaver, Transesterification of functional methacrylate monomers during alcoholic copper-catalyzed atom transfer radical polymerization: formation of compositional and architectural side products. *Polymer Chemistry* **3**, 2735-2738 (2012); DOI:10.1039/C2PY20280H.
24. C. Speyerer, K. Borchers, T. Hirth, G. E. M. Tovar, A. Weber, Surface etching of methacrylic microparticles via basic hydrolysis and introduction of functional groups for click chemistry. *Journal of Colloid and Interface Science* **397**, 185-191 (2013); DOI:10.1016/j.jcis.2013.02.003.
25. K. Matyjaszewski, S. G. Gaynor, A. Kulfan, M. Podwika, Preparation of hyperbranched polyacrylates by Atom Transfer Radical Polymerization. 1. Acrylic AB* monomers in "living" radical polymerizations. *Macromolecules* **30**, 5192-5194 (1997); DOI:10.1021/ma970359g.
26. J. C. Thomas, The determination of log normal particle size distributions by dynamic light scattering. *Journal of Colloid and Interface Science* **117**, 187-192 (1987); DOI:10.1016/0021-9797(87)90182-2.



Non-equilibrium molecular self-assembly

We discuss the theoretical frameworks for non-equilibrium self-assembly and illustrate these for the typical molecular self-assembly system. It is found that model predictions compare favourably to experimental results on an out-of-equilibrium gelating system. Extensions of the model to more interesting behaviour such as bi-stability due to non-linear and autocatalytic formation kinetics are discussed.



5

This chapter is published as: Koper G.J.M., Hendriksen W.E., Non-equilibrium molecular self-assembly, chapter 7 in Non-equilibrium Thermodynamics with Applications 2016.

5.1 Introduction

Structure formation in fluids is often too complex to allow for a full-fledged thermodynamic description. The classical approach to solution thermodynamics would be to capture such deviations from ideality in terms of activity coefficients or osmotic virial coefficients (1). These coefficients in principle can be rationalized by considering the molecular interactions between the solute as modulated by the solvent as is done by the McMillan-Mayer theory (2). Strong non-idealities leading to large values for these coefficients are usually the result of the more interesting chemical dissociation and association processes. For instance, activities in the case of ionic dissociation are almost completely described by what is known as the Van't Hoff factor and the degree of dissociation, and to a minor extent by the electrostatic interactions between the ions (3). Similarly, this is true for the association processes. This chapter will focus on the weak processes that give rise to aggregation while the molecules keep their identity and interact, for instance, through Van der Waals forces or hydrogen bonding. The strong processes such as polymerization involving covalent bonds are not considered here.

Weak association is occurring in almost all mixtures, even in the so-called simple solutions. In actual fact, weak association is often the precursor of phase separation which becomes more prominent, the closer the mixture approaches the limiting temperature or concentration (pressure is generally not a relevant variable). It usually gives rise to “soft” clusters of solute molecules as can be detected by light-scattering techniques (4) or crystals when a solid phase is near. The structure of the clusters highly depends on the nature of the solute molecules as well as on the solvent, and can either be ramified or compact with ill-defined aggregation numbers, or they can exhibit explicit structures such as spherical micelles or threadlike micelles, see Figure 5.1. Linear aggregates are the typical intermediates between a random structure with yet a clear organization. The formation of relatively well-defined clusters is what is presently called *molecular self-assembly*, the creation of soft matter in complex liquids (5).



Figure 5.1 Various aggregate structures, from left to right: ramified, compact, linear, spherical, micellar and wormlike micellar.

Even if self-assembly in itself is a kinetic process, and hence involves non-equilibrium processes, it is generally believed that there are striking differences depending on whether self-assembly occurs under equilibrium or non-equilibrium conditions. The spontaneously formed morphologies for equilibrium self-assembly show different dynamics and response than those for non-equilibrium self-assembly, sustained

through the continuous pumping of energy into the system. An example of the first kind can be found in the use of chemically designed systems to provide specific functionalities that allow for a rich variety of thermodynamic phases as a route to tune their self-assembly and material properties (6,7). An example of the second kind from Nature is the microtubule network, which is found in all eukaryotic cells that are involved in mitosis, cell motility, intracellular transport, and the maintenance of cell shape. This network is a non-covalent polymer network and assembles upon consumption of guanosine triphosphate (GTP), but depolymerises fast when the bound guanosine diphosphate (GDP) is lost. Inspired by processes in Nature, such as transient self-assembly, dynamic instability and reconfigurability, new systems have been developed (8-10). The self-assembling structures are generated through chemical reactions by supply of energy to these uphill conversions, determining the temporal properties of these structures. Alternatively driving fields, such as light, can be used to convert energy into molecular motion (11).

The emergence of new, so-called “dissipative structures”, can be understood theoretically and can be traced back to the pioneering work of Prigogine on dissipative self-sustained structures, see for instance the book by Nicolis and Prigogine (12). However, despite the work carried out relating these structures to dynamic systems, chaos theory and non-equilibrium phase transitions, a fundamental, general theoretical framework to understand non-equilibrium molecular self-assembly is still missing.

In equilibrium self-assembly, the structures and morphologies that can be obtained are constrained by the underlying thermodynamics of the system. Therefore, the possibility to design or tailor particular structures, relies essentially on the proper design of the system. One needs to modify the physical constituents to obtain desired morphologies. On the other hand, in non-equilibrium self-assembly, the external input might tune the properties of the emerging, self-assembled domains (13). As a result, this scenario in principle offers more flexibility to generate different kinds of structures. Moreover, these structures, sustained in steady state by the external supply of energy, can exhibit adaptive behaviour that offers the possibility to develop smart, highly responsive materials.

In general, the self-assembled systems out of equilibrium have stronger adaptability than their equilibrium counterparts, because they can change in response to modifications of the applied external fields that sustain them. Under certain conditions they can self-heal, such as when an external force drives the system to return to its initial state. The corresponding self-assembled structures react by returning to their previous configurations, resulting in self-healing. However, since the response is dynamic, different scenarios can be explored, providing further malleability to self-assembly. In some cases, the driving force could lead to two or more competing structures. Under those conditions, if variations with respect to a given driving force are small, the system will relax to the same type of structures, while under a large additional forcing it can lead

the system to accommodate to the second, allowed configuration. This will be discussed in Section 5.4. The energy consumption of these dissipative structures also provides a natural connection with the ability of living systems to self-replicate. However, the control of self-assembly to produce structures that self-replicate requires careful tuning and control of ambient conditions (14).

In this chapter we will discuss the fundamentals of molecular self-assembly in Section 5.2, and explain how this corresponds to out-of-equilibrium fuelled self-assembly in Section 5.3. The important effect of bistability and autocatalysis are discussed and related to the dynamic behaviour for natural out-of-equilibrium systems in Sections 5.4 and 5.5. Finally, the role of non-equilibrium thermodynamics is discussed in relation to self-assembly and future applications of the presented approach in Section 5.6.

5.2 General Principles

Equilibrium

From a formal point of view, molecular self-assembly can be regarded as an infinite chain of successive association equilibria as

$$\left\{ \begin{array}{l} S_1 + S_1 \rightleftharpoons S_2 \\ S_2 + S_1 \rightleftharpoons S_3 \\ \vdots \\ S_{n-1} + S_1 \rightleftharpoons S_n \\ S_n + S_1 \rightleftharpoons S_{n+1} \\ \vdots \end{array} \right. , \quad (5.1)$$

where S_n denotes an aggregate of n species. The set of equations implicitly contains the more general equilibria $S_n + S_m \rightleftharpoons S_{n+m}$ ($n, m = 1, 2, \dots$). When all these species are in chemical equilibrium their chemical potentials (per molecule) are identical and for sufficiently low mole fractions one may write

$$\mu_n = \mu_n^\oplus + \frac{k_B T}{n} \ln \frac{x_n}{n} = \mu_1 \quad (n = 1, 2, \dots), \quad (5.2)$$

in which k_B is Boltzmann's constant and T is temperature. The mole fractions x_n for molecules in aggregate S_n are constrained by the total amount of species x_t as

$$\sum_{n=1}^{\infty} x_n = x_t . \quad (5.3)$$

Once the standard chemical potentials μ_n^θ are specified, the set of eqns (5.1) - (5.3) can be solved, albeit most of the time only numerically. For instance, for linear aggregates with $n - 1$ bonds in a chain of n molecules, the standard chemical potentials are defined as

$$\mu_n^\oplus = \mu_1^\oplus + \left(1 - \frac{1}{n}\right)B \quad (n = 1, 2, \dots), \quad (5.4)$$

with B the bond Gibbs energy (15). For many common aggregates, such as sphere-like micelles, wormlike micelles and vesicles, approximate forms for the chemical potentials have been derived by Nagarajan and Ruckenstein (16,17).

Many types of aggregates, in particular the globular ones such as micelles, have a rather well defined aggregation number N , typical values are 50 – 100, so that for these structures the chain of equilibria in eqn (5.1) reduces to



see Figure 5.2a. The behaviour of this model is determined by two parameters only, the aggregation number, N , and the equilibrium constant*, K , that describe the equilibrium, eqn (5.5), between monomers and aggregates as

$$x_N = N \left(K x_1 \right)^N. \quad (5.6)$$

Together with mass conservation, this model can be numerically solved, see Figure 5.2b, for an example (15).

As long as the total mole fraction x_t remains below the critical aggregation concentration (cac), no aggregates are formed and the monomer mole fraction follows the total mole fraction. Beyond this cac, the monomer mole fraction remains virtually constant at the cac value and the remainder of the total mole fraction of monomers is aggregated. The cac is related to the chemical potential of the free monomers and of the monomers in aggregates by

$$x_c = K^{-N/(N-1)} \sim K^{-1} \text{ for } N \gg 1, \quad (5.7a)$$

where the equilibrium constant is given by

$$K = \exp \left\{ - \left(\mu_N^\oplus - \mu_1^\oplus \right) / (k_B T) \right\} \quad (5.7b)$$

* The conventional definition of association equilibrium, adopted here, deviates from the IUPAC convention. We follow literature convention (15) here to avoid confusion.

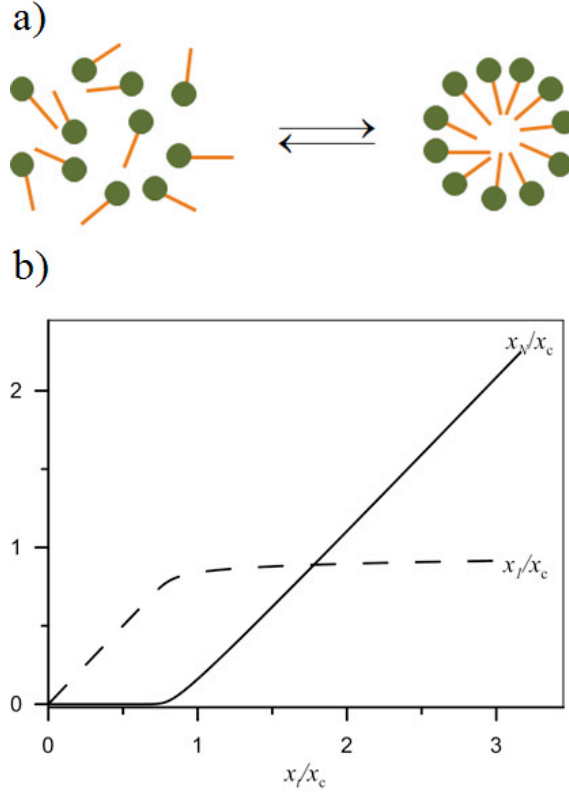


Figure 5.2 Schematic representation of self-assembly of monomers into aggregates (a) graphical example of monomer x_i , and aggregate mole fraction x_N as a function of total mole fraction x_i (b); x_c is the critical mole fraction of the self-assembly process, $N = 30$.

in terms of the standard chemical potentials introduced by eqn (5.2).

Gibbs energy of formation

In the hypothetical initial, non-self-assembled state, the chemical potential of the monomers (considered dilute) is given by

$$\mu_i = \mu_i^\circ + k_B T \ln x_i. \quad (5.8)$$

Hence, the molar Gibbs energy of formation (1) $\Delta_f G$ of the self-assembled state with respect to the non-self-assembled state is given by (The methodology to actually evaluate the Gibbs energies of formation is relatively unknown, see the discussion by Gerhartl (18) for an example)

$$\Delta_f G = x_i \mu_i + x_N \mu_N - x_i \mu_i - k_B T \ln \left\{ 1 - x_N \left(1 - \frac{1}{N} \right) \right\}. \quad (5.9)$$

Here the last term accounts for the change in the solvent entropy due to the change in mole fractions of monomers and aggregates; when considered at low monomer concentrations, it can be absorbed in the aggregate chemical potential. In Figure 5.3 the Gibbs energy of formation is plotted versus the conversion of monomers for a specific value of the total monomer mole fraction x_t . The conversion ξ is defined such that $x_1 = x_t(1-\xi)$ and $x_N = x_t\xi$ and as such gives the fraction of monomers that have been converted into aggregates.

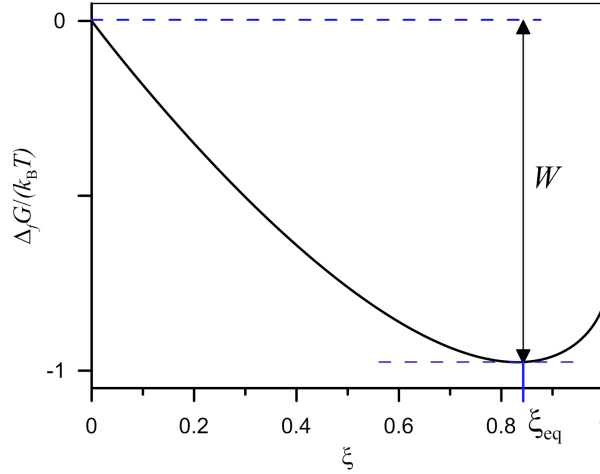


Figure 5.3 Graphical example of Gibbs energy of formation for the self-assembled state as a function of the conversion ξ . Indicated is the equilibrium conversion ξ_{eq} where the slope, the reaction Gibbs energy, vanishes. The formation Gibbs energy difference between the initial state and the equilibrium state is the maximum work W that is available by the self-assembly process.

Gibbs energy of reaction, the thermodynamic driving force

The Gibbs energy of reaction $\Delta_r G$ is the slope of the Gibbs energy of formation versus conversion, see Figure 5.3.

$$\Delta_r G = N(\mu_N - \mu_1) = k_B T \ln \left(\frac{x_N}{N(Kx_1)^N} \right). \quad (5.10)$$

It vanishes at the point ξ_{eq} where equilibrium is reached, see Figure 5.4. In addition, it provides for the driving force towards equilibrium when the system is away from it. We have expressed the Gibbs energy of reaction per aggregate rather than per monomer.

Conversion rate

The set of kinetic equations belonging to the chain of successive equilibria, given by eqn (5.1), forms a set of Becker-Döring equations (19) as have been formulated by Aniansson and Wall (20)

$$\left. \begin{array}{l} S_1 + S_1 \xrightleftharpoons[k'_2]{\tilde{k}_2} S_2 \\ S_2 + S_1 \xrightleftharpoons[k'_3]{\tilde{k}_3} S_3 \\ \vdots \\ S_{n-1} + S_1 \xrightleftharpoons[k'_n]{\tilde{k}_n} S_n \\ \vdots \end{array} \right\} \Rightarrow \left\{ \begin{array}{l} \frac{d}{dt} x_1 = -2\tilde{k}_2 x_1^2 + 2\tilde{k}'_2 x_2 \\ \quad + \sum_{m=3}^{\infty} (-\tilde{k}_m x_{m-1} x_1 + \tilde{k}'_m x_m) \\ \quad \vdots \\ \frac{d}{dt} x_n = \tilde{k}_n x_1 x_{n-1} - \tilde{k}'_n x_n \\ \quad - \tilde{k}_{n+1} x_n x_1 + \tilde{k}'_{n+1} x_{n+1} \\ \quad \vdots \end{array} \right. , \quad (5.11)$$

with for each aggregate size $n = 2, 3, \dots$ forward and backward rate coefficients \tilde{k}_n and \tilde{k}'_n respectively; t represents time. From experimental observations, as well as from an analysis of the equilibrium-size distribution (21) it is known that there is a significant amount of monomer still present and coexisting with a large amount of aggregated material. Typically, it is quite sharply peaked around the aggregation number N , as discussed above. There is little material in aggregated form with aggregation numbers between about 5 and N or much larger than N . Thus the range of aggregate sizes for which significant amounts of monomer are present divides naturally into two regions: firstly a region of small aggregates, dominated by the monomer form, but including a small number of dimers, trimers, and so on; and secondly a region centred on the most probable aggregate size, at which the size distribution has its maximum. These two regions are separated by a region of extremely low concentration of aggregates. The kinetics determining how such a system approaches equilibrium itself falls into two stages. Initially, the matter in each of these two regions self-equilibrates and then, over a much longer timescale, molecules are transferred from one region to the other, until the two regions eventually reach global equilibrium. This latter process has been modelled by a contraction of the full Becker-Döring scheme, eqn (5.11), into the simple rate equation (22) of monomers into aggregates that for the present situation reads

$$r \equiv r_1 - r_N = k_1 x_1^N - k_N \frac{x_N}{N}, \quad (5.12)$$

with forward and backward rate constants k_1 and k_N , respectively (rate constants differ from those in eqn (5.11) because of the contraction procedure.) By solving eqn (5.12) for stationarity, one easily verifies that the rate constants satisfy

$$\frac{k_1}{k_N} = K^N. \quad (5.13)$$

With the definitions of the chemical potentials in eqn (5.2), the conversion rate defined by eqn (5.12) can be written in terms of the driving force given by eqn (5.10) as

$$r = k_1 x_1^N \left[1 - \exp \left\{ -\frac{N(\mu_N - \mu_1)}{k_B T} \right\} \right] = k_1 x_1^N \left[1 - \exp \left\{ -\frac{\Delta_r G}{k_B T} \right\} \right]. \quad (5.14)$$

The final exponential form of reaction rate in terms of the driving force is what is found typically for chemical reactions and can be found in many text books (23,24). It has been derived from Mesoscopic Non-Equilibrium Thermodynamics (MNET)(25).

In Figure 5.4 the relationship of the formation rate as a function of the driving thermodynamic force is presented. It exhibits – as expected – a striking nonlinearity not unlike that of an electrical diode or electrode.

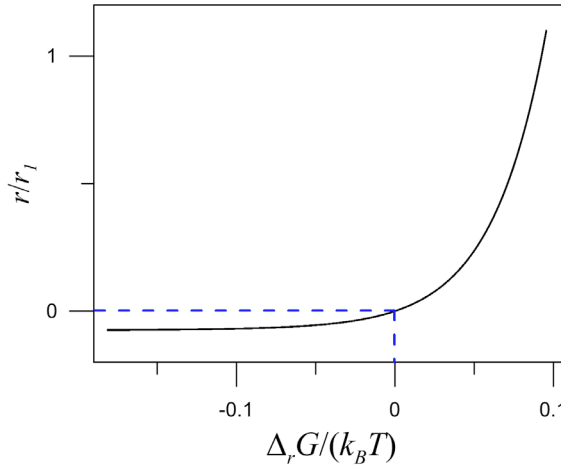


Figure 5.4 Graphical example of the relationship between formation rate and thermodynamic force for self-assembling systems.

Work: available and lost

The available work from the self-assembly reaction is given by the Gibbs energy of reaction, see also Figure 5.3. The rate at which the conversion takes place determines the rate at which this work can be delivered, so that

$$\dot{W} = -r \Delta_r G. \quad (5.15)$$

Under conditions where there is no coupling, this work is lost to the environment as there are no means to use it. It then is dissipated in the form of heat. With a coupled

electrochemical reaction, however, (some of) this work can be turned useful.

As mentioned above, see eqn (5.14), the theoretical framework provided by MNET, has been used to describe the dynamics of self-assembly (25) and to identify the relevant entropy production; it can be used, for example, to understand the energetics associated to the self-assembly process under generic non-equilibrium conditions. The change in entropy during the self-assembly process is closely linked to the reduction in phase space (26). Therefore, there is a clear connection between MNET and the complementary theoretical treatments that focus on quantifying the rate at which this configuration space decreases during self-assembly. The latter does not identify the relevant fluxes and forces controlling self-assembly, while the expression for the entropy production provided (25) by MNET can be used to quantify such shrinkage, hence connecting more clearly the intrinsic dissipative process with the theory of dynamical systems. Moreover, MNET does not only allow a proper understanding of self-assembly kinetics; its thermodynamic basis provides also a natural basis to describe consistently thermal fluctuations and correlations in such kinetic processes (27). It is also required to understand coupling with other processes such as an electrochemical process that uses the work produced by the self-assembly or thermal driving forces as we shall elaborate more on in Section 5.6.

5.3 Fuelled Self-Assembly

The simple self-assembly process described in the previous section has only one stationary state which is the equilibrium state. Its behaviour is fully described in terms of the “equilibrium constant” K that is related to the rate coefficients defined by eqn (5.13) and the aggregation number N . Driving such a system out of equilibrium by a constant supply of monomers might reveal more interesting dynamics. The aim is to reach a steady state other than the equilibrium state and, hence, monomers have to be taken out of the system as well.

In Figure 5.5 an out-of-equilibrium self-assembly experiment is sketched, where at a given constant feed rate, r_i , monomers are formed from pre-monomers, i.e. parts that form a monomer upon association. Subsequently, there are two decay channels from monomers back to pre-monomers: directly, with rate r_{L1} , and indirectly through the self-assembly step with rate r_{LN} . The direct rate depends on the population of the monomer state x_1 and is given by

$$r_{L1} = k'x_1, \quad (5.16)$$

whereas the indirect rate depends on the population of the self-assembled state x_N as

$$r_{LN} = kx_N \quad (5.17)$$

with rate constants k and k' .

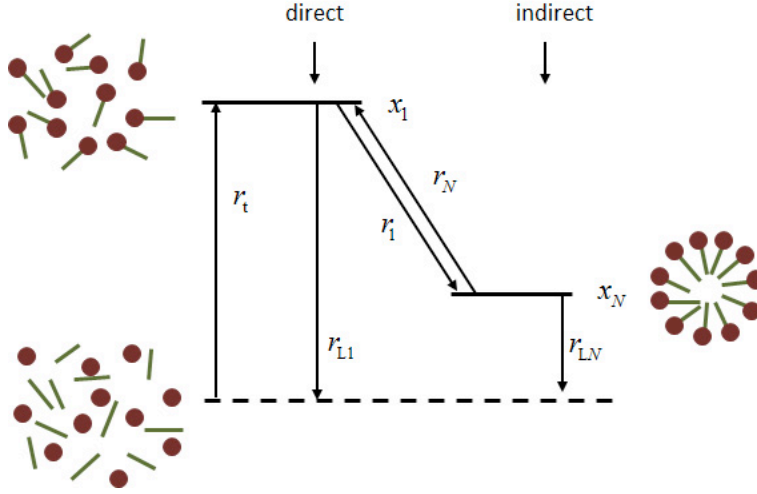


Figure 5.5 Schematic representation of a dual channel out-of-equilibrium self-assembly process. See the text for further details.

The indirect channel is coupled to the self-assembly process for which the rate is given by eqn (5.12). The continuous formation of new monomers drives the self-assembly out of equilibrium. The monomer formation reaction and the subsequent destruction may be assumed to be controlled by external reactions, hence the name fuelled self-assembly. At low feed rates, the monomer mole fraction x_1 remains low, below the cac, and, hence, there is no population of the self-assembled state. Therefore, the decay rate is solely via the direct channel as visualized in Figure 5.6. For larger feed rates, the self-assembled state is fully occupied and only a minority of the monomers – with mole fraction close to the cac – is still in the free monomer state. As a consequence, the larger part of the decay is through the indirect channel and the fraction that follows the direct channel is negligible, see Figure 5.6. The actual cross-over takes place around the critical aggregation concentration and is slightly modified by the relative rate factor

$$K_r = r_{L1}^{(c)} \left(\frac{1}{r_{LN}^{(c)}} + \frac{1}{r_1^{(c)}} \right) \quad (5.18)$$

where $r_{L1}^{(c)}$ is the direct rate, see eqn (5.16), $r_{LN}^{(c)}$ the indirect rate, eqn (5.17), and $r_1^{(c)}$ the forward aggregation rate, all at the cac as indicated by the superscript (c).

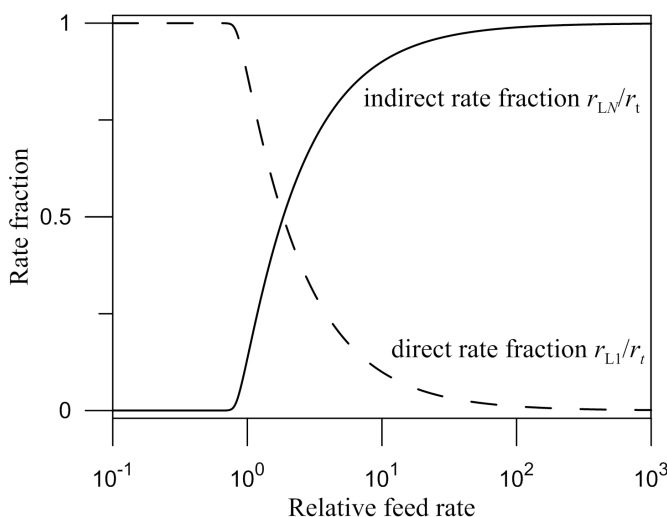


Figure 5.6 Direct and indirect rate fractions in the dual channel dissipative self-assembly process as a function of the relative feed rate $r_t / (k_1 x_c^N)$.

The result as sketched in Figure 5.6, albeit reminiscent of the equilibrium behaviour illustrated by Figures 5.3 and 5.4, is only achieved when the system is out of equilibrium. The true equilibrium state of the model is where there are only pre-monomers and no monomers or aggregates at all. This state is attained at vanishing feed rates. With finite feed rates, a non-equilibrium stationary state sets in of which the characteristics are described above. Importantly, the chemical potentials have values that differ significantly from those in equilibrium. In actual fact, work is delivered at a rate exactly given by eqn (5.15) with a non-vanishing Gibbs energy of reaction; it will vanish in equilibrium only.

In Chapter 3, we have shown the out-of-equilibrium formation of active materials (8,28), that exhibits a behaviour that is very reminiscent of what is described above, see Figure 5.7. In this system, the pre-monomer is a low molecular weight gelator N,N'-dibenzoyl-(L)-cystine (DBC) containing two carboxylate groups per molecule that reacts with alkylating fuels to form a neutral ester. The monomer is formed by removing the charge of the carboxylate, by forming the ester, and hence allows for the molecular self-assembly process and eventually gelation. The leakage reaction from monomer back to pre-monomer takes place when the ester undergoes spontaneous hydrolysis in aqueous environments leading to the formation of a charged carboxylate and an alcohol waste product. The hydrolysis of the ester group is dependent on the pH, and occurs faster at more basic conditions. During a reaction cycle, the pre-monomer reacts with the commercially available strong methylating agent dimethylsulfate (DMS, $(\text{CH}_3)_2\text{SO}_4$) under basic conditions. The batch-wise addition of DMS to buffered solutions the pre-

monomer results in its transient methylation, yielding increasing monomer levels.

The monomers self-assemble into fibres with a monodisperse 8 nm diameter and multiple micrometres in length. Typically, 20 minutes after addition of the fuel, the monomer concentration will reach the Critical Gelation Concentration (CGC), where the formation of fibres leads to macroscopic, semi-transparent gel materials. Over time, the monomers hydrolyse back to pre-monomers, leading to the breakdown of fibres and the dissolution of these gels. The viscoelastic behaviour of the gel as measured during the reaction cycle, see Chapter 3, reveals dynamics that is reminiscent of what is displayed in Figure 5.6. Importantly, in the experiment the decay rate from the self-assembled state to the pre-monomer state is much less than what results from the model described above. This is largely due to the fact, that in linear aggregates the terminating monomers are less tightly bound to the aggregates than those in between.

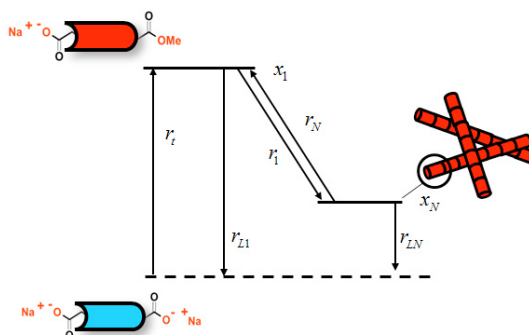


Figure 5.7 Chemically fuelled transient self-assembly. In a reaction cycle, pre-monomers DBC react with methylating agent DMS to give monomers that subsequently self-assemble into fibrous aggregates. The formed monomers can hydrolyse both in the assembled and free state to revert to the original pre-monomer. Overall, one full cycle produces methanol and monomethylsulfate as waste products.

5.4 Bistability

Micellar systems that catalyse their own formation have attracted considerable scientific interest (22,29-32). In particular, the example reported by Bachmann, Luisi, and Lang in 1992 (29) attracted quite some attention largely because of their hypothesis of “autopoietic self-replication” of micelles and their discussion with respect to the basic chemical mechanisms at the origin of Life (29). It was claimed that the biphasic alkaline hydrolysis of an ester shows highly nonlinear kinetics that could be attributed to the effect of micellar autocatalysis. In this reaction, ethyl caprylate (EC), which is practically immiscible with water, undergoes alkaline hydrolysis when placed in contact with an underlying aqueous solution. The reaction yields amphiphilic sodium caprylate, which is known to form anionic micelles in aqueous media. Many attempts have been made

to model this reaction until in 1997 Buhse et al. revealed that the behaviour was not so much due to autocatalysis, but rather arose from a transport phenomenon of EC-swollen micelles to the aqueous phase which sped up the hydrolysis reaction significantly (32).

Nevertheless, there are many reports in the literature where bistable behaviour is claimed for associating molecular systems, see for instance the short overview in the paper by Ball and Haymet (30). A relatively clear-cut experiment was reported by these authors (30) in which the charge-transfer interactions of drug molecules were studied. The conductivity of an aqueous iodine solution was measured while a solution of the amphiphilic drug amiodarone was added. In the reverse experiment, the conductivity of the amiodarone solution was followed as iodine solution was added. The conductivity curves provide clear evidence of bistability: the forward and reverse curves do not coincide. Similar results were obtained for the alkaline hydrolysis of C-4 to C-8 ethyl alkanoates (33). Another, relatively recent, example involves the Krafft temperature, i.e. the temperature at which a micellar solution of given concentration forms micelles (34). Such a transition can be followed by conductivity measurements, and also here the forward and reverse scans to find the temperature do not provide overlapping curves. In these experiments, significant time intervals of 30 minutes or more were built in to equilibrate the system. Unfortunately, no dependence on equilibration time was reported for these systems. Such information would aid in assessing the non-equilibrium character of these solutions.

A kinetic bistability can be demonstrated in a Continuously Stirred Tank Reservoir (CSTR), as shown by Buhse *et al.* for the above discussed biphasic surfactant system(31) and further discussed by Ball and Haymet (30). We shall here give a more intuitive presentation based on graphical analysis. Let us first review the CSTR, an idealized vessel where it is assumed that the contents are ideally mixed at all times. A solution of monomers is fed at a given volumetric rate Q and in order to maintain a constant volume V of liquid in the vessel, the content is discarded at the same rate. The important characteristic of a CSTR is its residence time of which the inverse is the refreshment rate

$$k_0 = \frac{Q}{V}. \quad (5.19)$$

Stationary states are reached after waiting out a few times the residence time. For the bistability experiment, let us assume a CSTR that initially is solely filled with solvent and that its feed consists of a solution of monomer mole fraction x_0 . As long as the reactor content has not reached the cac, the actual monomer mole fraction x_1 in the reactor increases with time t according to

$$\frac{dx_1}{dt} = k_0(x_0 - x_1) \quad \text{for } x_0 \ll x_c, \quad (5.20)$$

where the first term accounts for the feed and the second term for the discharge. Once the

monomer concentration is sufficient, the self-assembly reaction proceeds. Typically, there is a slow and non-catalysed process that runs whether aggregates are already present or not; for simplicity its rate is modelled as being first order, k_1x . A second, faster process does involve autocatalysis and, hence, must involve aggregates. The backward reaction, where aggregates disassemble into monomers is neglected here under the assumption that its time scale is too large compared to the residence time. A simple model rate would be $k_3x(x_0 - x)^2$ which involves the presence of two aggregates and one additional monomer. Other forms of rate are equally permissible, though. The overall reaction rate equation now takes the form

$$\frac{dx_1}{dt} = k_0(x_0 - x_1) - k_1x_1 - k_3x_1(x_0 - x_1)^2 \quad \text{for } k_0t \gg 1. \quad (5.21)$$

Graphically, the rate can be represented as in Figure 5.8a, where the feed rate is represented by the straight line and the chemical reaction is represented by the other line with a clear maximum and a small but nonzero rate when the monomer mole fraction in the reactor equals that of the feed. Crossings of these two lines indicate stationary states, i.e., it is where the overall reaction rate vanishes. The outer two crossings are stable stationary states and the middle one is not stable as one may easily verify by considering the mole fraction dependence of the rate. The bistability is best visualized in Figure 5.8b, where the stationary-state mole fraction of the reactor is given as a function of the feed rate. There are two branches: one at low feed rates, where the monomer mole fraction is low and aggregation takes place, and one at high rates, where there is no significant aggregation. The region in-between exhibits hysteresis as is typical for bistability.

5.5 Autocatalysis

The bistability example with the CSTR discussed above, Section 5.4, clearly illustrates that multistability, i.e., the occurrence of more than one stable stationary state, can be achieved with self-assembling molecular systems provided that the formation reaction is autocatalytic. The situation was different for the fuelled self-assembly, Section 5.3, which involved a regular aggregate formation reaction and did not exhibit multistability. Despite the obvious non-linearity of the aggregate formation rate there is only one stationary state. It is clear, however, that when the aggregate formation rate equation for this example would be autocatalytic this system would also show multistability. As discussed above, bistability has been found in self-assembling reactions, but so far these have not been related to autocatalysis. The bistability in the ethyl caprylate example discussed above was due to a phase transfer step and for the other two examples, which involved hysteresis in concentration and temperature respectively, no molecular mechanism was provided.

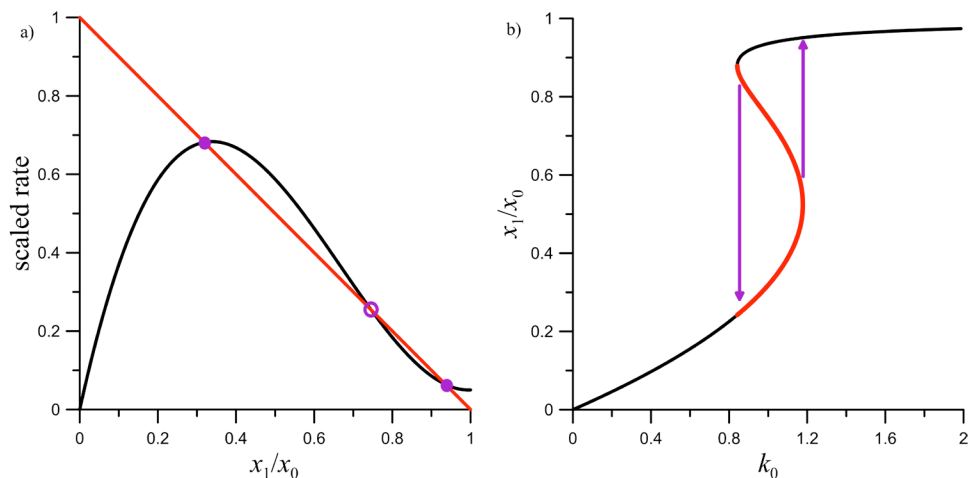


Figure 5.8 Graphical example of bistability in a continuously stirred tank reactor. *a)* Analysis of rate equation in linear part (red) and nonlinear part (black) where the closed circles indicate stable stationary points and the open circle an unstable one; rates scaled by $k_0 x_0$. *b)* Relative stationary monomer mole fraction as a function of feed rate. Hysteresis between two stable modes is indicated by arrows. Parameters chosen are $k_1 = 0.05 \text{ s}^{-1}$ and $k_3 = 4.5 \text{ s}^{-1}$; see eqn (5.21).

The question then arises whether molecular self-assembly itself can be autocatalytic. So far, the starting point for a theoretical analysis has been the set of Becker-Döring (BD) equations (19) which assumes the formation of aggregates to pass through a sequence of step-wise monomer additions or removals. The model has recently acquired some renewed interest for the archetypal molecular self-assembly system of micellar solutions (21). The result of a detailed analysis is that – given the presence of one stationary state identified as the equilibrium state – the kinetics as described by the BD-equations is not capable of properly describing the kinetics of experimental systems. Already long before the seminal work of Aniansson and Wall on the same model (20), it was known that the dynamics of micelle formation involves two characteristic time scales: a short time scale associated with the exchange of free monomers and monomers in aggregates and a long time scale associated with the break-up and formation of a whole aggregate. The problem that has been identified recently is, that the model predictions for the ratio of the long and the short time scale appears to be too large (21). In a subsequent analysis, the same authors discuss an extension of the model where the condition of step-wise monomer addition is relaxed. In particular, the break-up of aggregates in two halves as well as the formation of super-aggregates consisting of twice the average amount of monomers is allowed. It is the formation of super-aggregates that brings the separation of the short and long-time scale within experimentally accessible range (35). The authors conclude by the statement “Implicit in our model is that the formation of micelles in a supersaturated solution proceeds by accretion of monomers to a proper micelle to form a super-micelle followed by fission of the super-micelle to two proper micelles; the

formation of micelles is catalysed by micelles.”

Fusion and fission have been experimentally observed in micellar systems, for instance, involving the non-ionic surfactant Triton X-100 (36,37). It is deployed in systems where various reactants for a chemical reaction are transported by swollen micelles to react upon fusion. Also theoretically, fusion and fission have been assessed (35,38) and, apart from accelerating the formation kinetics, no information is available on autocatalytic effects. A simple effective rate equation as obtained by contraction of the Becker-Döring equations, such as eqn (5.12), is hence not known for such a case. The suggestion for a catalytic rate equation as made by writing eqn (5.21) for the demonstration of kinetic bistability was in actual fact inspired by the idea that two aggregates and monomers would coalesce into one super-aggregate that upon further growth would split into three proper aggregates. A similar approach can be found in the modelling of the dynamic instability for microtubules (39). For these systems, more is known about the actually occurring phenomena (40,41) in relation to their dynamic behaviour, albeit that many more factors contribute that are difficult to control. More experimental work is required to uncover the actual mechanisms responsible for autocatalytic behaviour in natural and synthetic systems.

5.6 Role of Non-equilibrium Thermodynamics for Self-Assembly

The Second Law of Thermodynamics provides a general framework for the assessment of the efficiency of a process. For the examples discussed here, it would state that the entropy produced during the process in a stationary state can be related to the difference in entropies of the input stream and the output stream. For the example of the fuelled self-assembly in Section 5.3, an earlier analysis has led to the conclusion that the dissipation is largely due to the reactions driving the self-assembly out of equilibrium (25). A similar conclusion is expected for the case where the reaction is carried out in a CSTR, see Section 5.4, as friction-loss values are typically orders of magnitude less than those connected to chemical energy changes.

The formalism of non-equilibrium thermodynamics allows for the identification of the various contributions to the entropy production. The examples here feature a set of coupled reactions (25) and the more general expression for the available and – in the absence of utilization – lost work reads

$$\dot{W} = - \sum_k r_k \Delta_r G_k, \quad (5.22)$$

where the sum includes all reactions. For the fuelled self-assembly, the summation would include a reaction driving the self-assembly, the self-assembly process itself and the leakage reaction. The reactions in general will be coupled and it is important to realize

that for any conjugate set of reaction rates and Gibbs energies of reactions, the expression (5.22) will hold (24). As for chemical reactions, the relation between self-assembly rate and the Gibbs energy of reaction can be non-linear, see eqn (5.14). As shown explicitly for chemical reactions, this does not impose any limitation to the validity of the non-equilibrium thermodynamics formalism (42). In particular, we showed the validity of eqn (5.14)(25). The work needed to maintain the non-equilibrium structure is drawn from the coupling of reactions, on the cost of some of the energy supply.

The coupling between fluxes and forces that contribute to entropy production becomes even more interesting when heat and mass transfer as well as electrochemical reactions are involved. As surmised before, the work lost in the self-assembly process could actually be put to some use in an electrochemical device. As an example, the hydrolysis occurring in the fuelled self-assembly process is readily performed electrochemically. This would open the route to store and retrieve energy from self-assembling systems. The associated coupling of reactions will be non-linear in character and as such only very few examples are worked out and none in detail (42-44).

5.7 Conclusion

In this chapter we have discussed the principles of molecular self-assembly processes and some systematic approaches to run these processes out of equilibrium. It was found that with regular aggregate-formation kinetics, a single stationary state is obtained that is reminiscent of the equilibrium steady state albeit that entropy is produced. Multiple stationary states are possible when aggregate formation is partially autocatalytic. So far, very few, if any, experimental model systems have been reported that exhibit this kind of behaviour although it is to be expected that some well-known systems showing fusion and fission of aggregates might demonstrate multistability.

The quantification of the lost work in terms of a non-linear relation between reaction rate and thermodynamic driving forces is one of the main contributions of this chapter regarding the non-equilibrium thermodynamic analysis. Further possibilities for thermodynamic analysis have been discussed for more complete systems involving self-assembly.

5.8 References

1. J. M. Smith, H. C. Van Ness and M. M. Abbott, *Introduction to Chemical Engineering Thermodynamics*, McGraw-Hill, New York, 2001.
2. T. L. Hill, *An Introduction to Statistical Thermodynamics*, Dover Publications, New York, 1960.
3. E. J. King, *Acid-base equilibria*, Macmillan, London, 1965.
4. M. Soos, M. Lattuada and J. Sefcik, *J. Phys. Chem. B*, 2009, **113**, 14962.
5. B. W. Ninham and P. L. Nostro, *Molecular Forces and Self Assembly*. In *Colloid, Nano Sciences and Biology*, Cambridge University Press, Cambridge, 2010.
6. T. Aida, E. W. Meijer and S. I. Stupp, *Science*, 2012, **335**, 813.
7. P. W. K. Rothmund, *Nature*, 2006, **440**, 297.
8. J. Boekhoven, A. M. Brizard, K. N. K. Kowligi, G. J. M. Koper, R. Eelkema and J. H. van Esch, *Angew. Chem. Int. Ed.*, 2010, **49**, 4825.
9. S. Debnath, S. Roy and R. V. Ulijn, *J. Am. Chem. Soc.*, 2013, **135**, 16789.
10. X. M. Miao, W. Cao, W. T. Zheng, J. Y. Wang, X. L. Zhang, J. Gao, C. B. Yang, D. L. Kong, H. P. Xu, L. Wang and Z. M. Yang, *Angew. Chem. Int. Ed.*, 2013, **52**, 7781.
11. R. Eelkema, M. M. Pollard, J. Vicario, N. Katsonis, B. S. Ramon, C. W. M. Bastiaansen, D. J. Broer and B. L. Feringa, *Nature*, 2006, **440**, 163.
12. G. Nicolis and I. Prigogine, *Self-Organization in Nonequilibrium Systems: From Dissipative Structures to Order Through Fluctuations.*, Wiley, New York, 1977.
13. M. Fialkowski, K. J. M. Bishop, R. Klajn, S. K. Smoukov, C. J. Campbell and B. A. Grzybowski, *J. Phys. Chem. B*, 2006, **110**, 2482.
14. P. L. Luisi and F. J. Varela, *Orig. Life. Evol. Biosph.*, 1989, **19**, 633.
15. J. N. Israelachvili, *Intermolecular and Surface Forces*, Elsevier, Amsterdam, 2011.
16. R. Nagarajan and E. Ruckenstein, *Langmuir*, 1991, **7**, 2934.
17. R. Nagarajan, *One Hundred Years of Micelles: Evolution of the Theory of Micellization*. In: *Surfactant Science and Technology: Retrospects and Prospects*, ed. L. Romsted, Taylor and Francis, New York, 2014.
18. F. J. Gerhartl, *J. Chem. Ed.*, 1994, **71**, 539.
19. R. Becker and W. Döring, *Ann. Phys.*, 1935, **24**, 719.
20. E. A. G. Aniansson, S. N. Wall, M. Almgren, H. Hoffmann, I. Kielmann, W. Ulbricht, R. Zana, J. Lang and C. Tondre, *J. Phys. Chem.*, 1976, **80**, 905.
21. I. M. Griffiths, C. D. Bain, C. J. W. Breward, D. M. Colegate, P. D. Howell and S. L. Waters, *J. Coll. Interf. Sci.*, 2011, **360**, 662.
22. P. V. Coveney and J. A. D. Wattis, *Proc. Roy. Soc. Lond. Ser. Math. Phys. Eng. Sci.*, 1996, **452**, 2079.
23. S. R. de Groot and P. Mazur, *Nonequilibrium Thermodynamics*, Dover publications, New York, 1984.
24. D. Kondepudi and I. Prigogine, *Modern Thermodynamics. From Heat Engines to Dissipative Structures*, Wiley, New York, 1998.
25. G. J. M. Koper, J. Boekhoven, W. E. Hendriksen, J. H. van Esch, R. Eelkema, I. Pagonabarraga, J. M. Rubí and D. Bedeaux, *Int. J. Thermophys.*, 2013, **34**, 1229.
26. R. Zwanzig, *Nonequilibrium Statistical Mechanics*, Oxford University Press, USA, 2001.
27. I. Pagonabarraga, A. Perez Madrid and J. M. Rubí, *Physica A.*, 1997, **237**, 205.
28. J. Boekhoven, *Multicomponent and Dissipative Self-Assembly Approaches*, Thesis, Delft University of Technology, Delft, the Netherlands, 2012.
29. P. A. Bachmann, P. L. Luisi and J. Lang, *Nature*, 1992, **357**, 57.
30. R. Ball and A. D. J. Haymet, *Phys. Chem. Chem. Phys.*, 2001, **3**, 4753.
31. T. Buhse, V. Pimienta, D. Lavabre and J. C. Micheau, *J. Phys. Chem. A*, 1997, **101**, 5215.
32. T. Buhse, R. Nagarajan, D. Lavabre and J. C. Micheau, *J. Phys. Chem. A*, 1997, **101**, 3910.
33. C. Roque, V. Pimienta, D. Lavabre and J. C. Micheau, *J. Phys. Chem. A*, 2001, **105**, 5877.
34. J. Z. Manojlovic, *Therm. Sci.*, 2012, **16**, S631.
35. I. M. Griffiths, C. J. W. Breward, D. M. Colegate, P. J. Dellar, P. D. Howell and C. D. Bain, *Soft Matter*, 2013, **9**, 853.
36. Y. Rharbi, M. A. Winnik and K. G. Hahn, *Langmuir*, 1999, **15**, 4697.
37. Y. Rharbi, M. Li, M. A. Winnik and K. G. Hahn, *J. Am. Chem. Soc.*, 2000, **122**, 6242.
38. A. K. Shchekin, M. S. Kshevetskiy and O. S. Pelevina, *Coll. J.*, 2011, **73**, 406.
39. R. Padinhateeri, A. B. Kolomeisky and D. Lacoste, *Biophys. J.*, 2012, **102**, 1274.
40. A. Desai and T. J. Mitchison, *Annu. Rev. Cell Devel. Biol.*, 1997, **13**, 83.
41. P. Maddox, A. Straight, P. Coughlin, T. J. Mitchison and E. D. Salmon, *J. Cell Biol.*, 2003, **162**, 377.
42. J. M. Rubí, D. Bedeaux, S. Kjelstrup and I. Pagonabarraga, *Int. J. Thermophys.*, 2013, **34**, 1214.
43. T. L. Hill, *Free energy transduction and biochemical cycle kinetics*, Springer-Verlag, New York, 1989.
44. H. Qian and D. A. Beard, *Bioph. Chem.*, 2005, **114**, 213.



Spatial and chemical controlled self-assembled material by reaction-diffusion

Reaction-diffusion (RD) offers great possibilities for the creation of nano- and microscale patterns, and the spatially resolved formation of functional materials. So far, this concept has mostly been applied to inorganic and biological materials, with a notable absence of organic reactions. Still, the use of organic chemistry in RD offers both an extremely wide range of possible chemical reactions and functionality, as well as the precise control over chemical kinetics across multiple time scales. Here we describe the combined reaction-diffusion and self-assembly (RD-SA) of a supramolecular gelator leading to the formation of organic material structures with controllable shape, size, and chemical functionalization. In this system, multiple components diffuse towards one another, to react at the crossing of the diffusional fronts and form hydrogelator molecules, eventually leading to a supramolecular structure through self-assembly. We show that the patterned structures can be chemically differentiated and used to form permanent chemical gradients. Furthermore, we are able to functionalize structures with molecular recognition sites for binding to proteins. Using typical RD parameters such as diffusion length and reaction kinetics, we are able to adjust the dimensions of the RD-SA structures via the reaction conditions. To our knowledge, this work is a first example of an RD based approach to the formation of organic materials. The versatility of organic chemistry combined with self-assembly greatly broadens the scope of materials made using reaction-diffusion

This chapter is in preparation for publication

6.1 Introduction

Reaction-diffusion and self-assembly processes are widespread throughout nature, controlling the formation of a range of structures, from actin filaments, to skin patterns (1-4). In Reaction-Diffusion (RD), two reactants diffuse and react, forming gradients and giving rise to localized structure formation of the reaction products in case of precipitation, polymerization or self-assembly (5). Depending on the initial localization of the reactants and typical RD parameters such as diffusion length and reaction kinetics, intricate product patterns can be formed (5). For instance printing or stamping techniques can be used to localize reactants. As such, materials produced through RD contain spatially heterogeneous distribution of matter and chemical gradients, which are unachievable through standard bulk production methods of materials (5, 6). Principles of RD also offer insights into the emergence of complex biological materials and functions, for example cell signaling, and ordering in bacterial colonies (3, 5, 7-9, *also see chapter 2*). Since the first precipitation patterns reported by Liesegang, RD has enjoyed significant attention (10), for example for the identification of antigens (11, 12) and in periodic precipitation systems (13-15). In recent years, especially the use of inorganic RD systems has expanded into a wide range of scientific and technological areas, such as biomineralization, and the formation of microlenses (5, 14). Researchers have used various methods for producing RD materials such as polymer film precipitations, stamping techniques, and chemical gradients (5, 14-19). That the use of gradients, which is inherent to RD, allows for accurate control over precipitation reactions is clear from a recent example in which remarkably complex architectures are obtained (17). The reported inorganic RD patterns and structures reach high levels of complexity and resolution, but remain limited to the diffusion and precipitation of salts. As such, they lack in chemical diversity and typically do not allow control over reaction kinetics or chemical functionalization. A few recent examples of RD using biological reactants have shown that chemical gradients can be programmed using DNA-based autocatalytic reaction networks (18, 20-23). Notably, the use of organic reactions is entirely absent in reported RD systems. Organic chemistry offers both an extremely wide range of possible chemical reactions and functionality, as well as the possibility to precisely control chemical kinetics across multiple time scales. In this chapter we describe the formation of localized organic RD materials through diffusion, reaction and self-assembly of small molecules, allowing control over the shape and size of the formed structures, as well as their chemical differentiation and functionalization.

6.2 Results & Discussion

In our approach we combine reaction-diffusion and self-assembly (RD-SA) to control the spatial distribution of supramolecular materials. RD-SA requires a multicomponent

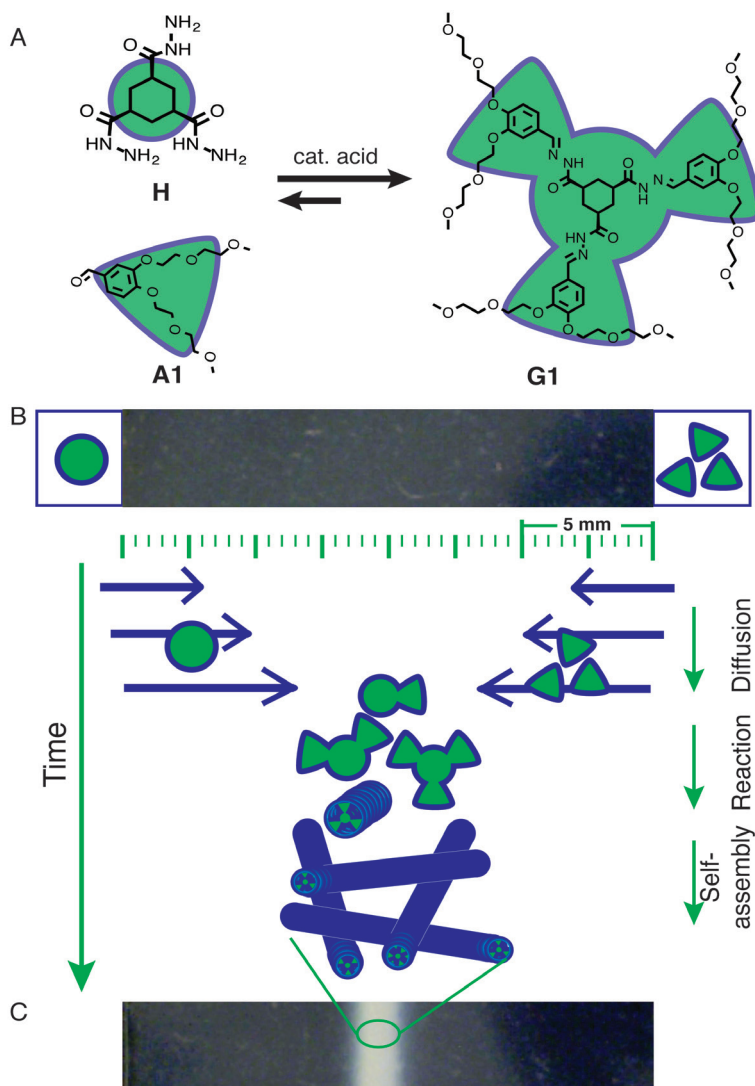


Figure 6.1: Reaction-diffusion of a two component self-assembling gelator. (A) **H** and **A1** react to form gelator **G1** under ambient conditions in water, with acid acting as a catalyst. (B) A schematic illustration of a space-time plot of the RD-SA process. Reactants **H** (circle, left) and **A1** (triangle, right) are placed on opposite sides of the agar gel matrix. Over time **H** and **A1** diffuse through the matrix, and react upon crossing to form gelator **G1**, which self-assembles into a fibrous gel network. This process results in the formation of a turbid white line consisting of gel fibers, within the diffusion matrix (C).

reaction inducing a self-assembly process, to allow independent diffusion of reactants and self-assembly of products at the crossing of the diffusional fronts. We recently reported a supramolecular hydrogelator that is formed in the gelation medium by a multicomponent chemical reaction. There, the acid catalyzed reaction of hydrazide **H** and aldehyde **A1** leads to the formation of the trishydrazone gelator **G1** (Fig. 6.1a)(23).

When **G1** reaches concentrations above its critical gelation concentration (CGC), it self-assembles into fibers and in-situ forms a non-transparent supramolecular network. The rate of formation of the supramolecular network can be controlled through the acid catalyzed hydrazone reaction, which depends on the concentration of reactants and the presence of a catalyst (23, 24). In our RD-SA approach, reactants **H** and **A1** diffuse over a distance and react upon crossing of the moving fronts, forming the product **G1** that self-assembles into a supramolecular material (Fig. 6.1b). In a typical RD-SA experiment, **H** and **A1** are placed at distance of 2 cm on the opposite sides of an agar gel matrix (acting as a diffusion medium), and left to diffuse over time (Fig. 6.1c). At the crossing of the diffusional fronts, the two components react in a multi-step reaction to form gelator **G1**. We observe that **G1** forms a non-transparent supramolecular structure within the agar matrix and appears as a turbid line at the intercept of the two diffusion fronts (Fig. 6.1c, 21). Structure formation is observed after ~10 hrs. It is also observed that the supramolecular structure vertically extends from the bottom of the Petri dish to the top of the agar matrix. The formed structures typically achieve a width of 2.5 mm within 24 hrs, with total experiment times reaching 78 hrs (Fig. 6.2a), and the formed structures are stable for months.

With this in hand, we set out to explore the potential of RD-SA to control shape, chemical differentiation and functionalization of the formed structures. At first, we looked at the influence of the initial localization of reactants, diffusion dimensions, and the use of different reactants on the formed shapes. By positioning the reactants in pre-designed locations, we anticipated to obtain a variety of 2D shapes (Fig. 6.2). For this purpose, we start with a basic method for placing the components relative to each other. This consists of cutting reservoirs out of an agar matrix and placing solutions with the components in the opposite reservoirs (Fig. 6.2a-b). After placing the components and agar matrix, the components diffuse through the agar matrix (Fig. 6.2a-f, also see experimental section). Where the diffusional fronts of **H** and **A1** meet, we observe the local formation of the supramolecular structure. To create a greater flexibility and robustness in producing of the shaped structures, we apply a method in which a mold with embossed reservoirs is used. These reservoirs are filled with the components in agar and after gelation, an additional agar matrix is placed on top of the mold. With this method we are able to form various continuous shapes such as circles, triangles and waves (Fig. 6.2 B, D, E). When the mold consists of a matrix of reservoirs, the formed structures consist of several connected segments generated by reactions of the diffusional patterns from the initial sources (Fig. 6.2f). In these shapes the center of the diffusional fronts can be distinguished from the edges as the connections between two adjacent gel lines are less dense than their centers (Fig. 6.2 c, f, g). Next, we tested if the components could also be printed as point sources on an unshaped agar matrix, from which they diffuse through the agar. Indeed, we observe that by printing reactant reservoirs on top of the matrix leads to the formation of supramolecular structures in the agar gel after diffusion and reaction

(Fig. 6.2g). The reservoirs are printed in the negative of the desired image, and as such we call this the ‘negative’ printing method. By precise positioning of reactant reservoirs with different methods, we are able to generate a range of shapes, including squares and grids, triangles, and even letters.

An advantage of our approach is that it easily allows changing of reactants, and we compared different aldehydes regarding their effect on the formation of supramolecular structures and their morphology. From previous work we know that the gelation properties of the supramolecular hydrazone gelator depend on the molecular design of the aldehyde used in the system (25). Replacing aldehyde **A1** with a slightly different benzaldehyde (**A4**) resulted in a change in the line width of the formed structure, most likely on account of a different CGC for the formed trishydrazone. Aldehyde **A2** (3,4-dihydroxybenzaldehyde) resulted in a more drastic change in the obtained material after RD-SA, as, apart from wider lines, the formed RD-SA structures show a more crystalline morphology, as observed visually (Fig. 6.2c). We are thus able to control the shape of supramolecular structures by reactant positioning, and adjust the morphology through choice of reactants.

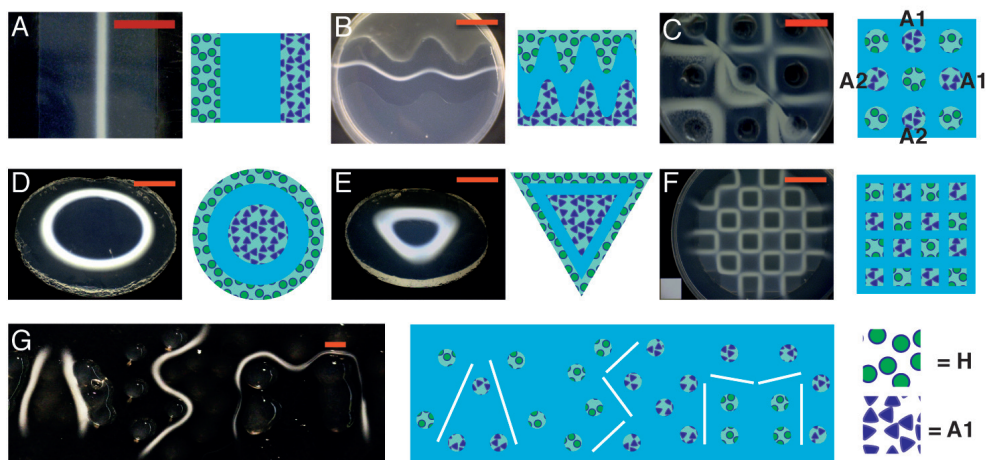


Figure 6.2: Diversity of the formed structures by RD-SA. In A-G, the structure (left) results from RD-SA run from a starting point configuration as shown in the cartoon on the right. The blue areas denote the agar matrix, circles and triangles represent **H** and **A1**, respectively. (A) An RD-SA supramolecular gel line formed by RD of **H**, from the left, and **A1**, from the right, in a pH 4 agar diffusion matrix. (B) By shaping the agar matrix, the RD-SA formed lines are obtained in different shapes such as waves. (C) An RD-SA grid made from aldehydes **A1** and **A2** to compare the difference in self-assembly behavior, (lower left **A2**, upper right **A1**). (D-F) To show the versatility of the RD formed gel structures, different designs are created by a mold approach to obtain a circle and a triangle. (F) A grid formed by RD-SA, by letting components diffuse from multiple sources from a mold below the agar matrix (SI). (G) Using the RD-SA approach to ‘negative print’ our research group name. Droplets of reactants in agar solutions are placed on top of a solidified agar layer, to diffuse and form supramolecular structures at the intersection of the diffusion gradients. Scale bars: a: 1cm; b–g: 2cm.

To further extend the scope of the system we aimed for chemical differentiation and functionalization of the formed supramolecular structures. We previously showed that fluorescent aldehyde probes can be mixed in with **A1** to label gel fibers (24, 25), allowing visualization by fluorescence microscopy. We used this methodology to chemically label RD-SA formed structures, by mixing fluorescent aldehyde in the solution of **A1**, preceding diffusion and reaction. The formed structures were shown to consist of a finely distributed network of supramolecular fibers, as visualized by confocal fluorescence microscopy. These observations confirm that the fluorescent dyes were incorporated into the supramolecular fibers and not just co-diffused with **A1**. Furthermore, these results confirm that the materials formed through RD-SA retain a fibrous nature similar to that observed in bulk (23). The formed fiber networks also have a visually observable color depending on the added probe, while forming white supramolecular structures in the absence of probe (Fig. 6.3a). To create chemically differentiated structures by RD-SA, reactants **H** and **A1** are placed alternately in an array of point sources, while each source of **A1** is mixed with a different color fluorescent aldehyde. By the RD-SA process, we then generate a grid of differently colored fiber network squares with each color belonging to a different fluorescent label indicative of chemical differentiation. Thus, we can observe chemical differentiation within the obtained structures, both optically and by fluorescence microscopy (Fig. 6.3a-b).

Next, we used a semi 1D RD-SA approach to form a diffusion oriented gradient in an attempt to show the formation of chemical gradients within the formed network structures. Spatial gradients of chemical cues lead to responses of many cell types (26). We mixed **H** in agar at a concentration of 40 mM and pH 4, and made an **H**-loaded agar matrix of 1 cm wide. **A1** was mixed with an aldehyde-fluorescent probe in buffer and allowed to diffuse in from one side of the agar matrix. During two weeks we observed formation of material within the agar matrix, and analysis by confocal fluorescence microscopy showed the formation of a permanent density gradient within the formed fiber network (Fig. 6.3c). The clusters of fibers formed close to the source of **A1** show a high fiber density, whereas the density is lower when moving further towards the other end of the matrix (Fig. 6.3c). This gradient in fiber network density is quantified by measuring the fluorescence intensity over the full distance (Fig. 6.3d). Surprisingly, the gradient is not completely gradual, but shows the formation of a band as the normalized fluorescence has a local minimum at ~1 mm distance from the source of **A1**, after which it gradually decreases towards the end. This phenomenon is observed in both local fiber density as well as in the summed fluorescence intensity, and may have an origin similar to the Liesegang patterns observed in precipitation systems (5, 10).

To further capitalize on the potential of chemical differentiation of organic materials made by RD-SA, we attempted to functionalize these structures with molecular recognition sites for proteins. Here, the modular nature of the self-assembling system employed in this work plays a pivotal role (25). We used the extensively described non-

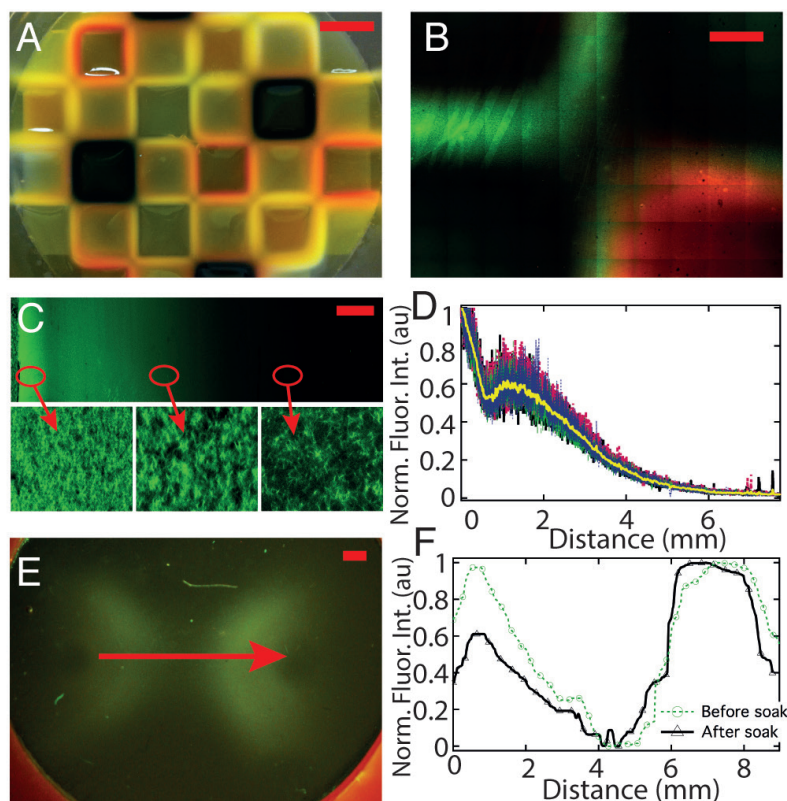


Figure 6.3. Chemical differentiation, gradient formation and functionalization of RD-SA structures. (a) A large grid made with several aldehyde-functionalized dyes, (yellow, orange and purple), added for chemical differentiation within a single structure (40mM **H**, 160mM **A1**, 1 mol% fluorescent aldehyde labels, 1 mass% agar with 100mM phosphate buffer, pH 4, SI). (b) Chemically differentiated gel cross, with two aldehyde-functionalized dyes (fluorescein, rhodamine) incorporated into the gel fibers, as imaged by confocal fluorescence microscopy. Image is a grid of 10x8 individual micrographs, leading to visible edges. (c) A permanent chemical gradient formed by letting **A1** diffuse from the left into a agar gel containing **H**, imaged by fluorescence imaging (Conditions: 40 mM **H** in 1%w/v agar, pH 4, and 240 mM **A1** in 100 mM phosphate buffer pH4, SI). (d) Fluorescence intensity measured from left to right in c, the yellow line is the average of multiple measurements. (e) Fluorescence image of ConA bound to a gel pattern made by RD-SA with mannose aldehyde incorporated in the right structure. Image is taken after removing unbound ConA by soaking. (f) Fluorescence intensity measured in e, along the red arrow. The green dashed data is before soaking, black is after soaking. Scale bars, a: 1cm; b, c, e: 1mm.

covalent binding of the lectin Concanavalin A (ConA) to mannose as a protein-ligand interaction (27, 28). As a start, we added mannose labeled aldehyde (**AM**) to a solution of **A1** (**A1** 160 mM, **AM** 1.6 mM, see experimental section 6.4). We printed **A1** and **A1+AM** reservoirs, and allowed diffusion and reaction with **H** using an RD-SA protocol similar

to the one in Fig. 6.3b . This resulted in the formation of mm-scale supramolecular shapes within the agar matrix. Because of the aldehyde printing pattern, of the two formed fiber shapes, only one was labeled with mannose. Next, fluorescein-labeled ConA was allowed to diffuse into the matrix, to bind to the mannose groups on the fibers. The entire matrix was subsequently soaked in buffer solutions for several days to remove unbound or unspecifically bound protein. Confocal microscopy shows that, after soaking, the amount of ConA relatively decreases more on the fiber structures without mannose functionalized groups, when compared to those that do contain mannose functionalized groups (Fig. 6.3e-f). The relative stability of ConA on the mannose-functionalized supramolecular structures shows the potential of chemical differentiation to position biological functionalities in space.

Controlling dimensions through reaction diffusion parameters

Having established the capability to pattern chemically differentiated and functionalized structures, we continued to investigate our approach for controlling the dimensions of the formed shapes. RD systems typically work under reaction or diffusion limited conditions, which is expressed by the Damköhler (Da) number, equation 1 (3, 5). Diffusion limited conditions ($Da > 1$) signify that the time for reaction is shorter than the time for diffusion, and the pattern dimensions are defined by diffusion. Oppositely, under reaction limited conditions ($Da < 1$) the reaction kinetics determine the pattern dimensions. For RD-SA, self-assembly is an additional process step to take into account, as structure formation will take place upon reaching the CGC.

$$Da = \frac{t_{diffusion}}{t_{reaction}} \quad (1)$$

$$Da = \frac{k_r C_1 L^2}{D_1} \quad (2)$$

To investigate the effect of reaction and diffusion parameters on the structure dimensions, we explored the parameter space of the Da number. We first adjusted reaction parameters such as pH and concentrations, and analyzed the formation and widths of the resulting RD-SA structures over time. The hydrazone forming reaction of **H** with **A1** is acid catalyzed and reaction kinetics is dependent on the pH in the agar matrix. This allows for adjusting the reaction rate constant (k_r) over 3 orders of magnitude between pH 3 and 7. It is observed that the width of the resulting line-shaped structures increases with increasing pH, ranging from 1.8 mm at pH 3.3 to 10 mm at pH 7 (Fig. 6.4a). Simultaneously, the formation time (t_{50}) of these lines also increases from 450 to 1000 minutes. When changing the concentrations of **H** and **A1** (at constant **H:A1** ratio) we observe that a minimal initial concentration of 10 mM of **H** is necessary for the formation of fiber structures. By adjusting the reaction parameters, pH and concentration, we are able to control the feature size of the RD-SA structures.

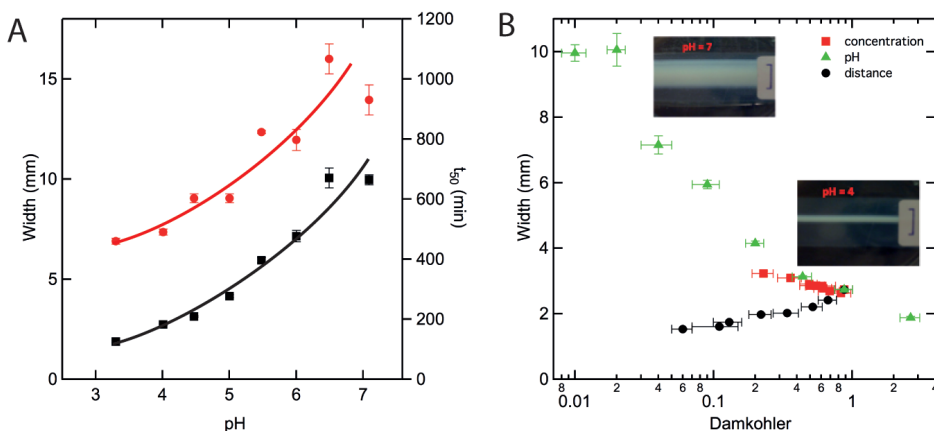


Figure 6.4. Dimension control of the RD-SA formed supramolecular structures (a) The graph gives the dependence of the line width (left, black markers) and t_{50} (right, red markers) on the pH used during the forming of the RD-SA structures. Lines are added to guide the eye. (b) The dependence of the observed line width on Da at the different RD conditions. The RD parameters for the individual experiments are used to calculate the Da , which is then plotted versus the obtained line width.

Next, we estimated Da for the various reaction parameters to indicate if the RD-SA process is reaction or diffusion limited, and compared the effect on the obtained line widths (Fig. 6.4c). At pH 7, the reaction is very slow and we estimate the Da number at 0.01 (SI). Under these conditions RD-SA leads to relatively wide lines (10 mm, Fig. 6.4b). At this low Da number the process is mainly reaction limited and the gelator products cross-diffuse until self-assembly occurs. The reactions are faster at lower pH or high concentrations of reactants, which results in higher Da numbers. Under these conditions, the formed RD-SA structures show a reduced width (Fig. 6.4b), with the smallest width of 1.8 mm occurring at a diffusion limited Da of 2.6 (+/-0.4) (conditions pH 3, 40 mM **H**, 160 mM **A1**, $L = 18$ mm, SI). Most of the performed experiments have estimated Da 's between 0.01 and 1, signifying that they are formed under reaction limited conditions. Under such conditions, the line widths are strongly dependent on the reaction kinetics, which is confirmed when comparing the different experiments for the pH and concentration series. There, we observe that the line width shows a similar dependence on the Da (Fig. 6.4b). For example, when comparing an experiment in the concentration series (pH 4, 15mM of **H**) with an experiment in the pH series (pH 4.5, 40 mM of **H**), both have a similar Da of 0.4 (+/-0.04) and result in lines of a similar width of 3.1 (+/-0.05) mm. These observations suggest that the Da number can be used to predict, to some extent, the feature size of the RD-SA structures.

To test to which extent the Da number can be used for predicting the feature sizes, we adjusted Da by changing the diffusion length (L). By decreasing L and keeping pH

and concentration constant, we vary Da between 0.05 and 1 (pH 4, 40 mM of **H**). Based on the results for the kinetic parameters we anticipate that a smaller Da gives larger widths. A typical experiment ($L = 9.5$ mm, pH 4, 40mM of **H**) with a Da of 0.9 results in a structure width of 2.7 mm (Fig. 6.4c, black circles). Lowering Da to 0.06 by changing L to 2.4 mm, results in obtained structure widths of 1.5 mm. We thus observed that decreasing Da by decreasing L leads to smaller instead of the large widths, in contrast to what was observed when changing the kinetic parameters. These results may be explained by considering the three-step process of RD-SA: diffusion, reaction and self-assembly. At low Da numbers, the diffusion times are shorter than reaction times and the process is reaction limited. The sequential process of reaction and self-assembly is limited by the moment of surpassing the critical gelation concentration of the reaction products. When the Da number is lowered by decreasing the length, the diffusional flux becomes larger and the concentrations at the crossing of the two initial component gradients rapidly increase in time. This causes the products to be formed at shorter timescales leading to more rapid surpassing of the critical gelation concentration (CGC). Upon crossing the CGC the products are more prone to aggregate instead of broadening by diffusion and form small feature sizes. Adjusting Da by changing L leads to smaller feature sizes and is reasoned to be caused by a more rapid surpassing of the CGC.

The self-assembly within the RD-SA approach shows an additional Da regime compared to typical RD systems, where the self-assembly of the molecular gelator determines the feature sizes of the formed structures. This regime is typically not observed for inorganic precipitation systems, as they generally operated under diffusion limited conditions. With a Da in the order of 0.1 to 1, our setup operates under reaction limited conditions, which is similar to the situation of cellular systems. Cells have typical Da 's of ~ 1 (3), suggesting that RD-SA may lead to similarly interesting and rich phenomena as seen in cells (3, 29).

6.3 Conclusions

Based on the in-situ formation of an organic supramolecular gelator in a multicomponent reaction, we developed the formation of organic material structures with controllable shape, size, and chemical functionalization through combined reaction-diffusion and self-assembly (RD-SA) of a supramolecular gelator. We showed that the patterned structures could be chemically differentiated and used to form permanent chemical gradients. Furthermore, we are able to functionalize structures with molecular recognition sites for binding to proteins. Using typical RD parameters like diffusion length and reaction kinetics, we are able to adjust the dimensions of the RD-SA structures via the reaction conditions. To our knowledge, this work is a first example of an RD based approach to the formation of organic materials. The ability to tune the material dimensions in RD

by changing the self-assembly and reaction kinetics of organic components is a unique possibility and has so far not yet been explored. The versatility of organic chemistry combined with self-assembly greatly broadens the scope of materials made using reaction-diffusion. Future research on organic based RD-SA will bring smart designs of new materials by synergistic combinations of self-assembly and reaction-diffusion processes.

6.4 Experimental section

Acknowledgements

The research in this chapter has been a cooperation with Matija Lovrak and I want to thank him for all the extensive discussions and research work on different experimental parts of this chapter. Especially for the RD experiments with reservoirs and molds, the time trace experiments.

Materials

All reagents were purchased from commercial sources and were used as provided unless stated otherwise. All experiments were performed using MilliQ water. During all experiments phosphate buffer was used, which was prepared at desired pH by adding the appropriate amounts of acid and base parts of phosphate salts at a total concentration 100 mM to Milique purified water. If necessary, the pH was adjusted with concentrated NaOH or H₃PO₄ solutions. All agar gels were prepared by dissolving agar at 1 w/v % in the phosphate buffer at the desired pH. To completely dissolve the agar, the mixtures were heated and stirred at ~90 °C until solution turned transparent and left to solidify.

Hydrazide **H**, aldehyde's **A1**, **A3**, **A4**, Aldehyde labeled Fluorescein (**AF**), Rhodamine (**AR**), Cyanine (**AC**), and Mannose (**AM**) were synthesized in-house according to reported methods (24, 30, 31).

Equipment

UV-Vis spectroscopic measurements were performed on an Analytik Jena Specord 250 spectrophotometer. Confocal Laser Scanning Microscopy (CLSM) micrographs were obtained using a Zeiss LSM 700 confocal laser scanning microscope, equipped with a 2.5X, 10X and 40X oil immersion objective and the sensitivity of detectors and filters were adjusted in order to obtain maximum signal to noise ratio. Time-lapse movies are recorded with a MicroCapture usb camera connected to a standard desktop computer, with suitable software. Data analysis was performed using MATLAB® 2011b and ImageJ (<http://imagej.nih.gov>).

Methods

General sample preparation

Stock solutions of hydrazide **H** (40 mM) and aldehyde **A1** (160 mM) were used, unless stated differently. Experiments were performed with an initial molar ratio of hydrazide **H**: aldehyde **A1** = 1 : 4, to ensure an excess of aldehyde groups per hydrazide group.

RD-SA experiments by cutting reservoirs in agar gels

To prepare the agar gel matrix for Reaction-Diffusion and Self-Assembly (RD-SA) experiments, 10 mL of 1 w/v % agar solutions in 100mM phosphate buffer at the desired pH were heated until dissolved. When still warm, these solutions were poured in a plastic Petri dish (diameter ca. 50 mm, height ca. 15 mm) and left to gelate upon cooling. A slab of the agar matrix with desired dimensions was made by cutting two parallel lines at equal distance from the center of the Petri dish. The two outer segments of agar were removed, forming two compartments. The two separated compartments for the RD solutions were completely separated, as the agar gel extends fully to the sides of the Petri dish, ensuring that no mixing of solutions occurs. The two RD components (**H**, **A1**) were dissolved in the same buffer as used for the agar gel preparation. The two solutions were then placed in the two separated compartments and left to diffuse in a closed humidified environment to prevent evaporation of liquids. When a 2-dimensional grid of points sources was used for the experiments, multiple holes, of 10mm in diameter, were cut in the gelled agar. The different components were then placed alternating in the sequential holes and left to diffuse in a closed and humidified environment. The reservoirs can be filled by either aqueous solutions of the components or with agar gels (1 w/v% in buffer) containing the components (Fig. 6.2b).

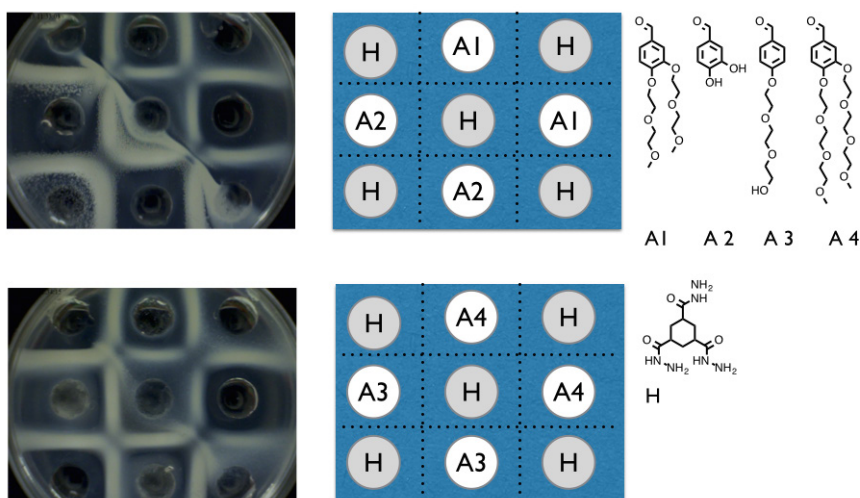
RD-SA by mold stamping

To form shapes of RD-SA structures, a PDMS mold inside a Petri dish was used containing the separate components. A PDMS mold is made by embossing shaped depressions into it, such as circles, triangles and squares or an array of squared depressions. These embossed depressions acted as reservoirs, and are filled with agar solutions containing **H** and **A1** in different reservoirs (40 mM **H**, 160 mM **A1**, pH 4).

The mold with the agar was left to cool down to room temperature, to allow the agar to gelate. A second agar layer was used as the diffusion and reaction layer for the formation of the RD-SA structure grid. Therefore, an agar solution layer (1 w/v %, pH 4) was poured on the top of the PDMS master with the solutions in agar and left to gelate. This setup was placed in a closed and humidified environment to allow for diffusion to take place. After 24 – 78 hrs the sample was taken out and the PDMS master was gently removed from the agar layer by pushing a glass slide between the PDMS master and the agar layer, which contained the formed RD-SA structures.

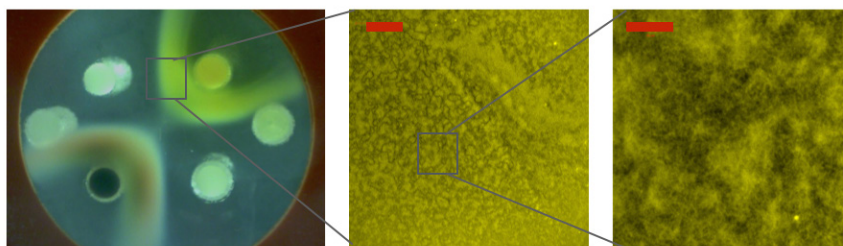
RD-SA by 'negative' printing

To form letters by RD-SA, we used the following procedure. Two separate solutions were prepared: one containing **H** (40 mM in 1 w/v % agar, pH 4) and one containing **A1** (160mM in 1 w/v % agar, pH 4). A plastic Petri dish was filled with an agar solution layer (1 w/v %, pH 4) and left to gelate. After cooling, the solutions containing **H** and **A1** were placed as viscous gel droplets on the agar layer, acting as diffusion and reaction medium. The droplets were placed as negative print of the desired final structure shape, such as the ASM abbreviation. We took care to ensure no direct contact was made between droplets containing the different components, also see Fig. 6.2g for illustration of starting positions for the 'negative print'. The sample was left standing for ~5 hr in a closed environment to allow the diffusion of **H** and **A1**.



Supplementary figure S6.1 RD-SA structures produced by different aldehydes in an agar matrix.

Left) Images of the formed structures, Middle) A scheme of the printing patterns. Right) the different molecules used. Conditions: 40 mM Hydrazide, 160 mM Aldehyde, pH 4, 1 w/v % agar as a matrix.



Supplementary figure S6.2 RD-SA structures produced by stamping, labeled with AF.

Left, image of the formed structures, middle and right images by CLSM. Conditions: 40 mM Hydrazide, 160 mM Aldehyde, pH 4, 1 w/v % agar as matrix, 40 μ M **AF**. Scale bars: middle, 200 μ m, right, 20 μ m.

Comparative self-assembly studies

To investigate the self-assembly behavior and morphology in the RD-SA setup different aldehydes were used within a single setup. Aldehyde solutions of 160 mM were prepared in phosphate buffer pH 4, using aldehydes **A1**, **A2**, **A3** and **A4** (Fig. S6.1), and a stock solution of hydrazide **H** (40 mM in phosphate buffer pH 4). A 3x3 matrix of holes was cut in a freshly prepared agar gel (1w/v %, pH 4) and the stock solutions were placed alternating as shown in figure S6.1 (middle), and the compounds were left to diffuse in a closed and humidified environment.

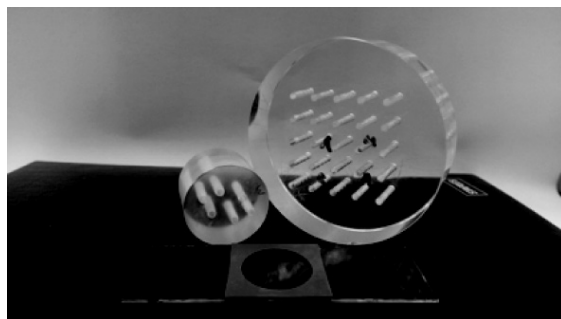
Chemically differentiation by fluorescent labeling of RD-SA structures

To chemically label the formed RD-SA structures, fluorescent labeled aldehydes (**AM**, **AR**, **AC**, solutions of 2 mM in MQ) were added to the aldehyde stock solutions (**A1**, 160 mM, pH 4), yielding final concentrations of ~40 μ M fluorophore labeled aldehyde. The stock solution of **A1** with fluorescent label was used as such in the setups as described in the other sections. The setup was left to diffuse in a closed and humidified environment to prevent evaporation of liquids. The setup was left standing in a closed and humidified environment to prevent evaporation of liquids to allow the compounds to diffuse (Fig. 6.2).

The formed structures were analyzed by fluorescence microscopy and/or CLSM, using the following settings: Fluorescein-aldehyde (Exc. 488nm, Em. 500-550nm), Rhodamine-aldehyde (Exc. 548nm, Em. 580-700nm), Cyanine-aldehyde (Exc. 633nm, Em. 650-750nm).

Stamping with the RD-SA approach

For the precise positioning of the RD-SA components a stamping method was developed using a home-made cell, consisting of a glass slide, a rubber gasket for spacing and a Perspex holder (figure S6.3). The Perspex holder has the following dimensions: diameter 60mm, height 20mm. It contains a grid of cylinders with inner diameter of 7mm. For these experiments, typically stock solutions of **H** (40 mM) and **A1** (160 mM) were prepared in a buffered agar medium (100 mM phosphate buffer, 1 w/v % agar). The cylinders of the Perspex holder were filled in an alternating fashion with the warm hydrazide agar solutions. These solutions were left to cool down and gelate, after which the remaining cylinders were filled with aldehyde agar solutions and left to cool. Cooling typically takes 5 minutes. To start the experiment, the cell chamber, consisting of a glass plate and rubber gasket, was filled with buffer or agar gel and the Perspex holder was placed on top.

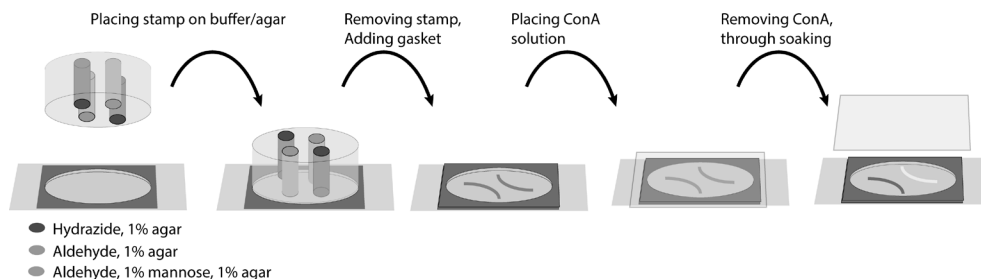


Supplementary figure S6.3 Photograph of two Perspex holders, with a rubber gasket for the experiments at a small scale. The cell-chamber, consisting of rubber gasket on a glass slide, is filled with the solution of agar in buffer or just buffer depending on the desired setup.

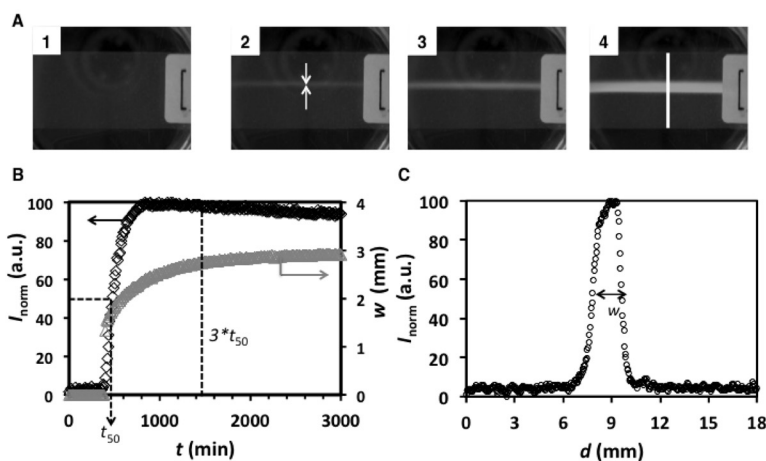
Chemical labeling for enzyme binding to RD-SA structures

For labeling the RD self-assembled structures with ConcavalinA (ConA), an aldehyde bound mannose (**AM**) was mixed in a solution of aldehyde **A1** (160mM **A1**, 1.6mM **AM**, pH4, 1 w/v % agar, 40 μ M **AR**). These were placed together in a Perspex holder (as described above), alternating with mixtures containing **H** (40 mM **H**, 1 w/v % agar, pH 4). The experiment was performed according to the procedure in figure S6.4. In short: the holder was placed on top of an agar gel and left to diffuse in a closed and humidified environment for 8hr. The time was kept intentionally short to prevent the formation of a dense supramolecular network, which would not allow the ConA to penetrate. Subsequently, the holder

was removed; another gasket was placed on top and filled with a buffered solution of ConA (2mM, pH 7). This was closed with a glass slide and left to diffuse in a closed and humidified environment for 12hr. After this period, the sample was analyzed using fluorescence microscopy. To remove the non-bound ConA, the top liquid was removed and fresh buffer was placed on top and left to stand for 72hr, with the top liquid being replaced every 24hr. The final sample was again imaged by fluorescence microscopy. Images were analyzed with ImageJ to extract the fluorescence intensity profiles.



Supplementary figure S6.4 Schematic image of the process used for the ConA binding setup.



Supplementary figure S6.5 Time-dependent formation of supramolecular hydrogel lines.

The formation of a supramolecular RD-SA structure is followed in time (A). Photo 1, $t = 0$ min, photo 2, $t = 400$ min first observation structure, photo 3, $t = 470$ min, 50% of maximum intensity, photo 4, $t = 2000$ min. B) Normalized intensity (black diamonds) was tracked at a spot on the agar strip where supramolecular hydrogel line was formed first (depicted by the arrows in photo 2). At 50 % of maximum the half-time of formation is determined, t_{50} . Along the line shown in photo 4, the intensity is measured to determine the width (w) of the supramolecular line at 50% of maximum normalized intensity (B, grey triangles, C). The vertical dashed line represents $3 \cdot t_{50}$ - time point at which the width of the supramolecular hydrogel line is determined.

Time traces of RD-SA structures for determining kinetics and widths by camera

To follow forming of RD gel patterns in time, the experiments were performed while monitored with a digital camera. A plastic Petri dish was filled with 1 w/v % agar at the desired pH and left to gelate. The desired dimensions were made with two parallel cuts, at equal distance from the center. The outer agar segments were removed, creating two containers for the solutions. The Petri dish with agar gel slab was placed on a flat Plexiglas plate above a digital microscope camera. The experiments were started at the moment that the two solutions of RD-SA components were placed in the separated compartments. Images were taken every 10 minutes. The experiments were continued for an appropriate time, for

20 to 120 hours depending on experimental conditions. The digital images were analyzed by ImageJ, extracting intensities from the images over the full diffusional length (fig. S6.5, purple line in inset photo 4) and storing the data. This data was then processed using custom built MATLAB 2011b code. This code contains the following steps: from the raw intensity profile, the background is subtracted, intensities are normalized, and the width of 1D RD hydrogel pattern is determined as the horizontal distance between two slopes at 50% of the maximum intensity (fig. S5, inset graph a), at each time point. The t_{50} was determined by taking the time value at 50% of the maximum reached intensity (fig. S6.5, green arrows in inset photo 2). The widths used for comparison between measurements are the widths measured at three times t_{50} . After three times t_{50} plateaus are observed in the width vs. time curves for the short lasting experiments. The moment of $3 \cdot t_{50}$ was chosen as moment to determine the structures width. All data is summarized in tables S6.2-S6.4

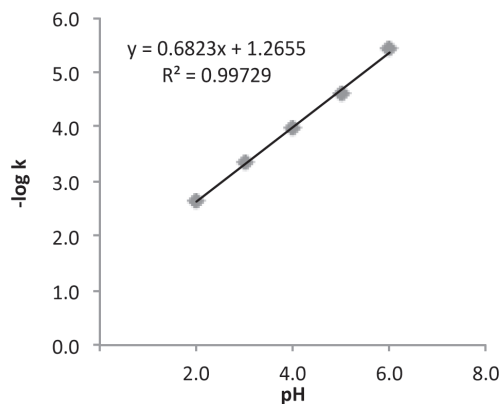
Diffusion behavior

Close analysis of the gel formation over time gives two important observations; the first observation is that the appearance of the gel typically occurs after ~10 hrs. As the components in these experiments had to diffuse over a cm distance, this timescale for these experiments matches with the timescale for diffusion. The second observation is that the initial gel line is formed to the side of **A1** from the middle and moves towards the side of **H** from the middle. As the used components are not completely equal in size, a small difference in diffusional speed is anticipated. This is confirmed by diffusion-nmr measurements (DOSY), giving diffusional coefficients of $9 \cdot 10^{-6} \text{ cm}^2/\text{s}$ and $5 \cdot 10^{-6} \text{ cm}^2/\text{s}$ for **H** and **A1**, respectively. The non-centered formation of the gel line is thus understood from the difference in diffusional speeds. The subsequent formation of the line towards the center of the sample is contributed to the multiple reactions that occur to form the final gelator **G1**, with the following argumentation; The mixing gradients react and produce a mixture of the **G1** component, with 1, 2, and 3 aldehyde groups attached. Upon reacting the diffusional speed of these species decreases inevitably. Due to the ration of **H** : **A1**, of 1:3, **A1** has a higher initial concentration and thus a greater flux than **H** passing the initial formed gel line. We thus reason that at the **H** side of the initial gel line the local concentration of **G1** keeps on increasing and the gel line expands towards the **H** side. This reasoning suggests that the reactions play a significant role in the formation of the gel structures.

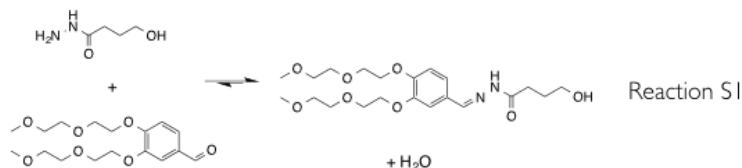
Structure dimension comparison

We compare the effects of the conditions on the dimensions of the RD-SA formed structures. We analyzed different conditions by changing the pH, L and concentrations. We used the RD-SA setup to form straight lines and systematically changed the conditions, with pH between 3 and 7, L between 0.25 and 1 cm, and concentration of **H** between 10 and 40 mM. All experiments were observed as time traces and accordingly analyzed, with the results of the separate experiments in table S6.2-S6.4. To be able to compare the obtained structure dimension between experiments, the Da for each experiment is determined and used to plot the structure widths. To determine the Damkohler (Da) number, the reaction diffusion equations are made dimensionless (eq. 1,2). The hydrazone formation reaction is described as a second order reaction, between hydrazide and aldehyde groups. We assumed that the supramolecular gel consists purely out of gelator **G1** and thus three sequent reactions between the hydrazide **H** and aldehyde groups have to occur. We assumed that the third reaction is limiting and only this reaction is taken into account. To determine the reaction constants we used the model reaction S1, which does not self-assemble allowing for kinetic analysis with UV-vis (fig. S6.6). The required reaction constants, at different pH, were measured by UV-vis for the hydrazone reaction S1. To estimate the k for each used pH, we measured the aldehyde-hydrazide reaction S1 by UV-vis and determined the individual k values at each pH (table S1). The $-\log(k)$ of this data is then plotted versus the pH and we obtained a linear fit with R^2 of 0.997 (fig. S6.6).

To calculate the Da for the different conditions we estimated the reactions constants (k) at the used pH, the diffusion coefficient (D_{A1}) and the used diffusion length (L). The k values for the pH as applied in the RD-SA setup were interpolated using the obtained fit. The diffusion constant of **G1** was estimated to be $4 \cdot 10^{-6} \text{ cm}^2\text{s}^{-1}$, based on the Stokes-Einstein relation and a molecular radius (r) of 1.2 nm. The diffusion length (L) was taken as half of the distance of the agar matrix, as determined from the images during the measurements. Concentrations (C_0) were taken as the initial concentration of the hydrazide component. The Da for each experiment was estimated, the data is summarized in the tables S6.2-S6.4 below, and results are plotted in figure 6.4B. The errors for Da were estimated based on the individual errors of the separate parameters in equation 2.



Supplementary figure S6.6. | pH dependence of the forward rate constant for the hydrazone formation reaction S1. The $-\log(k)$ of the determined rate constants is plotted versus the pH at which they are measured.



Supplementary figure S6.7. | The hydrazone formation reaction used for kinetic analysis

Table S6.1: Measured reaction constants for reaction S1, at pH

pH	2	3	4	5	6	7
$k_1 \text{ (M}^{-1}\text{s}^{-1}\text{)}$	2.37E-03	4.42E-04	1.04E-04	2.56E-05	3.82E-06	1.56E-09

Table S6.2: Conditions and outcomes for the concentrations series

H (mM)	A (mM)	pH	L (cm)	$k_f \text{ (M}^{-1}\text{s}^{-1}\text{)}$	$t_{50} \text{ (min)}$	$t_{\text{total}} \text{ (min)}$	Width (mm)	Da
10	40	4.01	0.96	1.0E-04	983 (±25)	7340	3.22 (±0.08)	0.23 (±0.04)
15	60	3.98	0.99	1.0E-04	887 (±10)	4000	3.09 (±0.04)	0.36 (±0.07)
20	80	4.01	1.00	1.0E-04	773 (±35)	2580	2.90 (±0.03)	0.49 (±0.07)
22.5	90	4.00	0.95	1.0E-04	647 (±15)	2900	2.86 (±0.01)	0.50 (±0.08)
25	100	4.06	0.95	1.0E-04	633 (±5)	2950	2.85 (±0.01)	0.55 (±0.08)
27.5	110	4.11	0.96	1.0E-04	630 (±10)	2810	2.77 (±0.01)	0.62 (±0.08)
30	120	4.09	0.97	1.0E-04	627 (±15)	3870	2.69 (±0.04)	0.69 (±0.12)
35	140	4.00	0.99	1.0E-04	557 (±10)	2820	2.64 (±0.02)	0.83 (±0.15)
*40	160	4.01	0.95	1.0E-04	490 (±10)	4150	2.74 (±0.04)	0.88 (±0.13)
25	100	4.00	1.00	1.0E-04	597 (±15)	2980	2.84 (±0.02)	0.61 (±0.15)

Table S6.3: Conditions and outcomes for the pH series

H (mM)	A (mM)	pH	L (cm)	k_f (M ⁻¹ s ⁻¹)	t_{50} (min)	t_{total} (min)	Width (mm)	Da
40	160	3.3	0.94	3.04E-04	460 (±10)	5410	1.88 (±0.04)	2.65 (±0.43)
40	160	4.01	0.95	9.96E-05	490 (±10)	4150	2.74 (±0.04)	0.88 (±0.13)
40	160	4.47	0.97	4.84E-05	603 (±15)	4130	3.13 (±0.03)	0.44 (±0.07)
40	160	5	0.98	2.10E-05	603 (±15)	1860	4.15 (±0.07)	0.20 (±0.03)
40	160	5.48	0.97	9.90E-06	823 (±5)	4320	5.95 (±0.13)	0.09 (±0.02)
40	160	6	0.97	4.37E-06	797 (±35)	5300	7.15 (±0.28)	0.04 (±0.01)
40	160	6.49	0.95	2.02E-06	1067 (±50)	4540	10.06 (±0.50)	0.02 (±0.003)
40	160	7.09	0.93	1.56E-06	930 (±50)	7460	9.96 (±0.25)	0.01 (±0.002)

Table S6.4: Conditions and outcomes for the length series

H (mM)	A (mM)	pH	L (cm)	k_f (M ⁻¹ s ⁻¹)	t_{50} (min)	t_{total} (min)	Width (mm)	Da
40	160	4.0	0.24	1.0E-04	100 (±1)	1440	1.53 (±0.03)	0.06 (±0.01)
40	160	4.0	0.34	1.0E-04	117 (±5)	2890	1.61 (±0.04)	0.11 (±0.04)
40	160	4.0	0.37	1.0E-04	137 (±5)	4090	1.75 (±0.01)	0.13 (±0.03)
40	160	4.0	0.48	1.0E-04	160 (±1)	1430	1.97 (±0.03)	0.22 (±0.04)
40	160	4.0	0.59	1.0E-04	233 (±5)	2860	2.02 (±0.02)	0.34 (±0.07)
40	160	4.1	0.73	1.0E-04	317 (±5)	1480	2.21 (±0.03)	0.52 (±0.09)
40	160	4.0	0.83	1.0E-04	390 (±10)	4270	2.41 (±0.05)	0.67 (±0.10)
40	160	4.0	0.95	1.0E-04	490 (±10)	4150	2.74 (±0.04)	0.88 (±0.13)

6.5 References:

1. G. M. Whitesides, B. Grzybowski, Self-Assembly at All Scales. *Science* **295**, 2418-2421 (2002); DOI:10.1126/science.1070821.
2. S. Kondo, T. Miura, Reaction-Diffusion Model as a Framework for Understanding Biological Pattern Formation. *Science* **329**, 1616-1620 (2010); DOI:10.1126/science.1179047.
3. S. Soh, M. Byrška, K. Kandere-Grzybowska, B. A. Grzybowski, Reaction-Diffusion Systems in Intracellular Molecular Transport and Control. *Angewandte Chemie International Edition* **49**, 4170-4198 (2010); DOI:10.1002/anie.200905513.
4. A. S. Mikhailov, B. Hess, Self-Organization in Living Cells: Networks of Protein Machines and Nonequilibrium Soft Matter. *Journal of Biological Physics* **28**, 655-672 (2002); DOI:10.1023/A:1021247024192.
5. B. A. Grzybowski, *Chemistry in Motion*. (John Wiley & Sons, Ltd, 2009).
6. B. A. Grzybowski, K. J. M. Bishop, C. J. Campbell, M. Fialkowski, S. K. Smoukov, Micro- and nanotechnology via reaction-diffusion. *Soft Matter* **1**, 114-128 (2005); DOI:10.1039/B501769F.
7. C. J. Allègre, A. Provost, C. Jaupart, Oscillatory zoning: a pathological case of crystal growth. *Nature* **294**, 223-228 (1981); DOI:10.1038/294223a0.
8. E. O. Budrene, H. C. Berg, Complex patterns formed by motile cells of *Escherichia coli*. *Nature* **349**, 630-633 (1991); DOI:10.1038/349630a0.
9. S. Kondo, R. Asai, A reaction-diffusion wave on the skin of the marine angelfish *Pomacanthus*. *Nature* **376**, 765-768 (1995); DOI:10.1038/376765a0.
10. R. E. Liesegang, Über einige eigenschaften von gallerten. 353-362 (1896).
11. G. Bailey, in *The Protein Protocols Handbook*, J. M. Walker, Ed. (Humana Press, 1996), pp. 749-752.
12. O. Ouchterlony, Antigen — Antibody Reactions In Gels. *Acta Pathologica Microbiologica Scandinavica* **26**, 507-515 (1949); DOI:10.1111/j.1699-0463.1949.tb00751.x.
13. I. Lagzi, *Precipitation Patterns in Reaction-Diffusion Systems*. (Research Signpost, 2010), pp. 236.
14. C. J. Campbell, R. Klajn, M. Fialkowski, B. A. Grzybowski, One-Step Multilevel Microfabrication by Reaction-Diffusion. *Langmuir* **21**, 418-423 (2005); DOI:10.1021/la0487747.
15. K. F. Mueller, Periodic Interfacial Precipitation in Polymer Films. *Science* **225**, 1021-1027 (1984); DOI:10.1126/science.225.4666.1021.
16. P. J. Bracher, M. Gupta, G. M. Whitesides, Shaped Films of Ionotropic Hydrogels Fabricated Using Templates of Patterned Paper. *Advanced Materials* **21**, 445-450 (2009); DOI:10.1002/adma.200801186.
17. W. L. Noorduin, A. Grinthal, L. Mahadevan, J. Aizenberg, Rationally Designed Complex, Hierarchical Microarchitectures. *Science* **340**, 832-837 (2013); DOI:10.1126/science.1234621.
18. S. M. Chirieleison, P. B. Allen, Z. B. Simpson, A. D. Ellington, X. Chen, Pattern transformation with DNA circuits. *Nature Chemistry* **5**, 1000-1005 (2013); DOI:10.1038/nchem.1764.
19. I. R. Epstein, K. Showalter, Nonlinear Chemical Dynamics: Oscillations, Patterns, and Chaos. *The Journal of Physical Chemistry* **100**, 13132-13147 (1996); DOI:10.1021/jp953547m.
20. A. S. Zadorin, Y. Rondelez, J.-C. Galas, A. Estevez-Torres, Synthesis of Programmable Reaction-Diffusion Fronts Using DNA Catalyzers. *Physical Review Letters* **114**, 068301 (2015); DOI:10.1103/PhysRevLett.114.068301.
21. S. N. Semenov, A. J. Markvoort, T. F. A. de Greef, W. T. S. Huck, Threshold Sensing through a Synthetic Enzymatic Reaction-Diffusion Network. *Angewandte Chemie International Edition* **53**, 8066-8069 (2014); DOI:10.1002/anie.201402327.
22. B. P. Fors, J. E. Poelma, M. S. Menyo, M. J. Robb, D. M. Spokoyny, J. W. Kramer, J. H. Waite, C. J. Hawker, Fabrication of Unique Chemical Patterns and Concentration Gradients with Visible Light. *Journal of the American Chemical Society* **135**, 14106-14109 (2013); DOI:10.1021/ja408467b.
23. J. Boekhoven, J. M. Poolman, C. Maity, F. Li, L. van der Mee, C. B. Minkenberg, E. Mendes, J. H. v. Esch, R. Eelkema, Catalytic control over supramolecular gel formation. *Nature Chemistry* **5**, 433-437 (2013); DOI:10.1038/nchem.1617.
24. J. M. Poolman, J. Boekhoven, A. Besselink, A. G. L. Olive, J. H. van Esch, R. Eelkema, Variable gelation time and stiffness of low-molecular-weight hydrogels through catalytic control over self-assembly. *Nature Protocols* **9**, 977-988 (2014); DOI:10.1038/nprot.2014.055.
25. J. Poolman, Maity, C., van der Mee, L., Boekhoven, J., Galan, E., Versluis, F., Eelkema, R., van Esch, J., A toolbox for controlling the properties and functionalization of hydrazone-based supramolecular hydrogels. *in preparation*, (2015).
26. H. L. Ashe, J. Briscoe, The interpretation of morphogen gradients. *Development (Cambridge, England)* **133**, 385-394 (2006); DOI:10.1242/dev.02238.
27. K. Tagawa, N. Sendai, K. Ohno, T. Kawaguchi, H. Kitano, T. Matsunaga, Recognition of Novel Amphiphiles with Many Pendant Mannose Residues by Con A. *Bioconjugate Chemistry* **10**, 354-360 (1999); DOI:10.1021/bc980083x.
28. J. C. Thomas, The determination of log normal particle size distributions by dynamic light scattering. *Journal of Colloid and Interface Science* **117**, 187-192 (1987); DOI:10.1016/0021-9797(87)90182-2.
29. J. Tabony, N. Glade, J. Demongeot, C. Papaseit, Biological Self-Organization by Way of Microtubule Reaction-Diffusion Processes. *Langmuir* **18**, 7196-7207 (2002); DOI:10.1021/la0255875.
30. Boekhoven, J., Poolman, J.M., Maity, C., Li, F., van der Mee, L., Minkenberg, C.B., Mendes, E., Esch, J.H. van, Eelkema, R., 2013. Catalytic control over supramolecular gel formation. *Nat Chem* **5**, 433-437. doi:10.1038/nchem.1617
31. Poolman, J.M., Boekhoven, J., Besselink, A., Olive, A.G.L., van Esch, J.H., Eelkema, R., 2014. Variable gelation time and stiffness of low-molecular-weight hydrogels through catalytic control over self-assembly. *Nat. Protocols* **9**, 977-988. doi:10.1038/nprot.2014.055



Supramolecular binding of proteins to lipid bilayers

In this work we report the binding of an Yellow Fluorescent Protein (YFP) protein to lipid bilayers, through host-guest binding of the guests WGG-YFP and membrane bound Methyl Viologen (MV^{2+}) with the cucurbit[8]uril (Q8) host. The temporary binding of peripheral proteins to cell membranes is in biological systems used to achieve functions, such as cell signaling. The binding of proteins onto lipid bilayers has seen many recent development but so far has not yet been achieved by the host-guest chemistry of Q8. In our approach, we make use of the ternary complex formed by Q8, MV^{2+} and tryptophan. To bind the MV^{2+} moieties to lipid membranes we coupled it to a cholesterol-anchoring group (MV-anchor). The binding of an YFP protein to lipid bilayers, through host-guest binding of the guests WGG-YFP and membrane bound MV^{2+} with the Q8 host. We find that a complex is formed between the lipid anchor bearing a MV^{2+} unit, the Q8 and tryptophan. This work forms a step towards the supramolecular binding of peripheral proteins onto lipid membranes.

This chapter is based on collaborative work and has partly been published in the Ph.D. thesis of dr. Ralph Bosmans (Eindhoven University of Technology) and as: R.P.G. Bosmans, Wouter E. Hendriksen, M. Verheijden, P. Jonkheijm, R. Eelkema, J. H. v Esch, and L. Brunsveld, Supramolecular protein immobilization on lipid bilayers, Chemistry –A European Journal, (2015) in press.

7.1 Introduction

Biological systems use the temporary binding of peripheral proteins to cell membranes to achieve functions, such as membrane trafficking, membrane shaping and cell signaling (1, 2). The localization of proteins on cell membranes is crucial for all organisms and increasing research in the last decades has revealed its importance for many cellular processes (3, 4). This anchoring of proteins occurs through both covalent and non-covalent linkages. Proteins are typically sensitive to small chemical alterations, leading to conformational changes and potentially protein inactivation. Therefore, anchoring processes work orthogonally to the active site to ensure protein functionality. The binding of proteins to cellular membranes is a dynamic process, where proteins reversibly bind to and perform an action on the membrane. The anchoring of these delicate proteins is also of great interest for biomaterial applications, such as drug screening and tissue engineering (5). While reversible binding of proteins is used for many cellular processes, it remains a scientific challenge to develop a reversible protein binding strategy for lipid bilayers.

Several strategies have been developed to immobilize proteins onto lipid membranes, using either covalently linking of proteins to lipids (6-9), or supramolecular binding. For the supramolecular strategies, the binding occurs between two complementary sites, one attached to a 'surface', the other one to the target protein (10, 11). Examples of strategies that have been developed range from the host-guest chemistry of cyclodextrine and adamantine, to the Cu^{2+} or Ni^{2+} mediated binding of His₆-tags with nitrilotriacetic acid surfaces (5), and coiled-coil peptide binding motifs (12). Other approaches use proteins as the binding sites, such as the SNAP fusion proteins (11), and the tetramer streptavidin that binds to biotin, a small molecule (5). The streptavidin-biotin is the strongest non-covalent binding strategy and has a binding constant in de order of $K_a \sim 10^{15} \text{ M}^{-1}$, making it a semi-covalent bond. These high binding constants limit the dissociation of the complex and thus the removal of the bound protein. Reversible binding can be achieved through weaker binding strategies such as a single HIS tag on nitrilotriacetic acid surfaces with a $K_a \sim 10^7 \text{ M}^{-1}$, but require the addition of heavy metals that could deteriorate the functionality of sensitive proteins (5). Especially strategies in which amino acids are used offer an attractive approach for the binding of proteins. It has been shown that dimerization of Yellow Fluorescent Proteins (YFP) with n-terminal expressed tryptophan (WGG-YFP) is achieved by using cucurbit[8]uril (Q8) as a host for two guest tryptophans (13).

The family of cucurbiturils is well known as synthetic hosts which form a donut-shaped molecule with a hydrophobic cavity and bind positively charged ammonium and metal salts (14-18). Q8 offers an exceptional possibility to bind two different guests within a single binding pocket (19-21). This heterogeneity of different guests offers unique possibilities to create binding strategies which are selective for hetero coupling of different

moieties based on the binding selectivity of Q8 with the guests. Examples of molecular guests are naphthalene (22), 2,7-dimethyldiazapyrenium (23) and methylviologen (MV^{2+}) (19), with binding constants up to $\sim 10^{11} M^{-2}$. The combination of MV^{2+} and tryptophan (W) is a well-known example, and has been extended to supramolecular binding of small peptides (19, 22). Through genetic coding, an N-terminal W can be installed on proteins and is used as a guest for the dimerization of proteins. This offers a binding strategy that is non-intrusive and easy to incorporate with different proteins. Despite the many recent developments of protein binding using Q8, the host-guest chemistry of Q8 has not yet been applied to the binding of proteins onto lipid bilayers.

Here we report a reversible binding strategy for proteins onto lipid bilayers, through host-guest chemistry with an anchored guest molecule. Binding proteins with the Q8 host-guest chemistry offers the potential for multiple guests, and intermediate binding strengths for reversible binding. By combining Q8 with a MV^{2+} bilayer bound guest and a WGG-YFP protein as a secondary guest, a ternary complex is formed (Fig. 7.1). As such this approach binds the YFP protein to lipid bilayers, both selectively and reversibly.

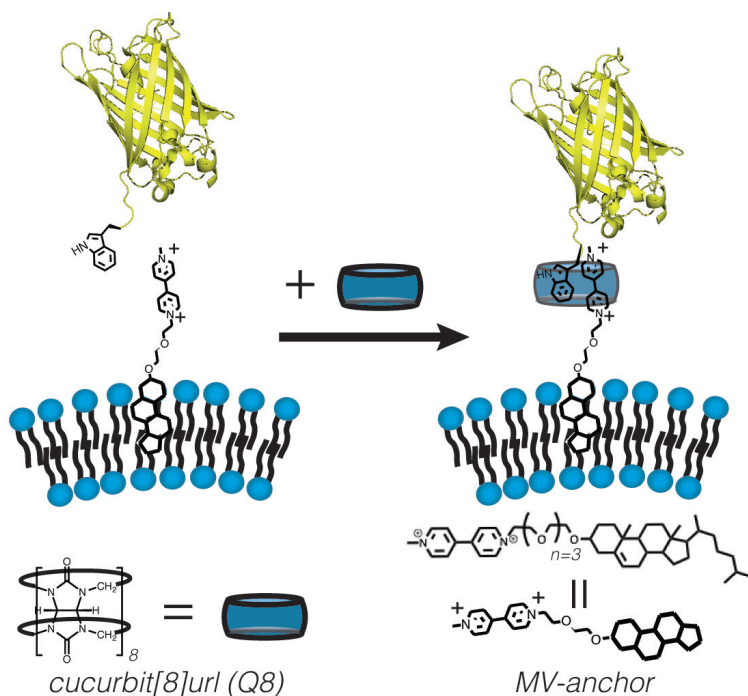


Figure 7.1. Illustration of WGG-YFP binding to a lipid bilayer through Q8 host-guest chemistry. The cucurbit[8]uril (Q8) and the methylviologen cholesterol anchor (MV-anchor) form a ternary 1:1:1 complex with the N-terminal tryptophan of the WGG-YFP, and bind the protein to a lipid bilayer.

7.2 Results & Discussion

To bind the YFP protein to lipid membranes, it needs to be coupled to a lipid membrane-anchoring group that contains the MV^{2+} moiety. For this we made a molecular design consisting of a hydrophobic anchoring group, a molecular spacer and the MV^{2+} head group (MV-anchor, Fig. 7.1). The design consists of a hydrophobic cholesterol as anchoring group, a tetra-oligoethylene (TEG) for solubility and linker of the MV^{2+} , which acts as a binding guest with the Q8 complex. Upon incorporation of the cholesterol group into a lipid bilayer, the MV^{2+} is directed towards the aqueous solution due to its hydrophilic nature. The Q8 is then able to bind to the MV^{2+} unit in solution. The MV-anchor requires an optimized synthesis strategy to combine the hydrophilic MV^{2+} head group and the hydrophobic cholesterol-anchoring unit. In our approach, we choose to initially attach a tetra-ethylene glycol (TEG) unit to the cholesterol, making it more hydrophilic and thus compatible with polar organic solvents for the next synthesis steps (Fig. 7.2A, B). In the following steps, we couple the TEG-cholesterol to a 4,4-bipyridine, and methylate the bipyridine, yielding the final compound. During the synthesis we are faced with different challenges, such as yields, solubility and purification. These challenges are mainly related to combining a very hydrophobic anchoring group with a hydrophilic head group. During the initial synthesis, we pegylated the mono-methylviologen first, and attached the cholesterol unit as a final step (Fig. 7.2A right). This approach turned out not to be possible due to the insolubilities of the different compounds in the same solvent, so we chose to inverse the synthesis strategy. In the optimized synthesis approach the purification of the MV-anchor (Fig. 7.2B, step 4) offers purification challenges due to the amphiphilic nature of the product, but is eventually achieved by precipitation of the desired product. The final compound is obtained as a red solid, with overall yield of 6% over 5 steps. The MV-anchor has an amphiphilic nature and it forms soapy aqueous solutions, which are opalescent and can be turned transparent upon heating to 50°C.

To test the formation of the ternary complex of Q8 with the MV-anchor and tryptophan, binding studies are performed using 1H -NMR and Isothermal Titration Calorimetry (ITC). The binding of methylviologen to Q8 is reported to induce a shift of the aromatic MV^{2+} signals, as measured by 1H -NMR (19). In the initial solution of the MV-anchor at 25°C, broad signals are obtained causing a non-optimal resolution. These effects are attributed to the self-assembly of the MV-anchor, due to the amphiphilic nature, as it is known for small molecule aggregation to have this effect on NMR resolution (24). Furthermore, upon mixing the MV-anchor and Q8 at room temperature, the solutions became turbid, indicating the formation of aggregates. Therefore, to increase the resolution of the signals and to lower the aggregation, the binding studies are performed at 50°C. After performing 1H -NMR of a solution of 0.2 mM of MV-anchor in D_2O , an equivalent amount of Q8 is added and new 1H -NMR measurements are performed (Fig. 7.3A). Upon addition of Q8 to the solution, the aromatic peaks of MV^{2+} show an upfield

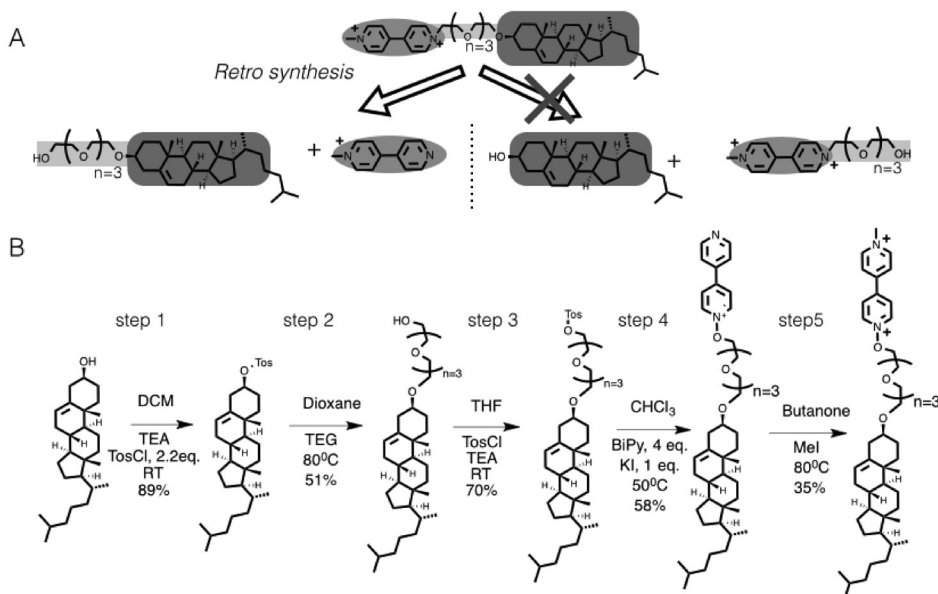


Figure 7.2. Synthesis strategy of MV-anchor, designed by retro-synthesis (A) and the used synthesis steps with conditions and solvents (B).

shift from 8.9 ppm and 8.3 ppm to 8.8 ppm and 7.7 ppm, respectively. Additionally, broadening of the peaks is observed, which can be explained by an increase of the relative size of the probed molecules. These observations show that a complex is formed between Q8 and the MV-anchor, which occurs on the MV²⁺, and are in agreement with literature (19).

To investigate the formation of the ternary complex, we use the MV-anchor/Q8 complex and add tryptophan. As a mimic for the N-terminal tryptophan on proteins, we use a tryptophan-methyl ester (TrpOMe), which has a K_a of $6.4 \cdot 10^4 \text{ M}^{-1}$ as a secondary guest in a MV²⁺/Q8 complex (19). Upon addition of TrpOMe to a solution of MV-anchor/Q8, the aromatic signals of the MV²⁺ decrease due to further line broadening. The aromatic peaks of the tosylate counter-ion however, are unaffected by the addition of TrpOMe confirming complex formation. The addition of Q8 to aqueous solutions of the MV-anchor and TrpOMe thus leads to the formation of ternary complexes of these three compounds.

The binding strength for the ternary complex of MV-anchor/Q8/TrpOMe at 25°C, is determined by performing ITC measurements. To a solution of 0.1 mM MV-anchor and 0.1 mM Q8 in 10 mM phosphate buffer at pH 7, a solution of 1.0 mM TrpOMe is titrated (Fig. 3B). The binding parameters are determined by measuring the released heats upon addition of the titrant and using a binding model to fit the data. Analyzing the raw heat data using a 1:1 binding model, reveals a binding constant of $K_a = 6.6 \cdot 10^4 \text{ M}^{-1}$ for TrpOMe and the Q8/MV-anchor complex (Table 7.1). The binding constant we found

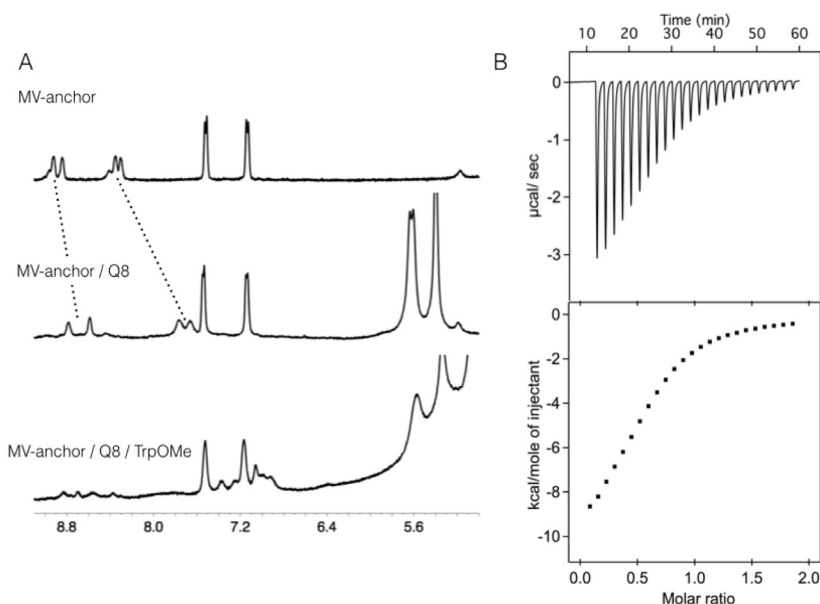


Figure 7.3. Binding of MV-anchor to Q8 and TrpOMe as determined by ¹H-NMR (A) and ITC (B). ¹H-NMR is performed in D₂O at 50°C, concentrations ~1 mM. The peaks of MV-anchor shift upfield from 8.9 ppm and 8.3 ppm to 8.8 ppm and 7.7 ppm, respectively, by addition of equimolar Q8. (B) ITC data for determining the binding constant of the MV-anchor/Q8 complex with TrpOMe. The top plot contains the raw data for power applied as function of time. In the bottom, the integrated values for the enthalpy are plotted as function of molar ratio (B). ITC conditions, 25°C, 10 mM phosphate buffer, pH 7.0. TrpOMe was titrated at 1mM into a 0.1 mM solution of MV-anchor/Q8.

is close to the reported literature value indicating that the TEG and cholesterol do not limit the binding (19). From the binding enthalpies the value for the ΔH is determined and combined with the K_a to calculate ΔG and $-T\Delta S$ (Table 7.1). These data indicate that the binding is enthalpically driven but entropically unfavorable, which is in agreement with literature (19).

To determine if our approach is able to bind proteins tot lipid bilayers, we

Table 7.1. Thermodynamic binding data for MV-anchor/Q8 with TrpOMe, as determined by ITC

Guest	K_a^a (M ⁻¹)	ΔG^b (kcal/mol)	ΔH^a (kcal/mol)	$-T\Delta S^c$ (kcal/mol)
TrpOMe	$6.6 (\pm 0.4) \times 10^4$	$-6.5 (\pm 0.1)$	$-11.1 (\pm 0.1)$	$4.5 (\pm 0.2)$

a) Mean value of two ITC measurements, using a 1:1 binding model. Error is given in parenthesis. b) Gibbs free energy is calculated from averaged association constant. c) Entropic contribution is calculated from ΔH and K_a .

investigate the binding of YFP with the Q8/MV-anchor complex on supported bilayers, by Quartz Crystal Microbalance with Dissipation monitoring (QCM-D). We use an YFP with a WGG peptide motif expressed at the N-terminal. This tripeptide has been shown to act as a guest with the Q8 host. The binding of the WGG-YFP to the MV-anchor is measured with and without Q8. Furthermore, the selectivity for WGG-YFP over MGG-YFP and the reversibility of our binding strategy are determined. In QCM, a quartz crystal oscillates at its acoustic frequency and with the addition of mass on the crystal a frequency change is measured. The viscoelasticity or softness of the adhered layer on the sensor surface is quantified by the dissipation factor (D). The frequency changes, Δf , are linearly related to the changes in mass by applying the Sauerbrey equation. This equation holds as long as the change in dissipation caused by the frequency change is less than 5% in Hz of the frequency change, as is the case for our measurements. To form a lipid bilayer on the silica coated QCM sensor, small unilamellar DOPC vesicles of 100 nm in diameter are flown over the crystal sensor. Initially these vesicles adhere to the sensor, decreasing the frequency Δf indicating addition of mass and increasing the dissipation ΔD indicating formation of a viscous layer. Next, the lipid vesicles rupture, releasing the entrapped water and form a rigid bilayer, which is observed by the decrease of the dissipation ΔD . The observed values for the frequency with a Δf of -25 Hz and dissipation ΔD of $\leq 0.5 \times 10^{-6}$ are similar to earlier reported values (25).

By QCM studies we show that the complex is formed between WGG-YFP, Q8 and the MV-anchor incorporated in a supported DOPC bilayer. By applying a solution of Q8 (50 μM) over the supported bilayer with an MV-anchor incorporated, we observe a Df of -1.5 Hz (Fig 7.4). This negative change in f indicates that additional mass adheres to the lipid bilayer, showing that Q8 binds to the incorporated MV-anchor (Fig 7.4, black line). Next, WGG-YFP (2 μM) is flown over the bilayer in the presence of Q8 (50 μM) and an additional Δf of -2.5 Hz is observed. This is understood as the binding of the WGG-YFP protein to the lipid bilayer through the MV-anchor / Q8 complex. Upon rinsing the surface with buffer, the frequency increases back to the levels before Q8 / YFP binding, 31 Hz, due to the disassembly of the complexes. These results show that WGG-YFP proteins are bound to lipid bilayer through the host-guest complex of WGG-YFP, Q8 and MV-anchor.

Furthermore, we observe that Q8 needs to be present during the addition of the WGG-YFP. When a solution of WGG-YFP is flown over the Q8 saturated bilayer, containing an MV-anchor, but without Q8 in solution, no binding occurs. We observe a slight decrease of f occurs initially, followed by a rapid increase ending at frequency levels of before Q8 saturation (Fig. 7.4, grey line). The initial slight decrease is explained by the rapid binding of the WGG-YFP to the Q8 complex. The subsequent increase is then understood by the release of the Q8/WGG-YFP complex and depletion of the Q8 from the surface. The absence of Q8 is confirmed by sequentially flowing buffer over the bilayer upon which no further change in f is seen. The concentration of Q8 in solution thus needs to be maintained during the experiments to stabilize the complex formation

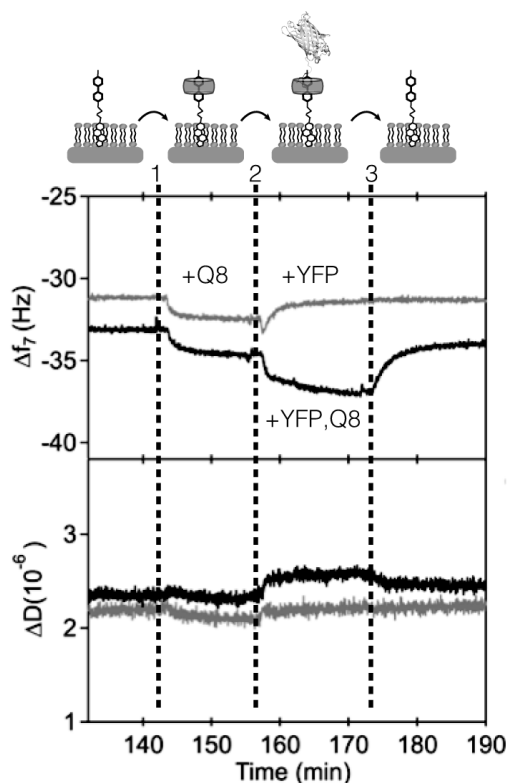


Figure 7.4. Binding of YFP to supported lipid bilayers as determined by QCM. QCM sensograms showing the binding process of WGG-YFP with Q8 (black line) and without Q8 (grey line) onto a DOPC bilayer containing MV-anchor. The top graph contains the change in frequency (Δf) and bottom graph the change in dissipation (ΔD). Dotted lines mark the administering of solution with (1) Q8 50 μ M, (2, grey line) WGG-YFP 2 μ M, (2, black line) WGG-YFP 2 μ M, Q8 50 μ M, (3) buffer.

and bind the WGG-YFP.

To test if the binding occurs through our proposed mechanism, several control experiments are performed. To determine a-specific binding, we flow solutions of WGG-YFP and WGG-YFP/Q8 or only Q8, up to concentrations of 75 μ M, over bare lipid bilayers without the MV-anchor. For all the different solutions, we do not observe changes of D_f nor DD . These results indicate that no a-specific binding of the protein WGG-YFP and Q8 on the bare DOPC lipid bilayer occurs.

Additionally, we measure the selectivity for binding of WGG-YFP over MGG-YFP. After preparing the lipid bilayer, with MV-anchor and Q8, the WGG-YFP and MGG-YFP proteins are flown over the lipid layers, on different QCM sensors. It is observed that the MGG-YFP leads to Δf of -7 Hz, whereas the WGG-YFP leads to Δf of -25 Hz, both in the presence of Q8 (50 μ M, Fig. 7.5 step 3). The larger decrease of f for WGG-YFP indicates that about three times more is bound to the bilayer, compared to MGG-

YFP. Our binding approach, using the Q8 host-guest chemistry, is thus more effective for WGG-YFP. However, the MGG-YFP also shows a binding, which is unexpected. Binding experiments of the tripeptide MGG and MGG-YFP by ITC, show that MGG does not have any binding to the Q8/MV²⁺ complex, but the MGG-YFP does show a binding (26). These observations show that an additional binding occurs on the protein itself. Comparing the binding constants of WGG-YFP and MGG-YFP in solution, gives similar values of $2.3(\pm 0.3) \times 10^5 \text{ M}^{-1}$ and $1.2(\pm 0.4) \times 10^5 \text{ M}^{-1}$, respectively (26). However, the binding of MGG-YFP is more entropically driven than WGG-YFP, which indicates that the mode of binding for both proteins is different. The binding of MGG-YFP is attributed to the presence of non-terminal aromatic moieties on the YFP protein, leading to the difference in binding kinetics. These results show that the binding with Q8 is more selective for the WGG-YFP over MGG-YFP and that an additional binding mode occurs through the non-terminal amino acids in the YFP.

During the QCM measurements, the complex formation is dynamic by nature and can be formed reversibly. Upon flowing a buffer solution over the lipid bilayers a rapid increase in the frequency is observed indicating the removal of the bound proteins (MGG/WGG-YFP, Fig. 7.5). We then test if this is indeed possible on the same bilayers by administering new solutions of WGG-YFP to both channels. Indeed, we observe a decrease of the Δf in both channels, indicating an increase of bound mass. For the sensor in which initially the WGG-YFP was administered (Fig 7.5, black line), the decrease of Δf is now smaller in respect to the first injection, Δf of -25 Hz versus 14 Hz. Repeating the process a third time shows a lower Δf of -8 Hz and indicates that the complex can be formed multiple times. The decrease in binding on the samples is explained by the loss of MV-anchor during the experiments. This experiment shows that the WGG-YFP protein can repeatedly be bound to the lipid surface through the host-guest complex with Q8/MV-anchor.

To investigate if our approach using the Q8/MV-anchor complex for binding proteins would also work on membranes in solution, we studied the binding of the WGG-YFP to lipid vesicles. By differential scanning calorimetry, we determine if the MV-anchor is incorporated in the DPPC vesicles (Fig 7.6A). We observe a broadening of the phase transition of the vesicles due to the cholesterol moiety of the MV-anchor. The MV-anchor is thus incorporated into the DPPC vesicles, which is in agreement with the QCM results for the supported bilayers. To analyze the formation of the WGG-YFP/Q8/MV-anchor complex on unilamellar vesicles, we perform confocal fluorescence microscopy studies using the fluorescence signal of the YFP. It is observed that solutions of DPPC vesicles (1 mM) with an MV-anchor (0.1mM) incorporated but without Q8 added, the WGG-YFP (2 μM) is spread homogeneous over the observed area (*data not shown*). However, upon addition of Q8 no significant changes are observed in these experiments, indicating that the binding of the YFP does not occur on the unilamellar vesicles.

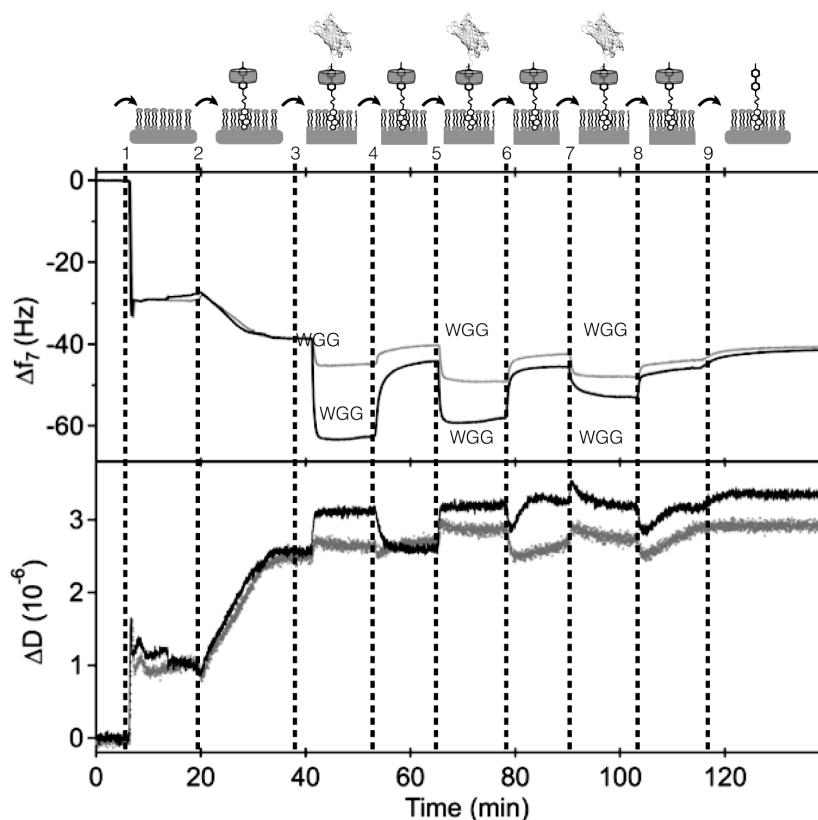


Figure 7.5. Determining the selectivity and reversibility of WGG-YFP by QCM.

The selectivity for WGG-YFP (B, black line) over MGG-YFP (B, grey line) is determined by comparison, flowing solutions of the proteins (2 μ M) and of Q8 (50 μ M) over MV-anchor incorporated bilayers. Next, WGG-YFP (2 μ M) with Q8 (50 μ M) is applied on both crystals to show the reversibility of the binding process. The top graph contains the change in frequency (Δf) and bottom graph the change in dissipation (ΔD). Dotted lines mark the administering of solution with (1) DOPC vesicles, 1mM, 100nm (2) MV-anchor 5 μ M, Q8 50 μ M, (3) MGG-YFP or WGG-YFP 2 μ M, Q8 50 μ M, (4) Q8 50 μ M, (5) WGG-YFP 2 μ M, Q8 50 μ M, (6) Q8 50 μ M, (7) WGG-YFP 2 μ M, Q8 50 μ M, (8) Q8 50 μ M, (9) buffer.

To further investigate the complex formation on unilamellar vesicles, we study the complex of TrpOMe/Q8/MV-anchor on lipid vesicles by fluorescence spectroscopy (Fig 7.6B, C). To determine the formation, the fluorescence signal of TrpOMe is analyzed upon binding to Q8 and the incorporated an MV-anchor. Upon binding of TrpOMe to Q8 a decrease of the fluorescence intensity occurs. Based on literature, it was anticipated that the sequential binding of MV²⁺ to this complex leads to a further decrease of intensity. However, in comparison with a control sample, vesicles without MV-anchor, the intensity decreased slightly less indicating that no significant binding occurs (Fig 7.6C). These

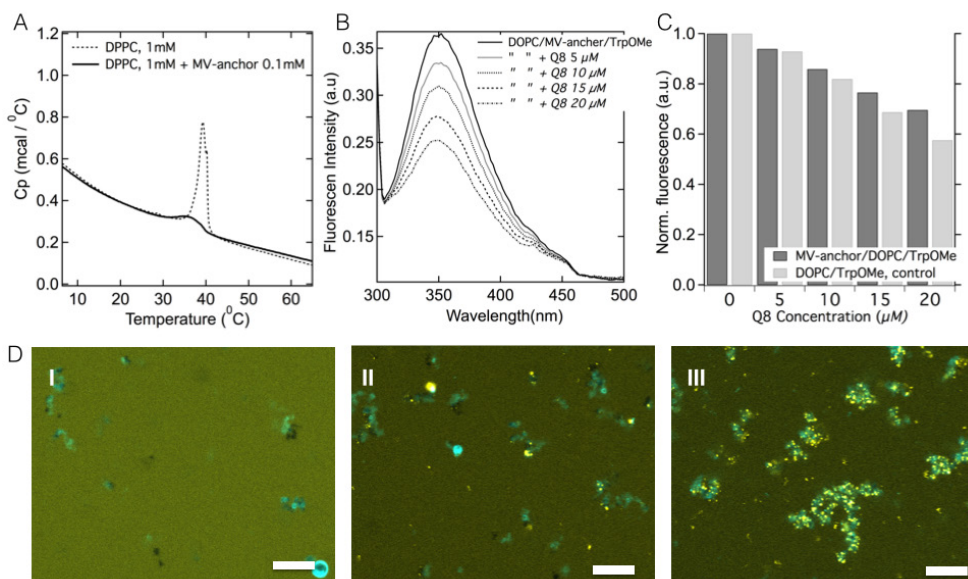


Figure 7.6. The study of WGG-YFP binding to vesicles with MV-anchor incorporated. (A) DSC melting curve of DPPC vesicles (1mM, 100nm) with 0.1mM MV-anchor, showing a broadening and lowering of the phase transition. (B) Fluorescence signal of TrpOMe in the presence of an MV-anchor incorporated in DOPC vesicles, 100nm 1mM and different concentrations of Q8. (C) Normalized fluorescence intensity at 350nm for TrpOMe for B and control sample of DOPC (1mM, 100nm) and TrpOMe, both with increasing concentrations of Q8. (D) Confocal microscopy images of aggregated vesicles, DPPC 1 mM, DPPC-NBD 1 μM (blue), MV-anchor 0.1 mM, WGG-YFP 2 μM (yellow) and Q8 at concentrations of 0 (I), 10 (II) and 25 (III) μM. With increasing concentrations of Q8, the YFP signal becomes more localized onto the surface of the DPPC vesicles.

results show that the TrpOMe/Q8/MV-anchor complex on the surface of vesicles does not form, which support our findings in the microscopy experiments.

Surprisingly, when we use aggregated multi-lamellar vesicles for the binding experiments of WGG-YFP, we do observe localization of the YFP onto the vesicles surfaces (Fig 7.6D). Without Q8 added, the YFP signal is homogeneously distributed over the observed area, but upon increased concentrations of Q8 in the samples we observe co-localization of the YFP and the vesicles. The YFP signal on the vesicles now forms individual spots on the aggregated vesicles surfaces and with increasing concentrations of Q8, the presence of these spots increases.

These results are interpreted as following: the binding strength of the WGG-YFP to the Q8/MV-anchor complex is in the order of 10^4M^{-1} and has a short lifetime. This relative weak binding is confirmed in the QCM measurements by the rapid removal of the bound proteins upon changing conditions. The WGG-YFP could bind through the single N-terminal W, but has multiple binding sites formed by the additional aromatic moieties on the YFP, as discussed. On unilamellar vesicles a single binding of the

N-terminal WGG-YFP will occur, but this binding is too weak for proper visualization. When aggregated vesicles are used they will form corners and pockets, in which the YFP is able to bind to multiple anchoring groups. The multiple binding will enhance the binding. The observed individual spots are strongly localized WGG-YFP and indicate an immobilization of the protein. Taking into account the relative sizes of the WGG-YFP and Q8, 42 and 17.5 Å respectively, a maximum of two Q8 can bind onto a single YFP through the non-terminal aromatic amino acids. Although these results are not conclusive, it is argued that immobilization of WGG-YFP on aggregated vesicles occurs through the Q8/MV-anchor complex with the non-terminal amino acids.

7.3 Conclusions

In this work we report the binding of an YFP protein to lipid bilayers, through host-guest binding of the guests WGG-YFP and membrane bound MV^{2+} with the Q8 host. We find that a complex is formed between the lipid anchor bearing a MV^{2+} unit, the Q8 and tryptophan. We are able to bind WGG-YFP proteins to supported bilayers, and show that the complexes are reversible and the binding process can be repeated multiple times. We further argue that the WGG-YFP is able to bind to aggregated vesicles through multiple binding sites. This work is an interesting step towards the supramolecular binding of peripheral proteins onto lipid membranes and the challenges that lie ahead.

7.4 Experimental

Acknowledgements

The research discussed in this chapter has been a collaboration with dr. Ralph Bosmans and prof. dr. Luc Brunsveld. I want to thank them for the extensive work, especially on the expression of the YFP-proteins, Qtof mass analysis and the Quartz Crystal Microbalance experiments.

Starting materials and buffer salts are obtained from Sigma and used without purification. ^1H NMR, and ^{13}C NMR spectra are performed in the appropriate deuterated solvents on a Bruker Avance Spectrometer 400 MHz or an Agilent 400 MHz NMR Spectrometer with one NMR probe at 400 MHz (^1H) or 100 MHz (^{13}C); chemical shifts (δ) are reported in parts per million. Measurements are performed at 298 K using residual protonated solvent signals as internal standard. HPLC-MS analysis is performed on a Shimadzu Liquid Chromatograph Mass Spectrometer, LCMS-2010, LC-8A pump with a diode array detector SPD-M20.

Synthesis MV-anchor

Cholesterol tosylation

The synthesis was adapted from reference 27 (27). To a solution of cholesterol (10.2 gr, 26.3 mmol, 1 eq.) in dry dichloromethane (DCM, 100 ml), is 3 eq. of TEA (10 ml) and 0.3 eq. of DMAP (0.9 gr) are added, and cooled on ice (0°C). A solution of TosCl (11.0 gr, 57.9 mmol, 2.2 eq.) in DCM (25 ml) is added, dropwise over a period of 30 minutes, and the mixture left to stir for 30 minutes on ice. The mixture turns dark red quickly after addition of TosCl solution. The mixture is left to stir for 2 days at RT. The reaction mixture is sequentially washed twice with NaCO_3 , 5 w%, and once with demi-water. All aqueous layers are combined and extracted twice with DCM. All organic layers are combined, dried on Na_2SO_4 and evaporated *in vacuo*. Multiple times recrystallization from DCM in MeOH gives the pure compound 1, yield: 12.6 gr, 89 %, 23.4 mmol (product rf~ 0.9, in CHCl_3).

^1H NMR: CDCl_3 : δ 7.80 (d, 2H, 8.0Hz, C=C, Tosyl group), 7.32 (d, 2H, 8.1 Hz, C=C, Tosyl group), 5.30 (br, 1H, C=CH, cholesteryl group), 4.32 (m, 1H, $\text{HC}(\text{CH}_2)\text{-O}$, cholesteryl group), 2.45 (s, 3H, $-\text{CH}_3$, Tosyl group), 2.4-2.2 (m, 2H, $\text{CH-CH}_2\text{-C}$, cholesteryl group) 2.0 – 1.8 (m, 4H, cholesteryl group), 1.7-0.8 (m, 34H, cholesteryl group), 0.66 (s, 3H, cholesteryl group).

^{13}C NMR: δ 144.3 ($\text{CH}=\text{C}$ cholesteryl), 138.9 ($-\text{CH}=\text{}$, Tosyl), 134.7 ($-\text{CH}=\text{}$, Tosyl), 128.7 ($-\text{CH}=\text{}$, Tosyl), 127.61 ($-\text{CH}=\text{}$ - CH_2 , Tosyl), 123.5 ($\text{CH}=\text{C}$, cholesteryl), 82.3 ($-(\text{C})\text{-O-}$, cholesteryl), 56 – 11 (carbons of the cholesteryl group).

TEG cholesterol

The synthesis was adapted from reference (28). A solution of Tos-cholesterol (5.1 gr, 9.4 mmol, 1 eq.), in dioxane (50 ml) is mixed with TEG (tetraethylene-glycol, 50 ml, 40 eq.) upon which an emulsion is formed. This mixture is refluxed under argon, and turns transparent around 60°C . Upon completion of the reaction, as checked by TLC, the reaction mixture is concentrated *in vacuo*, and diluted with DCM. The diluted mixture is sequentially washed twice with NaCO_3 , 5 w%, and once with demi-water. All aqueous layers are combined and extracted twice with DCM. All organic layers are combined, dried on Na_2SO_4 and evaporated *in vacuo*. A silica column is used to remove the excess of cholesterol from the product, with a gradient of CHCl_3 to 95 v% CHCl_3 : 5 v% MeOH (product rf ~0.4, in CHCl_3 , 5% MeOH), yield: 3.53 gr, 51 %, 4.8 mmol.

^1H NMR (CDCl_3): δ 5.32 (br, 1H), 3.71 (t, 2H, $\text{CH}_2\text{O-Cho}$), 3.65-3.59 (m, 16H, $\text{OCH}_2\text{CH}_2\text{O}$), 3.17 (m, 1H, chol), 2.4-2.2 (m, 2H, chol) 2.0 – 1.8 (m, 4H, chol), 1.7-0.8 (m, 34H, chol), 0.66 (s, 3H, chol).

^{13}C NMR (CDCl_3): δ 140.9 ($\text{CH}=\text{C}$ cholesteryl), 121.5 ($\text{CH}=\text{C}$, cholesteryl), 80 – 61 carbons of TEG), 11 – 56 (carbons of cholesteryl).

Tosyl-TEG-cholesterol

A solution of TEG-cholesterol (1.55 gr, 2.7 mmol), TEA (1 ml) and DMAP (10 mg, 0.03 eq.) in THF (50 ml) is cooled on ice to 0°C , and a solution of TosCl (0.8 gr, 4 mmol, 1.6 eq.) in THF (5 ml) is added dropwise of a period of 30 minutes. The solution is left stirring for 72 hours at room temperature, and a precipitate

is formed. The reaction mixture is concentrated in vacuo and the residue is redissolved in ethyl acetate (EtAc). This solution is washed twice with demi-water, dried on Na_2SO_4 and the EtAc is evaporated in vacuo. The pure product is obtained after a silica column with CHCl_3 , $r_f \sim 0.15$. Yield: 1.37 gr, 70%, 1.9 mmol.

^1H NMR (CDCl_3): δ 7.82(d, 2H, 8.3 Hz), 7.34 (d, 2H, 8.1Hz), 5.34 (m, 1H), 4.17 (t, 2H), 3.71-3.58 (m, 14H), 3.17 (m, 1H, chol), 2.46(s, 3H), 2.05-1.69 (m, 6H), 1.58-0.86 (m, 34H), 0.69 (s, 3H).

^{13}C NMR (CDCl_3): δ 144.3 (CH=C cholesteryl), 138.9 ((-CH=)-, Tosyl), 134.7 (-CH=, Tosyl), 128.7 (-CH=, Tosyl), 127.61 ((-CH=)- CH_3 , Tosyl), 123.5 (CH=C, cholesteryl), 80 – 61 carbons of TEG), 56 – 11 (carbons of cholesteryl).

Bipy-TEG-Cholesterol

A solution of Tos-TEG-Cholesterol (587 mg, 0.7 mmol), bipyridine (491 mg, 2.8 mmol, 4 eq.) and KI (110 mg, 0.7 mmol, 1 eq.) in CHCl_3 is heated to 50°C under nitrogen and reacted for 48 hr. The reaction mixture is concentrated in vacuo and redissolved in DCM, and washed with demi-water for 3 times. The combined organic layers and these are dried with MgSO_4 . The organic layers are evaporated and redissolved in MeOH, upon addition of diethyl ether a milky white precipitate is formed. The precipitate is captured and dried under vacuum. Yield: 354 mg, 0.4 mmol, 58%.

^1H NMR (CDCl_3): δ 9.21 (d, 2H, 6.2Hz), 8.65 (d, 2H, 5.3Hz), 8.19 (d, 2H, 6.2 Hz), 7.76 (d, 2H, 8.0Hz), 7.61 (d, 2H, 5.9Hz), 7.11 (d, 2H, 7.9Hz), 5.17 (s, 1H), 4.86 (bt, 2H), 3.82 (bt, 2H), 3.51-3.32 (m, 12H), 3.2 (m, 1H), 2.11 (s, 3H), 2.1-1.8 (m, 6H), 1.6-0.8 (m, 34H), 0.52 (s, 3H).

^{13}C NMR (CDCl_3): δ 153.6 (-C=, Bipy), 151.4 (-C=, Bipy), 146.7 (-C=, Bipy), 144.3 (CH=C cholesteryl), 143.6 (-C=, Bipy), 141.3 (-C=, Bipy), 140.5 (-C=, Bipy), 139.2 ((-CH=)-, Tosyl), 134.7 (-CH=, Tosyl), 128.6 (-CH=, Tosyl), 125.9 ((-CH=)- CH_3 , Tosyl), 123.5 (CH=C, cholesteryl), 81.1((-C)-O-, cholesteryl), 80 – 61 (carbons of TEG), 56 – 11 (carbons of cholesteryl).

MV-TEG-cholesterol

A mixture of Bipy-TEG-Cholesterol (110 mg, 0.1 mmol) with butanone (10 ml) is made and heated to 80°C to dissolve. Sequentially MeI (50 ml, 5 eq.) is added and the reaction mixture is left to stir at 80°C overnight. The reaction mixture is concentrated *in vacuo* and redissolved in EtAc (200 ml), washed with brine (600 ml) and the combined water layers are washed again with EtAc. The combined organic layers are dried *in vacuo* and redissolved in EtOH to remove left over salts, filtrated and dried under vacuum, to afford Mv-Teg-Cholesterol (45 mg, 0.04mmol, 35%). The MV^{2+} -anchor is well soluble in polar organic solvents, such as MeOH or EtOH, but is only slightly soluble in non-polar organic solvents, such as diethylether or choloform.

^1H NMR ($\text{DMSO}-d_6$): δ 9.25 (d, 2H, 6.9Hz), 9.18 (d, 2H, 6.7Hz), 8.66 (dd, 4H, 6.9Hz, 8.7Hz), 7.68 (d, 4H, 8.2Hz), 7.21 (d, 4H, 8.0Hz), 5.32 (s, 1H), 4.93(bt, 2H), 4.53 (s, 3H), 4.05 (bt, 2H), 3.67-3.59 (m, 12H), 3.2 (m, 1H), 2.36 (s, 6H), 2.1-1.8 (m, 6H), 1.6-0.8 (m, 34H), 0.69 (s, 3H) [WH78, LAST NMR].

^{13}C NMR ($\text{DMSO}-d_6$): δ 151.9 (-C=, Bipy), 148.4 (-C=, Bipy), 144.3 (-C=, Bipy), 142.2 (-C=, Chol), 130.4 (-C=, Tos), 128.5 ((-CH=)-, Tosyl), 127.5 (-CH=, Tosyl), 127.1 ((-CH=)- CH_3 , Tosyl), 123.5 (CH=C, cholesteryl), 81.1((-C)-O-, cholesteryl), 73 – 61 (carbons of TEG), 56 – 19, 12.9 (carbons of cholesteryl).

ESI-MS $\text{C}_{46}\text{H}_{72}\text{N}_2\text{O}_4^{2+}$, calculated m/z : 358.27, found: 358.6.

Maldi-TOF: measured 716.55, calculated 358.27 or 716.55 for reduced MV^+ .

Cholesterol-PEG-Methylviologen Anchor

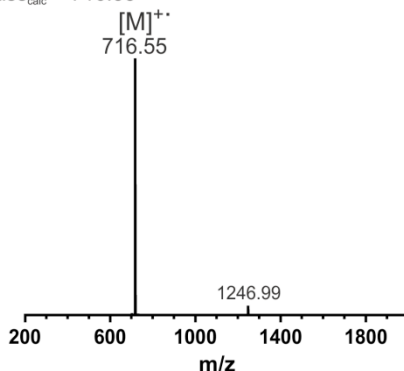
Mass_{calc} = 716.55

Figure S7.1 MALDI-TOF spectrum for MV-anchor. The observed $[M]^+$ equals the mass of a reduced MV-anchor, due to the ionization in MALDI. The mass is the same as the calculated mono-isotopic mass of 716.55Da. A small unknown impurity with a mass of 1246Da is observed.

NMR-binding study

^1H -NMR is used to determine the binding between MV-anchor and Q8 in solution. A 0.2 mM solution of MV-anchor in D_2O is measured to determine the peak positions of the aromatic MV^{2+} under aqueous conditions; δ 8.9 (d, 4H), δ 8.3 (d, 4H). Aromatic peaks of tosylate counterion; δ 7.5 (d, 4H), δ 7.1 (d, 4H). A weighted amount of Q8 is added to the solution and dissolved by sonication, 30 min at 40°C ; δ 5.6 (bs), δ 5.4 (bs). Addition of TrpOMe is achieved by adding an appropriate amount of a 10mM stock solution in H_2O to the D_2O NMR sample. The NMR measurement is then performed using solvent suppression.

Isothermal Titration Calorimetry (ITC)

Titration experiments are performed with a VP-ITC calorimeter from Microcal, Inc., using a 10 mM phosphate buffer, pH 7.0, at 25°C . In a typical experiment the MV^{2+} and Q8, at concentrations of 0.1 mM are in the sample cell and the secondary guest was injected from the injection syringe, at concentrations of 1 mM. A typical procedure of sample preparation is described for the binding of MV-anchor/Q8 complex with TrpOMe. For a 5 mL solution of 100 μM Q8, the desired amount of Q8 is weighted in a vial. In a second vial, from a stock solution of 10 mM MV-anchor in EtOH, an appropriate amount of solution is taken (~ 7.5 μL for 5 mL final volume) and the EtOH is evaporated under reduced pressure and at least 1 hr in a vacuum oven. To this vial, a 1 mL buffer is added, sonicated to dissolve the MV-anchor and concentration determined by UV-vis. This solution transferred to the Q8 vial to which the total required volume is made up by adding additional buffer. The Q8 is then dissolved by sonication for 30 minutes at 40°C . Solutions of secondary guest TrpOMe are made from a 10mM stock solution. Concentrations of solutions are determined afterwards by UV-vis using the extinction coefficient for TrpOMe of $\epsilon = 5690 \text{ M}^{-1} \text{ cm}^{-1}$, and for MV^{2+} using $\epsilon = 20400 \text{ M}^{-1} \text{ cm}^{-1}$ (29). Cucurbit[8]uril effective molecular weight was determined by titration as described by Kaifer (30).

The titration scheme consists of 25 injections of 10 μL with 120s between the injections. Binding constant and enthalpy are obtained by fitting the ITC data using a 1:1 binding model and performed with the supplied Microcal ITC software. The equilibrium distribution of the Q8/MV-anchor complex influences the initial concentration of this complex in solution, and would complicate the analysis strongly. As is reported the typical error due to this equilibrium is estimated to be $<5\%$ and is therefore ignored in the data presented here (19).

MALDI-TOF MS

Matrix-assisted laser desorption ionization time-of-flight mass spectrometry (MALDI-TOF MS) was performed on a Autoflex Speed MALDI-MS instrument (Bruker, Bremen, Germany) equipped with a 355 nm Nd:YAG smartbeam laser. MALDI-TOF MS experiments are performed by spotting samples on a MTP 384 target ground steel plate using an α -cyano-4-hydroxycinnamic acid (CHCA) (Fluka, Switzerland)

matrix. Samples are 1:1 premixed with CHCA in 50/50 acetonitrile/water supplemented with 0.1 % v/v trifluoroacetic acid (TFA). Mass spectra are acquired in reflector positive ion mode by summing spectra from 500 selected laser shots. The MS spectra are calibrated with cesium triiodide of known masses.

WGG-YFP and MGG-YFP expression and purification

YFP protein constructs featuring an N-terminal tryptophan or methionine were obtained by making use of intein splicing. The pTWIN vectors containing the DNA coding for WGG-YFP and MGG-YFP were obtained from Dung Dang. The pTWIN-1 plasmids were transformed in *E. coli* BL21(DE3) host strain (Novagen). The bacteria were cultured in 2 L LB medium containing 100 $\mu\text{g mL}^{-1}$ Ampicillin at 37 °C and 180rpm until an OD_{600} of ~0.7. Subsequently, protein expression was induced by adding isopropyl- β -D-thiogalactopyranoside (IPTG) to a final concentration of 0.5 mM. Cells were incubated for 7 hours at 25 °C and 180 rpm before being harvested by centrifugation (8000 g for 10 minutes). Bacterial cells were lysed by resuspending the pellet in Bugbuster Protein Extraction Reagent supplemented with benzonase (Novagen) and incubated for 1 hour at room temperature. The insoluble fraction was removed by centrifugation (40.000 g for 30 minutes). The soluble fraction was purified by applying it to a column filled with chitin beads (New England Biolabs) by gravity flow. The column was washed with 10 column volumes buffer (20 mM sodium phosphate, 150 mM sodium chloride, 1 mM ethylenediaminetetraacetic acid (EDTA), pH 7). The on-column intein splicing was incubated overnight at room temperature by closing the column. Cleaved proteins were eluted from the column by washing with the same buffer. Subsequently, the proteins were purified on Strong Ion Exchange Spin Columns (Pierce Thermo Scientific). Prior to loading the protein on the columns, the buffer was changed to buffer A (20 mM sodium phosphate, 50 mM sodium chloride, pH 8) by filtration (Millipore centrifugal filter device MWCO 10.000). Purified proteins were eluted with increasing amounts of sodium chloride in buffer A. Both proteins eluted at 78.5 mM sodium chloride. Buffer was changed to PBS buffer using a PD-10 desalting column (GE Healthcare). Proteins were concentrated using an Amicon Ultra centrifugal filter device (MWCO: 10 kDa) (Millipore). The purity and correct mass were confirmed by SDS PAGE electrophoresis and Qtof LC-MS. Finally, ~3 mg per liter culture for WGG-YFP and ~5 mg per liter culture for MGG-YFP yield was obtained. Concentrations were determined using the Nanodrop ND-1000 spectrophotometer using the reported extinction coefficient $\epsilon_{514} = 83400 \text{ M}^{-1}\text{cm}^{-1}$ (31). Proteins were stored at -80 °C.

Qtof-MS analysis

Purity and exact mass of the proteins were determined using a High Resolution LC-MS system consisting of a Waters ACQUITY UPLC I-Class system coupled to a Xevo G2 Quadrupole Time of Flight (Q-tof). The system was comprised of a Binary Solvent Manager and a Sample Manager with Fixed-Loop (SM-FL). Proteins were separated (0.3 mL min⁻¹) by the column (Polaris C18A reverse phase column 2.0 x 100 mm, Agilent) using a 15% to 75% acetonitrile gradient in water supplemented with 0.1% v/v formic acid before analysis in positive mode in the mass spectrometer. Deconvolution of the m/z spectra was done using the MaxENT1 algorithm in the Masslynx v4.1 (SCN862) software.

Quartz Crystal Microbalance

Silica-coated (50 nm) QCM-D sensors (QSX303) from LOT-Quantum were oxidized with UV/ozone for 30 minutes (UVP UV-Ozone photoreactor PR-100) and subsequently washed with EtOH and dried in a stream of nitrogen. The sensors were stored in milliQ water until use. QCM-D measurements were performed in a Q-Sense E4 4-channel quartz crystal microbalance with a peristaltic pump (Biolin Scientific). Before mounting the sensors in the microbalance they were once more washed with EtOH and dried using nitrogen flow. All experiments were performed in 0.5 times PBS buffer with a flow rate of 100 $\mu\text{L/min}$ at 22°C.

The lipid bilayer was formed by flowing 100 nm 1,2-dioleoyl-*sn*-glycero-3-phosphocholine (DOPC) (Avanti Polar Lipids) vesicles over the QCM-D sensor. Lipids were made as follows; DOPC was dissolved in chloroform and dried under nitrogen flow. Subsequently the DOPC was resuspended in milliQ water to a final concentration of 1 mg/ml. To get a size of 100 nm, the vesicles were 11 times extruded (pore size 100 nm). Size was verified by dynamic light scattering. Prior to flowing the vesicles over the QCM-D sensor, the vesicles were diluted 1:1 with PBS in order to enhance the vesicle rupture on the sensors. After a stable bilayer was formed, the different experiments were performed as discussed in the results section. The cucurbit[8]uril was purchased from Sigma Aldrich and the correct concentration was determined as described by Kaifer *et.al.* (30). In this report, the Δf and ΔD responses of the 7th overtone are depicted ($i = 7$).

To prepare the DOPC bilayers with incorporated MV-anchor, we flow a solution of MV-anchor (5 μ M) and Q8 (50 μ M) over bare DOPC bilayers. A decrease of the frequency of Df \sim 10 Hz is observed, whereas in the absence of Q8 the decrease is only Df \sim 4 Hz. As the dissipation change is $>5\%$, the Sauerbrey equation does not hold and the Df cannot be directly related to the difference in mass of the MV-anchor (717 Da) and the Q8/MV-anchor complex (717 + 1329 Da). Instead, the decrease of Df is explained by the more hydrophobic nature the Q8/MV-anchor complex, as is observed as well in earlier experiments as well. This provides a larger driving force for the MV-anchor/Q8 complex to be incorporated into the bilayer compared to the MV-anchor alone. These observations show that the incorporation of the MV-anchor into the DOPC bilayer is enhanced in the presence of Q8. For the experiments shown in figure 7.4A the surface was rinsed with buffer to remove Q8 from the surface. In the experiments shown in figure 7.4B, the WGG-YFP was directly applied after incorporation of the MV-anchor/Q8 complex.

Confocal laser scanning microscopy

For these studies, DOPC lipid vesicles are prepared, at concentrations of 1 mM, with up to 10 mol% of MV-anchor incorporated and 0.1mol% of NBD-lipid dye for imaging of the vesicles. To these solutions WGG-YFP (4 μ M) and different amounts of Q8 are added (0-25 μ M), in 10 mM phosphate buffer at pH 7.

Differential Scanning Calorimetry

DSC measurements are performed using a Microcal VP DSC calorimeter. Data were collected over a typical range of 5 $^{\circ}$ C to 75 $^{\circ}$ C at 1 $^{\circ}$ C/min, with the appropriate buffer as reference. Data is analyzed using the software provided by Microcal. Vesicles used for DSC analysis, are prepared as described below, using phosphate buffer, 10 mM pH 7.0. After preparation, the samples are cooled, degassed and placed using Hamiltonian gastight syringe.

Vesicle preparation

Vesicles are prepared using glass film rehydration and when necessary extrusion for adjusting size. Stock solutions of DPPC in chloroform (100 mM) and MV-anchor (10 mM) in EtOH are mixed in the appropriate amounts. In a typical preparation, for a 1 mL vesicle solution at 1mM DPPC and 10mol% MV-anchor, 10 μ L of DPPC and 10 μ L MV-anchor are mixed in a 4mL vial. A thin film is formed, by removing the organic solvents in vacuo under continuous rotation and the film is dried under vacuum for 2hrs. After addition of 1 mL buffer, the vial is vortexed at 200rpm for 30min at \sim 40 $^{\circ}$ C. To form unilamellar vesicle, 10 freeze-thaw cycles were applied by freezing in liquid N₂ and heating in a water bath at 70 $^{\circ}$ C. When required the vesicle solutions are extruded through polycarbonate membranes of 1000nm, 400nm and 100nm at 45 $^{\circ}$ C for the DPPC vesicles and RT for DOPC vesicles. Size distribution is checked using DLS, Zetasizer Malvern.

Amino acid sequence and molecular weight of the WGG-YFP

MW = 28685 Da

WGGASWSHPQ	FEKSAMVSKG	E E L	F T G V V P I
LVELDGDVNG	HKFSVSGE	GDATYGKLT	KFICTTGKLP VPWPTLVTF GYGLQCFARY
PDHMKQHDF	KSAMPEGYVQ	ERTIFFKDDG	NYKTRAEVKF E G D T L V N R I E
LKGIDFKEDG	NILGHKLEYN	YNSHNVYIMA	DKQKNGIKVN FKIRHNIEDG
SVQLADHYQQ	NTPIGDGPVL	LPDNHYLSYQ	SKLSKDPNEK RDHMLVLEFV
TAAGITLGMD	ELYK		

Amino acid sequence and molecular weight of the MGG-YFP

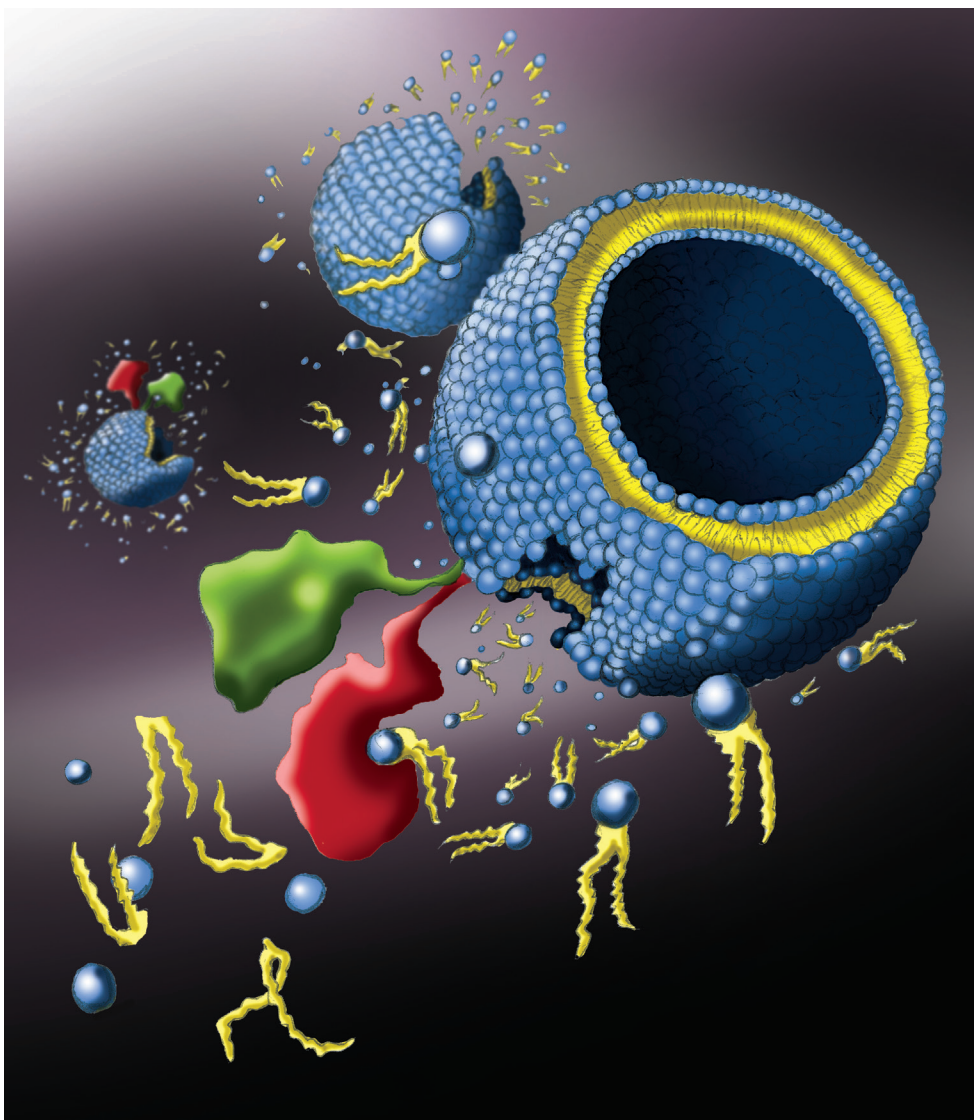
MW = 28630 Da

MGGASWSHPQ	FEKSAMVSKG	E E L	F T G V V P I
LVELDGDVNG	HKFSVSGE	GDATYGKLT	KFICTTGKLP VPWPTLVTF GYGLQCFARY
PDHMKQHDF	KSAMPEGYVQ	ERTIFFKDDG	NYKTRAEVKF E G D T L V N R I E
LKGIDFKEDG	NILGHKLEYN	YNSHNVYIMA	DKQKNGIKVN FKIRHNIEDG
SVQLADHYQQ	NTPIGDGPVL	LPDNHYLSYQ	SKLSKDPNEK RDHMLVLEFV
TAAGITLGMD	ELYK		

7.5 References

1. C. F. Snook, J. A. Jones, Y. A. Hannun, Sphingolipid-binding proteins. *Biochimica et Biophysica Acta (BBA) - Molecular and Cell Biology of Lipids* **1761**, 927-946 (2006); DOI:10.1016/j.bbalip.2006.06.004.
2. T. Baumgart, Mechanisms of Membrane Shaping by Peripheral Proteins. *Biophysical Journal* **108**, 353a (2015); DOI:10.1016/j.bpj.2014.11.1935.
3. W. Cho, R. V. Stahelin, Membrane-Protein Interactions in Cell Signaling and Membrane Trafficking. *Annual Review of Biophysics and Biomolecular Structure* **34**, 119-151 (2005); DOI:10.1146/annurev.biophys.33.110502.133337.
4. M. N. Teruel, T. Meyer, Translocation and Reversible Localization of Signaling Proteins: A Dynamic Future for Signal Transduction. *Cell* **103**, 181-184 (2000); DOI:10.1016/S0092-8674(00)00109-4.
5. P. Jonkheijm, D. Weinrich, H. Schröder, C. M. Niemeyer, H. Waldmann, Chemical Strategies for Generating Protein Biochips. *Angewandte Chemie International Edition* **47**, 9618-9647 (2008); DOI:10.1002/anie.200801711.
6. G. Triola, H. Waldmann, C. Hedberg, Chemical Biology of Lipidated Proteins. *ACS Chemical Biology* **7**, 87-99 (2012); DOI:10.1021/cb200460u.
7. L. Brunsveld, J. Kuhlmann, H. Waldmann, Synthesis of palmitoylated Ras-peptides and -proteins. *Methods* **40**, 151-165 (2006); DOI:10.1016/j.ymeth.2006.04.014.
8. E. Saxon, C. R. Bertozzi, Cell Surface Engineering by a Modified Staudinger Reaction. *Science* **287**, 2007-2010 (2000); DOI:10.1126/science.287.5460.2007.
9. Y. Teramura, Y. Kaneda, T. Totani, H. Iwata, Behavior of synthetic polymers immobilized on a cell membrane. *Biomaterials* **29**, 1345-1355 (2008); DOI:10.1016/j.biomaterials.2007.11.048.
10. A. K. Rudd, J. M. Valls Cuevas, N. K. Devaraj, SNAP-Tag-Reactive Lipid Anchors Enable Targeted and Spatiotemporally Controlled Localization of Proteins to Phospholipid Membranes. *Journal of the American Chemical Society* **137**, 4884-4887 (2015); DOI:10.1021/jacs.5b00040.
11. D. A. Uhlenheuer, D. Wasserberg, C. Haase, H. D. Nguyen, J. H. Schenkel, J. Huskens, B. J. Ravoo, P. Jonkheijm, L. Brunsveld, Directed Supramolecular Surface Assembly of SNAP-tag Fusion Proteins. *Chemistry – A European Journal* **18**, 6788-6794 (2012); DOI:10.1002/chem.201200238.
12. F. Versluis, J. Voskuhl, B. van Kolck, H. Zope, M. Bremmer, T. Albregtse, A. Kros, In Situ Modification of Plain Liposomes with Lipidated Coiled Coil Forming Peptides Induces Membrane Fusion. *Journal of the American Chemical Society* **135**, 8057-8062 (2013); DOI:10.1021/ja4031227.
13. H. D. Nguyen, D. T. Dang, J. L. J. van Dongen, L. Brunsveld, Protein Dimerization Induced by Supramolecular Interactions with Cucurbit[8]uril. *Angewandte Chemie International Edition* **49**, 895-898 (2010); DOI:10.1002/anie.200904413.
14. R. Behrend, E. Meyer, F. Rusche, I. Ueber Condensationsprodukte aus Glycoluril und Formaldehyd. *Justus Liebigs Annalen der Chemie* **339**, 1-37 (1905); DOI:10.1002/jlac.19053390102.
15. J. del Barrio, P. N. Horton, D. Lãirez, G. O. Lloyd, C. Toprakcioglu, O. A. Scherman, Photocontrol over Cucurbit[8]uril Complexes: Stoichiometry and Supramolecular Polymers. *Journal of the American Chemical Society* **135**, 11760-11763 (2013); DOI:10.1021/ja406556h.
16. A. González-Campo, M. Brasch, D. A. Uhlenheuer, A. Gómez-Casado, L. Yang, L. Brunsveld, J. Huskens, P. Jonkheijm, Supramolecularly Oriented Immobilization of Proteins Using Cucurbit[8]uril. *Langmuir* **28**, 16364-16371 (2012); DOI:10.1021/la303987c.
17. C. Márquez, R. R. Hudgins, W. M. Nau, Mechanism of Host–Guest Complexation by Cucurbituril. *Journal of the American Chemical Society* **126**, 5806-5816 (2004); DOI:10.1021/ja0319846.
18. W. Ong, A. E. Kaifer, Molecular Encapsulation by Cucurbit[7]uril of the Apical 4,4'-Bipyridinium Residue in Newkome-Type Dendrimers. *Angewandte Chemie International Edition* **42**, 2164-2167 (2003); DOI:10.1002/anie.200250214.
19. M. E. Bush, N. D. Bouley, A. R. Urbach, Charge-Mediated Recognition of N-Terminal Tryptophan in Aqueous Solution by a Synthetic Host. *Journal of the American Chemical Society* **127**, 14511-14517 (2005); DOI:10.1021/ja0548440.
20. H.-J. Kim, J. Heo, W. S. Jeon, E. Lee, J. Kim, S. Sakamoto, K. Yamaguchi, K. Kim, Selective Inclusion of a Hetero-Guest Pair in a Molecular Host: Formation of Stable Charge-Transfer Complexes in Cucurbit[8]uril. *Angewandte Chemie International Edition* **40**, 1526-1529 (2001); DOI:10.1002/1521-3773(20010417)40:8<1526::AID-ANIE1526>3.0.CO;2-T.
21. J. Kim, I.-S. Jung, S.-Y. Kim, E. Lee, J.-K. Kang, S. Sakamoto, K. Yamaguchi, K. Kim, New Cucurbituril Homologues: Syntheses, Isolation, Characterization, and X-ray Crystal Structures of Cucurbit[n]uril (n = 5, 7, and 8). *Journal of the American Chemical Society* **122**, 540-541 (2000); DOI:10.1021/ja993376p.
22. D. A. Uhlenheuer, J. F. Young, H. D. Nguyen, M. Scheepstra, L. Brunsveld, Cucurbit[8]uril induced heterodimerization of methylviologen and naphthalene functionalized proteins. *Chemical Communications* **47**, 6798-6800 (2011); DOI:10.1039/C1CC11197C.
23. V. Sindelar, M. A. Cejas, F. M. Raymo, W. Chen, S. E. Parker, A. E. Kaifer, Supramolecular Assembly of 2,7-Dimethyldiazapyrenium and Cucurbit[8]uril: A New Fluorescent Host for Detection of Catechol and Dopamine. *Chemistry – A European Journal* **11**, 7054-7059 (2005); DOI:10.1002/chem.200500917.
24. B. Escuder, M. LLusar, J. F. Miravet, Insight on the NMR Study of Supramolecular Gels and Its Application to Monitor Molecular Recognition on Self-Assembled Fibers. *The Journal of Organic Chemistry* **71**, 7747-7752 (2006); DOI:10.1021/jo0612731.
25. S. A. J. van der Meulen, G. V. Dubacheva, M. Dogterom, R. P. Richter, M. E. Leunissen, Quartz Crystal Microbalance with Dissipation Monitoring and Spectroscopic Ellipsometry Measurements of the Phospholipid Bilayer Anchoring Stability and Kinetics of Hydrophobically Modified DNA Oligonucleotides. *Langmuir* **30**, 6525-6533 (2014); DOI:10.1021/la500940a.

26. R. P. G. Bosmans, Technische Universiteit Eindhoven, (2015), Supramolecular systems to modulate protein assembly.
27. T. Felekis, L. Tziवेleka, D. Tsiourvas, C. M. Paleos, Liquid Crystals Derived from Hydrogen-Bonded Supramolecular Complexes of Pyridinylated Hyperbranched Polyglycerol and Cholesterol-Based Carboxylic Acids. *Macromolecules* **38**, 1705-1710 (2005); DOI:10.1021/ma047958p.
28. F. M. Menger, V. A. Azov, Cytomimetic Modeling in Which One Phospholipid Liposome Chemically Attacks Another. *Journal of the American Chemical Society* **122**, 6492-6493 (2000); DOI:10.1021/ja000504x.
29. V. Ramalingam, S. K. Kwee, L. M. Ryno, A. R. Urbach, A cucurbit[8]uril sponge. *Organic & Biomolecular Chemistry* **10**, 8587-8589 (2012); DOI:10.1039/C2OB26774H.
30. S. Yi, A. E. Kaifer, Determination of the Purity of Cucurbit[n]uril (n = 7, 8) Host Samples. *The Journal of Organic Chemistry* **76**, 10275-10278 (2011); DOI:10.1021/jo2018312.
31. R. H. Newman, M. D. Fosbrink, J. Zhang, Genetically Encodable Fluorescent Biosensors for Tracking Signaling Dynamics in Living Cells. *Chemical Reviews* **111**, 3614-3666 (2011); DOI:10.1021/cr100002u.



Enzymes coupled to self-assembled materials.

Illustration by Aaron Dijkstra.

The enzymes (green, red) are coupled to the vesicle surface, upon which they become active and are able to perform tasks, such as a chemical reaction. The above illustrated process was the original inspiration for the research in chapter 7 and forms an inspiring step towards complexity in materials.

Summary

Living creatures exist for an important part out of soft material, such as skin, organs and cells, that are formed by the self-assembly of molecular building blocks. Specific interactions of the molecular building blocks lead to the spontaneous assembly into larger organized structures, for example molecules that self-assemble into fibers and eventually form a macroscopic material, a gel. For the every day survival in nature, it is important that these materials show properties such as healing and self-organizing behavior. Biological cellular systems (materials) achieve this by sustaining dynamic processes within the cells through the consumption of chemical energy. This principle puts these materials out-of-equilibrium and the dynamic processes can only occur for as long as there is an energy source present.

Natural materials are continuously active with dynamic processes occurring, such as growth, shrinkage and transport mechanisms under the consumption of energy. For example, actin within cells forms self-assembled fiber networks under the consumption of a chemical fuel. The rapid growth and shrinkage of these networks leads to the movement of cells. The biological functioning and material properties of cells originate from the complexity of multiple interacting mechanisms, such as out-of-equilibrium self-assembled structures, reaction-diffusion processes and protein interactions. The research on out-of-equilibrium self-assembly for new soft material approaches forms a challenge that is addressed in this thesis. Extending the knowledge on out-of-equilibrium self-assembly and reaction-diffusion of self-assembling molecules will open new opportunities for programmable and self-healing materials.

In this thesis a new design approach for out-of-equilibrium formed self-assembled materials is described and tested experimentally. A key development is the chemical fuel driven self-assembly of molecular gelators and colloidal particles. Using thermodynamic insights for the out-of-equilibrium self-assembly an understanding of the different processes is obtained. Then the development of an organic reaction-diffusion based system results in the spatial organization of self-assembled materials. Finally, a step towards controlled enzyme interactions by materials is made through the immobilization of proteins to self-assembled materials.

First, the importance of new approaches for soft materials and the main challenges for this research are introduced in chapter 1. In chapter 2, the relevant developments in the fields of out-of-equilibrium self-assembly and Reaction-Diffusion (RD) systems are discussed, which are important in natural materials. For example skin patterns, which can be achieved by spatial organization of the components according to the RD model. Furthermore, from recent scientific examples of out-of-equilibrium self-assembled materials show that new functionalities can be achieved, for example directed movement.

In chapter 3, the new design approach for out-of-equilibrium active materials is introduced. It is demonstrated that by the supply of chemical energy, molecular

assemblies are formed far from thermodynamic equilibrium. The formed materials show properties and behavior, such as lifetimes and self-regeneration capability depending on fuel levels and are continuously active. These active materials are a key step towards synthetic self-organizing out-of-equilibrium systems.

In chapter 4, the design approach is used to develop a new colloidal out-of-equilibrium self-assembled system. To this end, colloidal particles are prepared with carboxylic acid carrying polymer hairs and the self-assembly process is driven by a methylation reaction. The aggregates show transient self-assembly and the particles can be recycled. This work shows the generality of the design principles for out-of-equilibrium self-assembly.

To understand the principles of out-of-equilibrium self-assembly, the thermodynamic framework is discussed, in chapter 5. Based on the thermodynamic principles of equilibrium self-assembly and extension is made to non-equilibrium situations. It is found that a stationary self-assembled situation can occur out-of-equilibrium, under the continuous consumption of chemical energy. Extensions of the model are discussed for more unique behavior such as bi-stability due to non-linear and autocatalytic formation kinetics.

In chapter 6, an organic self-assembling reaction-diffusion system is explored for the patterning and shaping of soft materials. The combined reaction-diffusion and self-assembly (RD-SA) of a supramolecular gelator leads to the formation of shaped organic soft material. The shape, size and dimensions are controlled through the used RD parameters, such as diffusion length and reaction kinetics. It is shown that the self-assembled structures can also be functionalized with molecular recognition sites for binding of proteins.

In the last chapter, the reversible binding of proteins to lipid bilayers is explored, as example for interactions between materials and proteins. The supramolecular host-guest binding of a Yellow Fluorescent Protein (YFP) to lipid bilayers is reported. The host-guest interactions of cucurbit[8]uril (Q8), the YFP and a lipid bound methyl viologen (MV^{2+}) are used for the successful binding to supported bilayers. This is a selective binding which is formed reversible. This work is an interesting step towards the supramolecular binding of peripheral proteins onto self-assembled materials.

In conclusion, the research in this thesis presents multiple new approaches to out-of-equilibrium self-assembled materials and forms an important development towards the complexity of biological materials. The first steps are taken into developing self-assembled material with programmable properties, leading to materials that are self-healing and re-usable. Through the findings in this research new applications for soft materials can be developed based on the out-of-equilibrium self-assembly.

Samenvatting

Levende wezens bestaan voor een belangrijk gedeelte uit zachte materialen, zoals de huid, organen en cellen. Deze materialen zijn gevormd door de zelfassemblage van moleculaire bouwstenen. De specifieke interacties tussen die moleculaire bouwstenen zorgen voor de spontane assemblage tot grote georganiseerde structuren, bijvoorbeeld moleculen die assembleren tot vezels en samen een macroscopisch materiaal vormen; een gel. Voor de dagelijkse overlevingsstrijd in de natuur is het belangrijk dat deze materialen eigenschappen bezitten zoals helend en zelforganiserend gedrag. Biologische cellen (materialen) gebruiken hiervoor continue dynamische processen, die door het verbruik van chemische energie onderhouden worden. Dit proces plaatst deze materialen uit hun thermodynamisch evenwicht en kan alleen doorgaan zolang er energie aanwezig is. Natuurlijke materialen zijn dus continu actief doordat er dynamische processen plaatsvinden, zoals groei, krimp en transportmechanismen. Een voorbeeld is het actinenetwerk in cellen, dat uit gezelfassembleerde fibers bestaat en gevormd wordt door verbruik van een chemische brandstof. Het voortdurend groeiende en krimpende gedrag van deze netwerken zorgt voor de beweging van cellen. De materiaaleigenschappen en het biologisch functioneren van cellen komt voort uit de complexiteit van meerdere interacterende processen, zoals uit-evenwicht zelfassemblage, reactie-diffusie processen en eiwitmechanismen. Onderzoek aan uit-evenwicht gezelfassembleerde structuren is een grote uitdaging en wordt behandeld in dit proefschrift. De inzichten en kennis van uit-evenwicht zelfassemblage zal nieuwe mogelijkheden creëren voor programmeerbare en zelfhelende materialen.

In dit proefschrift wordt een nieuwe ontwerpmethode van uit-evenwicht gevormde gezelfassembleerde materialen beschreven en experimenteel getest. Een belangrijk aspect van deze methode is de door chemische brandstof gedreven zelfassemblage van moleculaire gelatoren en colloïdale deeltjes. Inzicht in deze processen wordt verkregen aan de hand van thermodynamische principes voor de uit-evenwicht situatie. De ontwikkeling van een organisch reactie-diffusiesysteem (RD) resulteert in de ruimtelijke organisatie en controle van gezelfassembleerde materialen. Uiteindelijk wordt er een stap gemaakt naar materiaalgecontroleerde eiwitinteracties.

Eerst wordt het belang van een nieuwe aanpak voor zachte materialen uitgelegd, gevolgd door de belangrijkste uitdagingen in dit onderzoek. In hoofdstuk 2 worden vervolgens de relevante ontwikkelingen behandeld van uit-evenwicht zelfassemblage en reactie-diffusiesystemen, twee belangrijke aspecten van natuurlijke materialen. Volgens het RD-model ontstaan bijvoorbeeld huidpatronen door de ruimtelijke organisatie van de componenten. Recente wetenschappelijke onderzoeken met uit-evenwicht gezelfassembleerde materialen laten zien dat nieuwe functies, zoals gerichte beweging, kunnen ontstaan. Ruimtelijke organisatie en uit-evenwicht zelfassemblage zijn dus belangrijke onderdelen voor het functioneren van natuurlijke zachte materialen.

In hoofdstuk 3 wordt een nieuwe ontwerpmethode voor uit-evenwicht materialen

besproken evenals de experimentele ontwikkeling daarvan. Hier wordt getoond dat de moleculaire structuren in een uit-evenwicht situatie worden gevormd door de toevoer van chemische brandstof. De gevormde materialen hebben unieke eigenschappen, zoals levensduur en herstelcapaciteit, die afhankelijk zijn van het brandstofniveau en continu actief zijn. Deze actieve materialen zijn een belangrijke vooruitgang van natuurgeïnspireerde synthetische uit-evenwicht systemen.

In hoofdstuk 4 wordt de nieuwe ontwerpmethode toegepast ten behoeve van de ontwikkeling van een colloïdaal uit-evenwicht zelfassemblerend systeem. Hiervoor worden colloïdale deeltjes met reactieve haren gesynthetiseerd. Deze bevatten carbonzuurgroepen, zodat ze uit-evenwicht gedreven kunnen worden door een methyleringsreactie. De aggregaten vertonen tijdelijke zelfassemblage en de deeltjes kunnen worden gerecycled. Deze bevindingen laten zien dat de uit-evenwicht methode algemeen kan worden gebruikt, bijvoorbeeld voor de toepassing in colloïdale systemen.

Om de principes van uit-evenwicht zelfassemblage te begrijpen, wordt hiervan het thermodynamische raamwerk behandeld in hoofdstuk 5. Er wordt een theoretische uitbreiding gemaakt van de thermodynamische principes voor zelfassemblage naar een uit-evenwicht situatie. Een stationaire situatie kan gevormd worden indien de zelfassemblage plaatsvindt uit-evenwicht door het continue verbruik van chemische energie.

In hoofdstuk 6 wordt een organisch zelfassemblerend reactie-diffusiesysteem onderzocht voor de ruimtelijke organisatie van zachte materialen. Door de reactie-diffusie en zelfassemblage (RD-SA) van supramoleculaire gelatoren wordt materiaal gecreëerd met een gecontroleerde vorm en grootte. De dimensies van de materialen worden bepaald door de RD-parameters, zoals de diffusielengte en reactiesnelheid. De gevormde materiaalstructuur kan ook gefunctionaliseerd worden met moleculaire herkenningsmotieven voor het binden van eiwitten.

In het laatste hoofdstuk wordt het omkeerbaar binden van eiwitten aan gezelfassemblerde lipide bilagen verkend, als voorbeeld voor toekomstige terugkoppelingsmechanismen tussen materiaal en eiwitten. De binding van een Yellow Fluorescent Protein (YFP) aan lipide bilagen wordt bereikt door supramoleculaire 'host-guest' interacties. Deze binding is selectief en kan omkeerbaar gemaakt worden. Dit werk is een stap in de richting van het supramoleculair binden van perifere eiwitten aan gezelfassemblerde materialen.

Concluderend, het onderzoek in deze thesis toont meerdere nieuwe methoden en nieuwe uit-evenwicht gezelfassemblerde materialen, die samen een stap richting de synthese van de complexiteit van biologische materialen zijn. De nieuwe materialen hebben programmeerbare eigenschappen, zijn uit-evenwicht en vertonen daardoor zelfhelend gedrag of zijn herbruikbaar. Met de methoden in dit onderzoek kunnen nieuwe toepassingen voor zachte materialen worden ontwikkeld op basis van uit-evenwicht zelfassemblage.

Acknowledgements

You never reach the summit alone, especially something as challenging as a PhD. Facing this challenge has been a great experience, especially because of all the people around me, from whom I had help, support and friendship. Hereby I would like to thank all you supporters around me.

Jan, thank you for giving me this opportunity and for the continuous challenge during the four years. The problems we faced and solved have led to this thesis and some very nice publications. Thank you. Rienk, thank you for your support, sharp advice and always willing to listen to my questions and ideas. Without your support I would not have enjoyed and endured the PhD as good as I did now. Thank you. I also want to thank the committee members, Wilhelm, Thomas, Michiel, and Ernst for reviewing my work and challenging me during the defense. Luc, I want to thank you for your support and advice in the cooperation of me and Ralph in our complexity project. It was always pleasant to come to Eindhoven for our teamwork.

Ger, your faith, support and enthusiasm have helped me along the way. I always enjoyed our discussion and our cooperation's. Thank you for being my supporter. Stephen, as extra committee member, founder of the 'Elektrisch Kabinet' and your ever wondering questions and ideas have given me fun and challenges over the last years. Eduardo, for the talks about surfing and life. Thank you.

Ralph, it has been a memorable four years in which we challenged the complexity project together and gained new experiences for life. I'm proud on our cooperation and what we achieved, two thesis's and a good publication. Thank you.

As part of the ASM research group, I had a lot of 'scientific' friendship in the lab and fun outside our working space. The dinner parties, coffee breaks, trips abroad, or just drinking beers on Thursday, made my research so much better. Thank you all for that! Some of the persons I want to thank especially;

Elena, roommate and partner in crime for getting a new job. Sharing my ideas, and thoughts with you has been relieving and inspiring. Your passion and professionalism are inspirations to me and I know for certain that you are a great chemist and person, no doubt about that! Dainius, you have been my tutor from the start and unknowingly my inspiration to endure the hard challenges of a PhD, thank you. Emanuela, your enthusiasm, down-to-earth engineering mindset and party mode helped me throughout the years to overcome the ever-present challenges in a PhD. Thank you, also for being my paranymph. Simge, thank you for the food, coffee, parties and synthetic advice. The cat is still in the lab and will keep our history alive. Jos, our history goes back for a long way and I'm proud to have worked on your side. I know that you are able to finish the PhD and enjoyed your synthesis knowledge and 'funny' jokes. Matija, our teamwork has been challenging for us both and I've learned a lot of working together with you. All the

luck with your future projects and I hope that you will find your balance. Susan, already a year we've been working together and it's nice to see how fast you have developed into a self-supporting researcher. I'm proud to have worked together with you. Roman, thank you for the good times, the fun and the discussions. I always enjoyed your company and think it's very cool that you try to find your way in the Dutch industry. Chandan, thank you for our nice talks, working together and just enjoying the lab time. You have been like an big brother to me. I'm certain that you will find a nice place in academia and wish you all the luck in finding it. Vincent, Sander, Tony, thank you for your responsibility and the nice times around the lab. Frank, thank you for the help with the thesis and the nice talks. I'm grateful and proud to have worked together with all of you and am honored to call you my friends.

Mieke, Louw, Ben, Marcel, Lars, zonder jullie valt het ASM kaartenhuis in elkaar en ik dank jullie hartelijk voor alle steun en hulp. De afgelopen jaren heb ik misschien wel het meeste van jullie geleerd en respecteer ik jullie steun aan ons 'wetenschappers' het allermeeeste. Het is niet altijd gemakkelijk om zo'n team vol jonge enthousiaste honden ook hun rotzooi te laten opruimen maar jullie hielpen en steunden ons en corrigeerde daar waar nodig. Marcel, dank je wel voor de mooie momenten bij het Elektrisch Kabinet en onze leuke gesprekken. Lars, ik vind jouw levensinstelling prachtig en dank je hartelijk voor alle spontane acties. Louw, jouw ongezouten mening laat een grote indruk achter, maar voor mij ben je een zorgzame collega geweest, dank je wel. I also thank all the other group members for their enthusiasm; the pages are just too short to mention you all. Many of you have become my friends and I'm certain that we'll remain that until the end of days.

Over the years I enjoyed with many more in the ChemE building, and hereby I want to thank you all for that; Florian, Kathrin, Frank, Kristina, Ferdinand, Tom, Moreno, Bartek, Steffen, Jonathan, Caroline, Wuyuan, Jeroen, Ruben, Maarten, Louis, Daniela. Christophe, begonnen als collega en nu geëindigd als vriend. Dank je wel voor alle mooie momenten. Regilio, Joen, Dafne, Jesper en LO studenten, ik hoop dat ik een goede begeleider was voor jullie. Jullie waren mijn spiegel en de ontwikkelingen die jullie doorgingen maakten mij trotser dan de wetenschappelijke uitkomsten. Ieder van jullie heeft mij veel geleerd en ik ben daardoor een beter person geworden. Ik ben trots op ieder van jullie en wat we samen bereikt hebben. Dank jullie wel.

In dit werk heb ik veel samenwerkingsprojecten mogen opstarten en uitvoeren, met economen, wiskundigen en andere chemici. Ieder project en idee was weer een nieuwe mooie ervaring. Bas, het is prachtig om te zien hoe een simpel idee zo snel in een succesvol project kan ontwikkelen. Dank je wel voor de fijne samenwerking. Laten we onze best doen om het gepubliceerd te krijgen. Domenico, together we challenge the modeling of out-of-equilibrium materials but especially thank you for having such big faith in me.

Niels, als vriend, collega en paronym hebben we flink wat gewichten weg gezet. Het waren prachtige jaren samen en ik wens jou en Anne heel veel plezier met jullie eerste

kind. Bedankt.

Vele mooie momenten in Zandvoort en op andere universiteiten heb ik te danken aan de NWO Complexity groep. Wouter, Paul, Evelien, Otto en vele anderen, dank jullie wel voor de eeuwige interesse in de complexe andere kant van het verhaal maar ook gewoon een gezellig biertje drinken. Marieke, dank je wel dat alles altijd zo goed georganiseerd was en wij malle wetenschappers mochten discussiëren en leren van elkaar.

Christiaan, Jonne en Martijn, ik dank jullie voor de continue vriendschap en het surfen, ieder jaar weer een perfecte onderbreking. Zonder deze momenten en jullie steun was het allemaal een stuk minder leuk geweest. Bram, dank voor de gezellige avonden biertjes doen en over de promotie praten. Heel veel succes met je publicaties en aanvragen. Mark, Tim, Wouter en Pieter dank voor de lol, vriendschap en mountainbike weekenden. Patrick, succes met de laatste loodjes daarna gaan we weer naar een muziek optreden. Tijdens de afgelopen jaren heb ik nog heel veel mooie momenten gehad met vele vrienden, surfen, optredens, wielrennen, RepairCafe, culinaire etentjes, groentetuin, mountainbike weekenden, KHD wintersport, en nog veel meer. Bij deze wil ik iedereen ontzettend bedanken voor alle mooie momenten.

Natuurlijk wil ik mijn familie bedanken. Jullie steun, interesse en aanwezigheid heeft me altijd geholpen om verder te gaan en enthousiast te blijven. Lieve pap en mam, jullie steun en liefde heeft mij gemaakt wie ik ben en ik ben er trots op dat ik jullie zoon ben. Ben en Jolijn, dank jullie wel dat ik een onderdeel mag zijn van jullie familie. Broers, we vormen een mooi drietal en ik ben trots op jullie. Anja, Berto, schoonfamilie, ooms, tantes, neven en nichten, dank jullie allemaal. Het blijft voor mij geweldig om mijn onderzoek te mogen uitleggen aan mensen die zo oprecht geïnteresseerd zijn. Ondanks de vreemde woorden en rare teksten hoop ik dat dit boekwerk mijn onderzoek aan jullie een klein stukje duidelijker heeft gemaakt. Oma, u bent een inspiratie voor een ieder om u heen en ik ben blij dat ik u trots mag maken. Ik weet dat mijn gemiste Opa van Ek en Oma Hendriksen trots zijn op hun kleinkind.

Als laatste Janneke, de liefde van mijn leven. Jij hebt alles meegemaakt, de zwaarste momenten over je heen gekregen en hebt me altijd geholpen en vooruit gestuwd. Met jou zijn maakt mij een beter persoon en dit gehele boekwerk is een eerbetoon aan jou. Dank je wel en op naar een prachtige toekomst samen.

About the author

Wouter Egbert-Jan Hendriksen was born on the 4th of June 1985 in Beverwijk, the Netherlands. He obtained his B.Sc. degree in Molecular Science and Technology (2009) in the combined education of Leiden Universiteit and Technische Universiteit Delft. After this, he obtained his M.Sc degree in Chemical Engineering at the TU Delft (2011), where he did his masters project in the research group of prof. Jan van Esch. The project was aimed at the development of a self-assembling photocatalytic cell for direct hydrogen production from water. Furthermore, he did an industrial internship at Applied Materials, Alzenau, Germany in the field of silicon solar cells. After his masters degree he continued with a challenging Ph.D. research together with prof. Jan van Esch, and dr. Rienk Eelkema. This project was part of the NWO Complexity grand and in cooperation with prof. Luc Brunsveld, of the TU Eindhoven. The main research interests of Wouter are the development of new materials, products and the related processes. Combining his backgrounds in Chemical Engineering and Physical Chemistry he aims for creating more sustainable solutions for current industrial challenges.

In his spare time, Wouter is an enthusiastic wavesurfer and enjoys his racing bike, both throughout Europe. Furthermore, he frequently assists in het 'Elektrisch Kabinet' of prof. dr. Stephen Picken, showing the wonders of electricity and chemistry. When not working with chemistry, he is helping at the Repair Cafe in Den Haag. Here he repairs household equipment and learns guests how to do it themselves. With enthusiasm and a big smile he looks forward to a bright and more sustainable future.

List of Publications

1. J. Boekhoven, W. E. Hendriksen, G. J. M. Koper, R. Eelkema, J. H. v. Esch, Transient assembly of active materials fueled by a chemical reaction. *Science* **349**, 1075-1079 (2015); DOI:10.1126/science.aac6103.
2. C. Maity, W. E. Hendriksen, J. H. van Esch, R. Eelkema, Spatial Structuring of a Supramolecular Hydrogel by using a Visible-Light Triggered Catalyst. *Angewandte Chemie International Edition* **54**, 998-1001 (2015); DOI:10.1002/anie.201409198.
3. G. J. M. Koper, J. Boekhoven, W. E. Hendriksen, R. Eelkema, J. H. Van Esch, paper presented at the CSHM 2013: Proceedings of the 4th International Conference on Self-Healing Materials, June 16-20, 2013, Ghent, Belgium,, 2013-06-16 2013.
4. G. J. M. Koper, J. Boekhoven, W. E. Hendriksen, J. H. v. Esch, R. Eelkema, I. Pagonabarraga, J. M. Rubí, D. Bedeaux, The Lost Work in Dissipative Self-Assembly. *International Journal of Thermophysics* **34**, 1229-1238 (2013); DOI:10.1007/s10765-013-1464-5.
5. C. B. Minkenberg, W. E. Hendriksen, F. Li, E. Mendes, R. Eelkema, J. H. van Esch, Dynamic covalent assembly of stimuli responsive vesicle gels. *Chemical Communications* **48**, 9837-9839 (2012); DOI:10.1039/c2cc34863b.
6. R. P.G. Bosmans, Wouter E. Hendriksen, M. Verheijden, P. Jonkheijm, R. Eelkema, J. H. v Esch, L. Brunsveld, Supramolecular protein immobilization on lipid bilayers, *Chemistry –A European Journal*, (2015) *accepted*
7. J. S. Foster, J. M. Žurek, N.M. S. Almeida, Wouter E. Hendriksen, V. A. A. le Sage, V. Lakshminarayanan, R. Banerjee, R. Eelkema, H. Mulvana, M. J. Paterson, J. H. van Esch, G. O. Lloyd, Gelation Landscape Engineering using a Multi-Reaction Supramolecular Hydrogelator System, (2015) *submitted*.
8. Koper G.J.M., Hendriksen W.E., in Non-equilibrium Thermodynamics with Applications 2016, chapter 7, *Non-equilibrium molecular self-assembly, The Royal Society of Chemistry*, pp. 134–153.